Boston University

OpenBU **http://open.bu.edu**

Boston University Theses & Dissertations Boston University Theses & Dissertations

2014

Enhanced information extraction in the multi-energy x-ray tomography for security

https://hdl.handle.net/2144/11131

"Downloaded from OpenBU. Boston University's institutional repository."

BOSTON UNIVERSITY

COLLEGE OF ENGINEERING

Dissertation

ENHANCED INFORMATION EXTRACTION IN MULTI-ENERGY X-RAY TOMOGRAPHY FOR SECURITY

by

LIMOR MARTIN

B.Sc., Ben-Gurion University of the Negev, 2006
M.S., Boston University, 2010

Submitted in partial fulfillment of the

requirements for the degree of

Doctor of Philosophy

2014

© 2014 by
Limor Martin
All rights reserved

Approved by

First Reader [redacted]

W. Clem Karl, PhD
Professor of Electrical and Computer Engineering
Professor of Biomedical Engineering

Second Reader [redacted]

Prakash Ishwar, PhD
Associate Professor of Electrical and Computer Engineering

Third Reader [redacted]

David A. Castañón, PhD
Professor of Electrical and Computer Engineering

Fourth Reader [redacted]

Charles A. Bouman, PhD
Professor of Electrical and Computer Engineering
Professor of Biomedical Engineering
Purdue University

Acknowledgments

Over the course of my PhD studies I have been fortunate to work with highly knowledgeable and experienced researchers, whose guidance was invaluable to my success. First and foremost, I would like to thank my advisor Prof. Clem Karl for all his support and for showing me how to conduct principled research, as well as present my work effectively. I appreciate Prof. Karl's friendly and motivating advising style and have learned a lot from his approach to research and teaching. His suggestions have constantly made me aim for novelty and excellence in my work. I would also like to thank my co-advisor Prof. Prakash Ishwar who has worked closely with me throughout the years. His enthusiasm and meticulous research approach has helped tremendously to expand my thinking and develop my ideas. I wish to thank Prof. David Castañón and Prof. Charles Bouman, who were members of my dissertation committee, for their important feedback and advice. I am grateful for Prof. Castañón's guidance throughout my PhD. I have also worked with Dr. Homer Pien, Dr. Synho Do, Ahmet Tuysuzoglu and Dr. Carl Crawford, and I thank them for insightful discussions and collaboration. I would like to extend a special thanks to Prof. Michael Silevitch and the ALERT center of excellence for their efforts to support and educate myself and the other students.

Being part of the ISS lab has been a great experience. I wish to thank my BU friends who have made me feel at home away from home: Ahmet, Ajay, Anne, Aydan, Berkin, Birant, Bryan, Cem, Cristina, Darin, Delaram, Emir, George, Gilberto, Ivana, Karen, Ke, Kirill, Niloofar, Santosh, Sarah, Sonal, Shuchin, Theodora, Ye, and Zach. I especially thank my first office mate Sonal, who showed me the ropes, and my second office mate Berkin who made our office pleasant and fun. I am also grateful to my friends outside of BU, Noga, Sarit, Tali, Rotem and Nurit, who have not let time or distance affect our friendship.

Last but not least, I would like to thank my loving family. My wonderful parents, Miriam and David, have been a constant source of support and encouragement. My grandmother Frida has been proud of me and given me the confidence to succeed. My sister Idit and brother Ory and their families were there for me all along the way. My husband's parents Roz and Bill have helped and supported me. Most of all, I thank my dear husband Daniel for believing in me and cheering me on.

I would also like to acknowledge the funding agency. The material in this dissertation is based upon work supported by the U.S. Department of Homeland Security, Science and Technology Directorate. The views and conclusions contained in this document are those of the authors and should not be interpreted as necessarily representing the official policies, either expressed or implied, of the U.S. Department of Homeland Security.

ENHANCED INFORMATION EXTRACTION IN MULTI-ENERGY X-RAY TOMOGRAPHY FOR SECURITY

LIMOR MARTIN

Boston University, College of Engineering, 2014

Major Professors: W. Clem Karl, PhD
Professor of Electrical and Computer Engineering
Professor of Biomedical Engineering

Prakash Ishwar, PhD
Professor of Electrical and Computer Engineering
Professor of Biomedical Engineering

ABSTRACT

X-ray Computed Tomography (CT) is an effective nondestructive technology widely used for medical diagnosis and security. In CT, three-dimensional images of the interior of an object are generated based on its X-ray attenuation. Conventional CT is performed with a single energy spectrum and materials can only be differentiated based on an averaged measure of the attenuation. Multi-Energy CT (MECT) methods have been developed to provide more information about the chemical composition of the scanned material using multiple energy-selective measurements of the attenuation. Existing literature on MECT is mostly focused on differentiation between body tissues and other medical applications. The problems in security are more challenging due to the larger range of materials and threats which may be found. Objects may appear in high clutter and in different forms of concealment. Thus, the information extracted

by the medical domain methods may not be optimal for detection of explosives and improved performance is desired.

In this dissertation, learning and adaptive model-based methods are developed to address the challenges of multi-energy material discrimination for security. First, the fundamental information contained in the X-ray attenuation versus energy curves of materials is studied. For this purpose, a database of these curves for a set of explosive and non-explosive compounds was created. The dimensionality and span of the curves is estimated and their space is shown to be larger than two-dimensional, contrary to what is typically assumed. In addition, optimized feature selection methods are developed and applied to the curves and it is demonstrated that detection performance may be improved by using more than two features and when using features different than the standard photoelectric and Compton coefficients. Second, several MECT reconstruction methods are studied and compared. This includes a new structure-preserving inversion technique which can mitigate metal artifacts and provide precise object localization in the estimated parameter images. Finally, a learning-based MECT framework for joint material classification and segmentation is developed, which can produce accurate material labels in the presence of metal and clutter. The methods are tested on simulated and real multi-energy data and it is shown that they outperform previously published MECT techniques.

Contents

1 Introduction **1**

1.1 Dissertation contributions 2

1.2 Dissertation outline 4

2 Background **5**

2.1 Explosives detection 5

2.1.1 Identifying explosives 6

2.1.2 X-ray systems for explosives detection 7

2.2 X-ray computed tomography (CT) 8

2.2.1 The linear attenuation coefficient (LAC) 9

2.2.2 The scanning process 12

2.2.3 CT measurement model 14

2.2.4 Conventional CT image reconstruction 21

2.3 Multi-energy CT (MECT) 23

2.3.1 Acquisition methods 23

3 Current methods for MECT information extraction **25**

3.1 Models of the LAC 29

3.1.1 Photo-Compton 29

3.1.2 Basis materials 31

3.2 Pre-reconstruction MECT 32

3.2.1 Polynomial approximation of measurements 34

3.2.2 Constrained least-squares minimization 35

3.2.3 Empirical dual-energy calibration (EDEC) 36
3.3 Post-reconstruction MECT 38
3.3.1 Averaged image 38
3.3.2 Three-material decomposition 39
3.3.3 Basis material post-recon decomposition 40
3.3.4 ρZ Projection method 40
3.4 Other MECT techniques 42
3.4.1 Method for mismatched sinogram data 42
3.4.2 Alternating minimization algorithm for MECT 42
3.5 Experimental results with current methods 43
3.5.1 Estimation of effective atomic number and denisty using the ρZ projection method 43
3.5.2 Estimation of basis expansion coefficients from MECT measurements 52
3.5.3 Effect of calibration phantom design and materials on EDEC . 70

4 Estimating the dimensionality of the LACs **89**
4.1 Linear dimensionality estimation 90
4.1.1 Dimensionality of the exponentiated LACs 94
4.2 Nonlinear dimensionality estimation 95
4.3 Correlation between the LACs 98
4.4 Summary 100

5 Optimized LAC feature selection **101**
5.1 Feature selection methods 103
5.1.1 Unsupervised methods 104
5.1.2 Supervised methods 106
5.2 Classification performance evaluation 110

5.2.1 ROC curve metrics 110
5.2.2 Average classifier accuracy 112
5.3 Experimental results 113
5.3.1 Calculating the AUC 113
5.3.2 Energy level selection 115
5.3.3 Classification performance comparison 117
5.4 Summary 124

6 Reconstruction of material parameter images from MECT data 125

6.1 Extension of ρZ Projection for a larger set of materials 126
6.1.1 Experimental results 128
6.2 MECT reconstruction for mismatched ray paths 130
6.2.1 Experimental results 133
6.3 Empirical dual-energy calibration with kernel smoothing 138
6.4 Experimental results 140
6.4.1 Experiments with simulated data 140
6.4.2 Experiments with real data 144
6.5 Structure-preserving MECT inversion 152
6.5.1 Data weighting W_m 154
6.5.2 Solution approach 155
6.5.3 Practical implementation 156
6.5.4 Experimental results 156
6.6 Summary 165

7 Material identification using MECT 167

7.1 Dictionary based material labeling 169
7.1.1 Experimental results 172
7.2 Learning-based graph-cut material labeling 178

7.2.1 Method implementation 180
7.2.2 Experimental results 182
7.3 Summary 192

8 Conclusion **194**

8.1 Future work 196

A Compounds LAC database **198**

B Imatron scans database **211**

References **213**

Vita **220**

List of Tables

3.1 Z_{eff} and ρ estimates using the ρZ projection method applied to the DHS phantom. 47

3.2 Z_{eff} and ρ estimates using the ρZ projection method applied to slices from the Imatron scans database. 47

3.3 Combinations of basis materials giving the lowest percent errors according to LAC representation and according to EDEC performance. Materials on top give lowest error and the error increases as you go down the table. 87

5.1 Best single energy level and best combinations of two, three and four energy levels according to different criteria and methods. The energy levels are in keV. 116

6.1 $\hat{Z}_{eff}$ results for the materials in the simulants phantom. 2E refers to the ρZ projection method, and 4E refers to the extension of the method to four spectral functions. 129

A.1 Compounds dataset - materials properties 198

List of Figures

2·1 Z_{eff} vs. density ρ for common items found in airport luggage and for certain contraband and explosive materials [Eilbert and Krug, 1993]. 8

2·2 Illustration of Beer's Law (2.2) for a monochromatic X-ray beam through a homogeneous material. I_0 and I are the initial and final X-ray intensities and l is the length of the X-ray path. 9

2·3 Physical components of the mass attenuation coefficient for water (left) and iodine (right) [Berger et al., 2005] 10

2·4 X-ray CT scanner diagram [Zhang et al., 2007]. 12

2·5 Estimate of a 130 kVp X-ray source spectrum, Imatron CT scanner. Provided by Taly Gilat Schmidt, Marquette University. 13

2·6 Helical scan (left) versus step-and-shoot scan (right) 14

2·7 Geometry of tomographic measurements. An X-ray beam travels in a path defined by r and θ. The beam is attenuated by the object according to its size and chemical composition. The measurement at the detector is denoted by $p(r, \theta)$. The beam is assumed to be monochromatic. 16

2·8 Example of an object and the corresponding sinogram or Radon transform 17

2·9 Illustration of the LAC "volume" - depends on spatial location (x_1, x_2) and energy level E 17

2·10 Examples of two spectral weighting functions $W_1(E)$ and $W_2(E)$ [Heismann et al., 2003]. The functions are normalized to integrate to 1. The numbers 80kV and 140kV denote the maximum voltage applied across the X-ray tube for each spectra. 19

2·11 Illustration of beam hardening [Platten, 2007] 22

3·1 Diagram illustrating pre-reconstruction methods (on the left) and post-reconstruction methods (on the right) 28

3·2 Basis functions used in the Photo-Compton model. 30

3·3 The principle of three-material decomposition [Petersilka et al., 2008]. The basis materials (e.g., soft tissue, iodine, and bone) are connected by two vectors in a diagram that maps CT values obtained at low energy versus CT values obtained at high energy. The pixel shown between the two ideal lines contains both iodine and bone, quantified by the length of the respective dashed lines. 39

3·4 $F(Z)$ curve calculated using 80 kVp and 140 kVp Siemens spectral weighting functions 41

3·5 LLNL/DHS phantom 44

3·6 Siemens SOMATOM Definition dual-source scanner geometry 45

3·7 Images of results for DHS phantom. On the top are the reconstructed images of the same cross section obtained with different source spectra in HU. On the bottom are the corresponding Z_{eff} (left) and ρ (right). The images are 512×512. The objects from left to right are: water bottle, delrin bar and graphite rod. 46

3·8 ρZ projection method results for a slice with a graphite rod. On the top are the reconstructed images of the same cross section obtained with different source spectra in HU. On the bottom are the corresponding estimations Z_{eff} (left) and ρ (right). 48

3·9 ρZ projection method results for a slice with a Teflon rod. On the top are the reconstructed images of the same cross section obtained with different source spectra in HU. On the bottom are the corresponding estimations Z_{eff} (left) and ρ (right). 49

3·10 ρZ projection method results for a slice with a magnesium rod. On the top are the reconstructed images of the same cross section obtained with different source spectra in HU. On the bottom are the corresponding estimations Z_{eff} (left) and ρ (right). 50

3·11 ρZ projection method results for a slice with a silicon rod. On the top are the reconstructed images of the same cross section obtained with different source spectra in HU. On the bottom are the corresponding estimations Z_{eff} (left) and ρ (right). 51

3·12 Phantoms used for the simulations. On the top is the 'clean' phantom consisting of a body of water. On the bottom is the 'cluttered' phantom, which is same phantom with a small metal object. 53

3·13 Spectral weighting functions used in simulation of dual-energy measurements 54

3·14 Different initializations used. 55

3·15 Reconstruction of photoelectric coefficient image. The measurements are noise free. Each row shows the results for a different initialization: truth, zeros, flat and FBP. 56

3·16 Reconstruction of Compton coefficient image. The measurements are noise free. Each row shows the results for a different initialization: truth, zeros, flat and FBP. 57
3·17 Mean values of the photoelectric coefficient (top) and the Compton coefficient (bottom) inside the water region for the different initialization schemes. The pink dashed line indicates the true value. The errorbars represent plus and minus one standard deviation. 58
3·18 Reconstruction of photoelectric coefficient image using the different methods. Basic phantom. Top row: noise free; middle row: Low noise; Bottom row: high noise. Initialized with FBP. 59
3·19 Reconstruction of Compton coefficient image using the different methods. Basic phantom. Top row: noise free; middle row: Low noise; Bottom row: high noise. Initialized with FBP. 60
3·20 Mean values of the photoelectric coefficient (top) and the Compton coefficient (bottom) inside the water region for the different noise levels and the 'clean' phantom. The pink dashed line indicates the true value. The errorbars represent plus and minus one standard deviation. Initialization was done with the FBP method. 61
3·21 Reconstruction of photoelectric coefficient image using the different methods. Phantom with metal. Top row: noise free; middle row: Low noise; Bottom row: high noise. Initialized with FBP. 62
3·22 Reconstruction of Compton coefficient image using the different methods. Phantom with metal. Top row: noise free; middle row: Low noise; Bottom row: high noise. Initialized with FBP. 63

3·23 Mean values of the photoelectric coefficient (top) and the Compton coefficient (bottom) inside the water region for the different noise levels and the 'cluttered' phantom. The pink dashed line indicates the true value. The errorbars represent plus and minus one standard deviation. Initialization was done with the FBP method. 64

3·24 Effect of number of iterations on performance of AM algorithm. Low noise case, FBP initialization. 65

3·25 Photoelectric coefficient (left) and Compton coefficient (right) given by YNC (top), YNC-En (middle) and CM (bottom) for a 'clean' slice. The objects in this slice are a bottle of water and a bottle of doped water. Photoelectric image is in units of keV^3 and gray scale range [1000, 10000]. Compton image is in units of cm^{-1} and gray scale range [0, 0.3]. 68

3·26 Photoelectric coefficient (left) and Compton coefficient (right) given by YNC (top), YNC-En (middle) and CM (bottom) for a 'cluttered' slice. The objects in this slice include a teflon cube, a bottle of water and a stack of rubber sheets. Photoelectric image is in units of keV^3 and gray scale range [1000, 10000]. Compton image is in units of cm^{-1} and gray scale range [0, 0.3]. 69

3·27 Spectral weighting functions used in simulation of dual-energy measurements in EDEC experiments 70

3·28 Basis images $f_n(\vec{x})$ obtained in the calibration process using the Yin-Yang calibration phantom. n increases from left to right with $n = 0$ at the top left and $n = 24$ at the bottom right. 72

3·29 Histogram of values in reconstructed effective attenuation image $\bar{\mu}_2(\vec{x})$ of the Yin-Yang phantom used for constructing the template and weight images. The x-axis units are cm^{-1}. The horizontal yellow line shows the threshold we chose. By looking at the counts above the threshold, three distinct value ranges are given. The first range of values is between the red vertical lines. These values are close to zero and therefore correspond to the background. The second range of values is indicated by the green lines. It is close to 0.2 and corresponds to water. The third range, corresponding to aluminum, is indicated by the purple lines. 73

3·30 Summary of the EDEC calibration steps using the Yin-Yang phantom. Top: reconstructed effective attenuation images $\bar{\mu}_1(\vec{x})$ and $\bar{\mu}_2(\vec{x})$ obtained by applying FBP to $\tilde{I}_1$ and $\tilde{I}_2$. The lighter gray corresponds to the aluminum region and the darker gray corresponds to the water region. Middle: weight image $w_1(\vec{x})$, template image $t_1(\vec{x})$, and the final decomposed image $a_1(\vec{x})$ corresponding to water. Bottom: $w_2(\vec{x})$, $t_2(\vec{x})$ and $a_2(\vec{x})$ corresponding to aluminum. 74

3·31 Decomposed test phantom using Yin-Yang calibration. Left: water image. Right: aluminum image. The test phantom design is based on the standardized computed tomography dose index (CTDI) phantom and is composed of an ellipse of water with four small circles of aluminum and one small circle of graphite in the middle. 75

3·32 Calibration phantom designs (top) and test phantom design (bottom). Background (air) is in red, water is in green, aluminum is in blue and graphite is in purple (graphite is only in Figure (f)). 76

3·33 EDEC with Yin-Yang calibration phantom. Top: reconstructed effective attenuation images of the calibration phantom. Middle: estimated material coefficient images of the calibration phantom. Bottom: estimated material coefficient images of the test phantom 78
3·34 EDEC with half-half calibration phantom. Top: reconstructed effective attenuation images of the calibration phantom. Middle: estimated material coefficient images of the calibration phantom. Bottom: estimated material coefficient images of the test phantom 79
3·35 EDEC with two-cylinders calibration phantom. Top: reconstructed effective attenuation images of the calibration phantom. Middle: estimated material coefficient images of the calibration phantom. Bottom: estimated material coefficient images of the test phantom 80
3·36 EDEC with wedges calibration phantom. Top: reconstructed effective attenuation images of the calibration phantom. Middle: estimated material coefficient images of the calibration phantom. Bottom: estimated material coefficient images of the test phantom 81
3·37 EDEC with small wedges calibration phantom. Top: reconstructed effective attenuation images of the calibration phantom. Middle: estimated material coefficient images of the calibration phantom. Bottom: estimated material coefficient images of the test phantom 82
3·38 Images of the test phantom LAC at 70 keV. Top: true image. Middle and bottom: estimates obtained with the different calibration phantoms. 83

3·39 Top: general calibration phantom design, material 1 in blue, material 2 in green and background in red. Bottom left: test phantom without metals. The color of each small square represents a different material - from left to right, top to bottom - PVC, graphite, acrylic, polystyrene, Teflon, polypropylene, ABS, polycarbonate. Bottom right: test phantom with metals - PVC, graphite, aluminum, acrylic, polystyrene, Teflon, copper, iron, polypropylene, ABS, polycarbonate. 86

3·40 True LAC at 70 keV (top) and estimates of LAC at 70 keV (bottom). Test phantom with no metals on left and test phantoms with metals on right. The estimates were obtained using the best pair of calibration materials according to the EDEC criterion: graphite and aluminum for test phantom with no metals and Teflon and iron for test phantom with metals. The materials in the test phantom with no metals are - from left to right, top to bottom - PVC, graphite, acrylic, polystyrene, Teflon, polypropylene, ABS, polycarbonate. The materials in the test phantom with metals are - PVC, graphite, aluminum, acrylic, polystyrene, Teflon, copper, iron, polypropylene, ABS, polycarbonate. 88

4·1 Examples of LAC curves of a few materials 89

4·2 Singular values obtained for LACs of the different material classes. In each sub-plot different pre-processing was applied. The plots only show values greater than 10^{-2}. 94

4·3 Number of components needed for variation fraction to be greater than a threshold T as a function of T. The horizontal red dotted line shows the 2 component level. The vertical purple line shows the threshold considered by Alvarez of 0.9999. The numbers next to it indicate the number of components needed for each of the material classes to retain this threshold. 95

4·4 Number of components needed according to different criteria for the materials LACs. In each sub-plot different pre-processing was performed on the curves. The horizontal red dotted line shows the 2 component level. 96

4·5 Singular values of the LACs and exponentiated LACs for 'compounds' set. The plots only show values greater than 10^{-2}. 96

4·6 Intrinsic dimensionality of the "Swiss roll" dataset. The data is plotted on the left. The residual variance as a function of dimension is plotted on the right for Isomap and SVD. 97

4·7 Residual variance as a function of dimensionality for the compounds LACs database, using Isomap and SVD. 98

4·8 Correlation coefficients and Euclidean distances between pairs of LACs in the compounds database. Figures are in grayscale where black is zero and white is one. The dashed green line indicates the transition between materials from the explosive class and the non-explosive class. *Left:* correlation coefficient, larger means closer. Right: normalized pairwise Euclidean distance, smaller means closer. 99

5·1 Illustration of LAC feature space optimization by adaptive selection of projection directions or basis functions 103

5·2 Obtaining LAC features by energy-level selection - a special family of adaptive feature selection methods 105

5·3 Example of an ROC curve. The x-axis is the probability of false alarm, P_F, and the y-axis is the probability of detection, P_D. Any point on the ROC corresponds to a particular choice of threshold. 111

5·4 ROC estimates for a 1D Gaussian case. The density functions of the two classes are plotted on the left. The ROC estimates given by the different methods, along with the ground truth ROC, are plotted on the right. 114

5·5 Mean AUC estimates obtained with the different methods (in color) compared to the true AUC (in black). On the left the sample dimension is varied from 1 to 5 while holding the sample size fixed at 100. On the right the sample size is varied while holding the dimension fixed at 1. Errorbars show the mean plus or minus one standard deviation. . . 114

5·6 Area under the ROC curve for each single energy levels (left) and each combinations of two energy levels (right). In the image on the right the color at each pixel indicates the AUC value for the given combination of energies. 116

5·7 AUC for best single energy level and best combinations of two, three and four energy levels according to different criteria and methods . . 117

5·8 Scatter plot of the synthetic 2-class dataset. Class 0 is in blue and class 1 is in red. 119

5·9 Classification performance on a synthetic example using different classifiers (top), and using AUC (bottom) for the different dimensionality reduction methods applied to the synthetic dataset. The x-axis indicates the dimension the data was reduced to. The errorbars represent standard error. 120

5·10 Classification accuracy of different classifiers for the different feature selection methods applied to the compounds LAC database. The x-axis indicates the dimension the data was reduced to. The errorbars represent standard error. The results for PhCo and MatL, obtained with two-dimensional features, were extended horizontally by a dashed line. 122

5·11 ROC-based evaluation of the different feature selection methods applied to the compounds LAC database. On the left the AUC values are plotted and on the right the values of P_F for $P_D = 1$. Note that in the left plot higher values are better and in the right plot lower value are better. The x-axis indicates the dimension the data was reduced to. The errorbars represent standard error. The results for PhCo and MatL, obtained with two-dimensional features, were extended horizontally by a dashed line. 123

6·1 The six F(Z) curves. μ_1, μ_2, μ_3, μ_4 are the reconstructed attenuation values calculated by equation (3.30), using the 80, 100, 120, 140 kVp spectral weighting functions, respectively, of the Siemens SOMATOM scanner. 127

6·2 Cross section obtained with 80 kVp spectrum of the simulants phantom 128

6·3 Normalized photoelectric (left) and Compton (right) basis functions . 133

6·4 Real images (top) and batched solution (bottom). Photoelectric coefficient images are on the left with gray-scale range [0 0.94], Compton images are on the right with gray-scale range [0 0.34]. 134
6·5 IEKF solutions. Top: initialization with true field. Bottom: PR initialization. Photoelectric coefficient images are on the left with gray-scale range [0 0.94], Compton images are on the right with gray-scale range [0 0.34]. 136
6·6 IEKF with different initializations: error vs. rotation number 137
6·7 EDEC and K-EDEC(C) simulation results for the calibration scan containing graphite (bottom rod) and aluminum (top rod). Top: FBP reconstructed image from 130 kVp measurements. Middle: basis material images obtained with EDEC. Bottom: basis material images obtained with K-EDEC(C). 142
6·8 EDEC and K-EDEC(C) simulation results for the test scan containing graphite (bottom rod), aluminum (top rod) and plastic (square). Top: FBP reconstructed image from 130 kVp measurements. Middle: basis material images obtained with EDEC. Bottom: basis material images obtained with K-EDEC(C). 143
6·9 FBP reconstructions of a slice of the calibration phantom from 95 and 130 kVp measurements. Top: graphite and magnesium phantom. Bottom: graphite and aluminum phantom. The units are cm^{-1}. . . . 145
6·10 *EDEC* results for a water scan using graphite and magnesium calibration. Top left: graphite image. Top right: magnesium image. Bottom: estimated LAC at 60 keV in units of cm^{-1}. 146

6·11 K-EDEC(C) results for a water scan using graphite and magnesium calibration. Top left: graphite image. Top right: magnesium image. Bottom: estimated LAC at 60 keV in units of cm^{-1}. 147

6·12 K-EDEC(C+S) results for a water scan using graphite and magnesium calibration. Top left: graphite image. Top right: magnesium image. Bottom: estimated LAC at 60 keV in units of cm^{-1}. 148

6·13 K-EDEC(S) results for a water scan using graphite and magnesium calibration. Top left: graphite image. Top right: magnesium image. Bottom: estimated LAC at 60 keV in units of cm^{-1}. 149

6·14 SLS results for a water scan using graphite and magnesium calibration. Top left: graphite image. Top right: magnesium image. Bottom: estimated LAC at 60 keV in units of cm^{-1}. 150

6·15 EDEC results for a water scan using graphite and aluminum calibration. Top left: graphite image. Top right: magnesium image. Bottom: estimated LAC at 60 keV in units of cm^{-1}. 151

6·16 Data weighting function (6.18) with $c = 5$ 155

6·17 Data weights for example slice 2. The high energy sinogram is shown on the left and the corresponding data weights are shown on the right. Low weights are given to less reliable high sinogram values. 158

6·18 Estimated photoelectric (top) and Compton (bottom) coefficient images given by SPDE for example slice 2. Left: images obtained after the iterations with the first set of regularization parameters. Right: images obtained after the iterations with the second set of regularization parameters.The photoelectric image is in units of keV^3 and gray scale range [1000, 10000]. The Compton image is in units of cm^{-1} and gray scale range [0, 0.3]. 159

6·19 Estimated boundary field given by SPDE for example slice 2. Left: boundary field obtained after the iterations with the first set of regularization parameters. Right: final boundary field obtained after the iterations with the second set of regularization parameters. 160

6·20 Photoelectric and Compton coefficient images given by FBP (left) and SPDE (right) for example slice 2. The objects in this slice include a bottle of water and a thin rubber sheet. Image units and display ranges are the same as in Figure 6·18. 161

6·21 Photoelectric and Compton coefficient images given by FBP (left) and SPDE (right) for example slice 1. In this slice there is a bottle of water in between magnesium and silicon rods. Image units and display ranges are the same as in Figure 6·18. 162

6·22 Photoelectric and Compton coefficient images given by FBP (left) and SPDE (right) for example slice 2. The objects in this slice include a teflon cube, a bottle of water and a stack of rubber sheets. Image units and display ranges are the same as in Figure 6·18. 163

6·23 Mean percent improvement in SNR of SPDE relative to FBP. The mean was calculated across the selected objects. The errorbars represent standard error. 164

7·1 Object segmentation and labeling: decoupled (typical) versus joint (proposed) paths 168

7·2 Example of a material label image. The color in each pixel represents the materials label. 168

7·3 Material label images for a slice with graphite and magnesium rods using the dictionary labeling method. The graphite rod is on the right. Dictionary was composed of graphite and magnesium LACs. Graphite is labeled in green, magnesium is labeled in red and background is labeled in dark blue. Top: initialization. Bottom left: result with no MRF prior. Bottom right: result with an MRF prior. 174

7·4 MSE between measurements and modeled measurements using the labeling result shown in Figure 7·3. Dictionary was composed of graphite and magnesium LACs. Left: without MRF prior. Right: with MRF prior. 175

7·5 Material label images using the dictionary labeling method for a slice with graphite, magnesium and silicon rods placed with foam in a plastic container. The graphite rod is in the middle and silicon is on the right. Dictionary was composed of graphite, magnesium and silicon LACs. Graphite is labeled in light blue, magnesium is labeled in yellow, silicon is labeled in red and background is labeled in dark blue. Top: initialization. Bottom left: result with no MRF prior. Bottom right: result with an MRF prior. 176

7·6 MSE between measurements and modeled measurements using the labeling result shown in Figure 7·5. Dictionary was composed of graphite, magnesium and silicon LACs. Left: without MRF prior. Right: with MRF prior. 177

7·7 Illustration of the main components of the learning-based graph-cut labeling method. Top left figure shows the learned material appearance models. Top right figure shows an example of the data weighting scheme. Data points close to metal are given lower weights. The bottom figure shows the boundary-field used in the smoothing term. . . . 180

7·8 Scatter plots of the high energy image values $\bar{\mu}_2$ versus the low energy image values $\bar{\mu}_1$ of the training data for the different material labels. Left: without the metal label. Right: with the metal label. 183

7·9 Results for example slice 1. The slice has a water bottle in between magnesium and silicon rods. Top left: ML labeled image overlaid on the 130 kVp attenuation image. Top right: LCG labeled image overlaid on the 130 kVp attenuation image. Bottom: 130 kVp effective attenuation image. The attenuation images are in HU units displayed in the range [-1000, 1500] 184

7·10 Results for example slice 2. The slice has a water bottle on the right and a rubber sheet on top. Top left: ML labeled image overlaid on the 130 kVp attenuation image. Top right: LCG labeled image overlaid on the 130 kVp attenuation image. Bottom: 130 kVp effective attenuation image. The attenuation images are in HU units displayed in the range [-1000, 1500] 185

7·11 Results for example slice 3. The slice has a water bottle on the right and a rubber sheet on top. Top left: ML labeled image overlaid on the 130 kVp attenuation image. Top right: LCG labeled image overlaid on the 130 kVp attenuation image. Bottom: 130 kVp effective attenuation image. The attenuation images are in HU units displayed in the range [-1000, 1500] 186

7·12 Results for example slice 4. The slice has a stack of rubber sheets on the bottom and a bottle of doped water on the right. Top left: ML labeled image overlaid on the 130 kVp attenuation image. Top right: LCG labeled image overlaid on the 130 kVp attenuation image. Bottom: 130 kVp effective attenuation image. The attenuation images are in HU units displayed in the range [-1000, 1500] 187

7·13 Results for example slice 5. The slice has a stack of rubber sheets on the bottom and a bottle of doped water on the right. Top left: ML labeled image overlaid on the 130 kVp attenuation image. Top right: LCG labeled image overlaid on the 130 kVp attenuation image. Bottom: 130 kVp effective attenuation image. The attenuation images are in HU units displayed in the range [-1000, 1500] 188

7·14 Results for example slice 6. The slice has a bottle of water on the right. Top left: ML labeled image overlaid on the 130 kVp attenuation image. Top right: LCG labeled image overlaid on the 130 kVp attenuation image. Bottom: 130 kVp effective attenuation image. The attenuation images are in HU units displayed in the range [-1000, 1500] 189

7·15 Learning-based labeled images obtained with single energy data (left) and dual-energy data (right) overlaid on the 130KVP image. 191

B·1 Left: examples of objects appearing in the scans: a thin rubber sheet, a water bottle, and a Teflon cube. Right: estimates of the Imatron system spectra used when acquiring dual-energy measurements. . . . 211

List of Abbreviations

1D	.....	one dimensional
2D	.....	two dimensional
3D	.....	three dimensional
AUC	.....	area under the curve
CT	.....	computed tomography
DECT	.....	dual-energy computed tomography
DHS	.....	department of homeland security
EDEC	.....	empirical dual energy calibration
EDS	.....	explosives detection system
FBP	.....	filtered back projection
FOV	.....	field of view
HU	.....	hounsfield units
KDE	.....	kernel density estimation
keV	.....	kilo electron-volt
KNN	.....	K nearest neighbor
kVp	.....	peak kilovoltage
LAC	.....	linear attenuation coefficient
MAC	.....	mass attenuation coefficient
MECT	.....	multi-energy computed tomography
MRF	.....	Markov random field
MSE	.....	mean squared error
ROC	.....	receiver operating characteristic
SNR	.....	signal to noise ratio
SVM	.....	support vector machine

Chapter 1

Introduction

Explosives represent a continuing threat to aviation security. New challenges have been created by the emergence of an expanded set of explosive threats and their use by terrorists. These threats include new improvised explosives, the reemergence of old explosive materials (such as the use of black powder in the Boston bombing) and liquid explosive threats. The US department of homeland security (DHS) currently has requirements for future explosive detection systems (EDS) that include increased probability of detection and decreased probability of false alarm for a larger set of objects and with reduced minimum masses [Crawford et al., 2013]. To this end, new techniques are needed that increase discrimination between the explosive threats and the stream-of-commerce clutter in checked baggage and carry-on items.

An EDS usually uses computed tomography (CT) technology to automatically measure the physical characteristics of objects in baggage [Lord, 2011]. CT provides a 3D image of objects based on their X-ray attenuation. The attenuation depends on the material being scanned and is also a function of the energy of the incident X-ray photons. In conventional CT systems, also called single-energy CT, the scan is performed with a single source spectrum and energy-integrating detectors and the ability to determine the chemical composition of the scanned materials is limited. In Multi-Energy CT (MECT), multiple energy-selective measurements of the attenuation are taken. Since additional energy-dependent information can lead to superior material discrimination, MECT can potentially provide improved detection capability

over conventional single-energy CT.

Different MECT algorithms with the goal of extracting material information have been proposed since the 1970's. The existing methods mostly focus on medical applications and are generally applicable to a limited class of biologically inspired materials. The problems in security are more challenging due to the larger range of materials and threats which may be found. Objects may appear in high clutter and in different forms of concealment. Thus the medical domain information extraction methods may not be optimal for detection of explosives.

There has been little public literature on the proprietary methods used in the security industry. From what has been published we know that most existing multi-energy EDSs use just two spectral measurements (also known as dual-energy) and typically rely on relatively few, non-optimized material signatures (such as effective atomic number and density) for threat/non-threat discrimination. There has been little published work on development of principled methods to choose the best signature features to achieve optimal classification performance.

In this dissertation we apply the tools of optimal detection, estimation, and machine learning to provide new MECT algorithms for the purpose of accurate material classification in baggage. The new methods aim to help to increase detection probability, reduce false alarms, and improve system reliability.

1.1 Dissertation contributions

We begin by studying the fundamental information contained in X-ray sensing of materials which can be used for discrimination of explosives. This information is captured in the X-ray attenuation curves of materials and therefore we focus on analyzing the discriminatory information available in these curves. In the first contribution we study the dimensionality of the space of material attenuation curves using a database

of curves of 320 materials which we created. We show that the dimensionality of the curves for materials encountered in security applications is significantly higher than for biological materials, indicating that more or different material X-ray features than the features used in medical applications may be required.

The second contribution is the development of a leaning-based approach for optimization of material X-ray features. In contrast to existing methods which are based on medically motivated or ad hoc feature selection we focus on the explosive classification task and optimize the features specifically for this task. Examples of X-ray attenuation curves of explosive and non-explosive materials from the database are used to derive a small number of optimal projection directions and the corresponding coefficients are used as material features. We consider different ways of optimizing the projection directions and compare the features by calculating fundamental ROC-based metrics, as well as classifier accuracy. We show that using the optimized X-ray material features classification performance can improve relative to the standard photoelectric and Compton coefficients.

Most MECT techniques are based on creating material parameter images such as photoelectric and Compton images. Currently the use of these images is limited by artifacts caused by the large range of materials in baggage and the presence of metal and high clutter. To extend the discrimination ability of MECT systems, robust image generation capable of artifact suppression is needed. In the third contribution we propose a new structure-preserving MECT inversion method which uses data weighting and edge-based regularization to reduce noise and metal artifacts in the reconstructed material parameter images.

In MECT systems for security, potential threats are found by segmenting and labeling the scanned objects. The processes of segmentation and labeling are currently decoupled and multi-energy information is usually not used in the segmentation pro-

cess. We study ways of jointly identifying and segmenting the scanned materials from MECT measurements. The fourth contribution is the development of a learning-based approach applied to conventionally reconstructed attenuation images to obtain a material label image. The method provides accurate object segmentation and labeling even in the presence of high clutter and metal.

1.2 Dissertation outline

Background material is presented in Chapter 2. It includes background on explosives, tomographic measurements and inversion and MECT data acquisition. Current MECT information extraction methods are discussed in Chapter 3, including experimental results using some of the methods. In Chapter 4, the dimensionality of the space of materials in security is studied through the X-ray attenuation versus energy curves of materials. In Chapter 5, a learning-based approach is presented for optimizing X-ray material features for explosives detection. In Chapter 6, new methods for reconstruction of material-parameter images from MECT measurements are presented, which address the issues of high clutter and large material range in baggage. Chapter 7 presents a novel framework for material identification using MECT. In the first part a dictionary approach is presented for labeling materials directly from MECT measurements. In the second part a learning-based method for joint object segmentation and labeling is presented. Finally, in Chapter 8 the dissertation conclusions and future work are discussed.

Chapter 2

Background

MECT methods for explosives detection are based on the physical properties of the scanned materials as well as on the data acquisition process. In this chapter we provide background for both parts. In Section 2.1 we discuss explosives characterization, current challenges in explosives detection, and how X-ray systems can be used for explosives detection. Section 2.2 explains the physics of X-ray CT and how it is used for nondestructive imaging. We discuss the X-ray attenuation coefficient and the CT measurement model which most algorithms in this field use. We describe the conventional CT image reconstruction approach. Finally, in Section 2.3 we describe MECT data acquisition methods.

2.1 Explosives detection

Usually, explosive devices consist of two main components: an explosive agent and a detonating system [Hussein and Waller, 1998]. The blasting material consists primarily of inorganic nitrates and carbonaceous fuels and the detonators are made of metallic tubes or shells with an initiating explosive. There are more than 100 types of military and civilian explosives. The following list of explosive materials covers many of the threats existing today in the field of commercial aviation security [Icar, 2009, Schubert and Kuznetsov, 2004]. Each item on the list has unique properties in terms of density, absorption coefficient, and particle size distribution.

(a) Standard Military Explosives (difficult to obtain): cast explosives (TNT), plas-

tic explosives (C4, Semtex), Sheet explosives, Detonation cords, Smokeless powder, Nitroglycerin.

(b) Standard Commercial Explosives (accessible by special license): dynamite, water gel, ANFO (Ammonium Nitrate - Fuel Oil).

(c) Commercial substances suitable for explosives (freely available): black powder, smokeless powder, fire-works.

(d) Improvised Explosives (easy to produce): improvised ANFO, TATP (Triacetone Triperoxide), EGDN (Ethylene Glycol Dinitrate), potassium chlorate and sugar.

(e) Primary explosives (used for detonation): lead azide.

In terms of shape, explosives can be divided into sheets and bulks. The sheets category deals with special concealment in luggage shells. The main issue with sheet explosives is lack of resolution in many CT scanners. The bulk category covers all the explosives that don't fall into the sheets category.

Inert items, or confusers, are items whose physical properties are similar to explosive materials. Inert items have a major impact on the false alarm rate. In order to identify explosives with low false alarm rate, one must be able to reliably recognize the inert items. Inert items that are commonly found in luggage include the following: acrylonitrile butadiene styrene (ABS), aluminum, polypropylene (PP), shoes, food with the same density as explosives like chocolate, honey, and ketchup, cosmetics, electric appliances, and mechanical tools.

2.1.1 Identifying explosives

A number of explosive characteristics can be used for their detection [Singh and Singh, 2003]: geometry, density and elemental composition, and vapor emissions. The density of a material, denoted by ρ is a measure of how much mass is contained

in 1 cubic centimeter of the material. In this work we consider the density at room temperature. One indicator of the elemental composition is the "effective atomic number". The atomic number, Z, of an element is equal to the number of protons in the atomic nucleus. X-rays are attenuated by interactions with electrons, the number of which in a neutral atom is equal to Z. The atomic mass, A, is the total mass of protons, neutrons and electrons in a single atom (when the atom is motionless). The effective atomic number, Z_{eff}, of a compound is related to the atomic numbers of the elements in the compound and to their respective proportions. In [Macovski, 1983], a formula for the effective atomic number is given, which is based on the X-ray attenuation physical model:

$$Z_{\text{eff}} = \left(\sum_i \alpha_i Z_i^m \right)^{(1/m)} \tag{2.1}$$

where $m = 3.8$, and α_i is the electron fraction of the ith element in the compound given by

$$\alpha_i = \frac{w_i(Z_i/A_i)}{\sum_j w_j(Z_j/A_j)}$$

where w_i, Z_i, and A_i are the fraction by weight, atomic number, and atomic mass of element i, respectively.

When common substances found in luggage are plotted on a chart that maps Z_{eff} against density along with various threat materials (Figure 2·1), a pattern emerges that suggests a way to distinguish explosives from the vast majority of luggage content [Eilbert and Krug, 1993].

2.1.2 X-ray systems for explosives detection

X-ray systems have been widely used for detection of illicit materials in luggage. These systems are based on irradiating the object of interest with X-rays and obtaining an image from measurements of the radiation attenuation. The spatial resolution of X-

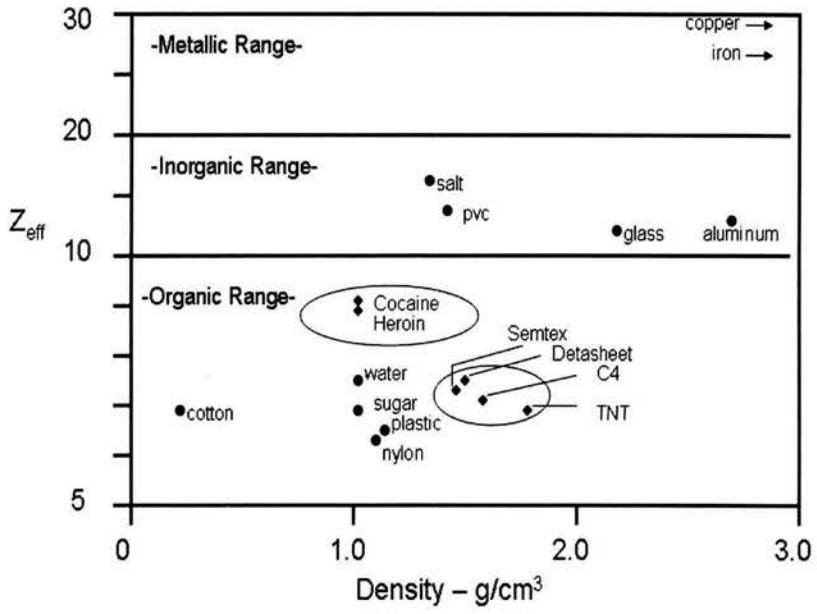


Figure 2·1: Z_{eff} vs. density ρ for common items found in airport luggage and for certain contraband and explosive materials [Eilbert and Krug, 1993].

ray systems is very high and allows nondestructive viewing of hidden objects. The use of X-ray CT systems for luggage scanning has become widespread [Smith and Connelly, 2011]. CT devices can provide a 3D image of the scanned object. In addition, if measurements are taken at different energies, one can compute material-specific parameters, such as Z_{eff} and density, of the different materials shown in the image.

2.2 X-ray computed tomography (CT)

CT is a technique used for generating an image of the inside of an object, i.e., cross-sectional imaging, based on X-ray transmission measurements. It has applications in diverse fields such as medical imaging, explosives detection, and non-destructive testing. The technique includes two steps: data acquisition and image reconstruction. In the data acquisition step, data is collected by illuminating the object from many

different directions. In the image reconstruction step, the cross-section image of the object is reconstructed from line integrals of the data. The pixel values in the final image correspond to a quantity called the "linear attenuation coefficient" (LAC).

2.2.1 The linear attenuation coefficient (LAC)

The LAC, denoted by μ, is a quantity that characterizes how easily a material can be penetrated by a beam of X-rays. It is defined through Beer's law which is illustrated in Figure 2·2 (see Section 2.2.3 for a derivation). The X-ray intensity (energy per unit area), I, for an X-ray with input intensity I_0 going through a material with LAC μ and length l is given by:

$$I = I_0 e^{-\mu l} \tag{2.2}$$

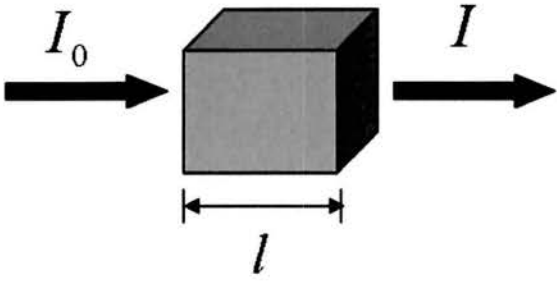


Figure 2·2: Illustration of Beer's Law (2.2) for a monochromatic X-ray beam through a homogeneous material. I_0 and I are the initial and final X-ray intensities and l is the length of the X-ray path.

The linear attenuation coefficient of a material depends on the photon energy of the beam and on the elemental composition of the material [Macovski, 1983]. Therefore, the LAC is usually written as $\mu(E)$, where E is the energy level. The units of the linear attenuation coefficient is inverse distance. The LAC is sometimes normalized by the material density ρ, producing a quantity known as the "mass

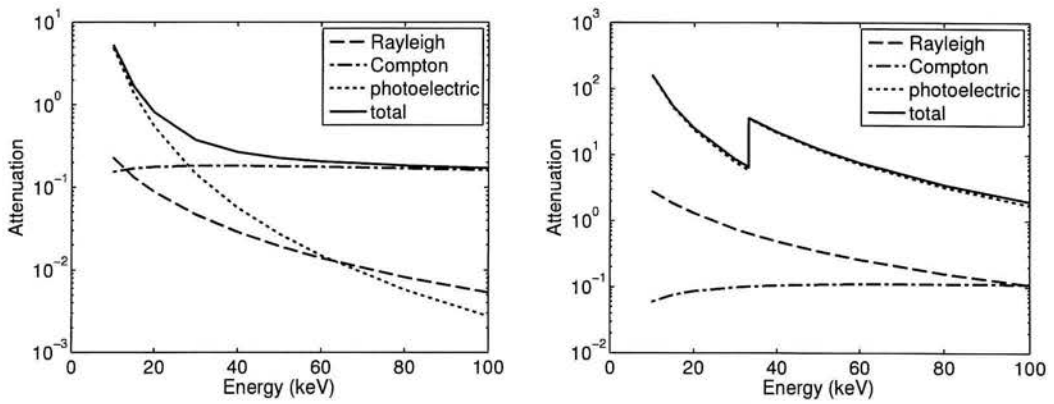
attenuation coefficient" (MAC). The MAC is denoted by $\mu_\rho(E)$ and is defined as

$$\mu_\rho(E) = \frac{\mu(E)}{\rho} \tag{2.3}$$

In the energy range of medical and baggage CT systems (approximately 10 to 150 KeV), three mechanisms dominate the attenuation: photoelectric absorption, Compton scatter (incoherent), and Rayleigh scatter (coherent). Since each interaction is independent, the overall attenuation coefficient is the sum of that due to photoelectric, Compton, and Rayleigh coefficients:

$$\mu(E) = \mu_P(E) + \mu_C(E) + \mu_R(E) \tag{2.4}$$

where $\mu_P(E)$, $\mu_C(E)$, and $\mu_R(E)$ are the photoelectric, Compton and Rayleigh components, respectively. To illustrate, Figure 2·3 shows the different components and the total LAC for water and iodine.



(a) water **(b)** iodine

Figure 2·3: Physical components of the mass attenuation coefficient for water (left) and iodine (right) [Berger et al., 2005]

Photoelectric absorption is the process in which a photon is completely absorbed in the atom, ejecting an orbital electron. The process dominates at low photon energies and atoms with large atomic numbers.

Incoherent or Compton scattering consists of a collision between an X-ray photon and either a free or a loosely bound electron in an outer shell. The energy of the X-ray photon is decreased when it interacts with the electron.

Coherent or Rayleigh scattering is the apparent deflection of X-ray beams caused by atoms being excited by the incident radiation and then re-emitting waves at the same wavelengths. The Rayleigh component is relatively small it is usually neglected in X-ray transmission methods.

For a compound or mixture, the assumption is that its MAC $\mu_\rho(E)$ is given by

$$\mu_\rho(E) = \sum_i w_i \mu_{\rho i}(E) \tag{2.5}$$

where $\mu_{\rho i}(E)$ is the MAC of element i and w_i the fraction by weight of element i in the compound. The LAC of the compound is then simply given by $\mu(E) = \rho\mu_\rho(E)$, according to Equation 2.3.

Absorption edges in the linear attenuation coefficient

An absorption edge is a sharp discontinuity in the attenuation coefficient that occurs when the energy of the X-ray photon corresponds to the energy of a shell of the atom (K, LI, LII, LIII, etc.). Specifically, the K-edge is a sudden increase in the attenuation coefficient occurring at a photon energy just above the binding energy of the K shell electron of the atom. For elements and materials with effective atomic number lower than 30, water and organic material for example, this K-edge occurs below 10keV, which is below the energy spectrum used in CT. For higher-atomic-number materials, such as iodine shown in Figure 2·3, this K-edge occurs within the spectrum of interest. This phenomenon is exploited in conventional medical CT to create contrast agents [Johnson et al., 2007].

In current MECT methods the LAC is typically assumed to be a smooth function

of energy, and the K-edges are not modeled. This leads to errors in the approximation of the LAC (to be discussed further in Chapter 3).

2.2.2 The scanning process

A typical CT scanner consists of a rotating frame which has an X-ray tube mounted on one side and an array of detectors mounted on the opposite side. A beam of X-ray photons is created as the rotating frame spins the X-ray tube and detectors around the object of interest (cf. Figure 2·4). When the X-rays hit the object they are either absorbed by the object, scattered, or travel through it in a straight line to the detector.

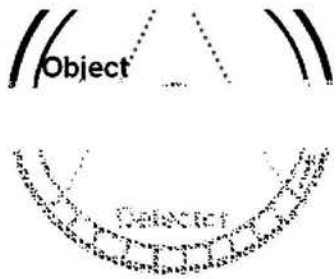


Figure 2·4: X-ray CT scanner diagram [Zhang et al., 2007].

X-rays are typically produced by an X-ray tube, consisting of a cathode and an anode in vacuum [Macovski, 1983]. Using a high voltage power source, an electron beam is accelerated from the cathode towards a metal target at the anode and the resulting energy is emitted in the form of X-rays or high-energy photons. The X-ray source has the Bremsstrahlung radiation spectrum. It is polychromatic, meaning that the beam has a broad energy spectrum. The source spectrum depends on the anode material and the accelerating voltage. It may be adjusted by changing the applied voltage and installing filters. X-ray spectra are labeled by kVp units, which are the

maximum voltage applied to the X-ray tube, determining the peak energy of the spectrum. An example of a 130 kVp spectrum is shown in Figure 2·5.

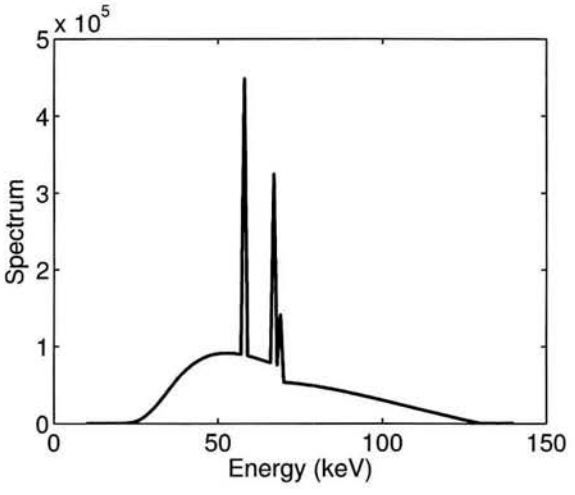


Figure 2·5: Estimate of a 130 kVp X-ray source spectrum, Imatron CT scanner. Provided by Taly Gilat Schmidt, Marquette University.

A wide variety of X-ray detectors is available, some counting single photons, some providing only measurements of count rate or total flux, others measuring the energy, position, and/or incidence time of each X-ray [Thompson et al., 2009]. Conventional CT detectors are energy-integrating detectors measuring the total beam flux rather than individual photons. Usually collimators are used at the detectors in order to reduce the amount of scattered photons reaching the detectors.

CT machines may take continuous measurements in a helical (or spiral) fashion or take a series of measurements of individual 2D slices of the object (also known as step-and-shoot mode). See Figure 2·6. In this thesis we will focus on individual 2D slices which may be obtained in step-and-shoot mode, however the methods can be extended to 3D volumes and helical scans. The CT measurement model will be described next.

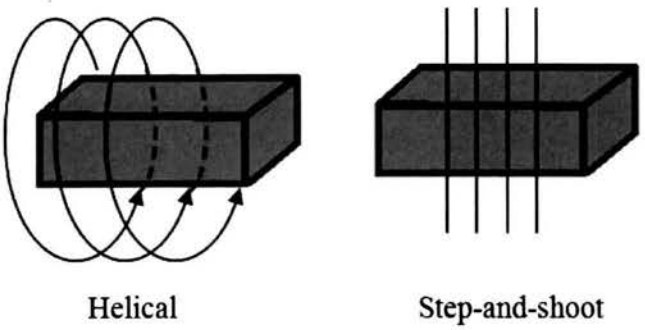


Figure 2·6: Helical scan (left) versus step-and-shoot scan (right)

2.2.3 CT measurement model

The measurement model describes the relationship between the number, or intensity, of the X-ray photons released by the source and the number, or intensity, of the photons collected by the CT detectors. We will develop the general measurement equation gradually.

First, for simplicity, we assume that the energy of all the transmitted photons is the same (monochromatic beam), and that only one homogeneous material is scanned. The photons either interact with a particle of matter or pass unaffected. The interaction results in the removal of the photon from the beam by scattering or absorption. The number of photons interacting and removed from the beam ΔN in a region of thickness Δx is given by [Macovski, 1983]:

$$\Delta N = -\mu N \Delta x \tag{2.6}$$

where N is the total number of impinging photons and μ the linear attenuation coefficient. ΔN is negative since the beam only loses photons. The number of photons interacting is proportional to the number of incident photons, the interacting distance, and the material.

If we start with N_{in} photons and, after a thickness l, have N_{out} photons, using equation (2.6) we have

$$\int_{N_{in}}^{N_{out}} \frac{dN}{N} = -\mu \int_{0}^{l} dx \tag{2.7}$$

Solving equation (2.7) we have the classical attenuation relationship

$$N_{out} = N_{in} e^{-\mu l} \tag{2.8}$$

Similarly, the detected intensity, I, in terms of the incident intensity I_0 is

$$I = I_0 e^{-\mu l} \tag{2.9}$$

The above equation is also known as Beer's law, which was described in Figure 2·2.

Second, we consider the more general case where the object being scanned varies spatially and may be composed of several materials. This means that the LAC, $\mu(x_1, x_2)$, is a function of spatial location $\vec{x} = (x_1, x_2)$, and that the detected intensity is a function of the line integral of $\mu(x_1, x_2)$ along the ray path (see Figure 2·7):

$$I(r, \theta) = I_0 e^{-p(r,\theta)} \tag{2.10}$$

where $p(r, \theta)$ is the line integral of $\mu(x_1, x_2)$ along the line at angle θ at distance r from the origin:

$$p(r, \theta) = \int \int \delta(x_1 cos\theta + x_2 sin\theta - r)\mu(x_1, x_2) dx_1 dx_2 \tag{2.11}$$

The line integral $p(r, \theta)$ may be obtained from the measurements by the following operations:

$$p(r, \theta) = -\ln\left(\frac{I(r, \theta)}{I_0}\right) \tag{2.12}$$

The collection of line integrals $p(r, \theta)$ for all angles θ and locations r is the Radon

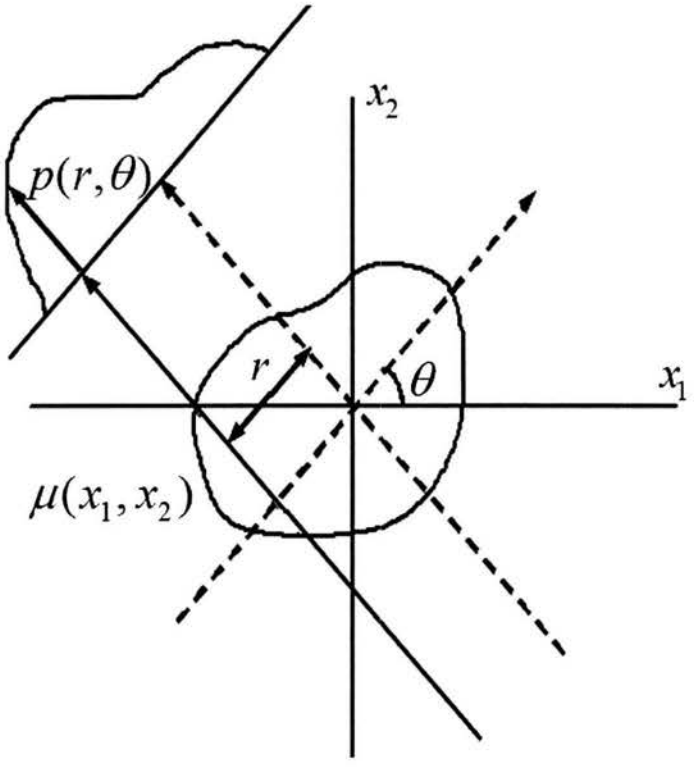
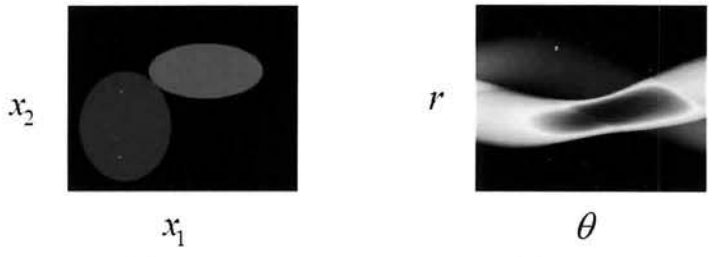


Figure 2·7: Geometry of tomographic measurements. An X-ray beam travels in a path defined by r and θ. The beam is attenuated by the object according to its size and chemical composition. The measurement at the detector is denoted by $p(r,\theta)$. The beam is assumed to be monochromatic.

transform of $\mu(x_1, x_2)$. The Radon transform is also referred to as a "sinogram". An example of a singoram is shown in Figure 2·8. The inverse Radon transform or filtered back projection (FBP) can be used to reconstruct the attenuation coefficient at every pixel [Kak and Slaney, 2001].

Finally, we consider the most general case where the object being scanned is composed of more than one material and the incident beam contains a spectrum of different energies (polychromatic beam). The energy-dependency of the LAC is now considered as well and we denote it by $\mu(x_1, x_2, E)$. Figure 2·9 illustrates the LAC "volume" - the dependency of the LAC on (x_1, x_2) and E.



(a) object (b) sinogram

Figure 2·8: Example of an object and the corresponding sinogram or Radon transform

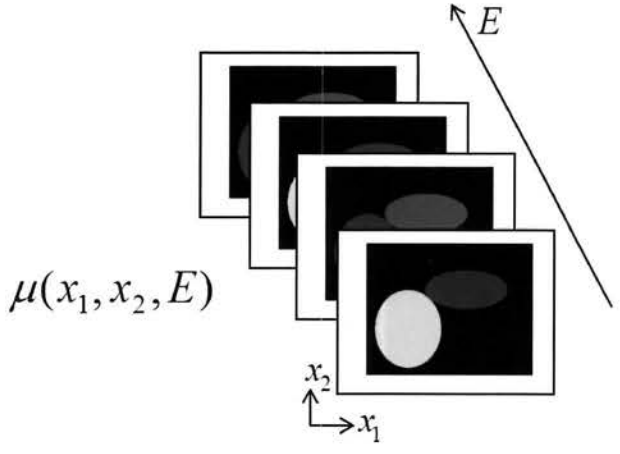


Figure 2·9: Illustration of the LAC "volume" - depends on spatial location (x_1, x_2) and energy level E

Expanding on equation (2.10), the overall intensity measured at the detector is given by

$$I(r, \theta) = \int W(E) e^{-p(r,\theta,E)} dE \tag{2.13}$$

where

E is the photon energy in KeV,

$p(r,\theta,E) = \int\int \delta(x_1 cos\theta + x_2 sin\theta - r)\mu(x_1,x_2,E)dx_1dx_2,$

$W(E)$ denotes the spectral weighting function

The spectral weighting function $W(E)$ is related to the system source spectrum $S(E)$ and detector response $D(E)$:

$$W(E) = S(E)D(E) \tag{2.14}$$

Suppose the variables r and θ define a ray path L_j. Then the line integral $p(r,\theta,E)$ can be replaced with

$$p(r,\theta,E) = p(L_j,E) = \int_{L_j} \mu(\vec{x},E)dl \tag{2.15}$$

and equation (2.13) can be rewritten as

$$I_j = \int W(E)e^{-\int_{L_j}\mu(\vec{x},E)dl}dE \tag{2.16}$$

In multi-energy CT, measurements are taken with multiple spectral weighting functions. The dependency on the spectral weighting function is incorporated by adding another index i to the measurement equation which corresponds to the spectral weighting function used in that particular measurement:

$$I_{ij} = \int W_i(E)e^{-\int_{L_j}\mu(\vec{x},E)dl}dE \tag{2.17}$$

Note that the ray path L_j in general may also depend on the spectral weighting function i. However, here we assume that the ray paths for each spectral weighting

function are the same, which is the case in many MECT systems.

From here onward we denote by I_i the collection of measurements I_{ij} for some spectral weighting i and all rays $j = 1, ..., N_d$.

The functions $W_i(E)$ are considered to be known in most cases. They can be estimated empirically or simulated based on the system characteristics [Duan et al., 2011, Sidky et al., 2005]. An example of two spectral functions for a Siemens scanner is shown in Figure 2·10.

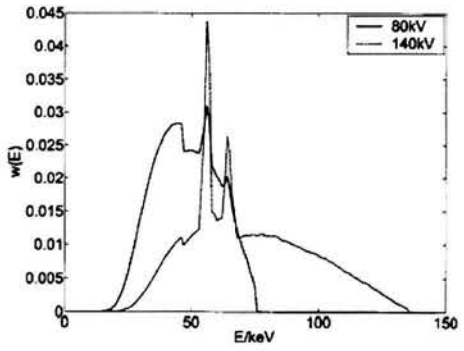


Figure 2·10: Examples of two spectral weighting functions $W_1(E)$ and $W_2(E)$ [Heismann et al., 2003]. The functions are normalized to integrate to 1. The numbers 80kV and 140kV denote the maximum voltage applied across the X-ray tube for each spectra.

Often the measurements I_{ij} are converted to the negative log-space in the following way:

$$\tilde{I}_{ij} = -\ln\left(\frac{I_{ij}}{\int W_i(E)dE}\right) \tag{2.18}$$

The collection of measurements $\tilde{I}_{ij}$ for some spectral weighting $i \in 1, ..., N_s$ and all rays $j = 1, ..., N_d$ are often referred to as a sinogram. We denote the sinogram by $\tilde{I}_i$.

The measurement model (2.17), or slight variations of it, is widely used in CT and MECT reconstruction algorithms. Some researchers consider the CT measurements to be deterministic and say that I_{ij} in (2.17) is the quantity measured by the detector [Alvarez and Macovski, 1976]. We will call this model the deterministic or noise-

free model. Alternatively, the measurements may be considered as Poisson random variables with mean I_{ij} [Fessler et al., 2002]. We will call this model the Poisson measurement model. For a Poisson random variable the variance is the same as the mean and therefore the signal to noise ratio (SNR) of a Poisson measurement is directly related the mean. In the case of I_{ij}, the SNR is controlled by the scale of the spectral weighting function $W_i(E)$. Low noise corresponds to high values of $W_i(E)$ and high noise corresponds to low values of $W_i(E)$.

In our work we often consider the discretized version of the measurement model (2.17), in which the integral over energy is approximated by a summation over a set of discrete energy levels, and the spatial location $\vec{x}$ is discrete (corresponds to a pixel). The LAC at every pixel for an energy level l is represented as a vector $\boldsymbol{u}_l$. The line integral can be replaced by an inner product of $\boldsymbol{u}_l$ with a projection vector $\boldsymbol{r}_j$. The value of the ith the spectral weighting function at energy level l is denoted by w_{il}. The discretized measurement model is given by:

$$I_{ij} = \sum_{l=1}^{N_e} w_{il} e^{-\boldsymbol{r}_j^T \boldsymbol{u}_l} \tag{2.19}$$

Furthermore, the vector containing the measurements at all ray paths $j = 1, ..., N_d$ for spectral function i, denoted I_i, can be written as:

$$I_i = \sum_{l=1}^{N_e} w_{il} e^{-R\boldsymbol{u}_l} \tag{2.20}$$

where R is the forward projection operator, with

$$R = \begin{bmatrix} \boldsymbol{r}_1^T \\ \boldsymbol{r}_2^T \\ \vdots \\ \boldsymbol{r}_{N_d}^T \end{bmatrix} \tag{2.21}$$

Note that the exponential in (2.20) is an elementwise operator, not a matrix expo-

nential.

If we denote the matrix containing the LAC at every pixel and energy level by $M_{N_p \times N_e}$, such that $M = [\boldsymbol{u}_1 \ \boldsymbol{u}_2 \ \ldots \boldsymbol{u}_{N_e}]$, then the vector of measurements I_i for spectral weighting function i can be written as:

$$I_i = e^{-RM} \boldsymbol{w}_i \tag{2.22}$$

where $\boldsymbol{w}_i = [w_{i1} \ w_{i2} \ \cdots \ w_{iN_e}]^T$ and the exponentiation is elementwise.

The normalized measurement in the negative log-space, $\tilde{I}_{ij}$ is defined in the discrete space as:

$$\tilde{I}_{ij} = -\ln \left(\frac{I_{ij}}{\sum_{k=1}^{N_e} w_{ik}} \right) \tag{2.23}$$

2.2.4 Conventional CT image reconstruction

In conventional CT systems the scan is performed with a single polychromatic source spectrum, which provides a single energy weighting function, $W_1(E)$. In the data processing stage, the polychromatic nature of the X-ray source is not taken into account, which is equivalent to assuming that $W_1(E)$ in (2.17) is a delta function. An aggregate attenuation quantity is reconstructed at every spatial location. The quantity is called the "effective attenuation coefficient" and is denoted by $\bar{\mu}(\vec{x})$. The reconstruction is typically achieved by applying FBP to the measurements in the negative log-space, $\tilde{I}_1$ [Kak and Slaney, 2001].

The quantity displayed in reconstructed images is usually the effective attenuation coefficient in Hounsfield units (HU), which is also known as the CT number. The relation between the effective attenuation coefficient $\bar{\mu}(\vec{x})$ and the CT number $H(\vec{x})$ is

$$H(\vec{x}) = 1000 \left(\frac{\bar{\mu}(\vec{x}) - \bar{\mu}_w}{\bar{\mu}_w} \right) \tag{2.24}$$

where $\bar{\mu}_w$ is the effective attenuation coefficient of water. These units put water at zero and air at -1000. In practice, the value of $\bar{\mu}_w$ is obtained by a calibration measurement. By using HU the variation in the effective attenuation values across different machines is reduced since they are referenced to the value of water on the machines.

The weakness of conventional single-energy CT is that materials that are different can have the same effective attenuation coefficient (e.g., tissues containing calcium and iodine [Steidley, 2008]). In addition, it is not possible to determine the chemical composition of the materials being scanned.

Conventional CT reconstruction also suffers from beam-hardening artifacts [Kak and Slaney, 2001]. Beam hardening is a phenomenon related to X-ray absorption when dealing with a polychromatic beam. The linear attenuation coefficient for many materials decreases as the X-ray energy increases. This causes the low energy photons to be preferentially absorbed, so that the beam becomes proportionally richer in high energy photons as it moves through an object. When the beam polychromaticity is ignored, this phenomenon leads to artifacts, such as cupping, streaks and whitening of certain areas in the image. An illustration of beam-hardening is shown in Figure 2·11.

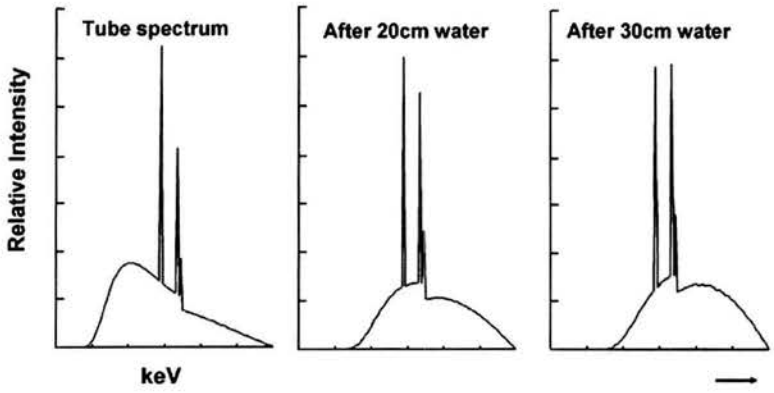


Figure 2·11: Illustration of beam hardening [Platten, 2007]

2.3 Multi-energy CT (MECT)

MECT has shown promise for material characterization and for providing quantitatively accurate CT values. MECT explicitly accounts for the energy dependence of the X-ray attenuation and thus can avoid the beam-hardening effect. In MECT, CT measurements are acquired with different source spectra, or using energy-sensitive detectors. These measurements are processed and estimates of different material features, such as atomic number, are obtained. Multi-energy measurements can be implemented by any technique that modifies, or is sensitive to, the energy spectrum of the detected photons - at the source, at the detector, or through the use of filters [Engler and Friedman, 1990]. The simplest approach would perhaps be to use monochromatic X-ray sources and directly sample the attenuation function at specific energies. However X-ray sources with narrow bandwidths are not used currently in CT systems due to their extremely high costs and space requirements [Achterhold et al., 2013].

MECT data acquisition methods are described below. MECT information extraction techniques will be discussed in detail in Chapter 3.

2.3.1 Acquisition methods

To date, existing MECT systems have mainly exploited just two spectral weighting functions and are referred to as dual-energy CT (DECT) systems. The existing dual-energy scanners work in one of the following configurations:

- Single source, two sequential scans with different source spectra. This can be achieved by any typical CT scanner through re-tuning. Advantage - full field of view (FOV) imaging. Disadvantage - significant time lag between different energy acquisitions.

- Single source, fast kVp switching. In this technique a filter is used to alternate

between spectra quickly throughout the scan. This is the way the dual-energy scanners of GE [Barnes, 2008] and Analogic [Gordon et al., 1997] work.

- Two sources operating simultaneously, each set to a different spectrum. Advantage - no added scan time. Disadvantages - scatter and misalignment of measurement ray paths. This is the way Siemens dual energy scanners work [Petersilka et al., 2008].

- Single source, dual-layer detector. Advantages - no added scan time, full FOV imaging. Disadvantage - requires advanced multi-layer, multi-energy CT detectors. This technology has been developed by Philips [Steidley, 2008].

In all the above methods, the measurement model (2.17) applies (perhaps with some variations).

Another approach to obtaining energy discrimination is by using energy-resolved photon-counting detectors [Wang et al., 2011]. In photon counting the energy is discriminated on the detector side, and the photons may be separated into a large number of narrow energy bins. To date, this detector technology is still limited due to the high count rates required to match the fluences of commercial machines. Therefore, it is not yet available in any commercial scanners [Shikhaliev, 2009].

Chapter 3

Current methods for MECT information extraction

In this chapter we give an overview of existing methods for information extraction in MECT. In general, the goal is to extract some material-specific parameters from MECT measurements.

Most existing algorithms are made up of the following two pieces:

1. Attenuation coefficient model

   The LAC of a material, $\mu(E)$, is typically represented as a linear combination of a few basis functions [Lehmann and Alvarez, 1986]:

   $$\mu(E) = \sum_{k=1}^{N_b} a_k f_k(E) \tag{3.1}$$

   where $f_k(E)$ are energy basis functions which depend on the energy E, a_k are the corresponding expansion coefficients, and N_b is the number of components (usually 2). The basis functions $f_k(E)$ are usually assumed to be known and are common to all the materials. The coefficients a_k vary for different materials.

   By decomposing the LAC using a model of the form (3.1) one can represent the LAC of some material, $\mu(E)$, by a small set of numbers a_k. By finding these numbers one can calculate material-specific parameters and identify the materials being scanned. The a_k are thus fundamental features of a material and the corresponding choice of $f_k(E)$ correspond to feature selection. Note

that (3.1) focuses on the subspace of dimension N_b spanned by the $f_k(E)$.

When considering a spatially varying scene, the LAC, $\mu(\vec{x}, E)$, is typically assumed to be separable in the spatial and energy dimensions:

$$\mu(\vec{x}, E) = \sum_{k=1}^{N_b} a_k(\vec{x}) f_k(E) \tag{3.2}$$

where $f_k(E)$ depend only on the energy E but not on spatial position $\vec{x}$, and $a_k(\vec{x})$ is the corresponding coefficient that varies spatially. The $a_k(\vec{x})$ are referred to as the coefficient images.

In the discrete case the LAC at every pixel and energy level, denoted by matrix M, can be represented as

$$\begin{aligned} M &= [\boldsymbol{a}_1 \ \boldsymbol{a}_2 \ \cdots \boldsymbol{a}_{N_b}] \begin{bmatrix} f_{11} & f_{12} & \cdots & f_{1N_e} \\ f_{21} & f_{22} & \cdots & f_{2N_e} \\ \vdots & & & \\ f_{N_b1} & f_{N_b2} & \cdots & f_{N_bN_e} \end{bmatrix} \\ &= CF \end{aligned} \tag{3.3}$$

where $\boldsymbol{a}_k$ is a vector containing the expansion coefficients a_{kj} for basis coefficient k and pixel j, f_{kl} is the sample of the kth basis function at energy level l, C is the expansion coefficient matrix, $C = [\boldsymbol{a}_1 \ \boldsymbol{a}_2 \ \cdots \boldsymbol{a}_{N_b}]$, and F is the expansion basis function matrix,

$$F = \begin{bmatrix} f_{11} & f_{12} & \cdots & f_{1N_e} \\ f_{21} & f_{22} & \cdots & f_{2N_e} \\ \vdots & & & \\ f_{N_b1} & f_{N_b2} & \cdots & f_{N_bN_e} \end{bmatrix}$$

Some common choices of basis expansion functions are described in Section 3.1.

2. Reconstruction method

MECT reconstruction is based on incorporating the LAC decomposition in the

measurement model. By substituting (3.2) into the MECT measurement model (2.17) we obtain:

$$\begin{aligned} I_{ij} &= \int W_i(E) e^{-\int_{L_j} \left(\sum_{k=1}^{N_b} a_k(\vec{x}) f_k(E) \right) dl} dE \\ &= \int W_i(E) e^{-\sum_{k=1}^{N_b} \left(\int_{L_j} a_k(\vec{x}) dl \right) f_k(E)} dE \end{aligned} \tag{3.4}$$

Recall that we denote by I_i the set of measurements I_{ij}, $j = 1, ..., N_d$.

Let the line integrals of the coefficients be denoted as $A_{kj} = \int_{L_j} a_k(\vec{x}) dl$. The measurement in terms of the line integrals of the coefficients is:

$$I_{ij} = \int W_i(E) e^{-\sum_{k=1}^{N_b} A_{kj} f_k(E)} dE \tag{3.5}$$

The collection $A_k = \{A_{kj}\}_{j=1}^{N_d}$ is called the sinogram of $a_k(\vec{x})$.

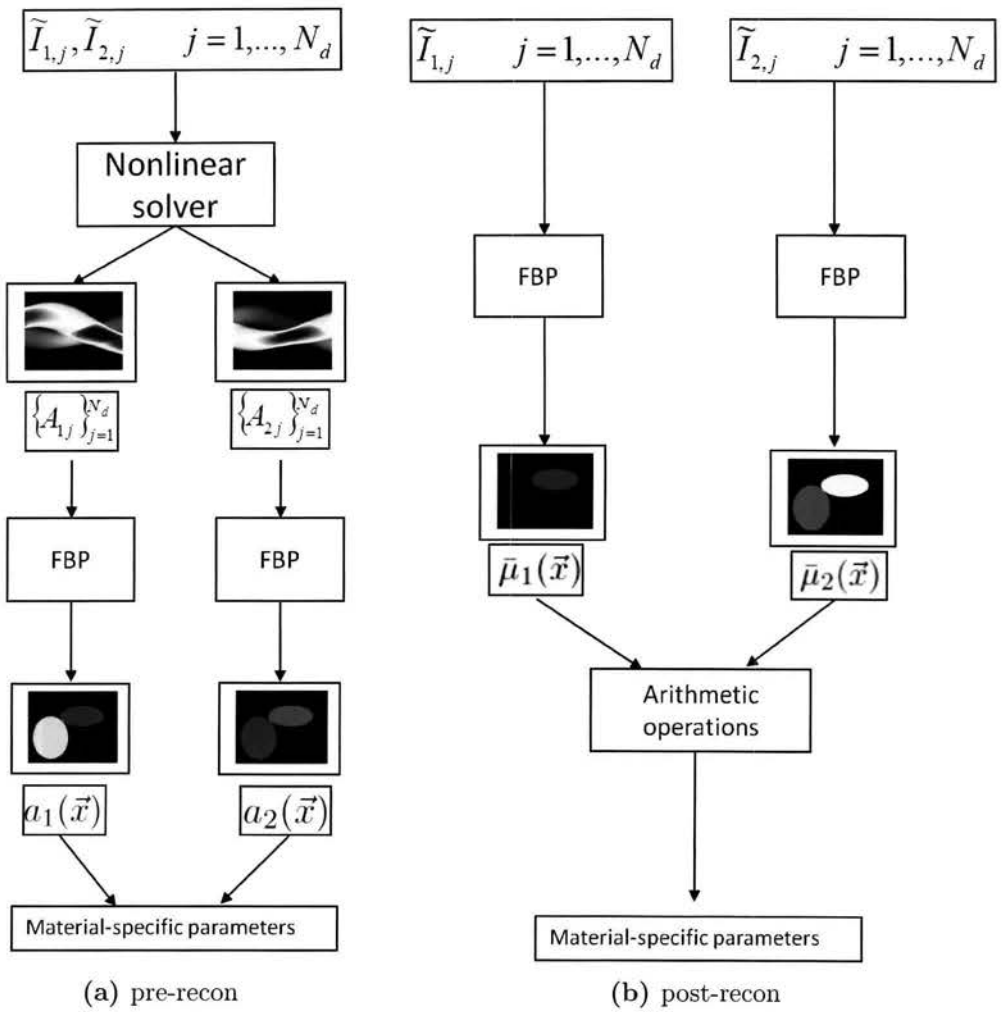
In the discrete case, based on Equations (3.3) and (2.22), the vector of measurements can be written as:

$$I_i = e^{-RCF} \boldsymbol{w}_i = e^{-AF} \boldsymbol{w}_i \tag{3.6}$$

where the kth column of A, A_k, is the forward projection of the kth coefficient vector, $A_k = R\boldsymbol{a}_k$, and R is the tomographic forward projection matrix defined in (2.21).

The goal, in general, is to reconstruct the coefficients $a_k(\vec{x})$ from MECT measurements I_{ij}. MECT methods vary in the way they obtain the estimates of the coefficient images, $a_k(\vec{x})$. Generally, the methods may be divided into pre and post-reconstruction categories [Engler and Friedman, 1990]. In pre-reconstruction methods the decomposition is preformed in the sinogram space first and then the coefficient images are reconstructed. In post-reconstruction

methods, first the effective attenuation images are reconstructed from the measurements and then the decomposition into coefficient images is performed. An illustration of the difference between the methods is shown in Figure 3·1.



(a) pre-recon (b) post-recon

Figure 3·1: Diagram illustrating pre-reconstruction methods (on the left) and post-reconstruction methods (on the right)

Different pre and post-reconstruction methods are described in Sections 3.2 and 3.3, respectively. Other methods which do not fall in either category are described in Section 3.4. Note that the majority of the published methods are aimed for medical applications. The amount of published literature on MECT methods for security

applications is very limited.

3.1 Models of the LAC

The commonly used choices of basis expansion functions of the LAC are listed below.

3.1.1 Photo-Compton

The Photo-Compton model for the attenuation coefficient is based on the two main physical phenomena which affect the LAC: the photoelectric effect and Compton scatter (see Section 2.2.1). The Rayleigh component is disregarded since it plays a relatively small role at the energies of interest. This model is a parametric representation of the LAC as a function of atomic number, electron density, and X-ray energy [Macovski, 1983]. For an LAC of a material, $\mu(E)$, the Photo-Compton model is the following special case of model (3.1):

$$\mu(E) = a_p f_p(E) + a_c f_c(E) \tag{3.7}$$

where a_p and a_c are characteristic positive constants of the material and $f_p(E)$ and $f_c(E)$ are the energy dependencies of photoelectric absorption and Compton scattering, respectively, which are independent of the material.

For a given known material the coefficients can be approximated by

$$a_p = \rho N_g C_P Z^m \qquad a_c = \rho N_g \tag{3.8}$$

where Z is the atomic number, ρ is the density, C_P is a constant, and N_g is the electron mass density in electrons per gram as given by

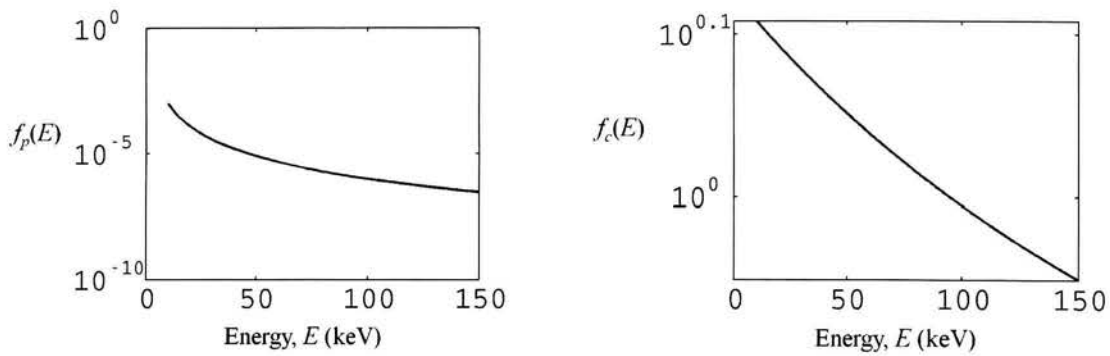
$$N_g = N_A \frac{Z}{\mathcal{A}} \tag{3.9}$$

where N_A is Avogadro's number and $\mathcal{A}$ is the atomic mass.

The Compton scattering function $f_c(E)$ can be given to a high degree of accuracy by the Klein-Nishina function:

$$f_{KN}(\alpha) = \frac{1+\alpha}{\alpha^2}\left[\frac{2(1+\alpha)}{1+2\alpha} - \frac{1}{\alpha}\ln(1+2\alpha)\right] + \frac{1}{2\alpha}\ln(1+2\alpha) - \frac{1+3\alpha}{(1+2\alpha)^2} \quad (3.10)$$

where $\alpha = E/510.975$ keV. The photoelectric function is approximated by $f_p(E) = \frac{1}{E^n}$. The exponent in the photoelectric component have been experimentally determined as $m = 3.8$, and $n = 3.2$, and the constant as $C_P = 9.8 \cdot 10^{-24}$. The functions $f_c(E)$ and $f_p(E)$ are shown in Figure 3·2. Note that their scales are very different.



(a) Photoelectric (b) Compton

Figure 3·2: Basis functions used in the Photo-Compton model.

The LACs of low-atomic number materials (Z<30) are smooth functions of energy (no K-edges) and they can generally be represented to a high degree of accuracy using the photoelectric and Compton basis functions, which are smooth as well.

In case of a scene with spatially varying materials, equation (3.7) becomes

$$\mu(\vec{x}, E) = a_c(\vec{x}) f_c(E) + a_p(\vec{x}) f_p(E) \quad (3.11)$$

An algorithm that uses the model (3.11) would attempt to find the coefficients $a_c(\vec{x})$ and $a_p(\vec{x})$ at each spatial location $\vec{x}$, and then estimate the atomic number Z and the density ρ via the nonlinear equations (3.8) and (3.9).

The advantage of this model is that it has a physical meaning and can be used to directly estimate Z and ρ. The disadvantage is that it can only accurately represent low-atomic number materials, whose K-edge is outside the energy range of interest, since the basis functions are smooth.

3.1.2 Basis materials

This model states that a material's attenuation coefficient can be expressed as a linear combination of the attenuation coefficients of previously chosen basis materials [Lehmann et al., 1981]:

$$\mu(E) = a_1\mu_\alpha(E) + a_2\mu_\beta(E) + ... \tag{3.12}$$

where $\mu_\alpha(E)$ is the attenuation coefficient of material α, $\mu_\beta(E)$ is the attenuation coefficient of material β and so on.

In case of a scene with spatially varying materials, equation (3.12) becomes

$$\mu(\vec{x}, E) = a_1(\vec{x})\mu_\alpha(E) + a_2(\vec{x})\mu_\beta(E) + ... \tag{3.13}$$

This model is more flexible than the Photo-Compton model, and therefore can be more accurate. The coefficients a_k do not have to be positive and are not defined by an approximate physical formula. In addition, this model can represent the attenuation coefficient of materials with a K-edge inside the used energy range. Examples of commonly used basis materials are soft tissue and bone [Sukovic and Clinthorne, 2000], and Lucite and aluminum [Lehmann et al., 1981]. The disadvantage of this model is that it does not provide a direct estimate of the atomic number and density.

When considering just two basis materials, $\mu_\alpha(E)$ and $\mu_\beta(E)$ can be decomposed with respect to the photoelectric and Compton functions, providing the following

relationship between the coefficients a_1 and a_2 in (3.12) and a_c and a_p in (3.7):

$$\begin{aligned}\mu(E) &= a_1\mu_\alpha(E) + a_2\mu_\beta(E) \\ &= a_1(a_{c\alpha}f_c(E) + a_{p\alpha}f_p(E)) + a_2(a_{c\beta}f_c(E) + a_{p\beta}f_p(E)) \\ &= \underbrace{(a_1a_{c\alpha} + a_2a_{c\beta})}_{=a_c} f_c(E) + \underbrace{(a_1a_{p\alpha} + a_2a_{p\beta})}_{=a_p} f_p(E) \end{aligned} \tag{3.14}$$

Thus, it is possible to go back and forth between the basis material model and the Photo-Compton model.

3.2 Pre-reconstruction MECT

Pre-reconstruction methods perform LAC decomposition directly to the projection data (i.e. before image reconstruction). The coefficient images $a_k(\vec{x})$ are estimated in the following way. Given MECT measurements $I_1, I_2, ..., I_{N_s}$, where $I_i = \{I_{ij}\}_{j=1}^{N_d}$ and I_{ij} is modeled by (2.17), and an LAC expansion model (3.1), first the coefficient sinograms A_k are estimated from the collection of measured projection data and then the corresponding coefficient images $a_k(\vec{x})$ are reconstructed (e.g., using FBP to each sinogram). See Figure 3·1. Pre-reconstruction multi-energy techniques theoretically allow reconstruction of images that are free of beam-hardening [Engler and Friedman, 1990, Remeysen and Swennen, 2006].

The main principle is that the line integrals of the attenuation coefficient can be found from the measured line integrals of the coefficients $a_k(\vec{x})$ [Alvarez and Macovski, 1976]. Equation (3.5) is considered and one can view this expression for a fixed value of j as a system of N_s nonlinear equations in N_b unknowns where the kth unknown is A_{kj}. If certain conditions are satisfied [Alvarez and Macovski, 1976], then for each ray L_j, one can solve these nonlinear equations yielding estimates $\hat{A}_{kj}$ of the A_{kj}'s. The collection $\left\{\hat{A}_{kj}\right\}_{j=1}^{N_d}$ is the estimated sinogram of $a_k(\vec{x})$, which means that $a_k(\vec{x})$

can be reconstructed from it by conventional FBP or iterative techniques.

The above is the basic framework for all the pre-reconstruction techniques [Alvarez and Macovski, 1976, Kalender et al., 1988, Ying et al., 2006, Noh et al., 2009, Stenner et al., 2007]. Generally the accuracy of pre-reconstruction methods depends on the accuracy of the nonlinear transformation of the MECT measurements and there is always a compromise between flexibility and precision [Zhang et al., 2008].

A big issue in pre-reconstruction techniques is how to solve the set of nonlinear equations (3.5). Alvarez and Macovski solved the problem numerically using a power series approximation [Alvarez and Macovski, 1976]. In [Kalender et al., 1988], a pre-calculated look-up table was used. Ying *et al.* posed the problem as a least squares minimization problem and solved it using iso-transmission curves [Ying et al., 2006]. A statistical approach was proposed in [Noh et al., 2009] in which the measurements are modeled as Poisson random variables. The problem is solved with penalized weighted least square and penalized likelihood methods.

Another issue is whether accurate analytic expressions of the source spectra functions and the detector gain (the components of $W_i(E)$ in equation (3.5)) are known. In the early technique suggested by Alvarez and Macovski, they assumed that the analytic forms of the spectra are not known. Instead, a general form of equation (3.5) with undetermined coefficients was introduced and the coefficients were determined experimentally. Alternatively, another method tries to approximate the spectra functions using expectation maximization [Zhang et al., 2008]. Ying *et al* [Ying et al., 2006] suggested a way to correct the final images for the spectral variations. In other methods the function $W_i(E)$ is assumed to be known [Noh et al., 2009].

If the spectral weighting functions are assumed to be known, using the measurement model (3.6) the problem of mapping the multi-energy measurements to basis

coefficient sinograms may be formulated as the following least-squares minimization:

$$\underset{A}{\text{minimize}} \left\{ \sum_{i=1}^{N_s} \left(I_i - e^{-AF} \boldsymbol{w}_i \right)^2 \right\} \tag{3.15}$$

where I_i is the vector of measurements with spectral weighting function i and $A = [A_1 \; A_2 \cdots \; A_{N_b}]$. We will call this formulation sinogram least squares (SLS).

Following is an overview of specific implementations of the pre-reconstruction technique.

3.2.1 Polynomial approximation of measurements

One of the first dual-energy techniques was this pre-reconstruction method proposed by Alvarez and Macovski [Alvarez and Macovski, 1976]. The LAC is represented using the Photo-Compton model as in Equation (3.11). Based on the measurement model (3.5) the following set of two nonlinear equations is formed:

$$I_1(A_1, A_2) = \int W_1(E) \exp\left(-A_1 f_1(E) - A_2 f_2(E)\right) dE \tag{3.16}$$

$$I_2(A_1, A_2) = \int W_2(E) \exp\left(-A_1 f_1(E) - A_2 f_2(E)\right) dE \tag{3.17}$$

where I_i is the set of measurements at all the ray paths with spectral weighting functions i, A_i is the sinogram of coefficient image $a_i(\vec{x})$, and $f_1(E)$ and $f_2(E)$ are the photoelectric and Compton basis functions, respectively.

To solve the nonlinear equations, a general form of Equations (3.16) and (3.17) based on polynomials is introduced:

$$\ln I_1 = b_0 + b_1 A_1 + b_2 A_2 + b_3 A_1^2 + b_4 A_2^2 + b_5 A_1 A_2 + b_6 A_1^3 + b_7 A_2^3 \tag{3.18}$$

$$\ln I_2 = c_0 + c_1 A_1 + c_2 A_2 + c_3 A_1^2 + c_4 A_2^2 + c_5 A_1 A_2 + c_6 A_1^3 + b_c A_2^3 \tag{3.19}$$

The coefficients b_i and c_i are determined experimentally by measuring the trans-

mission through materials with known values of A_1 and A_2 and using a least squares curve fitting procedure. Once the sets of coefficients b_i and c_i are determined, Equations (3.18) and (3.19) become two simultaneous cubic equations which may be solved numerically for A_1 and A_2 using a generalization of the Newton-Raphson method. Images of $a_1(\vec{x})$ and $a_2(\vec{x})$ are then reconstructed from A_1 and A_2 using FBP.

3.2.2 Constrained least-squares minimization

Ying *et al.* from Analogic Corporation formed the nonlinear inversion as a constrained minimization problem [Ying et al., 2006, Ying et al., 2007]. As in Alvarez and Macovski's method, the measurements are modeled by Equations (3.16) and (3.17), using the Photo-Compton decomposition. As opposed to the approach of Alvarez and Macovski, the assumption is that the spectral weighting functions $W_i(E)$ are known.

The problem is posed as the following constrained least squares minimization:

$$(\hat{A}_1, \hat{A}_2) = \arg \min_{(A_1, A_2)} (I_1(A_1, A_2) - I_1^m)^2 + (I_2(A_1, A_2) - I_2^m)^2 \tag{3.20}$$

subject to the constraints:

$$A_1 \geq 0 \qquad A_2 \geq 0 \tag{3.21}$$

where I_1^m and I_2^m are dual-energy measurements, $I_1(A_1, A_2)$ and $I_2(A_1, A_2)$ are the modeled measurements (Equations (3.16) and (3.17)). The above constrained optimization problem is solved using a root finding Newton's method. If one of the estimates is negative, then one of A_1 or A_2 is set to zero and the problem is solved for the other. Once A_1 and A_2 are estimated, the coefficient images $a_1(\vec{x})$ and $a_2(\vec{x})$ are reconstructed from A_1 and A_2 using FBP.

3.2.3 Empirical dual-energy calibration (EDEC)

The empirical dual-energy calibration method (EDEC), proposed in [Stenner et al., 2007], decomposes a scanned object into two basis material images $a_1(\vec{x})$ and $a_2(\vec{x})$. No explicit knowledge of the system spectra is required. This is done by scanning a calibration phantom composed of both basis materials and then estimating a polynomial function which maps the dual-energy measurements to material-selective sinograms.

The dual-energy measurements I_1 and I_2 are modeled by Equation 3.5, with $N_b = 2$. The basis functions $f_1(E)$ and $f_2(E)$ are LACs of two basis materials. The measurements are normalized and converted to 'minus log' space according to Equation 2.18. The normalized converted measurements are denoted by $\tilde{I}_1$ and $\tilde{I}_2$.

The inverse mapping from the polychromatic measurements $\tilde{I}_1$ and $\tilde{I}_2$ to the material-basis coefficient sinogram data A_1 and A_2 is modeled as a weighted sum of polynomial functions $b_n(\tilde{I}_1, \tilde{I}_2)$:

$$A_k = \sum_{n=0}^{N-1} c_{kn} b_n(\tilde{I}_1, \tilde{I}_2), \quad k = 1, 2 \tag{3.22}$$

where $b_n(\tilde{I}_1, \tilde{I}_2)$ is given by

$$b_n(\tilde{I}_1, \tilde{I}_2) = \tilde{I}_1^s \tilde{I}_2^t \tag{3.23}$$

for $s = 0, ..., S$, $t = 0, ..., T$, and $n = s(T + 1) + t$. Note that $b_n(\tilde{I}_1, \tilde{I}_2)$ are basis functions in the sinogram space.

In the calibration process, a phantom is used to obtain the coefficients of the polynomials, c_{kn}. The calibration steps are:

1. Take dual-energy measurements of the calibration phantom to obtain dual-energy sinograms $\tilde{I}_1$ and $\tilde{I}_2$.

2. Evaluate the basis functions $b_n(\tilde{I}_1, \tilde{I}_2)$ using Equation (3.23) at the observed points.

3. Apply standard reconstruction to each basis function $b_n(\tilde{I}_1, \tilde{I}_2)$ to obtain basis images $f_n(\vec{x})$.

4. Construct template images, $t_1(\vec{x})$ and $t_2(\vec{x})$, and weight images, $w_1(\vec{x})$ and $w_2(\vec{x})$, according to a priori knowledge. Specifically, $t_k(\vec{x})$ and $w_k(\vec{x})$ are defined as:

$$t_k(\vec{x}) = \begin{cases} 1 & \text{for } \vec{x} \in \text{ material i} \\ 0 & \text{otherwise} \end{cases} \tag{3.24}$$

$$w_k(\vec{x}) = \begin{cases} 1 & \text{for } \vec{x} \in \text{ material 1 or 2 or air} \\ 0 & \text{eroded boundaries, unknown material} \end{cases} \tag{3.25}$$

   The regions of materials 1 and 2 are found by thresholding of a standard FBP reconstruction of $\tilde{I}_2$, denoted $\bar{\mu}_2(\vec{x})$.

5. Find the coefficients c_{1n} and similarly c_{2n}, by minimizing the following quantity (we omit the first index k):

$$\int w(\vec{x}) \left(\sum_n c_n f_n(\vec{x}) - t(\vec{x}) \right)^2 dx_1 dx_2 \tag{3.26}$$

   The solution is given by

$$\mathbf{c} = B^{-1}\mathbf{a} \tag{3.27}$$

   where $\mathbf{c} = [c_1\ c_2\ \cdots]^T$. The elements of B are $B_{mn} = \int w(\vec{x}) f_n(\vec{x}) f_m(\vec{x}) dx_1 dx_2$, and $a_n = \int w(\vec{x}) f_n(\vec{x}) dx_1 dx_2$.

Once we have the coefficients we can take dual-energy measurements of any scene, pass them through the estimated functions (3.22) to get the material-specific sinogram data and use standard FBP reconstruction to obtain decomposed images (an image of basis material 1 and an image of basis material 2).

3.3 Post-reconstruction MECT

Post-reconstruction MECT is another approach for obtaining estimates of the coefficient images $a_k(\vec{x})$ from MECT measurements. Post-reconstruction methods perform reconstruction of the separate scans and perform LAC decomposition using the reconstructed images. First a set of reconstructed effective attenuation images, $\bar{\mu}_i(\vec{x})$, $i = 1, ..., N_s$, is produced by applying conventional CT reconstruction, as described in Section 2.2.4, to the measurements obtained with the different spectral weighting functions. These images are generally generated automatically by the scanner software. Then, the images are combined to produce estimates of the coefficient images $a_k(\vec{x})$. See Figure 3·1. Post-reconstruction techniques are computationally simple because they require only simple arithmetic operations at each corresponding pixel of the CT images. In addition, post-reconstruction techniques provide the only alternative when one does not have access to the projection data or the reconstruction software, which are required by the pre-reconstruction techniques.

Below we describe a few current post-reconstruction MECT techniques.

3.3.1 Averaged image

The simplest post-reconstruction technique is to examine two effective attenuation images obtained with low and high spectral functions and to construct an averaged image [Johnson et al., 2007, Yu et al., 2009]. Commercial medical DECT scanners offer this feature nowadays to the radiologists. This method allows to reduce the noise level compared to conventional single-energy reconstruction and enhance contrast. However, quantitative information about the chemical composition of the scanned object cannot be obtained in this way.

3.3.2 Three-material decomposition

This post-reconstruction method was proposed in [Petersilka et al., 2008]. Using two effective attenuation images, obtained with low and high spectral functions, two CT numbers are given at every spatial location or pixel, $H_1(\vec{x})$ and $H_2(\vec{x})$. The two CT numbers at each pixel are represented by a point in a coordinate system (see Figure 3·3). There are three points in this diagram which represent the CT numbers of three chosen idealized materials (e.g., soft tissue, bone, iodine). Two ideal vectors are constructed using those three points. These vectors define a new coordinate system. Based on this coordinate transformation, a material separation and a subsequent segmentation can be performed. This method may perform well if all the scanned materials are in fact composed of the three idealized materials (which is the situation with most materials found in the body). However, it may not be useful for other materials.



Figure 3·3: The principle of three-material decomposition [Petersilka et al., 2008]. The basis materials (e.g., soft tissue, iodine, and bone) are connected by two vectors in a diagram that maps CT values obtained at low energy versus CT values obtained at high energy. The pixel shown between the two ideal lines contains both iodine and bone, quantified by the length of the respective dashed lines.

3.3.3 Basis material post-recon decomposition

A post-reconstruction method, discussed in [Engler and Friedman, 1990] and implemented by researchers from General Electric [Walter et al., 2006], is based on using the basis material model (3.12) in the post-reconstruction mode:

$$\bar{\mu}_L(\vec{x}) = a_1(\vec{x})\bar{\mu}_{\alpha L} + a_2(\vec{x})\bar{\mu}_{\beta L} \tag{3.28}$$

$$\bar{\mu}_H(\vec{x}) = a_1(\vec{x})\bar{\mu}_{\alpha H} + a_2(\vec{x})\bar{\mu}_{\beta H} \tag{3.29}$$

where the subscripts L and H denote the low and high energy spectral functions, respectively, $\bar{\mu}_{\alpha L/H}$ are the values of the effective attenuation images for material α, $\bar{\mu}_{\beta L/H}$ are the values of the effective attenuation images for material β, and $\bar{\mu}_{L/H}(\vec{x})$ are the values of effective attenuation images of the scanned object.

The solution of the above equation on a pixel-by-pixel basis gives the basis material weighting parameters $a_1(\vec{x})$ and $a_2(\vec{x})$, which can be used to calculate Z_{eff} and ρ (see Photo-Compton model in Section 3.1). As with any post reconstruction method, the accuracy of the results is contingent on the amount of beam hardening and artifacts encountered in the reconstructed images.

3.3.4 ρZ Projection method

In [Heismann et al., 2003] a post-reconstruction dual-energy method called "ρZ Projection" is proposed. As input data the method uses two values of the reconstructed attenuation coefficient, $\bar{\mu}_1(\vec{x})$ and $\bar{\mu}_2(\vec{x})$, obtained with two different source spectra (with subscript 1 corresponding to the lower energy spectrum). The output is the effective atomic number and density, which are assumed to be a function of the ratio $\frac{\bar{\mu}_1(\vec{x})}{\bar{\mu}_2(\vec{x})}$.

Specifically, the effective atomic number in the ρZ projection method is estimated in the following way:

- The values of $\bar{\mu}_1$ and $\bar{\mu}_2$ are predicted for all elements with atomic number $Z < 30$ using a simplified approximate model:

$$\bar{\mu}_i \backsimeq \int \widehat{W}_i(E)\mu(E)dE \tag{3.30}$$

where $\mu(E)$ is the linear attenuation coefficient of the element, and $\widehat{W}_i(E)$ is the ith normalized spectral weighting function, which is related to the source spectra $S_i(E)$ and detector response $D(E)$ as follows

$$\widehat{W}_i(E) = \frac{S_i(E)D(E)}{\int S_i(E)D(E)dE} \tag{3.31}$$

$\widehat{W}_i(E)$ is assumed to be known.

- The ratio $\frac{\bar{\mu}_1}{\bar{\mu}_2}$ for each element is calculated based on the results of (3.30). The ratio as a function of atomic number Z is denoted $F(Z)$. An example is shown in Figure 3·4.

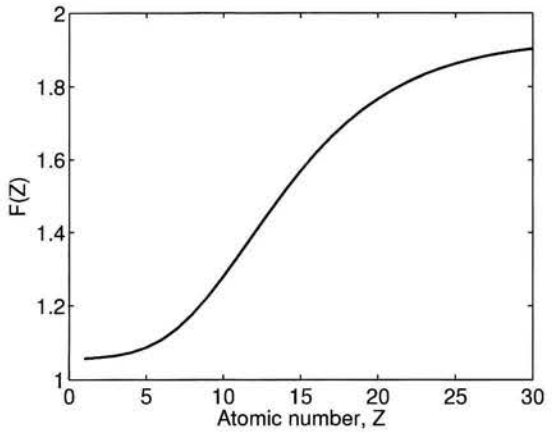


Figure 3·4: $F(Z)$ curve calculated using 80 kVp and 140 kVp Siemens spectral weighting functions

- Since $F(Z)$ is a monotonically rising function of Z for $Z < 30$, one can calculate the inverse function by numerical interpolation for any set of measured values.

The estimated effective atomic number at each spatial location is obtained by $Z_{\text{eff}}(\vec{x}) = F^{-1}\left(\frac{\bar{\mu}_1(\vec{x})}{\bar{\mu}_2(\vec{x})}\right)$

The density $\rho(\vec{x})$ is assumed to be a function of $\bar{\mu}_1(\vec{x}) - c\bar{\mu}_2(\vec{x})$, where c is a constant, and is found in a similar manner.

The ρZ projection method works well for materials with density and atomic number close to water. However, it fails when dealing with materials with relatively high atomic number and density because of the model mismatch (the high-atomic number materials have K-edges which are not captured by the model) [Liu et al., 2009].

3.4 Other MECT techniques

Some methods do not fall in the pre-reconstruction or post-reconstruction categories. Below are a few examples.

3.4.1 Method for mismatched sinogram data

One example is the enhanced image-based DECT method [Maass et al., 2009]. This is an image-based method whose goal is to combine mismatched sinogram data for DECT information. Sinogram data is mismatched if the ray paths of the measurements with one spectral function are different from the ray paths of the measurements with the other spectral functions. The method allows for implementation in the sinogram data pre-processing stage or may be used in the image domain. It is shown that among the image-based methods that can be performed with completely mismatched raw data sets, the method is superior in its ability to deal with beam hardening artifacts.

3.4.2 Alternating minimization algorithm for MECT

This method approaches the problem of reconstructing the material-dependent decomposition coefficients $a_k(\vec{x})$ from MECT measurements as a maximum likelihood

estimation problem [O'Sullivan and Benac, 2007]. The measurements I_i are assumed to be the mean of a Poisson random variable. The spectral weighting functions W_i are assumed to be known. The coefficient images $a_k(\vec{x})$ are estimated directly from the measurements. The problem is reformulated as a double minimization of the I-divergence. An alternating minimization algorithm that monotonically decreases the objective function is suggested. Simulations demonstrate the ability to correct the beam hardening artifacts and the ability to reduce streaking artifacts that arise from beam hardening and background events.

3.5 Experimental results with current methods

Most of the methods for information extraction in MECT described in the literature are motivated by medical applications and were applied and tested in the medical domain. In order to deepen our understanding of their performance when applied to security problems we implemented them and tested their performance using simulated and real MECT data with characteristics closer to those arising in the security domain. Here we present some of the results. In Section 3.5.1 we show results using one of the post reconstruction methods described in Section 3.3 called ρZ projection [Heismann et al., 2003]. We test the method on reconstructed images obtained from real DECT measurements of security inspired phantoms. In Section 3.5.2 we compare a few current methods for estimating the coefficient images $a_k(\vec{x})$ from MECT data. We use simulations and real data and study the performance of the methods on clean and cluttered cases.

3.5.1 Estimation of effective atomic number and denisty using the ρZ projection method

We implemented the ρZ projection method, explained in Section 3.3.4, and applied it to reconstructed images obtained from real dual-energy data.

The first dataset we used was a scan of a phantom (a set of specially designed objects to be scanned) provided by Lawrence Livermore national laboratory and the department of homeland security (DHS). The phantom can be seen in Figure 3·5. The phantom was scanned with a Siemens SOMATOM Definition dual-source CT scanner by Homer Pien, Synho Do, and Mannudeep K. Kalra at MGH. The SOMATOM scanner has two X-ray sources separated by 90 degrees, which can operate simultaneously. Each source can be set to a different spectrum. In this scanner one of the sources has a wider angular view than the other. Figure 3·6 shows the scanner geometry. Figure 2·10 shows the normalized spectral weighting functions. In our experiment one source was set to 140 kVp, and the other source to 80 kVp. The scanner software was used to reconstruct images of the effective attenuation for both spectra.

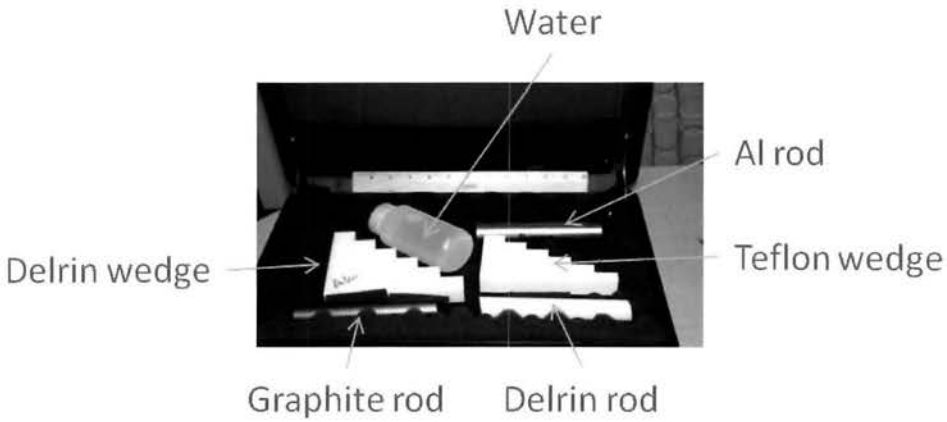


Figure 3·5: LLNL/DHS phantom

The $F(Z)$ curve was calculated using Equation (3.30) with spectral functions provided by Siemens and with element attenuation coefficients downloaded from the XCOM database [Berger et al., 2005]. It is shown in Figure 3·4. At each pixel we calculated the inverse mapping from $F(Z)$ to Z and obtained estimated images of Z_{eff} and ρ. We used the 140 kVp reconstructed attenuation image to obtain an air mask by thresholding it at -900 HU. The estimated Z_{eff} and ρ images were set to zero

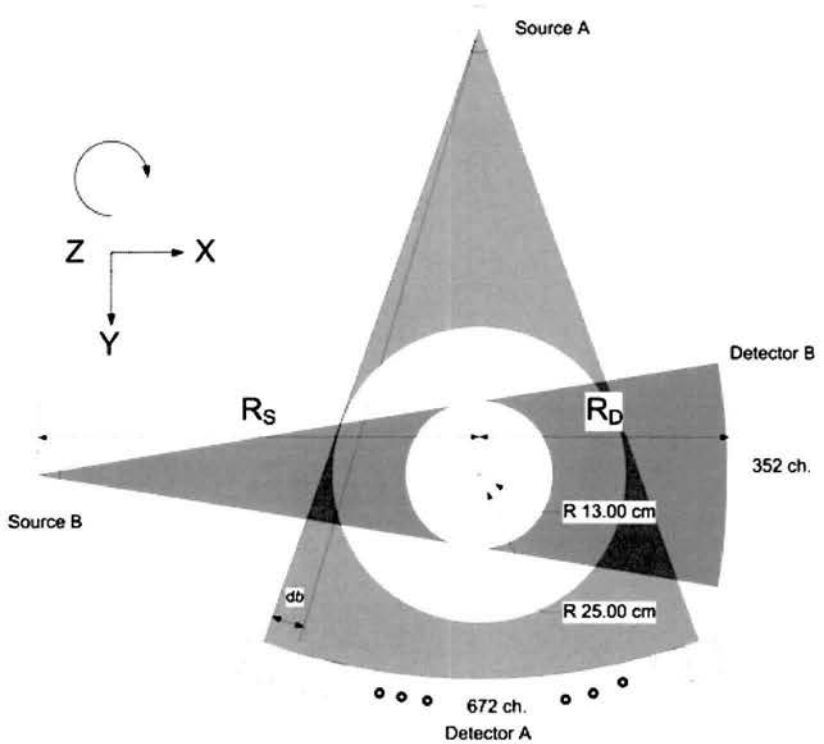
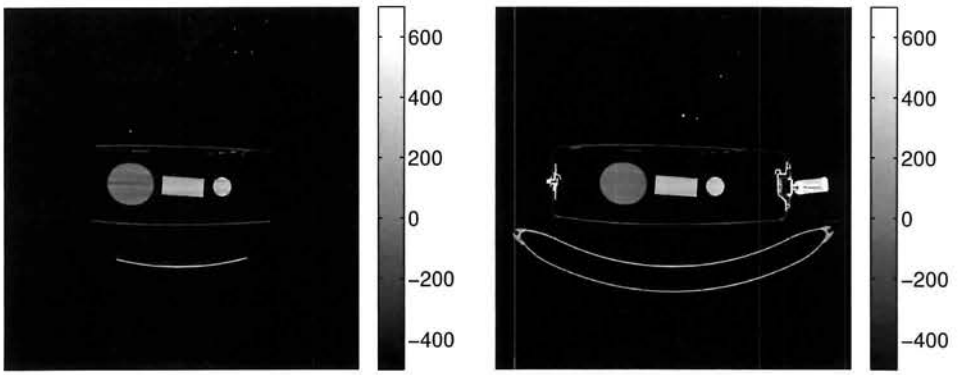


Figure 3·6: Siemens SOMATOM Definition dual-source scanner geometry

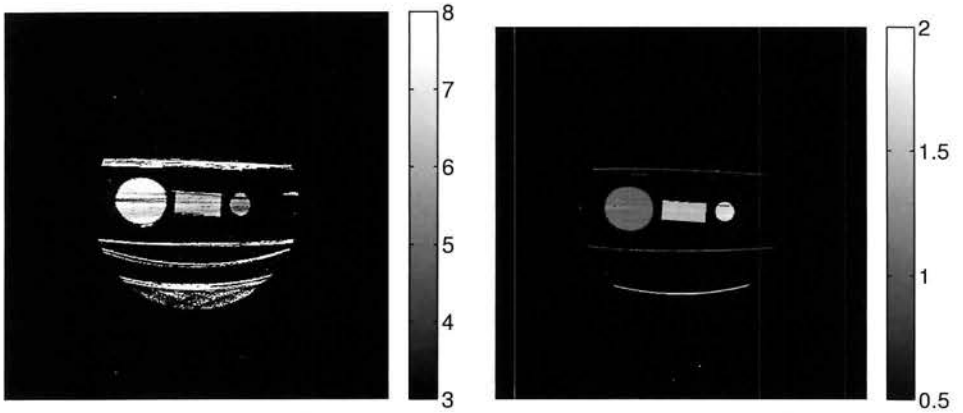
in all the air pixels.

The results for a slice of the phantom containing a water bottle, a delrin bar and a graphite rod can be seen in Figure 3·7. The reconstructed attenuation images are shown on the top and the estimates of Z_{eff} and ρ are shown on the bottom. The streaks in the water bottle are metal artifacts caused by the metal in the suitcase containing the objects. For each material in this slice we manually selected a group of about 400 pixels inside the material and calculated the mean and standard deviation of the estimates. These numerical results are summarized in table 3.1. The theoretical value of the effective atomic number was calculated by equation 2.1 with m=2.94. The results suggest that the ρZ projection method preforms reasonably well for these materials which have a relatively low atomic number.

We also applied the ρZ projection method to a few slices from the Imatron scans



(a) 80 kVp recon (b) 140 kVp recon



(c) Estimated Z_{eff} (d) Estimated ρ

Figure 3·7: Images of results for DHS phantom. On the top are the reconstructed images of the same cross section obtained with different source spectra in HU. On the bottom are the corresponding Z_{eff} (left) and ρ (right). The images are 512×512. The objects from left to right are: water bottle, delrin bar and graphite rod.

database described in Appendix B. These are dual-energy scans obtained with a 95 kVp and 130 kVp source spectra. The reconstructed attenuation images were given by the scanner software. Figures 3·8-3·11 show the results for four different slices, each contains a rod of a different material- graphite, teflon, magnesium and silicon. These slices represent low-clutter cases and there is no metal in the scene. The reconstructions have correctly captured the shape of the objects and they are fairly homogeneous. For each material we manually selected a group of pixels inside

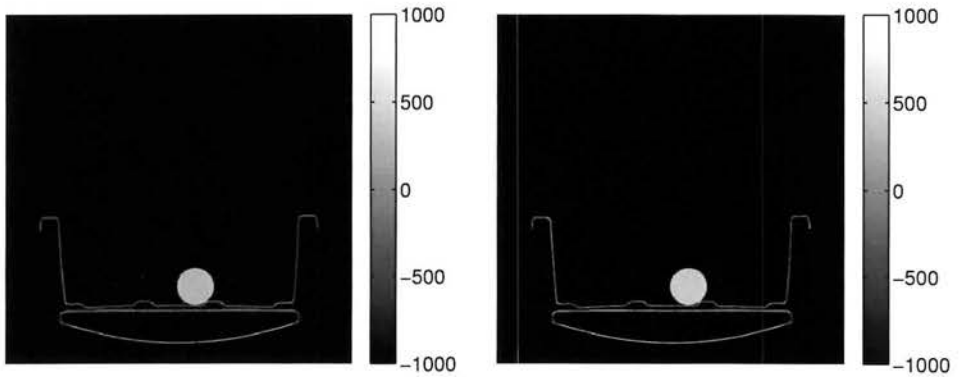
Material	Z_{eff}			ρ		
	theoretical	mean	std	theoretical	mean	std
water	7.42	7.11	1.00	1.00	1.11	0.07
delrin	6.95	6.21	0.91	1.41	1.53	0.12
graphite	6	4.80	1.46	1.68	1.65	0.26

Table 3.1: Z_{eff} and ρ estimates using the ρZ projection method applied to the DHS phantom.

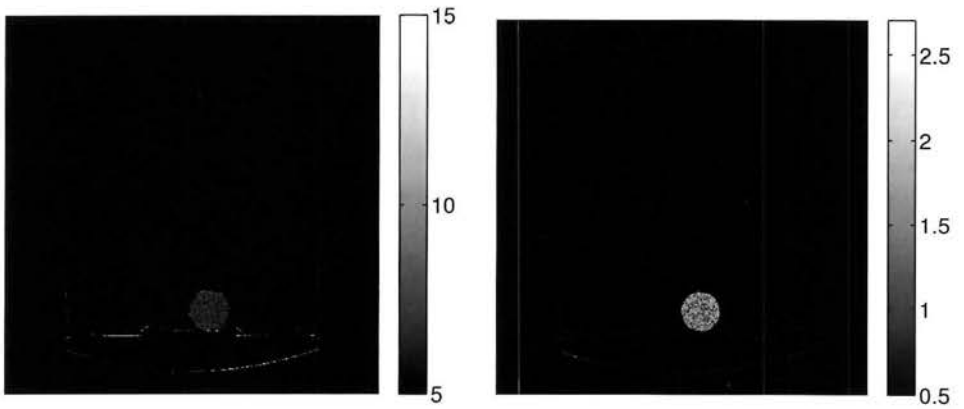
the material and calculated the mean and standard deviation of the estimates. The results are summarized in Table 3.2. For these materials the estimates are close.

Material	Z_{eff}			ρ		
	theoretical	mean	std	theoretical	mean	std
graphite	6	5.96	2.70	1.68	1.49	0.57
Teflon	8.44	8.44	1.77	2.13	2.05	0.31
magnesium	12	12.09	0.70	1.74	1.61	0.13
silicon	14	13.48	0.78	2.33	2.03	0.21

Table 3.2: Z_{eff} and ρ estimates using the ρZ projection method applied to slices from the Imatron scans database.

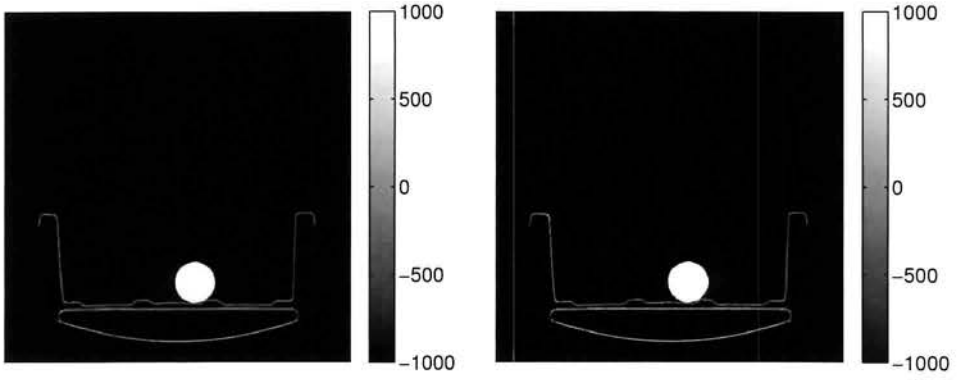


(a) 95 kVp recon (b) 130 kVp recon

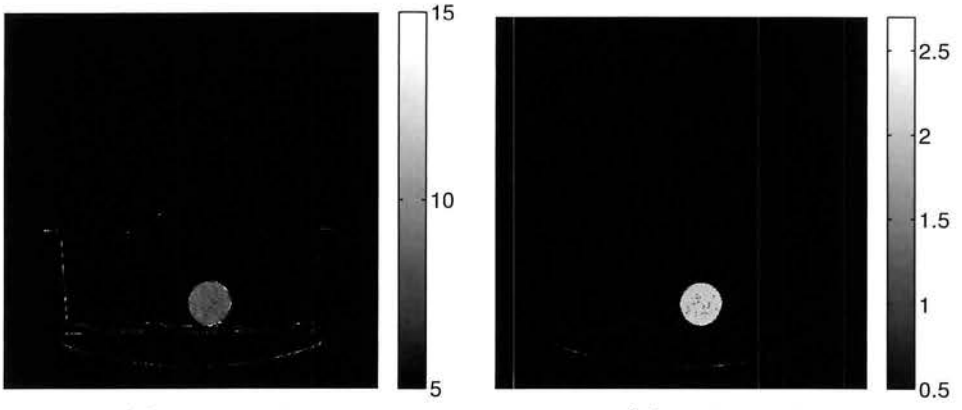


(c) Estimated Z_{eff} (d) Estimated ρ

Figure 3·8: ρZ projection method results for a slice with a graphite rod. On the top are the reconstructed images of the same cross section obtained with different source spectra in HU. On the bottom are the corresponding estimations Z_{eff} (left) and ρ (right).

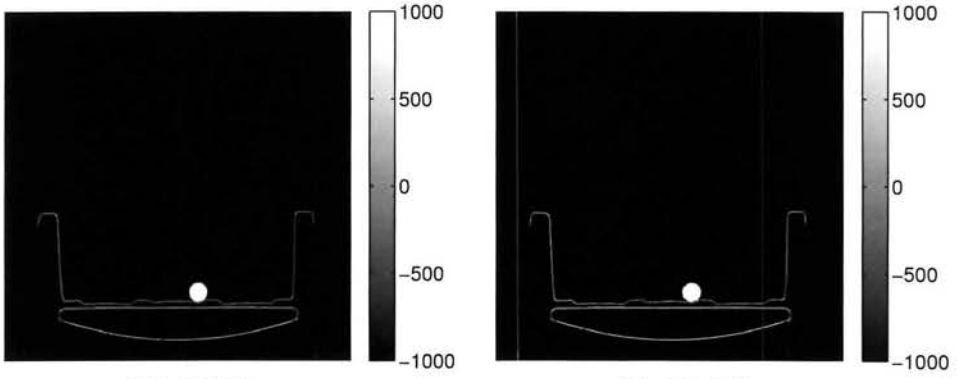


(a) 95 kVp recon (b) 130 kVp recon

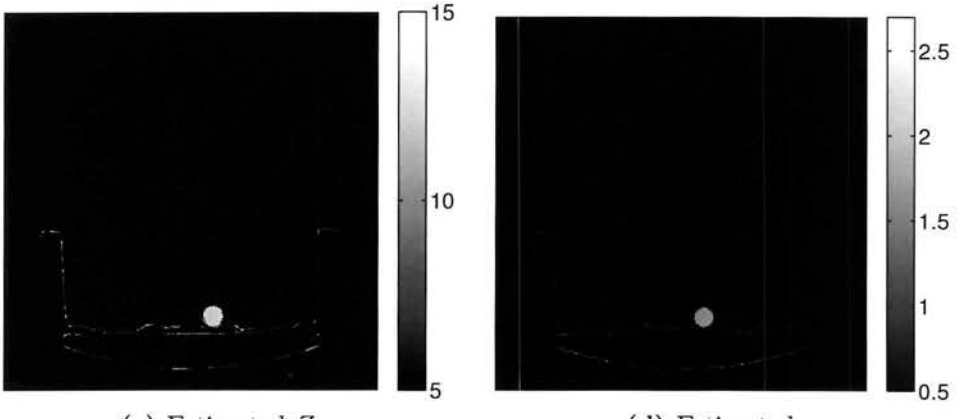


(c) Estimated Z_{eff} (d) Estimated ρ

Figure 3·9: ρZ projection method results for a slice with a Teflon rod. On the top are the reconstructed images of the same cross section obtained with different source spectra in HU. On the bottom are the corresponding estimations Z_{eff} (left) and ρ (right).

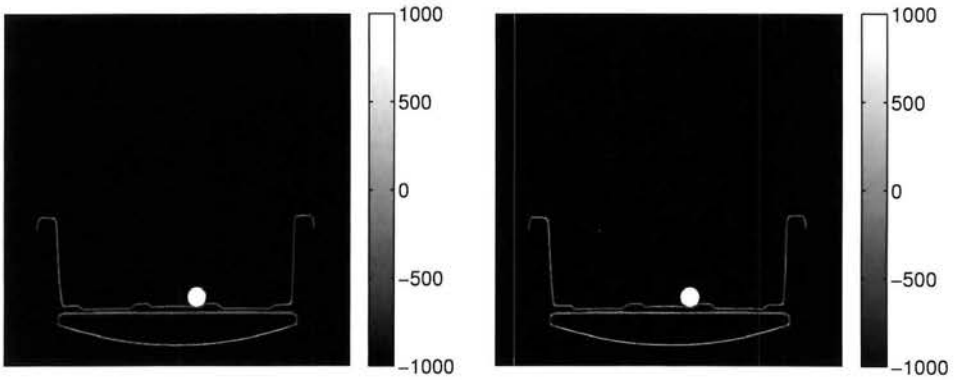


(a) 95 kVp recon **(b)** 130 kVp recon

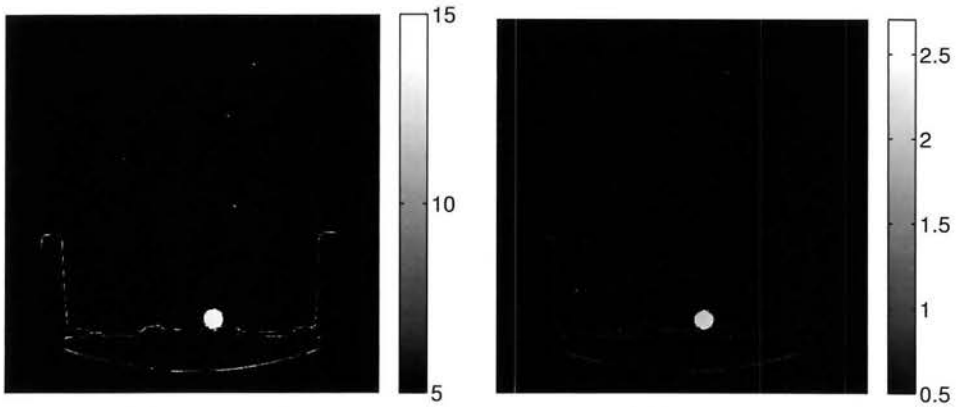


(c) Estimated Z_{eff} **(d)** Estimated ρ

Figure 3·10: ρZ projection method results for a slice with a magnesium rod. On the top are the reconstructed images of the same cross section obtained with different source spectra in HU. On the bottom are the corresponding estimations Z_{eff} (left) and ρ (right).



(a) 95 kVp recon (b) 130 kVp recon



(c) Estimated Z_{eff} (d) Estimated ρ

Figure 3·11: ρZ projection method results for a slice with a silicon rod. On the top are the reconstructed images of the same cross section obtained with different source spectra in HU. On the bottom are the corresponding estimations Z_{eff} (left) and ρ (right).

3.5.2 Estimation of basis expansion coefficients from MECT measurements

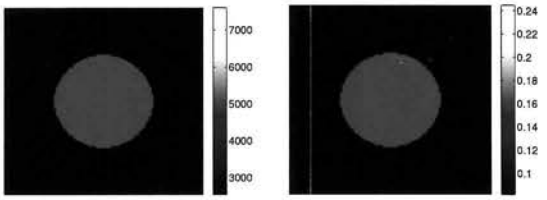
Here we compare a few of the methods described in the previous sections for estimating the expansion coefficient images from dual energy measurements. We use the Photo-Compton model for the LAC decomposition. Given a set of dual-energy measurements I_1 and I_2 (where index 1 corresponds to the lower energy spectrum), the goal is to reconstruct the photoelectric and Compton coefficient images, denoted by $a_1(\vec{x})$ and $a_2(\vec{x})$, respectively. The measurements are related to the coefficient images via Equation (3.6).

Experiments with simulated data

Here we compare the following methods: (i) polynomial approximation (PA) described in Section 3.2.1, (ii) constrained least-squares minimization (CM) described below, (iii) constrained least-squares minimization using Newton's method (CMN) described in Section 3.2.2, and (iv) alternating minimization algorithm for MECT (AM) described in Section 3.4.2.

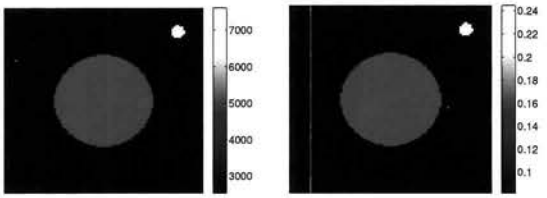
The CM method is our own implementation of solving the SLS problem (3.15). We use a trust-region algorithm implemented by Matlab's nonlinear solver [Mathworks, 2013] to estimate A_1 and A_2 with a non-negativity constraint. Then $a_1(\vec{x})$ and $a_2(\vec{x})$ are reconstructed from A_1 and A_2 individually using FBP.

We simulated dual-energy measurements of two different phantoms according to Equation 3.6 with the photoelectric and Compton basis functions. The phantoms are 100×100 pixels (10000×1 stacked). The forward projection operator R was generated using Matlab's 'radon' function with rays at angles $\theta = 0, 1, ..., 179\,°$, and 145 distances r. The 'clean' phantom consists of a homogeneous body of water in air. The 'cluttered' phantom consists of a body of water and a small iron rod in air. The photoelectric coefficient of water is 5.0684E+3 and the Compton coefficient is



(a) clean: photoelectric

(b) clean: Compton



(c) cluttered: photoelectric

(d) cluttered: Compton

Figure 3·12: Phantoms used for the simulations. On the top is the 'clean' phantom consisting of a body of water. On the bottom is the 'cluttered' phantom, which is same phantom with a small metal object.

0.1631. The photoelectric coefficient of iron is 1.396E+3 and the Compton coefficient is 5.3537. These values were calculated by a least-squares fit of the LACs to the Photo-Compton model. The photoelectric and Compton images of the phantoms are shown in Figure 3·12.

As the spectral weighting functions $W_1(E)$ and $W_2(E)$ we used the Siemens scanner 80 kVp and 140 kVp spectra estimates which appear in [Heismann et al., 2003] and are shown in Figure 3·13.

For the calibration phase in the PA method we used plastic as a calibration material, with photoelectric coefficient of 4.5053E+3 and Compton coefficient of 0.1879. The implementation of the CMN method was based on code provided by Oguz Semerci from Tufts University.

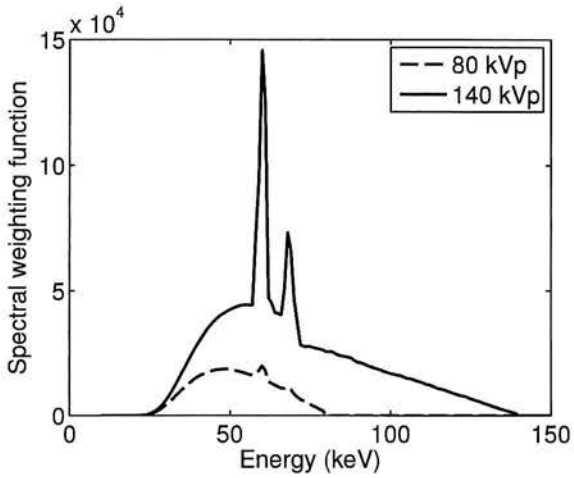
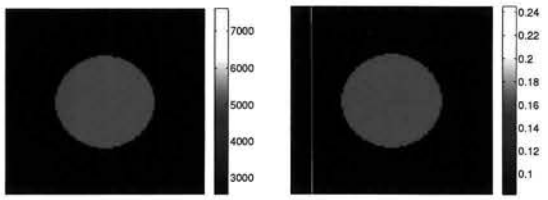


Figure 3·13: Spectral weighting functions used in simulation of dual-energy measurements

Effect of initialization:

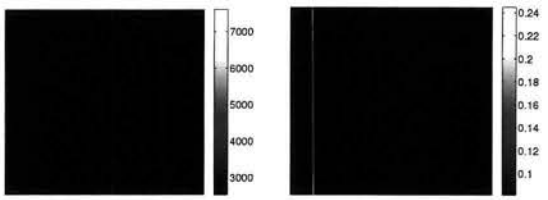
First we simulated noise-free measurements of the 'clean' phantom and examined the effect of initialization on the performance of the methods. Four different initializations were applied: (1) truth: the true photoelectric and Compton images; (2) zeros: all zeros; (3) flat: photoelectric image initialized with flat field of the photoelectric coefficient of Lucite (3.7151E+3), Compton image initialized with flat field of the Compton coefficient of Lucite (0.1909); (4) FBP: we apply FBP to minus the log of I_1, normalize the image to be between zero and one, and multiply it by the photoelectric and Compton coefficients of Lucite to initialize the photoelectric and Compton images, respectively. For the pre-reconstruction methods, the initialization was the Radon transform of the initial photoelectric and Compton images. The initializations are shown in Figure 3·14.

The reconstruction of the photoelectric image for the different initializations can be seen in Figure 3·15. The Compton images are shown in Figure 3·16. The mean and standard deviation of the reconstructed water coefficients are shown in Figure 3·17. In general, the estimates of the Compton coefficient are better than the estimates of



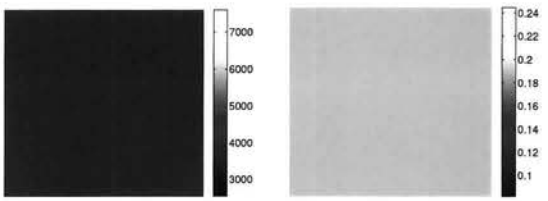
(a) Truth, photoelectric

(b) Truth, Compton



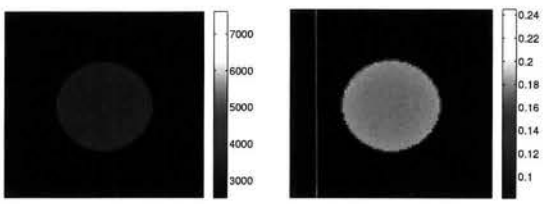
(c) Zeros, photoelectric

(d) Zeros, Compton



(e) Flat, photoelectric

(f) Flat, Compton

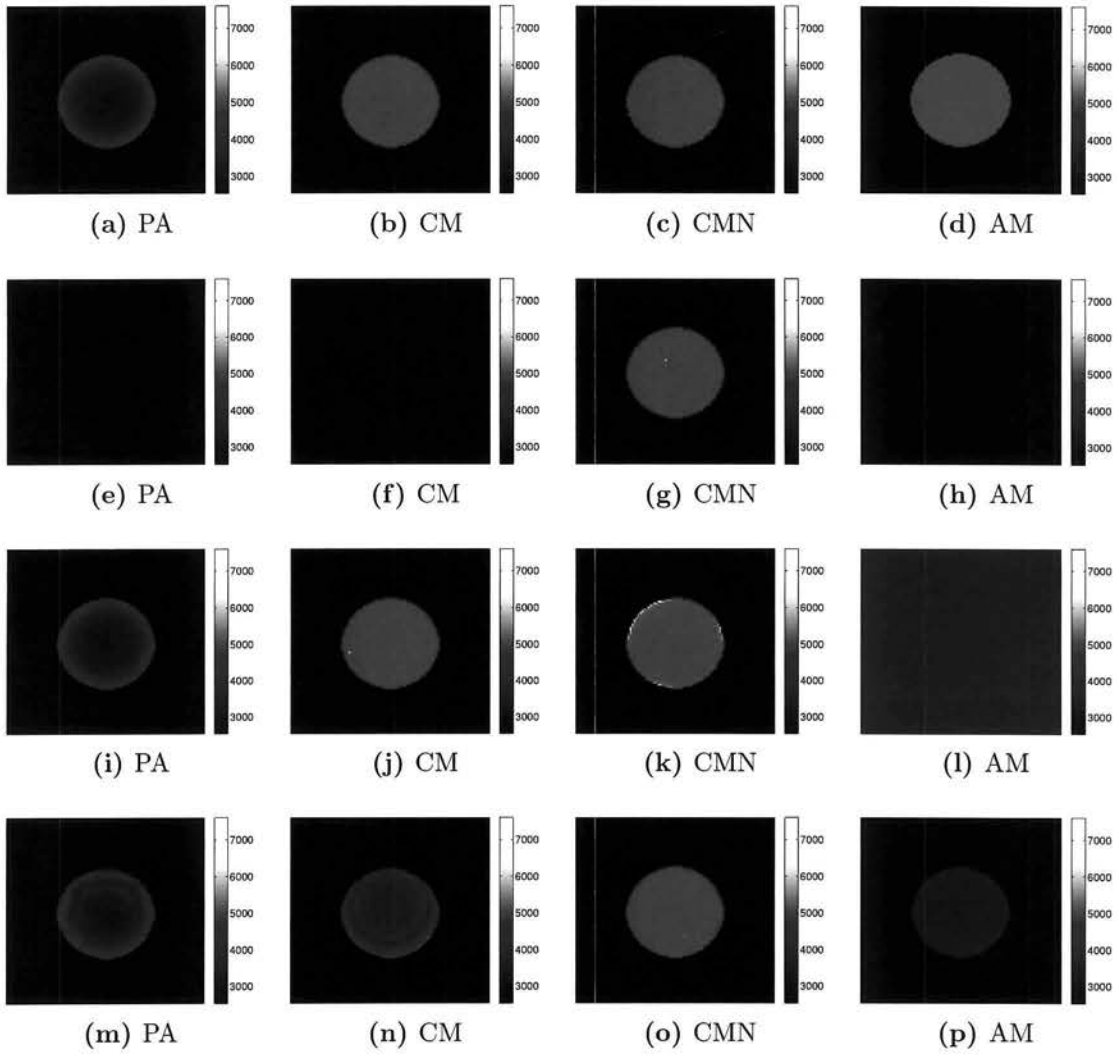


(g) FBP, photoelectric

(h) FBP, Compton

Figure 3·14: Different initializations used.

the photoelectric coefficient. It can be seen that the best initializations besides using the true images is FBP or flat. In addition, CMN has the best performance in the noise-free case. AM is sensitive to initialization, especially in the estimation of the photoelectric image, and has artifacts in the Compton image.



(a) PA (b) CM (c) CMN (d) AM

(e) PA (f) CM (g) CMN (h) AM

(i) PA (j) CM (k) CMN (l) AM

(m) PA (n) CM (o) CMN (p) AM

Figure 3·15: Reconstruction of photoelectric coefficient image. The measurements are noise free. Each row shows the results for a different initialization: truth, zeros, flat and FBP.

Effect of measurement noise:

We simulated noisy measurements of the 'clean' phantom using the Poisson measurement model (setting the values given by Equation 3.6 as the mean of a Poisson random variable). By scaling the spectral weighting functions shown in Figure 3·13 we created a high-noise and a low-noise case. In the low noise case the spectra were scaled by 1 which provided a total spectrum sum of 2.83×10^6 for 140 kVp and

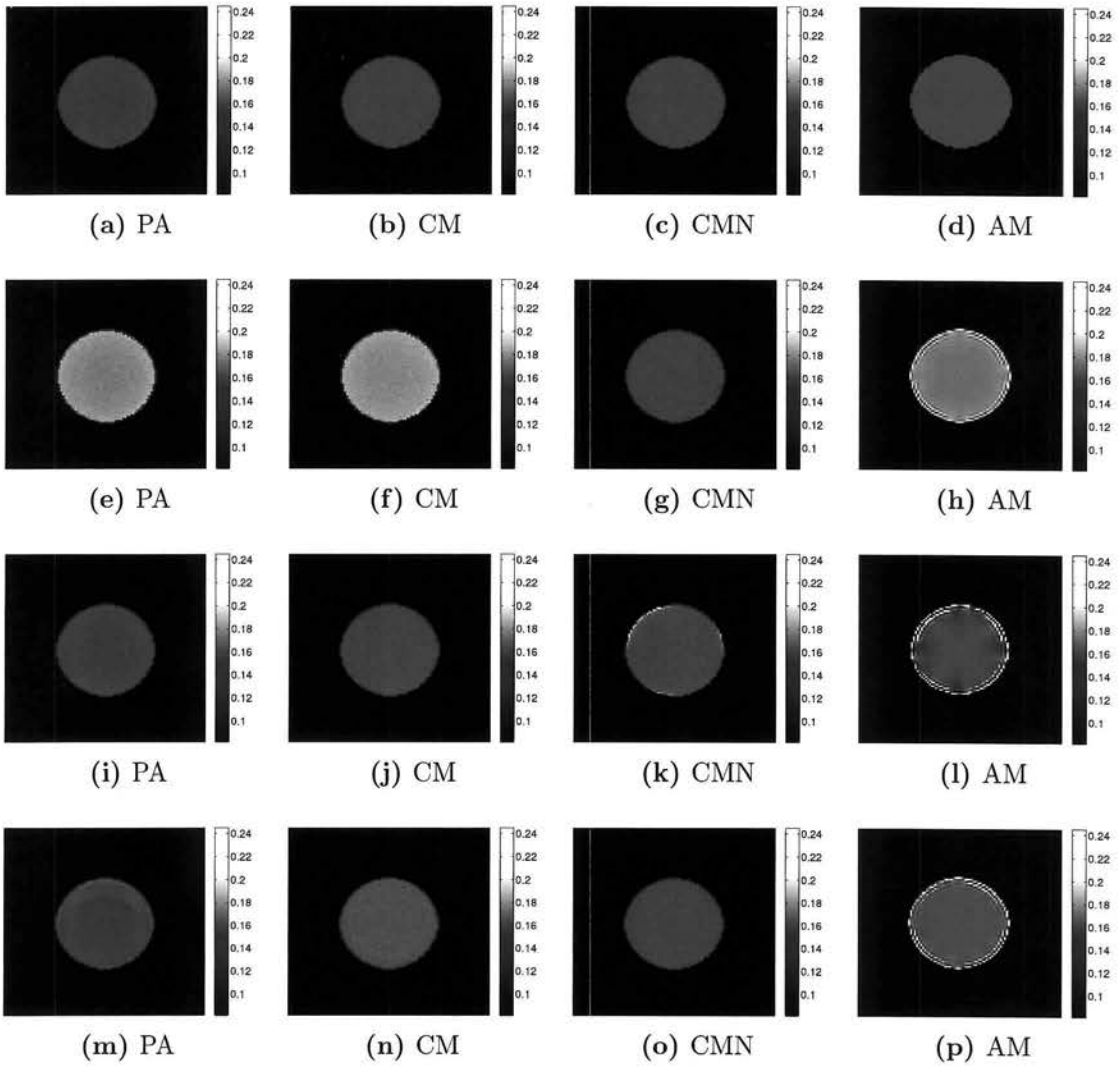
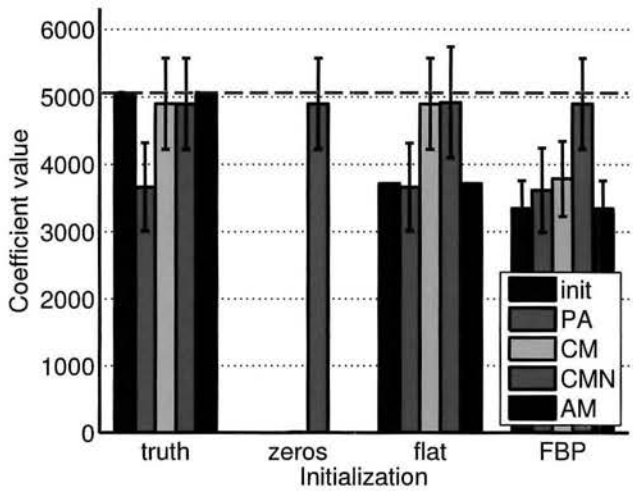


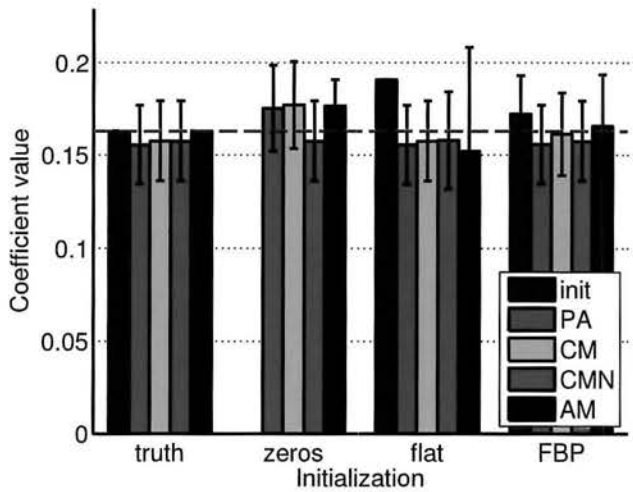
Figure 3·16: Reconstruction of Compton coefficient image. The measurements are noise free. Each row shows the results for a different initialization: truth, zeros, flat and FBP.

6.38×10^5 for 80 kVp. In the high noise case the spectra were scaled by 0.1, and the total sums were 2.83×10^5 for 140 kVp and 6.38×10^4 for 80 kVp . We applied the CM, CMN, PA and AM methods to the noisy measurements and produced estimates of the photoelectric and Compton images. We initialized the methods with the 'FBP' initialization.

Figures 3·18 and 3·19 show the reconstructed photoelectric and Compton images



(a) photoelectric



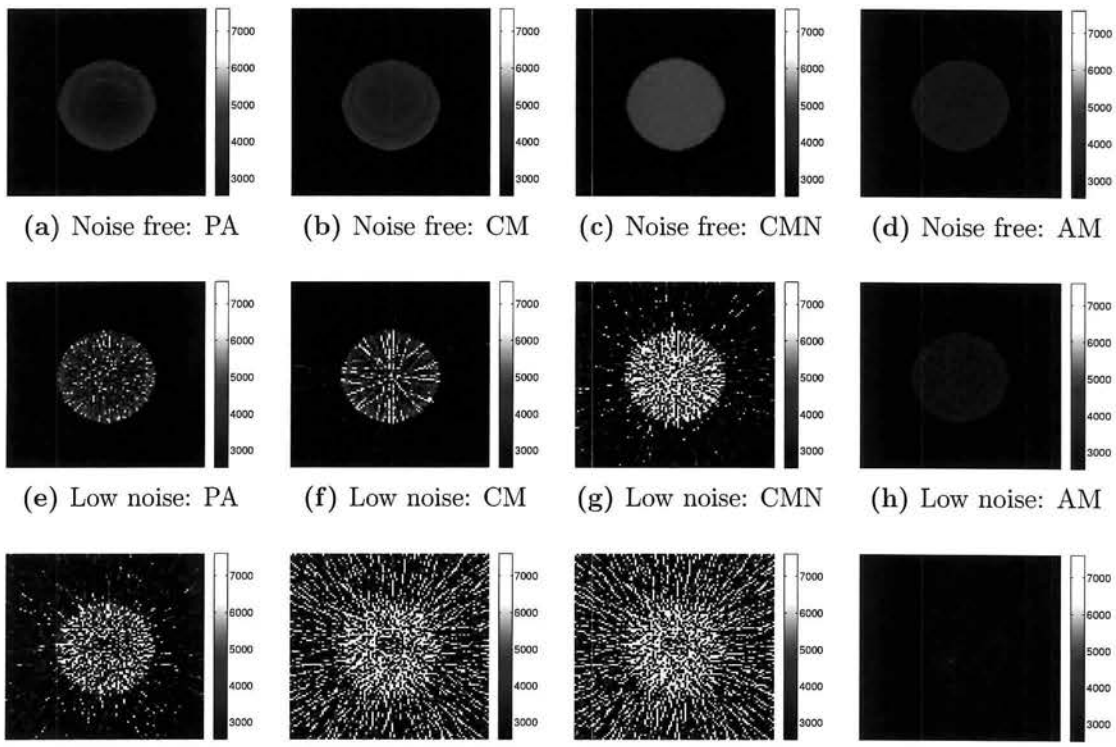
(b) Compton

Figure 3·17: Mean values of the photoelectric coefficient (top) and the Compton coefficient (bottom) inside the water region for the different initialization schemes. The pink dashed line indicates the true value. The errorbars represent plus and minus one standard deviation.

using the different methods for the noise-free, low-noise and high-noise cases. The estimated coefficients are compared in Figure 3·20. It can be seen that AM is more robust to noise, however there are some artifacts in the Compton image. PA and CM perform better than CMN in the noisy cases.

We repeated this for the 'cluttered' phantom. The results are shown in Fig-

ures 3·21-3·23. Again, it can be seen that PA and CM perform better than CMN in the noisy cases. AM estimates of the photoelectric coefficient for all noise levels are very bad.



(a) Noise free: PA (b) Noise free: CM (c) Noise free: CMN (d) Noise free: AM

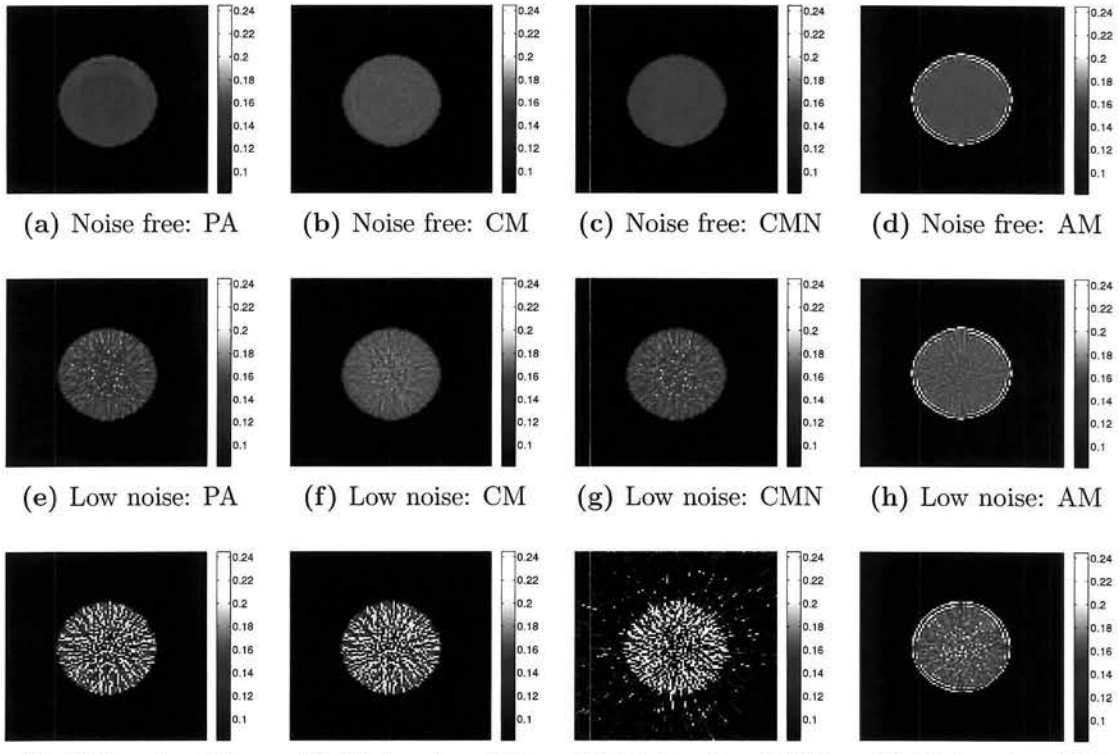
(e) Low noise: PA (f) Low noise: CM (g) Low noise: CMN (h) Low noise: AM

(i) High noise: PA (j) High noise: CM (k) High noise: CMN (l) High noise: AM

Figure 3·18: Reconstruction of photoelectric coefficient image using the different methods. Basic phantom. Top row: noise free; middle row: Low noise; Bottom row: high noise. Initialized with FBP.

Effect of number of iterations in AM method:

In all the experiments so far we used 1000 iterations for the AM algorithm. Figure 3·24 shows additional results with 10000 iterations. It can be seen that the photoelectric image isn't altered much when the number of iterations change. The Compton image shows more artifacts when the number of iterations is higher.

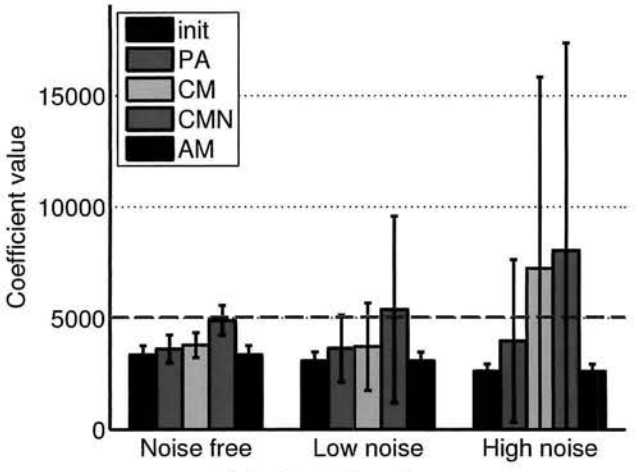


(a) Noise free: PA (b) Noise free: CM (c) Noise free: CMN (d) Noise free: AM

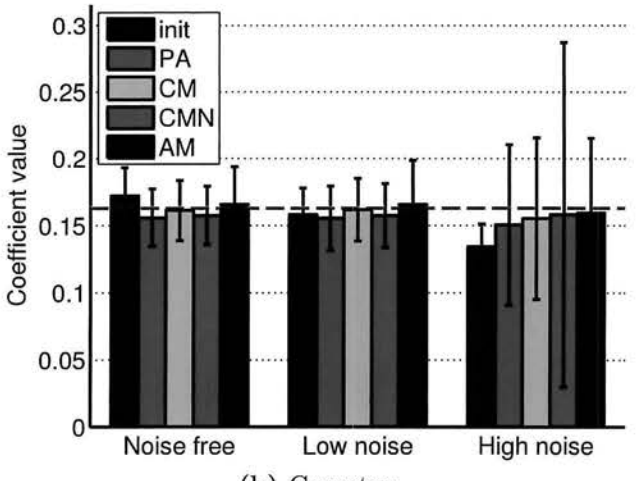
(e) Low noise: PA (f) Low noise: CM (g) Low noise: CMN (h) Low noise: AM

(i) High noise: PA (j) High noise: CM (k) High noise: CMN (l) High noise: AM

Figure 3·19: Reconstruction of Compton coefficient image using the different methods. Basic phantom. Top row: noise free; middle row: Low noise; Bottom row: high noise. Initialized with FBP.

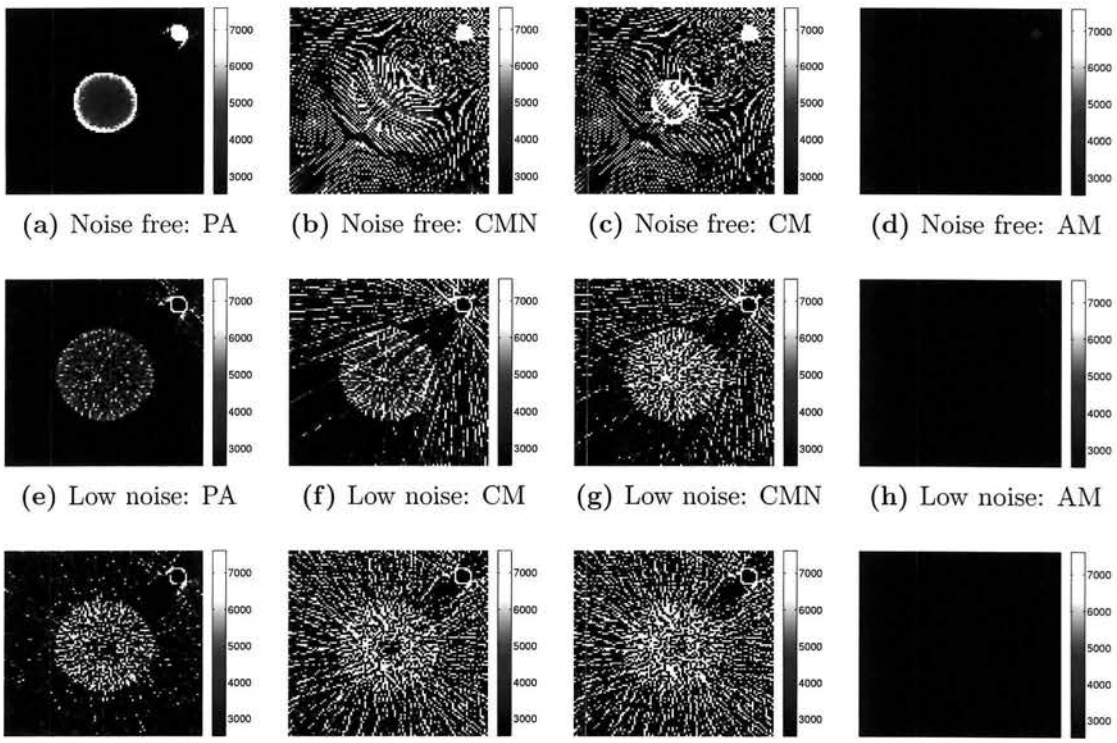


(a) photoelectric



(b) Compton

Figure 3·20: Mean values of the photoelectric coefficient (top) and the *Compton* coefficient (bottom) inside the water region for the different noise levels and the 'clean' phantom. The pink dashed line indicates the true value. The errorbars represent plus and minus one standard deviation. Initialization was done with the FBP method.

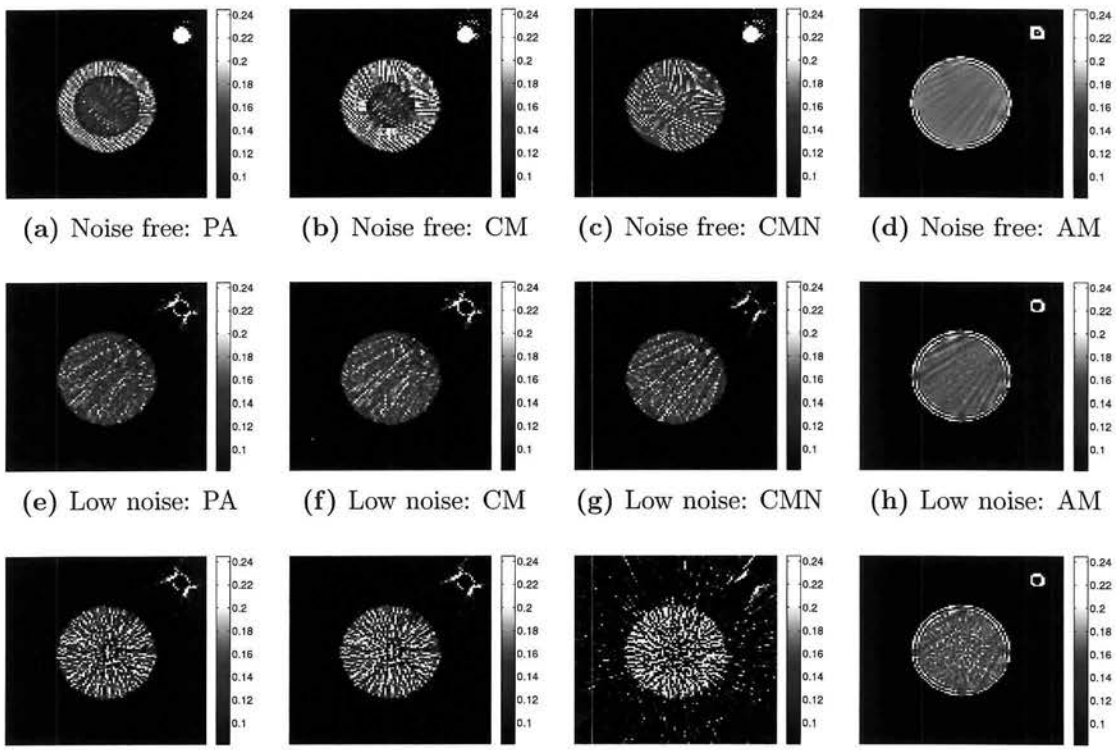


(a) Noise free: PA (b) Noise free: CMN (c) Noise free: CM (d) Noise free: AM

(e) Low noise: PA (f) Low noise: CM (g) Low noise: CMN (h) Low noise: AM

(i) High noise: PA (j) High noise: CM (k) High noise: CMN (l) High noise: AM

Figure 3·21: Reconstruction of photoelectric coefficient image using the different methods. Phantom with metal. Top row: noise free; middle row: Low noise; Bottom row: high noise. Initialized with FBP.

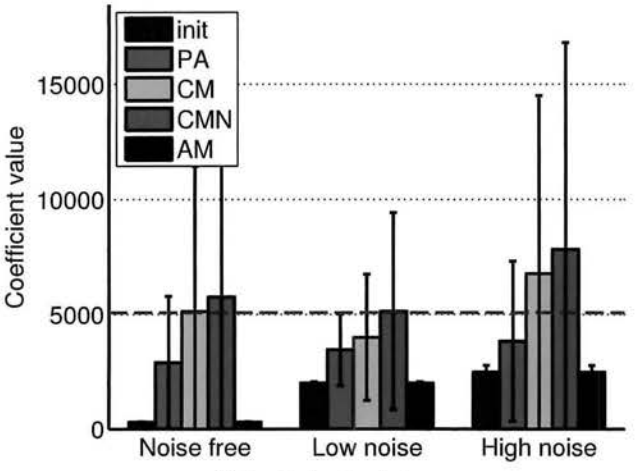


(a) Noise free: PA (b) Noise free: CM (c) Noise free: CMN (d) Noise free: AM

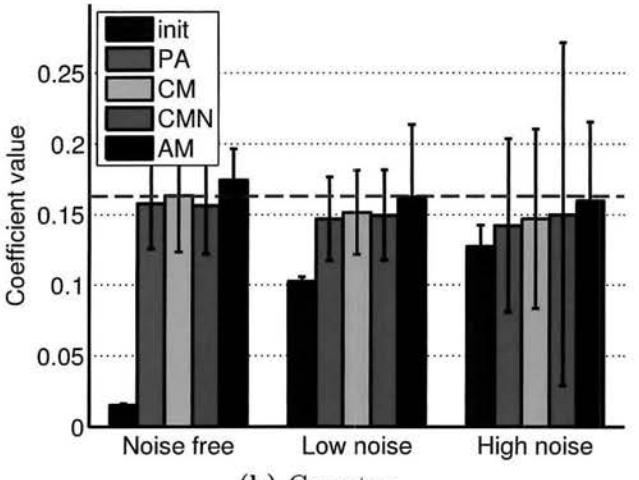
(e) Low noise: PA (f) Low noise: CM (g) Low noise: CMN (h) Low noise: AM

(i) High noise: PA (j) High noise: CM (k) High noise: CMN (l) High noise: AM

Figure 3·22: Reconstruction of Compton coefficient image using the different methods. Phantom with metal. Top row: noise free; middle row: Low noise; Bottom row: high noise. Initialized with FBP.

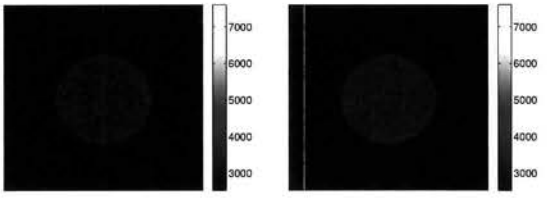


(a) photoelectric



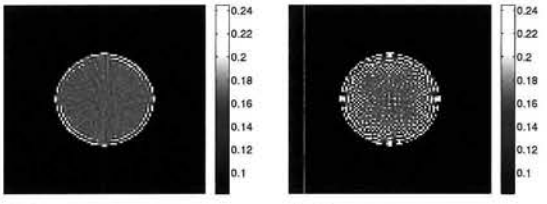
(b) Compton

Figure 3·23: Mean values of the photoelectric coefficient (top) and the Compton coefficient (bottom) inside the water region for the different noise levels and the 'cluttered' phantom. The pink dashed line indicates the true value. The errorbars represent plus and minus one standard deviation. Initialization was done with the FBP method.



(a) 1000 iterations, photoelectric

(b) 10000 iterations, photoelectric



(c) 1000 iterations, Compton

(d) 10000 iterations, Compton

Figure 3·24: Effect of number of iterations on performance of AM algorithm. Low noise case, FBP initialization.

Experiments with real data

In this section we present results obtained with the Imatron scans database, described in Appendix B, using a few different methods for estimating the photoelectric and Compton coefficient images.

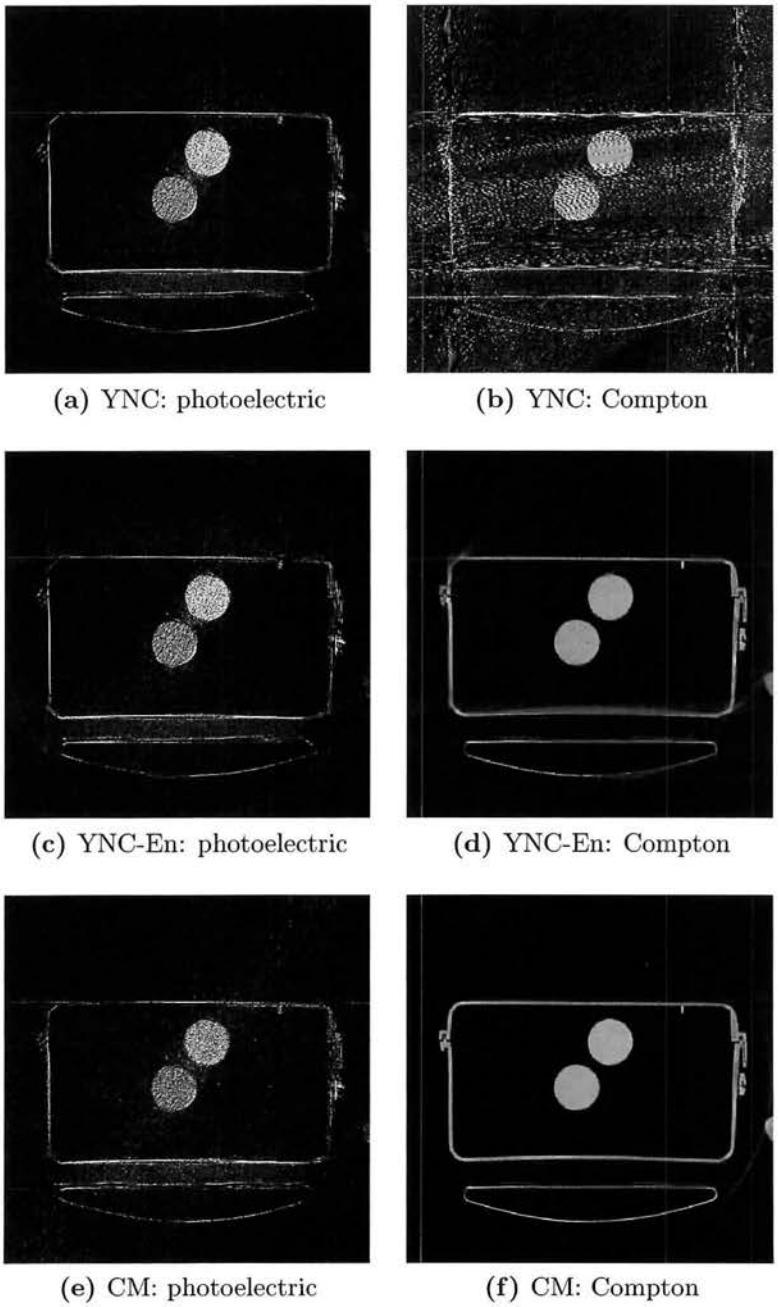
In [Ying et al., 2006], the constrained least-squares method described in Section 3.2.2 was proposed, along with other practical data correction steps. In our experiments we implemented the following steps from the paper: (i) solution of the constrained optimization problem as described in Section 3.2.2 and (ii) destreaking. We did not implement the scatter correction step, since the Imatron data was already scatter corrected and the parameters used for scatter correction were not specified in the paper. We will call this method YNC. It is similar to the CMN method described in Section 3.5.2, but has the additional destreaking step.

For the scans we have available, YNC results in many zeros in the photoelectric and Compton sinograms (approximately 25% of the photoelectric sinogram and 3% of the Compton sinogram is zero). The subsequent FBP reconstruction then results in very noisy streak filled images. This is probably related to the fact that the dual-energy data was acquired using spectra which had low kVp's and were not well separated, compared to the system used in [Ying et al., 2006]. In order to improve the results, we also consider a method which starts with YNC and adds a step of sinogram inpainting. The zero values in both the photoelectric and Compton sinograms were replaced by interpolated values from neighboring pixels. We call this method YNC-Enhanced, or in short YNC-En.

We also implemented the CM method described in Section 3.5.2 using Matlab's 'lsqnonlin' function. In all the methods we used FBP code provided by Dr. Patrick La Riviere from Univeristy of Chicago, which is based on the Imatron inversion software, to invert the photoelectric and Compton sinograms and obtain the photoelectric and

Compton coefficient images [Crawford et al., 2013].

We tested the methods YNC, YNC-En and CM on 'clean' and 'cluttered' data. Figure 3·25 shows the estimated photoelectric and Compton images for a 'clean' slice containing a bottle of water and a bottle of doped water. For this slice all the methods provide reasonable results, with the exception of the YNC Compton image which has many streaks that are not apparent in the YNC-En and CM Compton images. Figure 3·26 shows the results for a 'cluttered' slice containing metal objects. For this slice all the photoelectric images suffer from severe streaks. The YNC Compton image is very noisy, relative to the YNC-En and CM Compton images. The YNC-En and CM Compton images have many metal artifacts (e.g., the dark strip at the bottom of the teflon cube). These results indicate that for high-cluttered scenes a better method is needed, which reduces noise and metal artifacts. Such a method is proposed and discussed in Section 6.5.

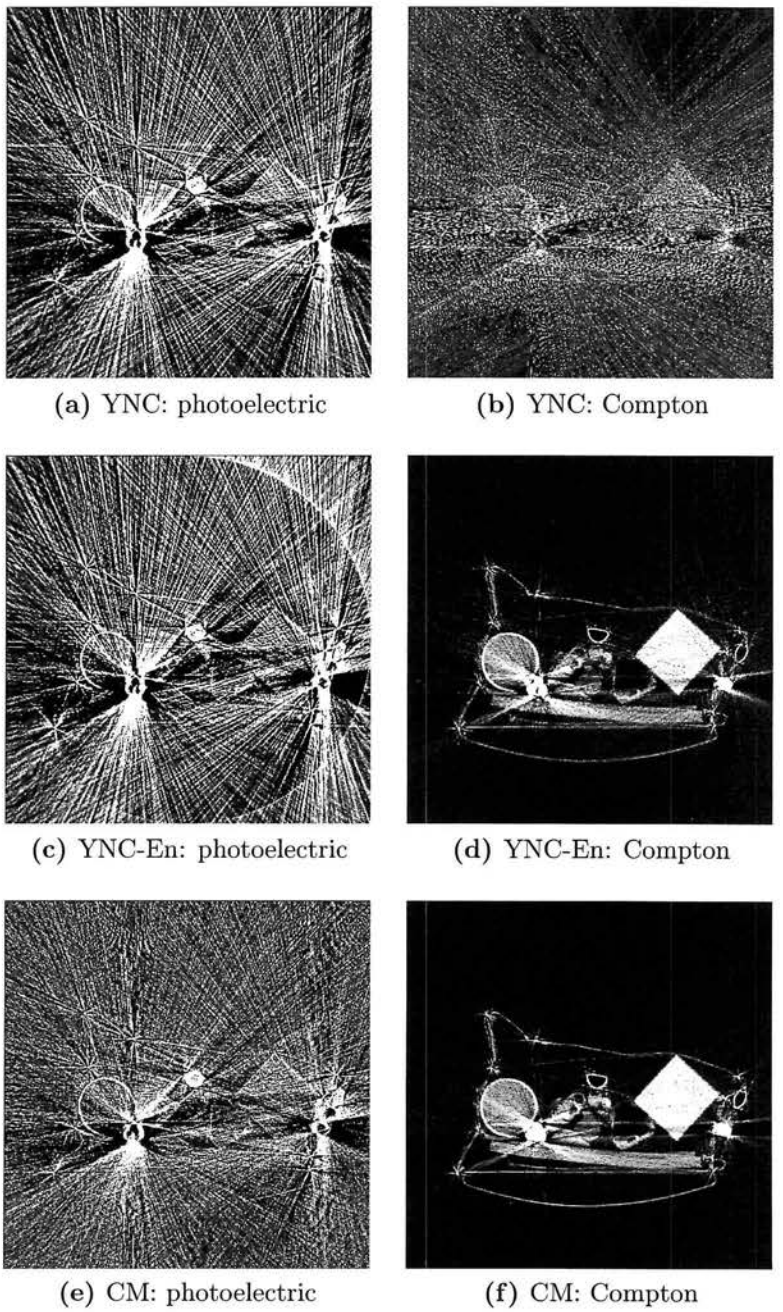


(a) YNC: photoelectric **(b)** YNC: Compton

(c) YNC-En: photoelectric **(d)** YNC-En: Compton

(e) CM: photoelectric **(f)** CM: Compton

Figure 3·25: Photoelectric coefficient (left) and Compton coefficient (right) given by YNC (top), YNC-En (middle) and CM (bottom) for a 'clean' slice. The objects in this slice are a bottle of water and a bottle of doped water. Photoelectric image is in units of keV^3 and gray scale range [1000, 10000]. Compton image is in units of cm^{-1} and gray scale range [0, 0.3].



(a) YNC: photoelectric

(b) YNC: Compton

(c) YNC-En: photoelectric

(d) YNC-En: Compton

(e) CM: photoelectric

(f) CM: Compton

Figure 3·26: Photoelectric coefficient (left) and Compton coefficient (right) given by YNC (top), YNC-En (middle) and CM (bottom) for a 'cluttered' slice. The objects in this slice include a teflon cube, a bottle of water and a stack of rubber sheets. Photoelectric image is in units of keV^3 and gray scale range [1000, 10000]. Compton image is in units of cm^{-1} and gray scale range [0, 0.3].

3.5.3 Effect of calibration phantom design and materials on EDEC

Below are experimental results obtained using the EDEC method described in Section 3.2.3 with simulated dual-energy data. Our goal is to understand the effect of the choice of basis materials and calibration phantom design on the performance of the method. This will also help in the design of experiments with real data.

In these experiments we simulate the measurements using Equation 3.6. The spectral weighting function $W_1(E)$ (80 kVp) and $W_2(E)$ (140 kVp) are shown in Figure 3·27. The total sum for 80 kVp is 2.26×10^13 and for 140 kVp is 1×10^14. The phantoms are 100×100 pixels (10000×1 stacked). The forward projection operator R was generated using Matlab's 'radon' function with rays at angles $\theta = 0, 1, ..., 179°$, and 145 distances r. The matrix F contains the LACs of the two basis materials.

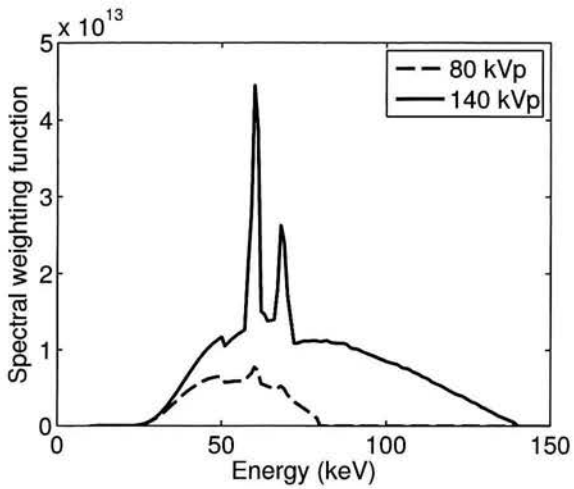


Figure 3·27: Spectral weighting functions used in simulation of dual-energy measurements in EDEC experiments

Implementing the calibration steps

First we wanted to understand the EDEC calibration steps described in Section 3.2.3 and validate our implementation. As in [Stenner et al., 2007], we used a Yin-Yang phantom design and water and aluminum as basis materials. The measurements

were simulated using the noise-free measurement model (the measurement values were given by Equation 3.6).

We set $S = T = 4$ in (3.23), as in the paper. We construct the template and weight images according to thresholding of the reconstructed attenuation image $\bar{\mu}_2(\vec{x})$. To perform the thresholding, first we calculate a histogram of the image values. Since the calibration phantom only contains those two materials and background the values in the histogram concentrate around three peaks. According to the location of the peaks we obtain the ranges of values corresponding to material 1 (water), material 2 (aluminum) and background. Template image 1, $t_1(\vec{x})$, is set to 1 where the values of $\bar{\mu}_2(\vec{x})$ are in the range of material 1 and zero otherwise. Template image 2, $t_2(\vec{x})$, is set to 1 where the values are in the range of material 2 and zero otherwise. The weight image $w_1(\vec{x})$ is set to 1 where the values are in the range of material 1 or material 2 and also surrounding the border of the object. $w_2(\vec{x})$ is the set to be the same as $w_1(\vec{x})$.

The reconstructed basis functions $f_n(\vec{x})$ which were used in the calibration process are shown in Figure 3·28. Figure 3·29 shows a histogram of the values of $\bar{\mu}_2(\vec{x})$ which guided the generation of the template and weight images $t_k(\vec{x})$ and $w_k(\vec{x})$ which appear in Figure 3·30. The chosen material thresholds are displayed as well.

A summary of the calibration steps using the Yin-Yang phantom is shown in Figure 3·30. The top row shows the reconstructed effective attenuation images $\bar{\mu}_1(\vec{x})$ and $\bar{\mu}_2(\vec{x})$ obtained by applying FBP to $\tilde{I}_1$ and $\tilde{I}_2$. The lighter gray corresponds to the aluminum region and the darker gray corresponds to the water region. The second row shows the weight image $w_1(\vec{x})$, template image $t_1(\vec{x})$, and the final decomposed image $a_1(\vec{x})$ corresponding to water. Similarly, the third row shows $w_2(\vec{x})$, $t_2(\vec{x})$ and $a_2(\vec{x})$ corresponding to aluminum. The decomposed images $a_1(\vec{x})$ and $a_2(\vec{x})$ were obtained by treating the calibration phantom as a test phantom and passing

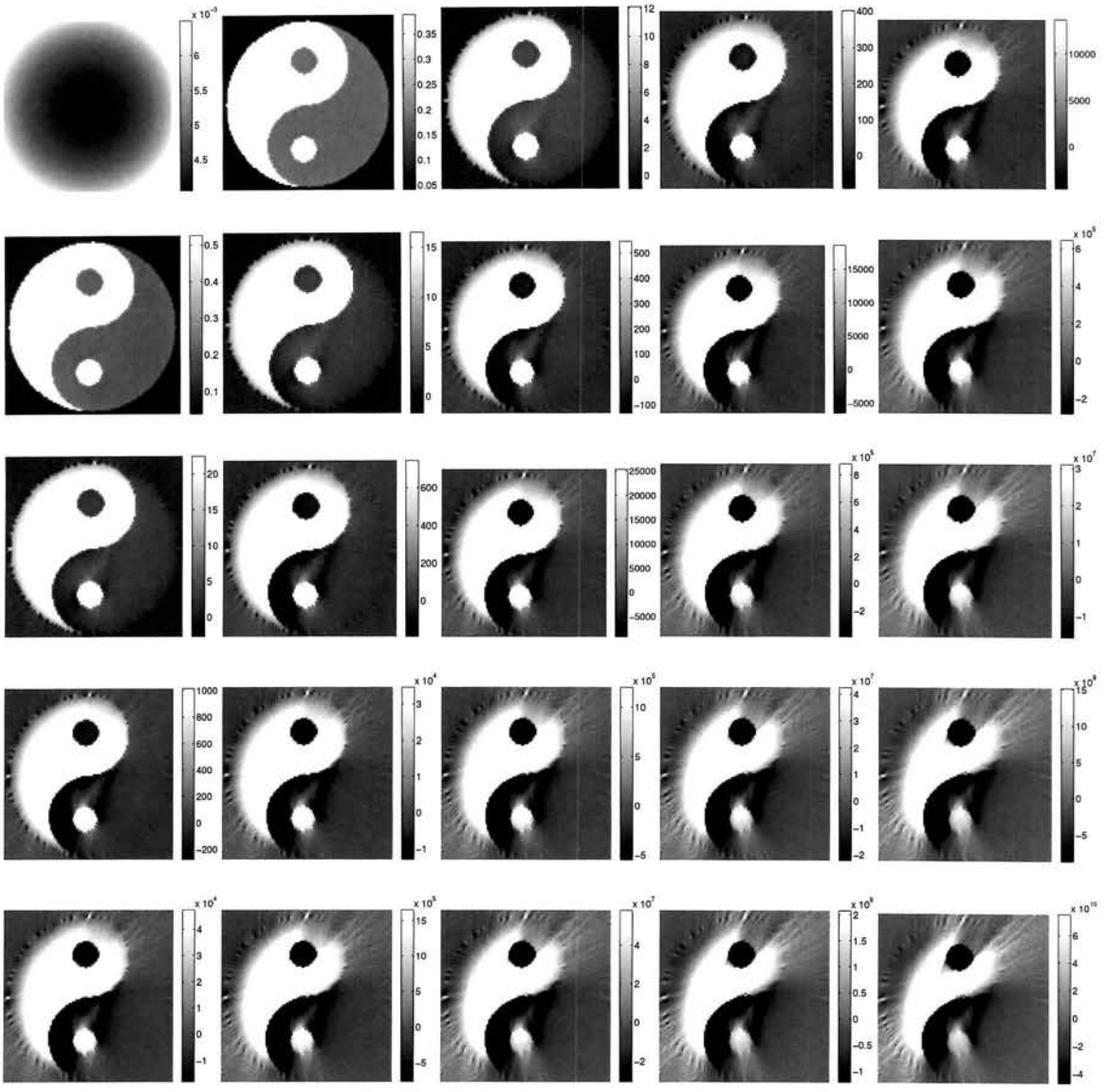


Figure 3·28: Basis images $f_n(\vec{x})$ obtained in the calibration process using the Yin-Yang calibration phantom. n increases from left to right with $n = 0$ at the top left and $n = 24$ at the bottom right.

the measurements through the estimated functions (3.22) to get the material-specific sinograms and then using standard FBP reconstruction to obtain the decomposed images. It can be seen that the template images $t_1(\vec{x})$ and $t_2(\vec{x})$ capture the material regions correctly and the decomposition into coefficient images $a_1(\vec{x})$ and $a_2(\vec{x})$ is successful. Figure 3·31 shows the results of using the estimated functions obtained

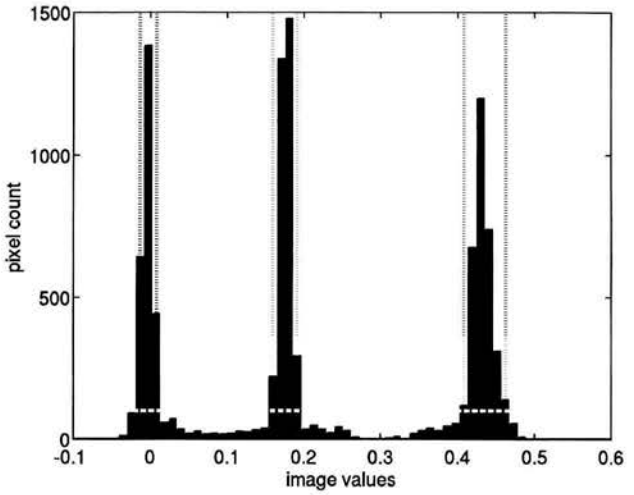
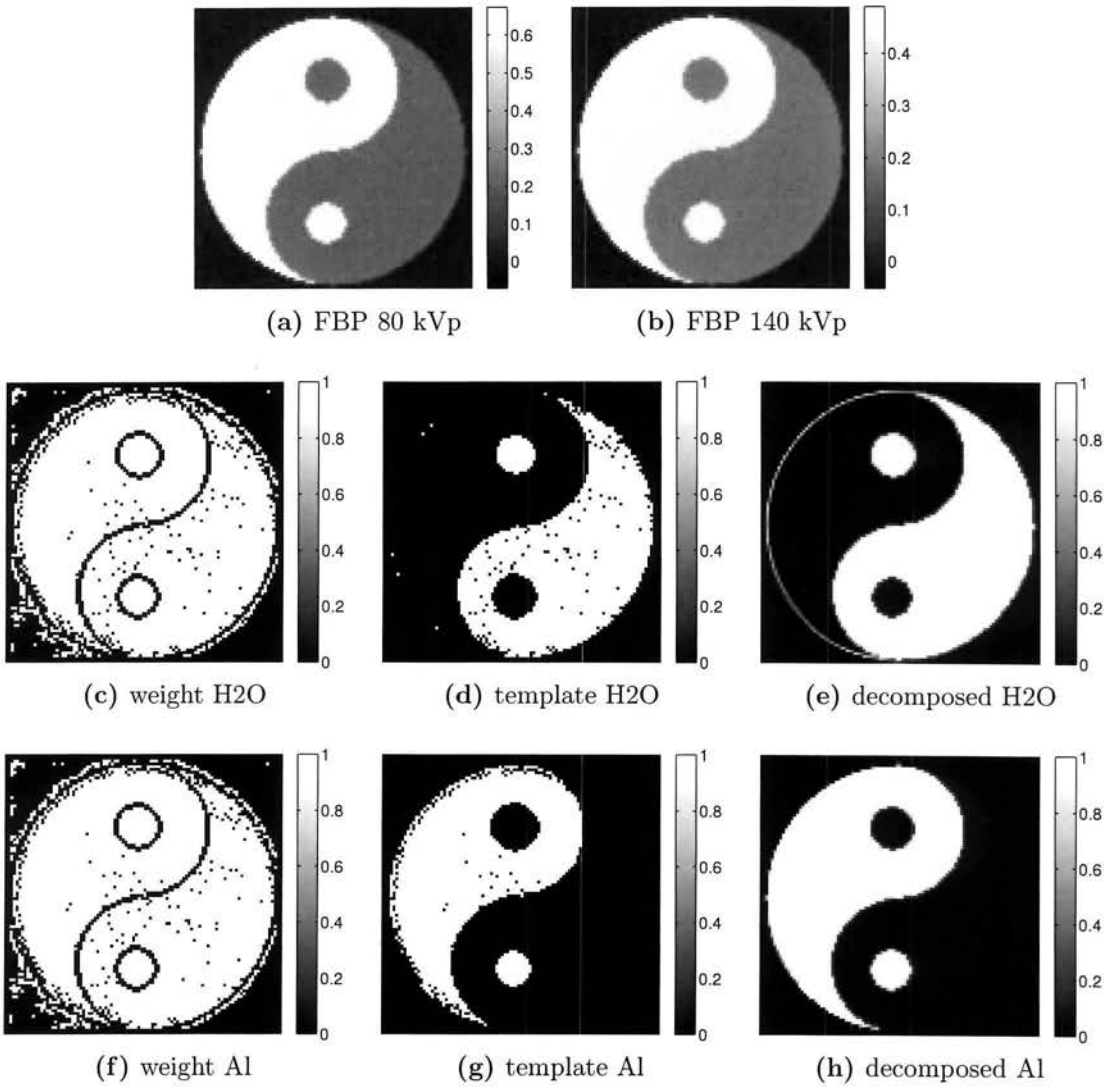


Figure 3·29: Histogram of values in reconstructed effective attenuation image $\bar{\mu}_2(\vec{x})$ of the Yin-Yang phantom used for constructing the template and weight images. The x-axis units are cm^{-1}. The horizontal yellow line shows the threshold we chose. By looking at the counts above the threshold, three distinct value ranges are given. The first range of values is between the red vertical lines. These values are close to zero and therefore correspond to the background. The second range of values is indicated by the green lines. It is close to 0.2 and corresponds to water. The third range, corresponding to aluminum, is indicated by the purple lines.

in the calibration phase to decompose a test phantom into water and aluminum coefficient images. The test phantom design is based on the standardized computed tomography dose index (CTDI) phantom and is composed of an ellipse of water with four small circles of aluminum and one small circle of graphite in the middle. The resulting water and aluminum regions in the decomposed images are correct.

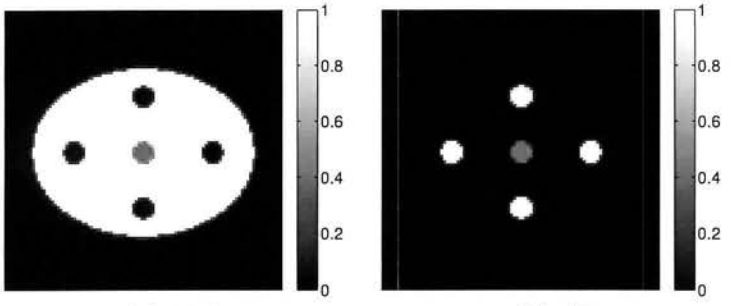


(a) FBP 80 kVp (b) FBP 140 kVp

(c) weight H2O (d) template H2O (e) decomposed H2O

(f) weight Al (g) template Al (h) decomposed Al

Figure 3·30: Summary of the EDEC calibration steps using the Yin-Yang phantom. Top: reconstructed effective attenuation images $\bar{\mu}_1(\vec{x})$ and $\bar{\mu}_2(\vec{x})$ obtained by applying FBP to $\tilde{I}_1$ and $\tilde{I}_2$. The lighter gray corresponds to the aluminum region and the darker gray corresponds to the water region. Middle: weight image $w_1(\vec{x})$, template image $t_1(\vec{x})$, and the final decomposed image $a_1(\vec{x})$ corresponding to water. Bottom: $w_2(\vec{x})$, $t_2(\vec{x})$ and $a_2(\vec{x})$ corresponding to aluminum.

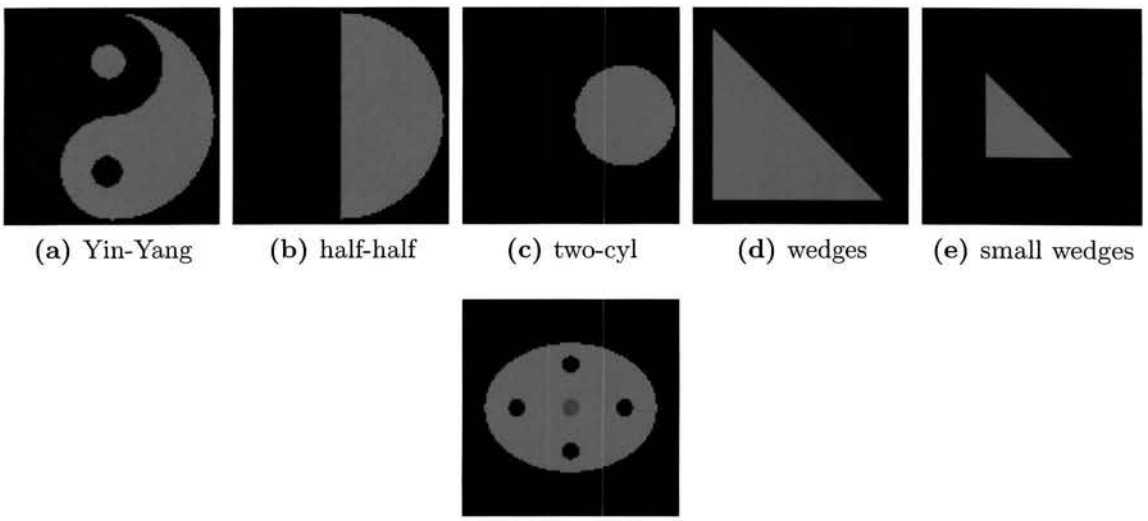


(a) H2O (b) Al

Figure 3·31: Decomposed test phantom using Yin-Yang calibration. Left: water image. Right: aluminum image. The test phantom design is based on the standardized computed tomography dose index (CTDI) phantom and is composed of an ellipse of water with four small circles of aluminum and one small circle of graphite in the middle.

Choice of calibration phantom design

In order to study the effect of calibration phantom design on the performance of EDEC we tested the method using a few different designs: Yin-Yang, half-half, two-cylinders, wedges, and small wedges. We also created a test phantom based on the standardized CTDI phantom. The phantoms are shown in Figure 3·32. We fixed the choice of basis materials as water and aluminum, which are the materials used in [Stenner et al., 2007].



(a) Yin-Yang (b) half-half (c) two-cyl (d) wedges (e) small wedges

(f) CTDI

Figure 3·32: Calibration phantom designs (top) and test phantom design (bottom). Background (air) is in red, water is in green, aluminum is in blue and graphite is in purple (graphite is only in Figure (f)).

The simulated dual-energy measurements were based on the Poisson measurement model (setting the values given by Equation 3.6 as the mean of a Poisson random variable). The spectral weighting functions in Figure 3·27 were used, which provided very high SNR. Figure 3·33 shows the reconstructed effective attenuation images of the calibration phantom, the estimated material coefficient images of the calibration phantom and the estimated material coefficient images of the test phantom, for the Yin-Yang calibration phantom. As expected, the aluminum areas have values close

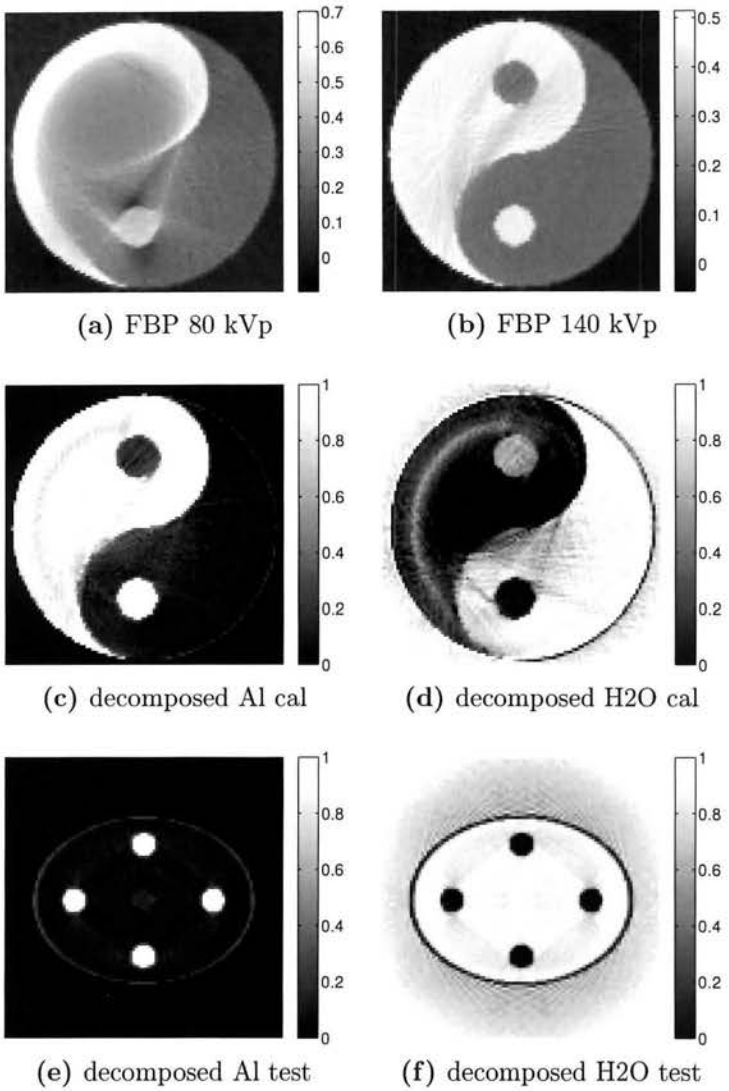
to one and the water areas have values close to zero in the aluminum image. The opposite is true for the water image. There are some issues, however, with the values in the background area, especially in the water images, and also with the boundaries. In addition, some streaks and artifacts are noticeable in all the images. For example, there are streaks between each pair of aluminum rods in the test phantom water image.

Figure 3·34 shows the results for the half-half calibration phantom. It shows similar performance to the Yin-Yang phantom.

Figure 3·35 shows the results for the two-cylinders calibration phantom. There are slightly less artifacts and less issues with the background and boundaries compared to the Yin-Yang and half-half phantoms.

Figures 3·36 and 3·37 show the results for the wedges and small wedges calibration phantom. It can be seen that there are less artifacts in the results with the small wedges. Generally, the small wedges seem to give the cleanest decomposition results compared to all the other calibration phantom designs. This may be because smaller objects attenuate the transmitted X-rays less, resulting in higher reliability of the measurements and better reconstructions.

Using the estimated material coefficient images and based on Equation (3.3) we generated an estimate of the LAC at 70 keV for the test phantom. The results are shown in Figure 3·38. It can be seen that in all cases the EDEC method produces some artifacts in the LAC at 70 keV image. The background values are inaccurate for the Yin-Yang and half-half calibrations. The graphite values are inaccurate for the two-cylinder calibration. The best results are achieved with the wedges and small wedges calibration phantoms.

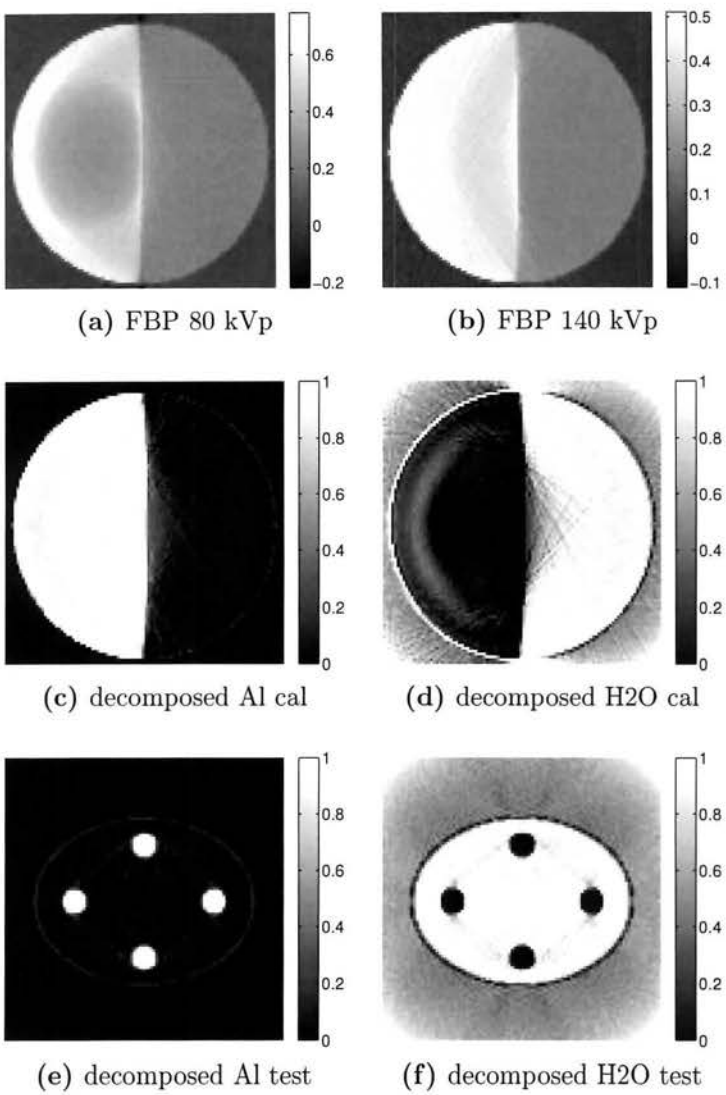


(a) FBP 80 kVp **(b)** FBP 140 kVp

(c) decomposed Al cal **(d)** decomposed H2O cal

(e) decomposed Al test **(f)** decomposed H2O test

Figure 3·33: EDEC with Yin-Yang calibration phantom. Top: reconstructed effective attenuation images of the calibration phantom. Middle: estimated material coefficient images of the calibration phantom. Bottom: estimated material coefficient images of the test phantom

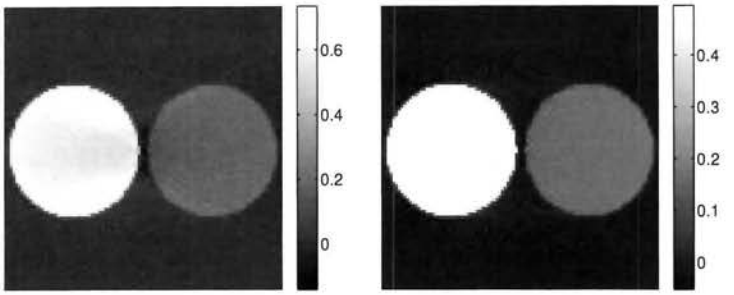


(a) FBP 80 kVp (b) FBP 140 kVp

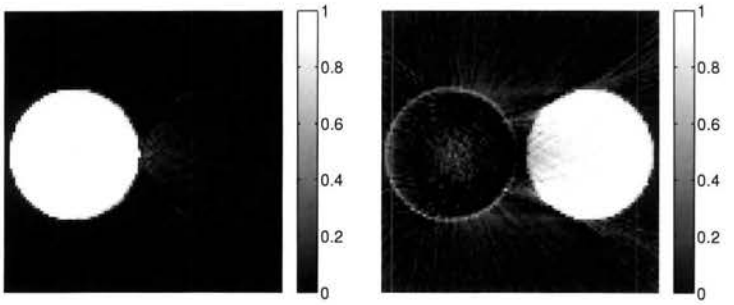
(c) decomposed Al cal (d) decomposed H2O cal

(e) decomposed Al test (f) decomposed H2O test

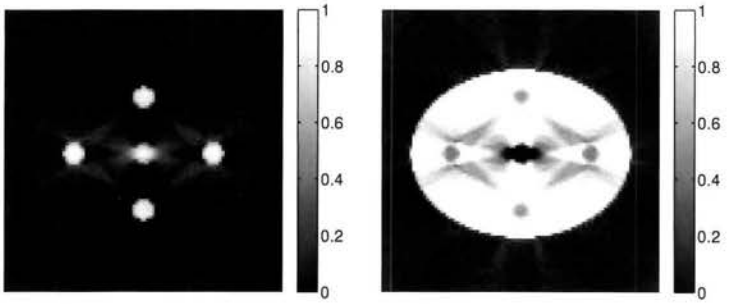
Figure 3·34: EDEC with half-half calibration phantom. Top: reconstructed effective attenuation images of the calibration phantom. Middle: estimated material coefficient images of the calibration phantom. Bottom: estimated material coefficient images of the test phantom



(a) FBP 80 kVp (b) FBP 140 kVp

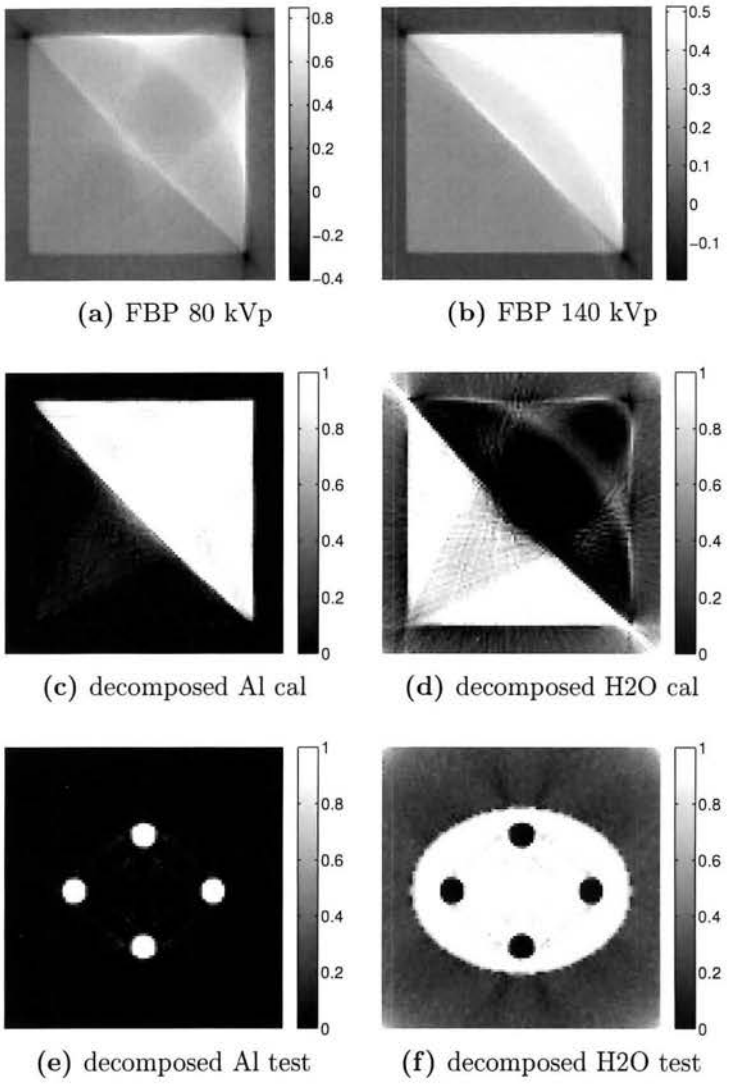


(c) decomposed Al cal (d) decomposed H2O cal



(e) decomposed Al test (f) decomposed H2O test

Figure 3·35: EDEC with two-cylinders calibration phantom. Top: reconstructed effective attenuation images of the calibration phantom. Middle: estimated material coefficient images of the calibration phantom. Bottom: estimated material coefficient images of the test phantom

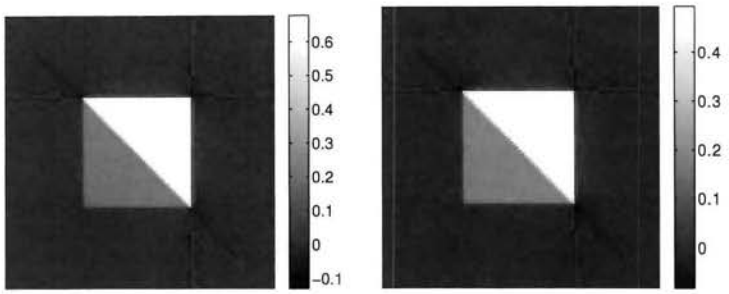


(a) FBP 80 kVp **(b)** FBP 140 kVp

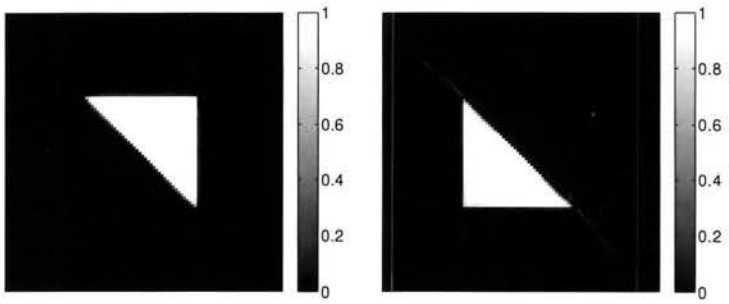
(c) decomposed Al cal **(d)** decomposed H2O cal

(e) decomposed Al test **(f)** decomposed H2O test

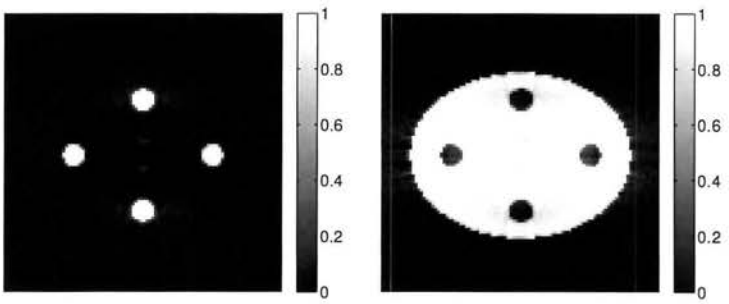
Figure 3·36: EDEC with wedges calibration phantom. Top: reconstructed effective attenuation images of the calibration phantom. Middle: estimated material coefficient images of the calibration phantom. Bottom: estimated material coefficient images of the test phantom



(a) FBP 80 kVp (b) FBP 140 kVp

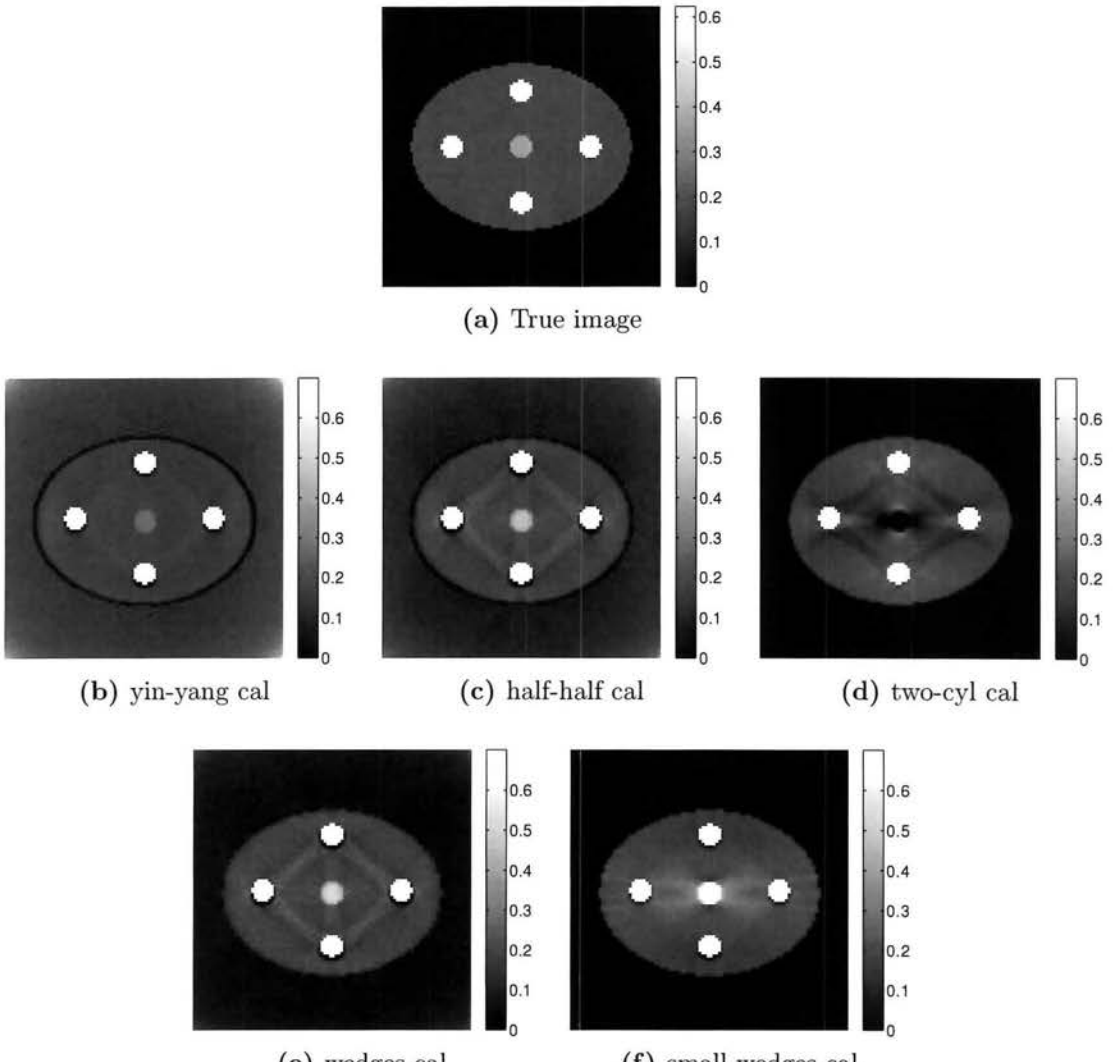


(c) decomposed Al cal (d) decomposed H2O cal



(e) decomposed Al test (f) decomposed H2O test

Figure 3·37: EDEC with small wedges calibration phantom. Top: reconstructed effective attenuation images of the calibration phantom. Middle: estimated material coefficient images of the calibration phantom. Bottom: estimated material coefficient images of the test phantom



(a) True image

(b) yin-yang cal

(c) half-half cal

(d) two-cyl cal

(e) wedges cal

(f) small wedges cal

Figure 3·38: Images of the test phantom LAC at 70 keV. Top: true image. Middle and bottom: estimates obtained with the different calibration phantoms.

Choice of calibration phantom materials

Here we studied the effect of the choice of basis materials, which are also the materials composing the calibration phantom, on the performance of EDEC. As possible basis materials we considered materials which may possibly be used in practice. We compiled the following list of 11 materials out of which a pair of calibration materials may be selected: PVC, graphite, acrylic, Teflon, polypropylene, ABS, polystyrene, aluminum, copper, iron, and polycarbonate.

We also used the list of possible calibration materials to create two material test groups. The first group consists of the 8 non-metals, which are all the materials besides aluminum, copper, and iron. The second group includes the metals and consists of all 11 materials.

Using the test groups, we ranked the pairs of calibration materials according to the following two criteria:

1. LAC representation

   The LACs of the 11 materials in the list are sampled at energy levels 10 to 150 keV in steps of 1 keV. For each pair of calibration materials we set their LACs as the basis functions $f_k(E)$ in (3.1). Then for each test material under consideration we find the basis coefficients a_k by least-squares. We calculate the percent of absolute error between the resulting LAC estimate and the true LAC of the test material. We take the average of the error over the materials and over the energies. After doing this for each pair of calibration materials we sort the pairs in ascending order of the average error. Note that this method does not take into account the MECT observation model. It is assumed that the entire LAC curve is available.

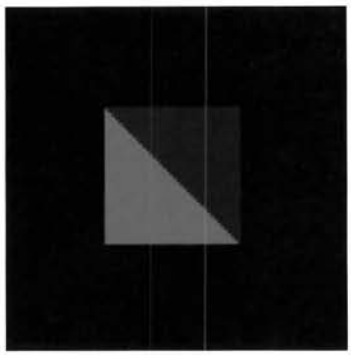
2. EDEC performance

   We directly evaluate the performance of EDEC with each pair of basis materi-

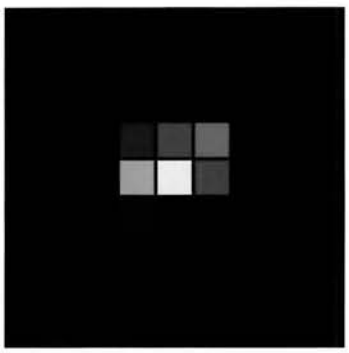
als. We fix the calibration phantom design to the small wedges phantom shown in Figure 3·39a. We simulate dual-energy measurements using the Poisson measurement model, as in Section 3.5.3. For each pair of calibration materials out of the list of 11 materials given above we carry out the calibration procedure to obtain the mapping functions from measured data to material sinograms. Then we test the decomposition on a test phantom which is composed of the test materials. The test phantom for the group with no metals is shown in Figure 3·39b and the test phantom for the group with metals is shown in Figure 3·39c. After decomposing the test phantom into the basis materials we estimate the LAC at every pixel using Equation 3.2. For each test material we take the average of the estimated LAC over the pixels in which it is located and calculate the percent error with the true LAC. Then we take the average of the error over the materials and over the energies. After doing this for each pair of calibration materials we sort the pairs in ascending order of the average error.

The ranking of the calibration material pairs according to the two criteria for the test material group without metals and the test group with metals is shown in Table 3.3. The table shows the 10 highest ranking pairs. It can be seen that the ranking according to both criteria for each type of test phantom is slightly different, but generally the high ranking pairs appear in both lists. Most of the pairs are combinations of a low attenuating material, such as graphite, and a high attenuating material, such as aluminum. When the test phantom does not contain metals, aluminum is chosen many times as one of the calibration materials. When the test phantom contains metals, copper is chosen many times and the highest ranking pairs include iron. This may be because copper and iron are much more attenuating than aluminum and they are needed in order to represent a set of materials which includes metals.

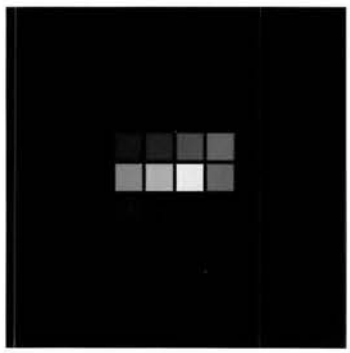
Estimates of the LAC at 70 keV derived from the EDEC results are shown in Fig-



(a) Calibration phantom



(b) Test phantom no metals



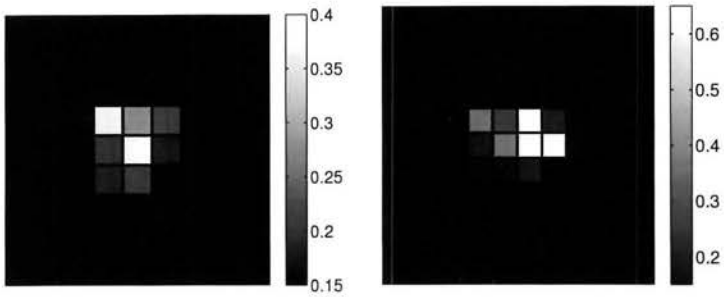
(c) Test phantom with metals

Figure 3·39: Top: general calibration phantom design, material 1 in blue, material 2 in green and background in red. Bottom left: test phantom without metals. The color of each small square represents a different material - from left to right, top to bottom - PVC, graphite, acrylic, polystyrene, Teflon, polypropylene, ABS, polycarbonate. Bottom right: test phantom with metals - PVC, graphite, aluminum, acrylic, polystyrene, Teflon, copper, iron, polypropylene, ABS, polycarbonate.

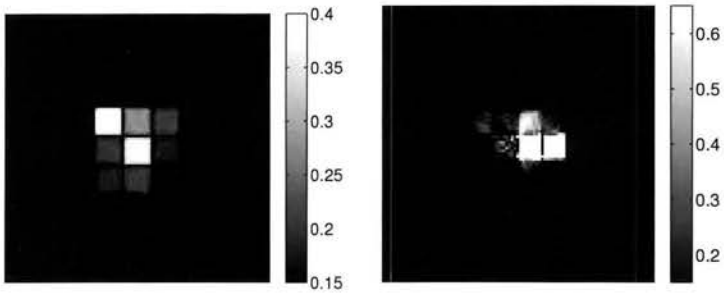
ure 3·40. The calibration materials were chosen as the highest ranking pair according to the EDEC performance criterion: graphite and aluminum for the test phantom with no metal and teflon and iron for the test phantom with metals. It can be seen that for the phantom with no metals the estimated image looks close to the true image. For the phantom with metals, the estimate is better for the metals than the non-metals. In order to obtain good estimates for materials near metal a different criterion for choosing the basis functions may be required.

Rank	no metals in test		with metals in test	
	LAC representation	EDEC performance	LAC representation	EDEC performance
1	graphite-PVC	graphite-aluminum	acrylic-iron	Teflon-iron
2	polycarbonate-PVC	ABS-aluminum	Teflon-iron	graphite-copper
3	ABS-PVC	polypropylene-aluminum	polycarbonate-iron	polypropylene-copper
4	polystyrene-PVC	polystyrene-aluminum	acrylic-copper	ABS-copper
5	acrylic-PVC	polycarbonate-aluminum	graphite-iron	polystyrene-copper
6	polypropylene-PVC	polypropylene-PVC	Teflon-PVC	Teflon-aluminum
7	polycarbonate-aluminum	polystyrene-PVC	polycarbonate-copper	acrylic-copper
8	graphite-aluminum	acrylic-aluminum	ABS-iron	polycarbonate-copper
9	ABS-aluminum	acrylic-PVC	polystyrene-iron	Teflon-copper
10	acrylic-aluminum	ABS-PVC	acrylic-PVC	Teflon-PVC

Table 3.3: Combinations of basis materials giving the lowest percent errors according to LAC representation and according to EDEC performance. Materials on top give lowest error and the error increases as you go down the table.



(a) True, no metals (b) True, with metals



(c) Estimated, no metals (d) Estimated, with metals

Figure 3·40: True LAC at 70 keV (top) and estimates of LAC at 70 keV (bottom). Test phantom with no metals on left and test phantoms with metals on right. The estimates were obtained using the best pair of calibration materials according to the EDEC criterion: graphite and aluminum for test phantom with no metals and Teflon and iron for test phantom with metals. The materials in the test phantom with no metals are - from left to right, top to bottom - PVC, graphite, acrylic, polystyrene, Teflon, polypropylene, ABS, polycarbonate. The materials in the test phantom with metals are - PVC, graphite, aluminum, acrylic, polystyrene, Teflon, copper, iron, polypropylene, ABS, polycarbonate.

Chapter 4

Estimating the dimensionality of the LACs

Material energy dependence is reflected in the linear attenuation coefficient (LAC) versus energy curve of a material (see examples in Figure 4·1). The fundamental separability of materials in X-ray transmission sensing is derived from the LAC curves of the materials. The information available in the LACs impacts the limits of X-ray based detection.

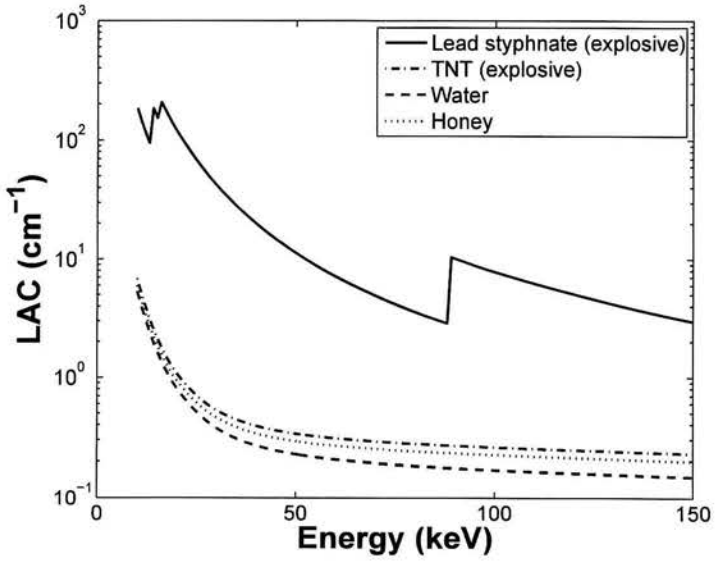


Figure 4·1: Examples of LAC curves of a few materials

MECT measurements are used to estimate various material-specific parameters which are often the coefficients of a basis expansion of the LAC. Seminal work in the medical domain argued that the LAC space of low atomic number, biomedical materi-

als (i.e., tissues) can be well approximated by a two-dimensional basis consisting of the photoelectric and Compton scatter components [Alvarez and Macovski, 1976], whose coefficients can be found using only two CT scan energy spectra. Subsequent work retained this focus on a two-dimensional LAC representation, but used the LACs for two materials in the scene (e.g., soft tissue and bone) [Sukovic and Clinthorne, 2000]. While some work has focused on extensions to include, e.g., contrast agents, the dimensionality considered has remained very low. For explosives detection, however, the set of materials to be considered is much greater and more diverse. Therefore, considering higher-dimensional features is appropriate.

In this chapter we study the space of the LACs of materials in the security application. Specifically, we study the dimensionality of the space, which is related to the number of basis functions needed to represent the LACs, and to the number of material features needed for discrimination. The identification of material feature dimensionality can inform the design of next generation MECT systems and estimation methods for explosives detection.

For this study we created a database of LACs of different explosive and non-explosive compounds. The database is described in detail in Appendix A. For each material we have tabulated its chemical composition and density and generated samples of its LAC curve at energy levels 10-150.

4.1 Linear dimensionality estimation

As explained in Section 2.2.1, the LAC of a compound is assumed to be a linear combination of the mass attenuation coefficients of its composing elements (Equation 2.5). This implies that the linear dimensionality of all the LACs is at most the number of elements composing all the compounds (44 in the case of our compounds database).

An interesting and useful question is what is the minimum number of basis functions needed to represent the LACs, or equivalently, what is the linear dimensionality of the space of LACs for the materials of interest. If we densely sample the LAC curves at N_e fixed equidistant energy levels then each LAC becomes a N_e-dimensional vector, denoted by $\boldsymbol{\mu}$. We would like to estimate the intrinsic dimensionality of the space spanned by these vectors. One tool for dimensionality estimation for a set of vectors is the singular value decomposition (SVD). In general, the number of non-zero singular values indicates the linear dimensionality of the space of the vectors. SVD is closely related to principal component analysis (PCA) [Madsen et al., 2004].

A procedure for evaluating the dimensionality of the LACs of a set of biological materials based on SVD is described in [Alvarez, 2011]. It is demonstrated that for normal body materials the dimensionality is two and when iodine is included, the dimensionality is at least three.

To the best of our knowledge this type of analysis has not yet been applied to a more broad set of compounds, including explosives and materials which can be found in luggage. Extending the results to these materials can help in the development of MECT methods for the security application.

We apply Alvarez's procedure to the LACs in our compounds database (Table A.1). We consider three material classes: 'compounds', 'explosives' and 'biological'. The 'compounds' set consists of all the 320 materials in our compounds database. In the 'explosives' set we have 124 explosive materials (TNT, RDX, etc.). In the 'biological' set we have 12 materials found in the human body (bone, soft-tissue, etc.). The 'explosives and 'biological' sets are both subsets of the 'compounds' set.

In [Alvarez, 2011], Alvarez raises the question if the analysis should be done on the LACs themselves or if some operations should be performed on them first, such

as mean-subtraction or scaling. He decides to subtract the mean and divide by the standard deviation to standardize the LACs before applying SVD. He claims that not doing it may change the resulting principal values but won't affect the basic conclusions about the dimensionality for the set of biological materials which he considered.

In our work, we perform the analysis on the LACs themselves, as well as on the standardized LACs. We would like to see how standardizing affects the dimensionality estimate for our database.

Our procedure is as follows:

1. Sample the materials LACs at a fixed set of energies: 100 energies equally spaced from 20 to 150 keV.

2. If examining standardized LACs, for each sampled curve we subtract its mean and divide by its standard deviation.

3. Place the resulting curve samples in the columns of a matrix.

4. Compute the SVD of the matrix. Denote the singular values vector by $\mathbf{s}$, where it is assumed that $s_i \geq s_j$ for $i < j$. Denote the vector of elementwise squares of the singular values as vector $\mathbf{q}$.

5. Calculate the 'variation fraction' for $\mathbf{s}$ and $\mathbf{q}$, where variation fraction for any vector $\mathbf{x}$ is defined by:

$$v_r(\mathbf{x}) = \frac{\sum_{i=1}^{r} x_i}{\sum_{i=1}^{N} x_i} \tag{4.1}$$

and r is the number of components used. In the rest of this document the term variation fraction will refer to $v_r(\mathbf{q})$ unless noted otherwise, following Alvarez's notation.

6. Estimate the dimensionality by finding the number of components needed to satisfy each of the following criteria:

   (a) 'Kaiser': Number of singular values $\mathbf{s}$ which are greater than one [Kaiser, 1960]

   (b) 'Scree': Cattell's scree test [Cattell, 1966]. Plot the singular values $\mathbf{s}$ in descending order, look for the 'elbow' in the plot and keep the number of components above the elbow. Note that picking the 'elbow' can be subjective.

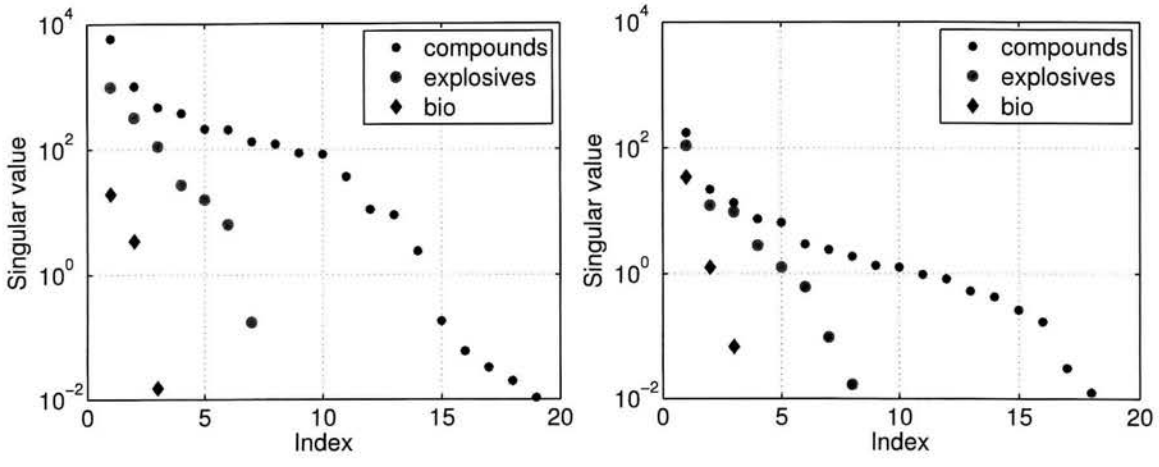
   (c) 'Var': Number of components r is chosen such that $v_r(\mathbf{s}) \geq 0.9$ [Wikipedia, 2012].

   (d) 'Var Alv': Number of components r is chosen such that $v_r(\mathbf{q}) \geq 0.9999$ [Alvarez, 2011].

The singular values $\mathbf{s}$ for the material LACs are shown in Figure 4·2. It can be seen that there is no clear "elbow" in the plots, and the number of significant components is difficult to estimate visually. It is noticeable that the decay rate of the principal values for 'compounds' and 'explosives' is much lower than for 'biological'.

Figure 4·3 shows the number of components r^* as a function of variation fraction threshold T such that $v_{r^*}(\mathbf{q}) \geq T$. It can be seen that a larger number of components is needed to keep the same variation fraction for the 'explosives' set than the 'biological' set, and a much larger number is needed for the 'compounds' set. This implies that the number of significant components is much larger for the 'compounds' set than the 'biological' and 'explosives' sets.

Figure 4·4 shows the dimensionality of the different sets according to the different criteria for the materials LACs. It can be observed that using the 'Var Alv' criterion for example, the dimensionality of the sets is estimated at 10 for 'compounds', 5



(a) No operation (b) Standardize

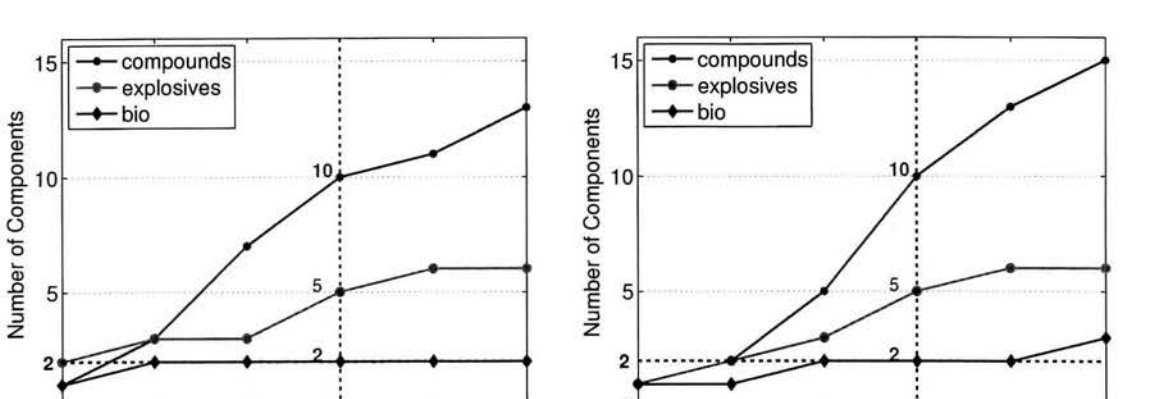
Figure 4·2: Singular values obtained for LACs of the different material classes. In each sub-plot different pre-processing was applied. The plots only show values greater than 10^{-2}.

for 'explosives' and 2 for 'biological'. Other than the 'biological' set, the different criteria provide different estimates. This demonstrates the challenge of estimating the dimensionality in a consistent manner. As in the previous figures, there is only a minor difference between the results for the standardized and non-standardized LACs.

Overall, the SVD-based analysis shows that the dimensionality of the space of LACs which include explosives and other benign materials is 2 to 5 times larger than the dimensionality in the case of solely biological materials.

4.1.1 Dimensionality of the exponentiated LACs

The polychromatic X-ray model (2.17), is a nonlinear function of the LAC. The measurements are inner products of the exponentiated LAC with the spectral weighting functions. We would like to know how the non-linearity affects the dimensionality of the LAC space. We compare the dimensionality of the LACs, $\boldsymbol{\mu}$, and the dimensionality of the exponentiated LACs, $e^{-\boldsymbol{\mu}}$.



(a) No operation (b) Standardize

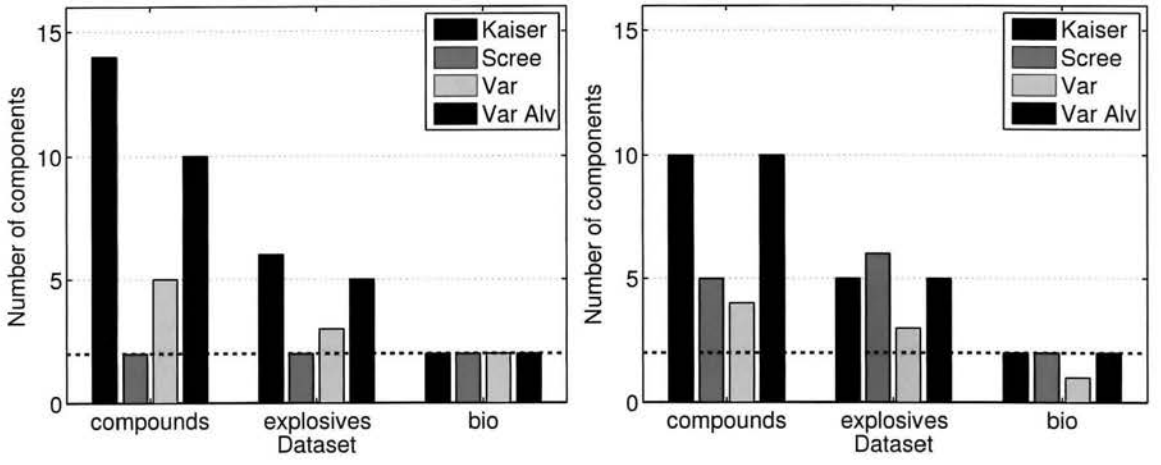
Figure 4·3: Number of components needed for variation fraction to be greater than a threshold T as a function of T. The horizontal red dotted line shows the 2 component level. The vertical purple line shows the threshold considered by Alvarez of 0.9999. The numbers next to it indicate the number of components needed for each of the material classes to retain this threshold.

We found the singular values for the exponentiated LACs of the 'compounds' set. We compare them with the singular values of the LACs of the same set. The results are shown in Figure 4·5. It can be seen that when the curves are standardized the singular values of the LACs and exponentiated LACs are similar. In the other case the significant singular values of the exponentiated LACs are smaller, which indicates lower dimensionality.

The results of this analysis indicate that the dimensionality of the exponentiated LAC curves is comparable to the dimensionality of the LAC curves, but possibly slightly smaller.

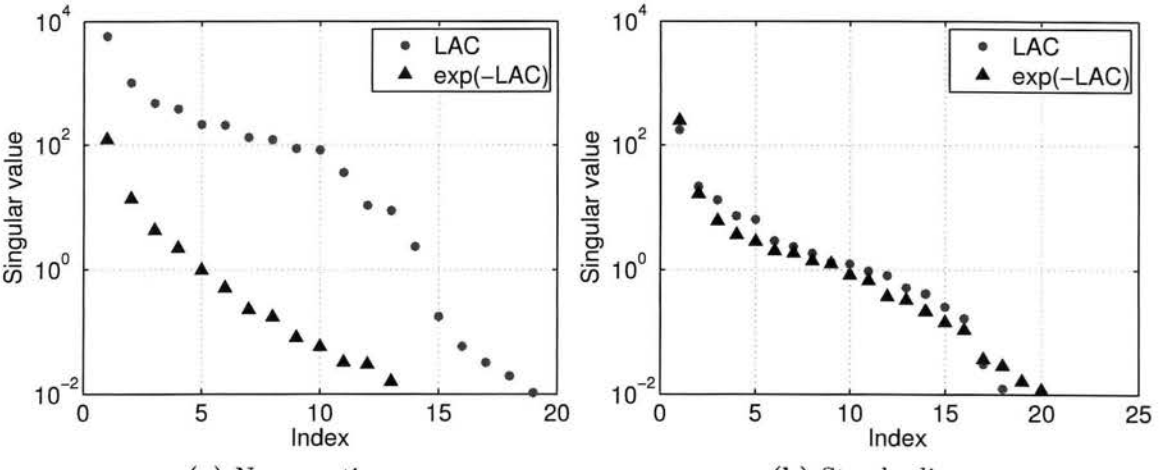
4.2 Nonlinear dimensionality estimation

In some cases high-dimensional data can be embedded on a low-dimensional nonlinear manifold. One technique which finds such low-dimensional representations is called



(a) No operation (b) Standardize

Figure 4·4: Number of components needed according to different criteria for the materials LACs. In each sub-plot different pre-processing was performed on the curves. The horizontal red dotted line shows the 2 component level.



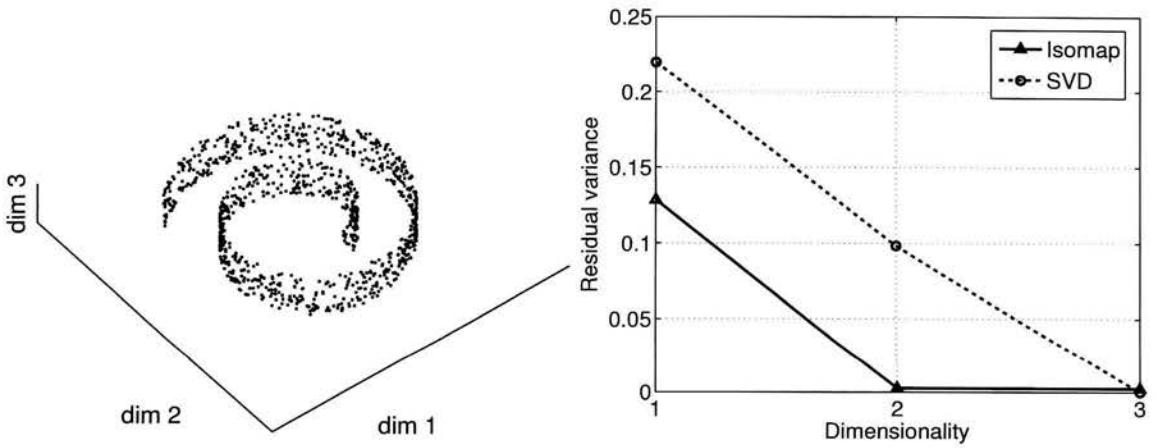
(a) No operation (b) Standardize

Figure 4·5: Singular values of the LACs and exponentiated LACs for 'compounds' set. The plots only show values greater than 10^{-2}.

Isomap [Tenenbaum et al., 2000]. Isomap preserves the intrinsic geometry of the data, as captured in the geodesic manifold distances between all pairs of data points.

Isomap can be used to estimate the dimensionality of a dataset. In [Tenenbaum

et al., 2000], the residual variance of the embedding is plotted against the embedding dimensionality. The intrinsic dimensionality of the data can be estimated by looking for the "elbow" at which this curve ceases to decrease significantly with added dimensions. Figure 4·6 shows an example of dimensionality estimation for the "Swiss roll" dataset. The data points are three-dimensional and they lie on a two-dimensional manifold. Following [Tenenbaum et al., 2000], Isomap is applied to the data to obtain a lower dimensional embedding and the residual variance is calculated. For comparison, a similar analysis based on SVD is applied as well. In the SVD scheme the data is arranged in the columns of a matrix and the SVD of the matrix is calculated. Then a lower dimensional representations of the data is achieved by projecting the data onto the first N left singular vectors corresponding to the N largest singular values, where $N = 1, 2, 3$. It can be seen that for this dataset only the geodesic distances reflect the true low-dimensional geometry of the manifold. Linear methods such as SVD effectively see just the Euclidean structure and fail to detect the intrinsic two-dimensional structure.



(a) Data (b) Residual variance

Figure 4·6: Intrinsic dimensionality of the "Swiss roll" dataset. The data is plotted on the left. The residual variance as a function of dimension is plotted on the right for Isomap and SVD.

We applied Isomap to the LACs in our compounds database to estimate their dimensionality. The residual variance as a function of dimensionality is shown in Figure 4·7. We used ϵ-Isomap [Tenenbaum et al., 2000], with $\epsilon = 4$. Note that the residual variance for Isomap is not guaranteed to decrease as the dimensionality increases. It can be seen that for Isomap the residual variance stops decreasing significantly at a dimensionality of 3, whereas for SVD it stops decreasing at a dimensionality of 8. This may indicate that the LACs lie on a three-dimensional nonlinear manifold.

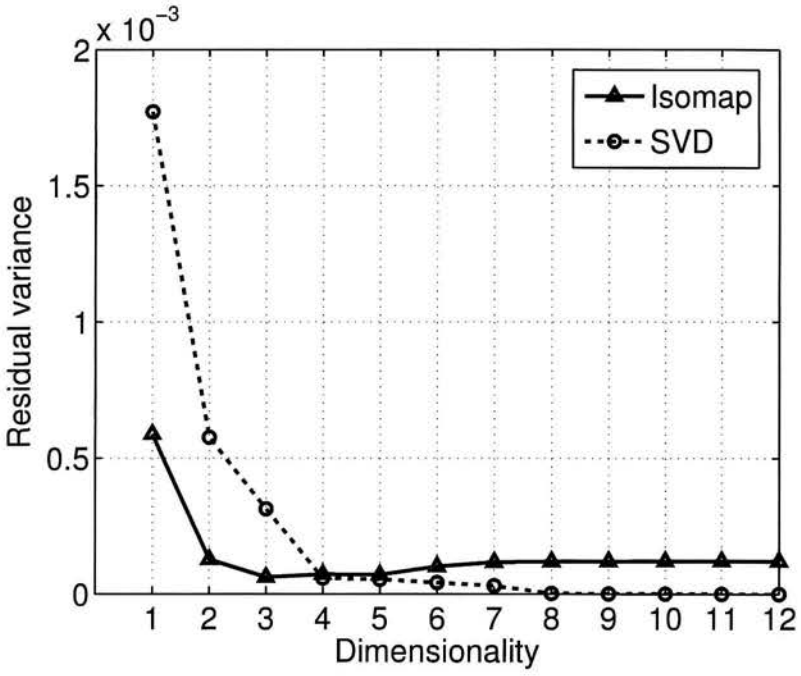


Figure 4·7: Residual variance as a function of dimensionality for the compounds LACs database, using Isomap and SVD.

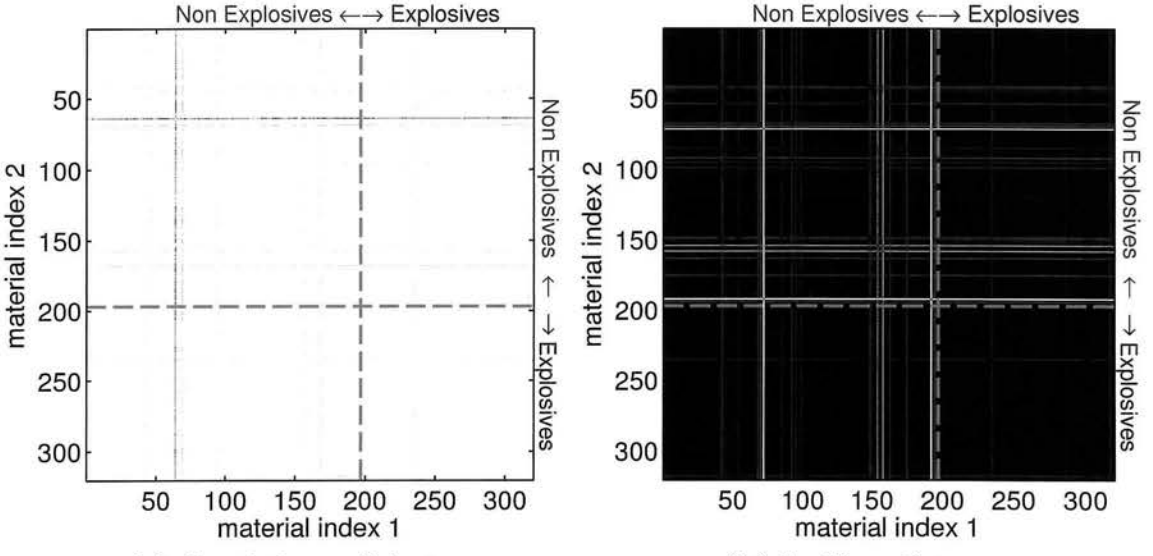
4.3 Correlation between the LACs

To better understand the space of the compounds LACs we calculated the correlation coefficient between each pair of LACs. The correlation coefficient between two vectors

$\boldsymbol{x}$ and $\boldsymbol{y}$ is defined as

$$\rho = \frac{\boldsymbol{x} \cdot \boldsymbol{y}}{\|\boldsymbol{x}\| \, \|\boldsymbol{y}\|} \tag{4.2}$$

We also calculated the pairwise Euclidean distances of the LACs. Figure 4·8 shows the results. Note that the correlation coefficient is higher for LACs which are closer, whereas the Euclidean distance is lower for LACs which are closer. It can be seen that many of the LACs from both the explosive and non-explosive classes are very close to each other. There is a small number of material pairs for which the correlation is small and the distance is large. The smallest correlation coefficient is 0.41, for potassium chloride and helium. The largest Euclidean distance is 9.47E+03, for tungsten and helium.



(a) Correlation coefficient

(b) Euclidean distance

Figure 4·8: Correlation coefficients and Euclidean distances between pairs of LACs in the compounds database. Figures are in grayscale where black is zero and white is one. The dashed green line indicates the transition between materials from the explosive class and the non-explosive class. Left: correlation coefficient, larger means closer. Right: normalized pairwise Euclidean distance, smaller means closer.

4.4 Summary

In this chapter we discussed estimating the intrinsic dimensionality of the LACs of different explosive and benign materials. This analysis can help in developing MECT methods for the security application. We studied the dimensionality using SVD with different criteria for determining the number of components needed. We applied the methods to a database of compound LACs which we had created. We found that two components are insufficient for accurate description of the curves and that a higher dimensional representation is needed, contrary to the prevailing wisdom in the medical domain. Part of this work was presented in [Eger et al., 2011a].

In addition, we applied Isomap to the compounds LACs and found that using this nonlinear embedding technique less components may be required to represent the LACs than using the linear SVD method.

Finally, we calculated the correlation coefficient and Euclidean distances between each pair of materials and showed that the LACs of many of the materials are very close, which makes material discrimination challenging.

Chapter 5

Optimized LAC feature selection

In X-ray transmission sensing the LAC captures the material information. As discussed in Section 2.3, estimating the entire LAC curve at every spatial location is not feasible with existing MECT systems. Therefore, the LAC of a material $\mu(E)$ is usually represented as a linear combination of a few basis functions $f_k(E)$, and the corresponding coefficients a_k are estimated and used as the material features:

$$\mu(E) = \sum_{k=1}^{N_b} a_k f_k(E) \tag{5.1}$$

In existing MECT techniques the choice of basis functions for the decomposition of the LAC has been based on approximate physical models, such as the Photo-Compton, or on attenuation coefficients of a few basis materials [Fessler et al., 2002]. These choices are focused on representation of the data and work well when there are a limited number of known materials in the scene, such as in medical imaging, or when the physical modeling error is small (e.g., Photo-Compton for low-Z materials). In the case of explosive detection in luggage, the set of underlying materials is very large and the materials cannot all be accurately described using the Photo-Compton model. In addition, the Photo-Compton model is not specifically designed for the explosives detection task. Therefore, there is reason to believe that the ability to discriminate explosives may be improved by using features that are different from the Photo-Compton based features.

We present a learning-based approach for optimizing the LAC features specifically

for the task of explosive discrimination. The goal is to extract the information that is most useful for detecting explosives. By using examples of materials' LACs a set of basis functions can be learned whose corresponding coefficients may act as superior features for explosives versus non-explosives classification, compared to the photoelectric and Compton coefficients.

The optimization of the LAC feature space may be achieved by different adaptive basis selection methods. Some of the methods are supervised, i.e., they take into account the class labels. These methods aim at *separating* the features of the different classes. The other methods are unsupervised, providing low-dimensional features which best *represent* the high-dimensional data.

In a special family of methods that we consider, a subset of energy levels is selected and the values of the LACs at those energy levels are used as features. These methods may specifically help with processing data acquired by systems with energy-sensitive detectors such as photon-counting detectors.

Since we are interested in accurate classification of explosives and non-explosives using the selected features, we would like to compare the classification performance of the different feature selection methods. We follow two approaches to obtain this comparison. The first is based on the receiver operating characteristic curve (ROC) and metrics derived from it. The ROC captures the fundamental feature performance and is independent of the choice of classifier. Accurate calculation of the ROC is challenging when the number of samples in the dataset is relatively small. We explore different ways of carrying out the calculation. The second approach is training a nominal classifier, such as support vector machine (SVM), and measuring the classification accuracy.

In this chapter we first describe the adaptive feature selection methods which we consider. Then we discuss the different ways of comparing the performance of

the methods. Finally, we give experimental results using synthetic data and the compounds LAC database described in Appendix A.

5.1 Feature selection methods

We optimize the LAC feature space by selecting the basis functions based on examples of material LACs from the security domain. Adaptive basis selection is related to the field of linear dimensionality reduction in machine learning [Raich et al., 2008]. The goal in linear dimensionality reduction is to provide a few projection directions based on a set of training data, according to some criterion. The data is projected onto the space spanned by the learned projection directions and the resulting low-dimensional representation of the data is used as features. Linear dimensionality reduction techniques can be applied to the LACs in order to find a small number of projection directions, or equivalently basis functions, such that the corresponding features will be good for material classification (supervised) and/or efficient representation (unsupervised). An illustration of the approach is shown in Figure 5·1.

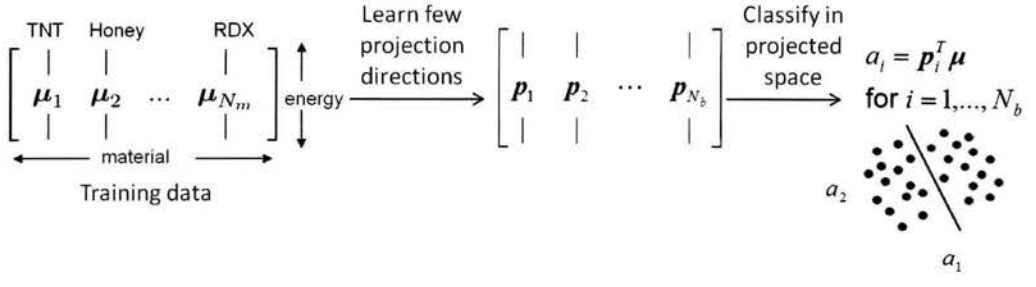


Figure 5·1: Illustration of LAC feature space optimization by adaptive selection of projection directions or basis functions

The general framework is the following. Suppose we have N_m training data samples $\{\boldsymbol{\mu}_i | \boldsymbol{\mu}_i \in \mathbb{R}^{N_e}\}_{i=1}^{N_m}$, where $\boldsymbol{\mu}_i$ is a vector containing samples of the LAC of material i. The corresponding class labels are denoted by $\{y_i | y_i \in \{0,1\}\}_{i=1}^{N_m}$, where class 1 represents the explosive materials and class 0 represents the non-explosive materials.

Let $y_i = 0$ for $i \in C_0$ and $y_i = 1$ for $i \in C_1$. Using the training data, a projection matrix $P = [\boldsymbol{p}_1 ... \boldsymbol{p}_{N_b}] \in \mathbb{R}^{N_e \times N_b}$ is found, with $N_b << N_e$. The resulting N_b-dimensional feature vector for a material with LAC $\boldsymbol{\mu}$ is $\boldsymbol{a} = P^T \boldsymbol{\mu}$.

Different criteria and methods for finding the projection matrix P will be considered. Below we describe a few of the methods which we consider. In Section 5.1.1 we describe the unsupervised methods, which are generally based on representation of the data regardless of class label. In Section 5.1.2 we describe the supervised methods, which take into account the class labels and aim at separation of the classes in the projected space.

5.1.1 Unsupervised methods

Singular value decomposition (SVD)

The SVD is a way of factoring matrices which exposes the underlying rank structure of the matrix [Golub and Reinsch, 1970]. Given a group of training samples, we arrange them in the columns of a matrix X, and calculate the SVD of the resulting matrix:

$$X = \begin{bmatrix} | & | & & | \\ \boldsymbol{\mu}_1 & \boldsymbol{\mu}_2 & \cdots & \boldsymbol{\mu}_{N_m} \\ | & | & & | \end{bmatrix} = USV^T \tag{5.2}$$

where U is a matrix containing the left singular vectors in its columns, S is a diagonal matrix with the singular values on the diagonal, and V is a matrix containing the right singular vectors in its columns.

The N_b projection directions are then given by the left singular vectors (the columns of U) corresponding to the N_b largest singular values. Note that this method aims at data representation and attempts to minimize the energy of the approximation error. The projection directions are obtained with all the samples pooled together, regardless of their class.

Unsupervised energy-level selection

A special family of LAC feature selection methods is based on energy-level selection. Out of the N_e energy levels for which we have samples of the LACs, a subset of energy levels are selected and the values of the LACs at those energy levels are used as features. In this case the projection matrix P has a special structure - each column has one element which is equal to one and the rest of the elements are zero. An illustration is given in Figure 5·2.

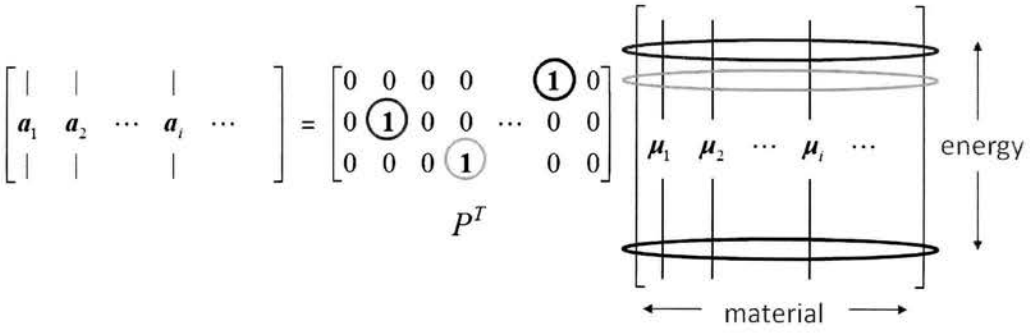


Figure 5·2: Obtaining LAC features by energy-level selection - a special family of adaptive feature selection methods

We look at the following unsupervised criteria and methods to choose the energy levels:

- SVD band subset selection (SVDSS):

  This method formulates the band/energy subset selection problem as a constrained rank approximation and a heuristic algorithm for its solution is provided in [Velez-Reyes and Jimenez, 1998]. This method does not require an exhaustive search over all the energies.

- Sammon's loss criterion (Sammon):

  Select the energies which best preserve the pairwise Euclidean distances between

the LACs by minimizing Sammon's loss function [Sammon, 1969]:

$$f^S(\mathcal{E}) = \sum_{i,j} \delta_{ij}^{-1} \left(\delta_{ij} - \tilde{\delta}_{ij}(\mathcal{E})\right)^2 / \sum_{i,j} \delta_{ij} \tag{5.3}$$

where $\mathcal{E}$ is the set of selected energy-levels, δ_{ij} is the Euclidean distance between the full LACs of materials i and j, and $\tilde{\delta}_{ij}(\mathcal{E})$ is the Euclidean distance between the low-dimensional versions of the LACs of the same materials.

- Absolute value criterion (Abs):

  Select the energies which best preserve pairwise Euclidean distances between the LACs by minimizing the absolute value cost function:

$$f^{Abs}(\mathcal{E}) = \sum_{i,j} |\delta_{ij} - \tilde{\delta}_{ij}(\mathcal{E})| \tag{5.4}$$

  where δ_{ij} and $\tilde{\delta}_{ij}(\mathcal{E})$ are defined above.

5.1.2 Supervised methods

Local discriminant embedding (LDE)

The LDE method for dimensionality reduction achieves good discriminating performance by integrating the information of neighbor and class relations between data points [Chen et al., 2005]. LDE seeks to dissociate the submanifold of each class from one another, and specifically derives the embedding for nearest neighbor classification in a low-dimensional Euclidean space. The aim is to derive projection directions such that in the low-dimensional projected space neighboring points are kept close if they have the same label, and points of other classes are prevented from entering the neighborhood. The details are given in [Chen et al., 2005].

Nonparametric discriminant analysis (NDA)

NDA is a supervised linear dimensionality reduction method which is based on non-parametric extensions of scatter matrices [Fukunaga and Mantock, 1983]. NDA follows the principles of Fisher's linear discriminant analysis (LDA). In contrast to LDA, which provides only one projection direction, NDA provides multiple projection directions.

In LDA, the projection space is chosen to maximize the ratio of between-class variation and within-class variation. A between-class scatter matrix S_b and a within-class scatter matrix S_w are constructed from the labeled data as follows:

$$S_b = (\boldsymbol{\xi}_1 - \boldsymbol{\xi}_0)(\boldsymbol{\xi}_1 - \boldsymbol{\xi}_0)^T \tag{5.5}$$

$$S_w = \frac{1}{|C_0|}\sum_{j \in C_0}(\boldsymbol{\mu}_j - \boldsymbol{\xi}_0)(\boldsymbol{\mu}_j - \boldsymbol{\xi}_0)^T + \frac{1}{|C_1|}\sum_{j \in C_1}(\boldsymbol{\mu}_j - \boldsymbol{\xi}_1)(\boldsymbol{\mu}_j - \boldsymbol{\xi}_1)^T \tag{5.6}$$

where $\boldsymbol{\xi}_i = \frac{1}{|C_i|}\sum_{j \in C_i}\boldsymbol{\mu}_j$.
LDA then finds a projection direction $\boldsymbol{p}^*$ via the following maximization problem:

$$\boldsymbol{p}^* = \arg\max_{\boldsymbol{p}} \frac{\boldsymbol{p}^T S_b \boldsymbol{p}}{\boldsymbol{p}^T S_w \boldsymbol{p}} \tag{5.7}$$

The solution is given by

$$\boldsymbol{p}^* = \alpha S_w^{-1}(\boldsymbol{\xi}_1 - \boldsymbol{\xi}_0) \tag{5.8}$$

where α is chosen such that $\boldsymbol{p}^{*T}\boldsymbol{p}^* = 1$.

For the two-class problem the between-class scatter matrix S_b only has rank 1 and LDA gives only one optimal projection direction. This is sufficient for class separation when the class likelihoods are all Gaussian and homoscedastic. In non-Gaussian or heteroscedastic settings we may potentially gain from having additional projection directions. We will show that for our problem adding more projection directions is beneficial. In NDA, the between-class scatter matrix is replaced with a full-rank,

nonparametric version, providing multiple projection directions in closed form. The NDA algorithm is discussed in detail in [Fukunaga and Mantock, 1983].

Sequential linear discriminant analysis (SLDA)

We propose another way to obtain multiple projection directions using LDA. The additional directions are found sequentially. The first projection direction is set to the direction given by conventional LDA (described above). The second direction is found by projecting the data onto the space perpendicular to the first direction and applying LDA again in that (lower-dimensional) space. The resulting direction is orthogonal to the first one. The process is repeated several times to obtain a set of orthogonal projection directions. A similar process was suggested in [Foley and Sammon, 1975]. The algorithm is summarized below.

SLDA algorithm summary

1. Set $\boldsymbol{\mu}_j^{(0)} = \boldsymbol{\mu}_j,\ j = 1, ..., N_m$.

2. For $k = 0, ..., N_b - 1$, calculate:

   (a) $\boldsymbol{\xi}_i^{(k)} = \frac{1}{|C_i|} \sum_{j \in C_i} \boldsymbol{\mu}_j^{(k)},\ i = 0, 1$

   (b) $S_w^{(k)} = \sum_{i=0}^{1} \left\{ \frac{1}{|C_i|} \sum_{j \in C_i} (\boldsymbol{\mu}_j^{(k)} - \boldsymbol{\xi}_i^{(k)})(\boldsymbol{\mu}_j^{(k)} - \boldsymbol{\xi}_i^{(k)})^T \right\}$

   (c) $\boldsymbol{p}^{(k)} = \alpha S_w^{(k)^{-1}} (\boldsymbol{\xi}_1^{(k)} - \boldsymbol{\xi}_0^{(k)})$, where α is chosen such that $\boldsymbol{p}^{(k)T} \boldsymbol{p}^{(k)} = 1$

   (d) $\boldsymbol{\mu}_j^{(k+1)} = (I - \boldsymbol{p}^{(k)} \boldsymbol{p}^{(k)T}) \boldsymbol{\mu}_j^{(k)},\ j = 1, ..., N_m$

The SLDA projection directions are the set of N_b vectors $\boldsymbol{p}^{(k)}$ obtained at each iteration.

Supervised energy-level selection

In this special family of basis selection methods, described in Section 5.1.1 for the unsupervised case, a reduced subset of energy levels are chosen and the values of the LACs at those energy levels are used as features. We look at the following supervised criteria and methods to choose the energy levels:

- Area under the ROC criterion (AUC):

  The subsets of energy levels are exhaustively searched and the ones which provide features with the largest AUC are picked as the best. The AUC calculation is discussed in more detail in Section 5.2.1.

- Kullback-Leibler divergence criterion (KLD):

  The subsets of energy levels are exhaustively searched and the ones which provide features with the largest Kullback-Leibler (KL) divergence are picked as the best.

  To calculate the KL divergence for a set of selected energy levels $\mathcal{E}$ of size N_b, we regard the LAC values at energies $\mathcal{E}$ as samples of the explosive distribution, $\{\boldsymbol{a}_i,\ i \in C_1\}$, and samples of the non-explosive distribution, $\{\boldsymbol{a}_i,\ i \in C_0\}$. We calculate the sample means of each class, $\boldsymbol{m}_0$ and $\boldsymbol{m}_1$, and sample covariances, S_0 and S_1 as follows:

$$\boldsymbol{m}_0 = \frac{1}{|C_0|}\sum_{i\in C_0}\boldsymbol{a}_i \qquad S_0 = \frac{1}{|C_0|}\sum_{i\in C_0}(\boldsymbol{a}_i - \boldsymbol{m}_0)(\boldsymbol{a}_i - \boldsymbol{m}_0)^T$$
$$\boldsymbol{m}_1 = \frac{1}{|C_1|}\sum_{i\in C_1}\boldsymbol{a}_i \qquad S_1 = \frac{1}{|C_1|}\sum_{i\in C_1}(\boldsymbol{a}_i - \boldsymbol{m}_1)(\boldsymbol{a}_i - \boldsymbol{m}_1)^T$$

  We then calculate the Kullback-Leibler divergence between the two distributions

under a Gaussianity assumption [Kullback, 1997]:

$$d_{KL} = \frac{1}{2}\left\{\mathrm{tr}(S_1^{-1}S_0) + (\boldsymbol{m}_1 - \boldsymbol{m}_0)^T S_1^{-1}(\boldsymbol{m}_1 - \boldsymbol{m}_0) - N_b - \ln\frac{|S_0|}{|S_1|}\right\} \quad (5.9)$$

5.2 Classification performance evaluation

We describe two types of metrics for evaluating the features given by the different methods. We describe two metrics which are related to the receiver operating characteristic (ROC) curve. Then we describe a metric related to the performance of a specific nominal classifier.

5.2.1 ROC curve metrics

Let $p(\boldsymbol{a}|H_i)$, $i \in \{0, 1\}$, be the probability density function of the observation $\boldsymbol{a}$ given that hypothesis H_i is true (we assume that the density exists). In hypothesis testing, a Bayes/Neyman-Pearson optimal decision rule is to compare a function $L(\boldsymbol{a})$, called the likelihood ratio, to a threshold η. This is known as the likelihood ratio test (LRT):

$$L(\boldsymbol{a}) = \frac{p(\boldsymbol{a}|H_1)}{p(\boldsymbol{a}|H_0)} \underset{H_0}{\overset{H_1}{\gtrless}} \eta \quad (5.10)$$

A powerful tool for evaluating classification performance in hypothesis testing is the ROC curve, which is a graph of the probability of detection P_D versus the probability of false alarm P_F, which are defined as:

$$P_D = P(\text{decide } H_1|H_1 \text{ true}) \qquad P_F = P(\text{decide } H_0|H_1 \text{ true}) \quad (5.11)$$

The ROC for the LRT (5.10) is a function of the conditional densities $p(\boldsymbol{a}|H_0)$ and $p(\boldsymbol{a}|H_1)$ and the threshold η and does not depend on the choice of classifier. An example of an ROC curve is shown in Figure 5·3.

Although the ROC fully characterizes the performance of LRT-based decision

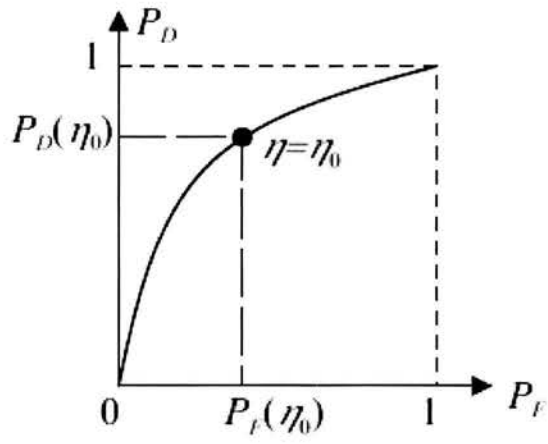


Figure 5·3: Example of an ROC curve. The x-axis is the probability of false alarm, P_F, and the y-axis is the probability of detection, P_D. Any point on the ROC corresponds to a particular choice of threshold.

rules, it is desirable to have a single metric which reflects the performance. Such a measure is the area under the ROC curve (AUC), which varies between 0.5 (classification no better than flipping a coin) and 1 (best possible classification). It has been shown that the AUC is a good measure of the overall discrimination capability that does not depend on the prior probabilities of the two classes [Wickens, 2001].

Another useful measure which can be derived from the ROC curve is the value of P_F for a fixed value of P_D. Lower values of P_F are desirable.

ROC calculation

To calculate the ROC and the related metrics, an estimate of the likelihood ratio is required. One commonly used technique to estimate the likelihood ratio is to estimate each density function individually using kernel density estimation (KDE) and then evaluating the ratio [Hastie et al., 2005]. Density estimation requires a large number of samples to provide accurate results and is known to be a hard problem.

An alternative way to estimate the likelihood ratio is to directly estimate the ratio from the data without explicitly calculating the density functions. A related

method was suggested in [Kanamori et al., 2009]. The method, called least squares importance fitting (LSIF), estimates a ratio between two density functions directly from the samples. The ratio is not a likelihood ratio, but rather the ratio between the density of the samples in the training set and the density of the samples in the test set, a quantity known as "importance". We propose to apply the method to the calculation of the likelihood ratio.

5.2.2 Average classifier accuracy

Another way to evaluate the value of features is using the classification accuracy of a nominal classifier. Compared to the AUC, this metric is a more direct measure of classification performance, which is obtained with a specific practical classifier.

We train a classifier to obtain a function $y = f(\boldsymbol{a})$ which maps a sample $\boldsymbol{a}$ to a label y. We apply the classifier to the test data and calculate the average classification accuracy:

$$\frac{1}{N}\sum_{i=1}^{N}\mathbb{1}\{f(\boldsymbol{a}_i) = y_i\} \tag{5.12}$$

where $\mathbb{1}\{f(\boldsymbol{a}_i) = y_i\}$ is equal to 1 when the label is correct and zero otherwise, and N is the total number of samples. A higher average classification accuracy is better.

The classifiers which we consider are support vector machine (SVM) with linear and Guassian kernels, and the K-nearest neighbor (KNN) classifier [Hastie et al., 2005]. These classifiers are very common, and used in practice in many applications. Using both linear (SVM-linear) and nonlinear (SVM-Gaussian and KNN) classifiers we can learn the structure of the features, i.e., whether they are linearly separable or require a nonlinear transformation achieve separability.

Each classifier has some parameters which require tuning (e.g., the soft margin parameter in SVM and the number of nearest neighbors in KNN). To optimize the classifier parameters a cross-validation procedure is used.

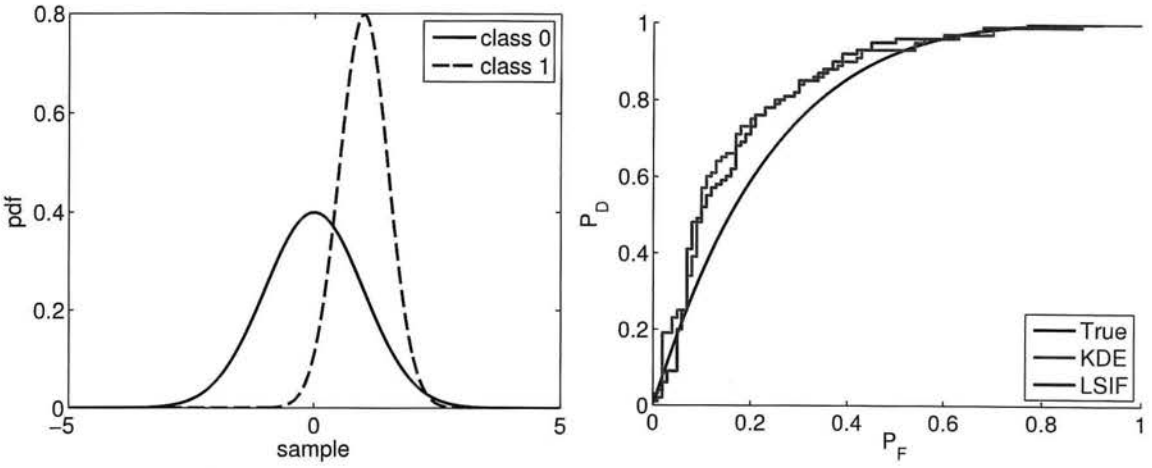
5.3 Experimental results

5.3.1 Calculating the AUC

In this experiment we compare the two methods described in Section 5.2.1 for estimating the AUC. As our data we use random samples from two multi-dimensional Gaussian distributions with the following parameters: $m_0 = \mathbf{0}$, $m_1 = [1\ 1\ ...\ 1]^T$, $C_0 = I$, $C_1 = 0.5I$, where m_i and C_i are the mean and covariance of class i. We estimate the likelihood ratio using the KDE and LSIF methods, construct an ROC by comparing the likelihood ratio against different thresholds and then calculate the AUC. For the KDE method implementation, we estimate the conditional densities using previously published code [Ihler, 2003]. We estimated the density at each sample using a leave-one-out procedure - first we estimate the density function using all the other samples and then we evaluate the density at the sample. For the LSIF our implementation was based on the code in [Sugiyama, 2011].

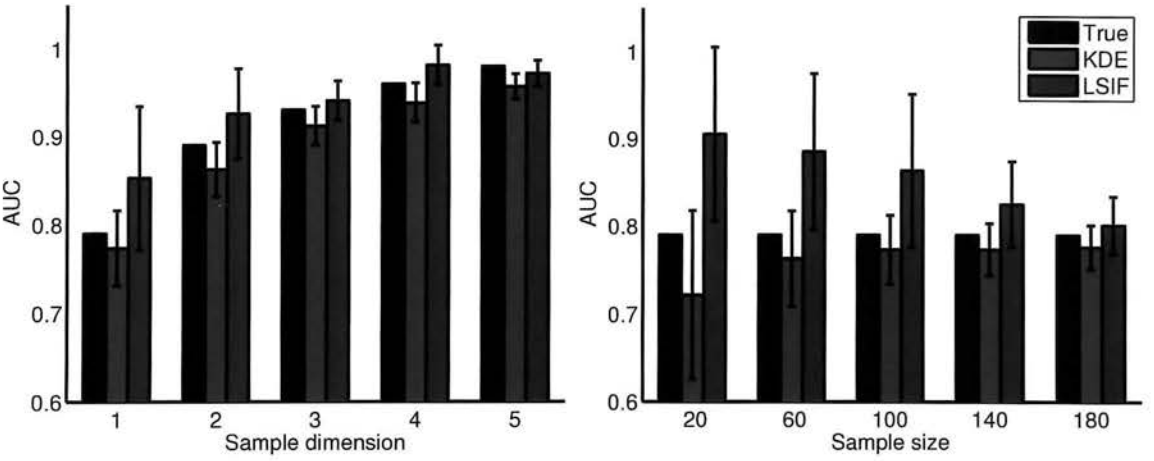
Figure 5·4 shows the ROC estimates for a 1D example. 100 samples were generated from each class and the three methods were applied. The ROCs obtained with the different methods for this example seem very close to each other and also close to the ground truth.

We calculated the average mean square error (MSE) of the methods as a function of sample dimension and a function of sample size. The average was calculated over 100 independent runs. When the sample dimension was varied the sample size of each class was set to 100. When the sample size was varied the sample dimension was set to 1. In all of these experiments the number of samples (sample size) from each class was the same. The results are shown in Figure 5·5. It can be seen that in most cases KDE gives the closest estimate to the ground truth with lower standard deviation. For large sample dimension and large sample size the methods have very similar performance.



(a) Density functions (b) ROC estimates

Figure 5·4: ROC estimates for a 1D Gaussian case. The density functions of the two classes are plotted on the left. The ROC estimates given by the different methods, along with the ground truth ROC, are plotted on the right.



(a) AUC vs. dimension (b) AUC vs. sample size

Figure 5·5: Mean AUC estimates obtained with the different methods (in color) compared to the true AUC (in black). On the left the sample dimension is varied from 1 to 5 while holding the sample size fixed at 100. On the right the sample size is varied while holding the dimension fixed at 1. Errorbars show the mean plus or minus one standard deviation.

Given the results in this analysis we decided to use KDE for the evaluation of the AUC in the rest of the experiments in this chapter.

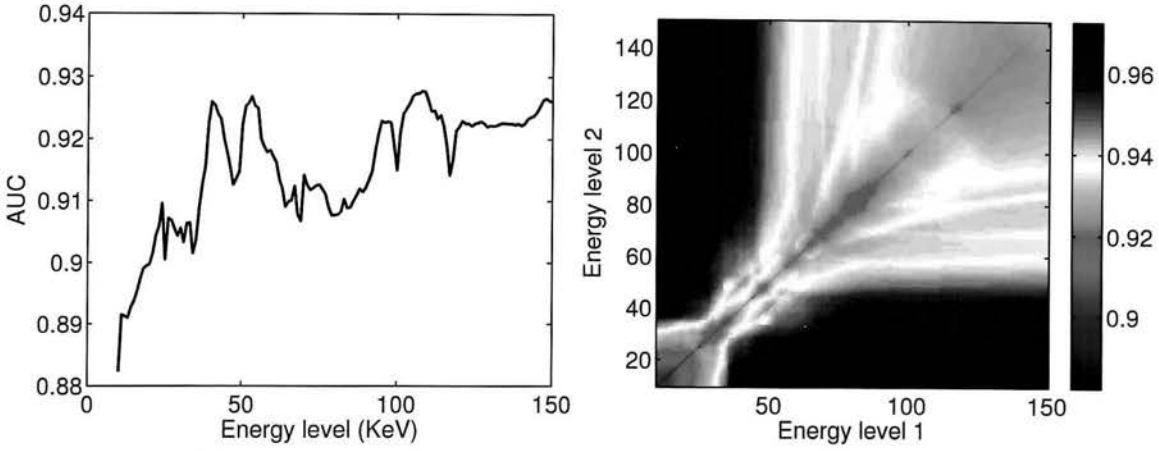
5.3.2 Energy level selection

The energy level selection methods described in Section 5.1 apply different criteria to select a subset of energy levels, such that the LAC values at those levels may act as features for explosives versus non-explosive classification. We applied the methods to the LACs in our compounds database. The energy levels in the candidate collection were in the range of 10-150 keV, in steps of 1 keV. There was no division into training and testing sets. All the LACs in the database were used together for training and testing. Note that this analysis was done on an earlier version of the compounds database, which had about 100 less examples than the current database described in Appendix A.

Figure 5·6 shows the AUC values for the selection of a single energy level, as well as combinations of two selected energy levels. It is interesting to note that in the 2D case combinations of high and low energy levels result in a high AUC.

Table 5.1 shows the optimum energy level choices using the different methods. It can be seen that the unsupervised methods select the lower energies. This is because at low energies the LACs have very large values, which means, for example, that the pairwise distances between the LACs are large. The energy levels selected by the AUC method seem to be both low and high. The levels selected by KLD are approximately in the middle of the range.

Figure 5·7 shows the AUC values for the energy levels listed in Table 5.1. The supervised methods provide higher AUC than the unsupervised methods, as expected. The AUC values for the supervised method based on the AUC criterion are much larger than the AUC values for all the other methods for all feature dimensions. The AUC values for the unsupervised methods are comparable, for the most part. In



(a) single energy **(b)** two energies

Figure 5·6: Area under the ROC curve for each single energy levels (left) and each combinations of two energy levels (right). In the image on the right the color at each pixel indicates the AUC value for the given combination of energies.

	Supervised		**Unsupervised**		
	AUC	**KLD**	**SVDSS**	**Sammon**	**Abs**
1 energy	108	84	12	10	10
2 energies	10,115	80,81	10,14	10,11	10,12
3 energies	10,11,122	77,80,81	10,12,16	10,11,12	10,11,12
4 energies	10,11,91,131	80,81,82,83	10,11,12,16	10,11,12,13	10,11,12,14

Table 5.1: Best single energy level and best combinations of two, three and four energy levels according to different criteria and methods. The energy levels are in keV.

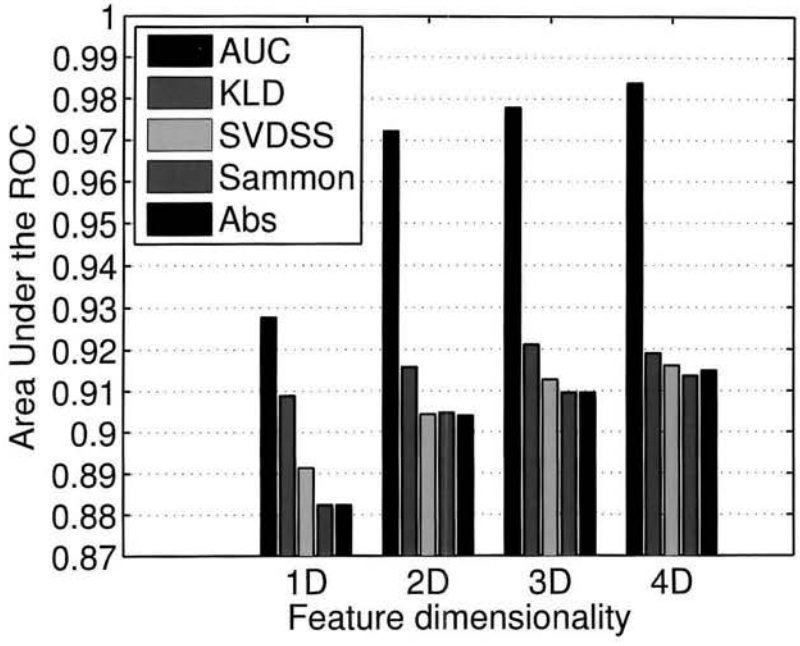


Figure 5·7: AUC for best single energy level and best combinations of two, three and four energy levels according to different criteria and methods

general, as feature dimensionality increases the AUC values increase as well, with the most significant increase in the transition from one to two dimensions.

It is shown that the choice of energy levels at which to sample the LAC curves of materials is different for supervised and unsupervised criteria. The results suggest that as more energy levels are added, classification performance may be improved. Note that this analysis is based solely on the LAC curves, and does not take into account practical sensing constraints. In current systems attenuation information at low energies ($\sim$ below 30 keV) is very limited.

5.3.3 Classification performance comparison

In this section we study the performance of the features given by the adaptive feature selection methods described in Section 5.1. The performance is evaluated with the AUC and classifier accuracy criteria, as explained in Section 5.2, using a synthetic

dataset and the compounds LAC database.

We apply a cross-validation procedure. In each of the cross-validation runs we perform the following:

1. We randomly divide the data into two equally sized groups - training and testing. In each group we have almost an equal number of members from each class.

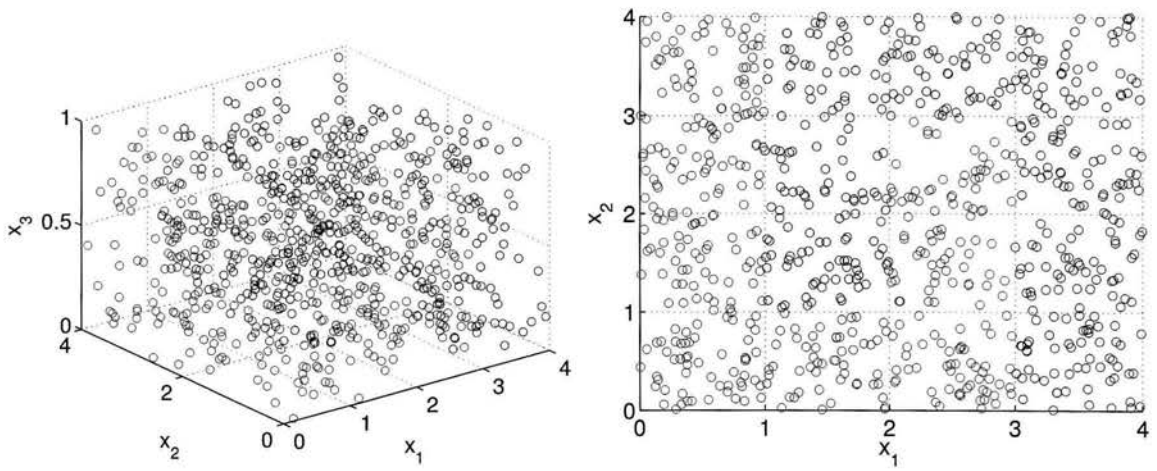
2. *The training phase:* We find the projection directions using the training data according to the method from Section 5.1 being examined. The training data is then projected onto the projection directions. The resulting low-dimensional features are used to train the classifiers.

3. *The testing phase:* We use the projection directions obtained in the training phase and project the test data onto those directions to obtain low-dimensional features. These features are used in the trained classifiers from step 2. The corresponding AUC and classifiers accuracy is then calculated.

For each of the adaptive methods, we evaluate the classification performance using one feature (corresponding to the first projection direction), two features (corresponding to the first and second projection directions), three features (corresponding to the first three projection directions), and so on.

Three different classifiers were used in these experiments: support vector machine with a linear kernel (SVML), support vector machine with a Gaussian kernel (SVMG), and k-nearest neighbors (KNN) [Hastie et al., 2005]. The SVML and SVMG parameters are tuned according to [Hsu et al., 2003]. The k parameter in KNN is chosen using an inner cross-validation loop.

The AUC calculation is carried out as follows: For each data point we estimate the H_0 and H_1 conditional densities using all the points except the current point by KDE; Then we evaluate both densities at the point we left out, and obtain the likelihood



(a) 3D scatter (b) View from top

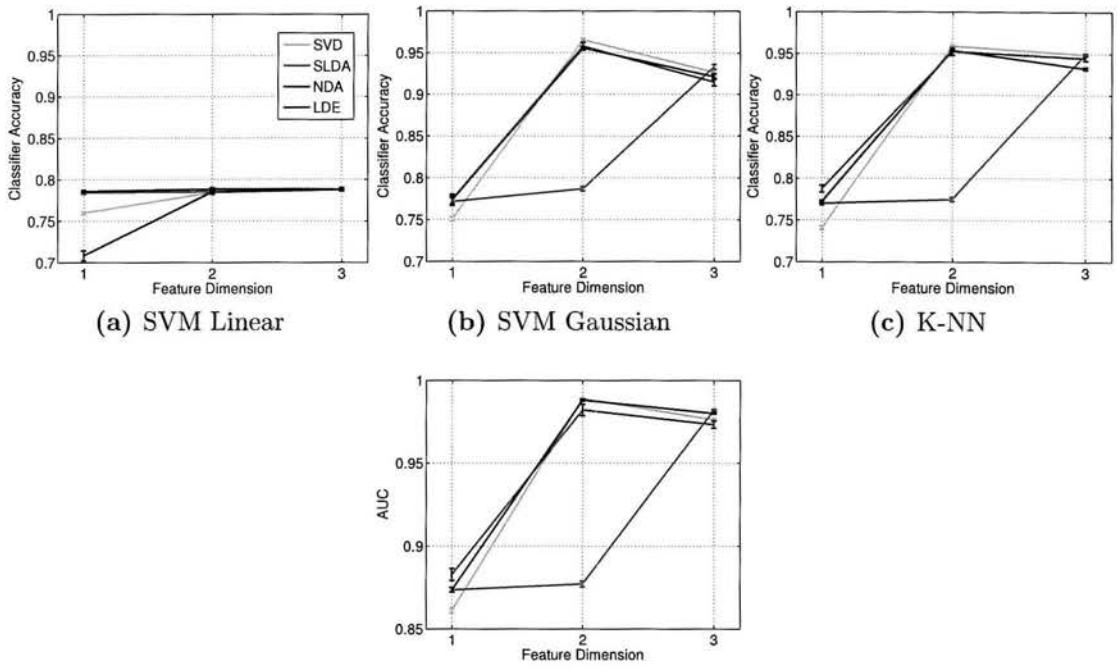
Figure 5·8: Scatter plot of the synthetic 2-class dataset. Class 0 is in blue and class 1 is in red.

ratio value for that point by calculating the ratio between the two density values; Once we have the likelihood ratio for all the points we compare it to different thresholds, construct an ROC and calculate the area under the ROC using the MATLAB function 'perfcurve'.

Results with a synthetic dataset

To evaluate the basis selection methods using data with known structure and validate the implementation of the methods we tested the methods on a synthetic 2-class dataset. The data is 3-dimensional, with 400 samples from each class. The classes can be perfectly separated by using just two of the three coordinates. A scatter plot of the data is shown in Figure 5·8.

We followed the cross-validation procedure and applied SVD, SLDA, NDA and LDE to the data. Figure 5·9 shows the classifier accuracy and AUC for the different methods and for different feature dimensions. The highest classifier accuracy is given by SVMG and KNN classifiers. The data is not linearly separable and therefore the SVML does not perform as well. The SVMG and KNN plots show similar behavior to



(a) SVM Linear (b) SVM Gaussian (c) K-NN

(d) AUC

Figure 5·9: Classification performance on a synthetic example using different classifiers (top), and using AUC (bottom) for the different dimensionality reduction methods applied to the synthetic dataset. The x-axis indicates the dimension the data was reduced to. The errorbars represent standard error.

the AUC plot: most of the dimensionality reduction methods perform well when only two dimensions of the data are used, as expected. Only SLDA requires the additional third dimension to achieve high classification accuracy.

Results with the compounds LAC database

We compare the features obtained by adaptive dimensionality reduction with the features obtained by conventional LAC basis decompositions described in Section 3.1. The first conventional method is photo-Compton (3.7), denoted here as PhCo. The projection space is spanned by the discretized photoelectric and Compton basis functions. The second conventional method is basis-material (3.12), denoted here as BMat. The projection space is spanned by the LACs of Lucite and aluminum follow-

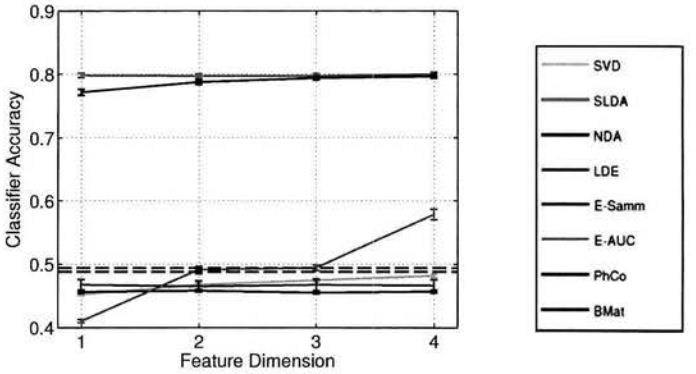
ing [Lehmann et al., 1981].

The adaptive basis selection methods we apply are SVD, SLDA, NDA, LDE. We also include the results with energy-subset selection by Sammon criterion (E-Samm) and energy-level selection by AUC criterion (E-AUC) for comparison. For the energy-level selection methods we fix the energy levels to the ones previously obtained, and listed in Table 5.1.

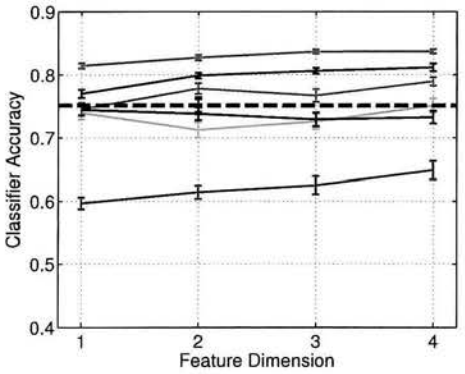
Due to computational considerations, we pre-process the training data by projecting them onto the first N singular vectors obtained by the SVD of all the training LACs. The parameter N is chosen as the numerical rank of the LAC matrix, according to Matlab's 'rank' function. N is relatively large and therefore the information is maintained.

Figure 5·10 shows the classification performance of the different features for the compound LACs, as measured by classifier accuracy. The classifier accuracy is plotted against feature dimension for the SVM-linear, SVM-Gaussian and KNN classifiers. In Figure 5·11 the classification performance is evaluated using the AUC and P_F for $P_D = 1$. In all the figures the performance of the two-dimensional features obtained with the conventional PhCo and BMat methods is extended horizontally with a dashed line. It can be seen that the features obtained with SLDA and NDA provide the highest classification accuracy and AUC compared to the other methods, even with just one feature dimension. The results using the conventional PhCo and BMat methods are similar to each other, and both show worse performance relative to SLDA and NDA. This suggests that using optimized features classification performance may be improved relative to the conventional features. It can also be seen that the energy level selection by AUC, E-AUC, is comparable to the conventional methods and E-Samm is usually worse. Most of the methods fail when the SVM with a linear kernel is used. This may be because the data is not linearly separable. In general, as the

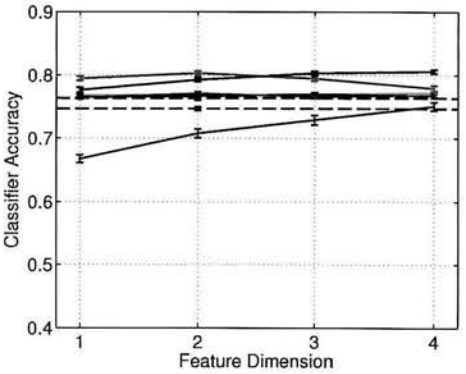
feature dimension increases, the performance improves. The improvement from three to four dimensions, however, is not significant for most methods, which suggests that three dimensional features may be sufficient for explosive discrimination.



(a) SVM Linear

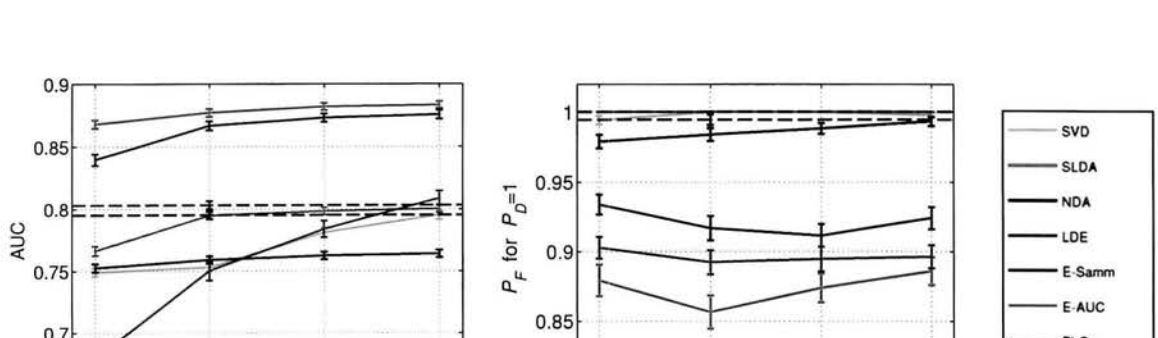


(b) SVM Gaussian



(c) KNN

Figure 5·10: Classification accuracy of different classifiers for the different feature selection methods applied to the compounds LAC database. The x-axis indicates the dimension the data was reduced to. The errorbars represent standard error. The results for PhCo and MatL, obtained with two-dimensional features, were extended horizontally by a dashed line.



(a) AUC (b) P_F for $P_D = 1$

Figure 5·11: ROC-based evaluation of the different feature selection methods applied to the compounds LAC database. On the left the AUC values are plotted and on the right the values of P_F for $P_D = 1$. Note that in the left plot higher values are better and in the right plot lower value are better. The x-axis indicates the dimension the data was reduced to. The errorbars represent standard error. The results for PhCo and MatL, obtained with two-dimensional features, were extended horizontally by a dashed line.

5.4 Summary

In this chapter we presented a learning-based approach for choosing features related to the X-ray attenuation curves of materials for the task of explosives versus non-explosives classification. We used an LAC database which we created with examples of different explosive and non-explosive materials. We compared different feature selection methods and showed that using the SLDA method classification performance was the highest, even with just one-dimensional features. In addition, the performance improved as feature dimension was increased. This suggests that using adaptive classification-aware methods for feature selection may improve detection of explosives relative to conventional basis-decompositions such as photo-Compton. An earlier set of these results was presented in [Eger et al., 2011b].

Chapter 6

Reconstruction of material parameter images from MECT data

In Chapters 4 and 5 we studied the fundamental information available in LAC curves of materials and presented ways of optimizing LAC-based features for the task of explosives detection. In this chapter we focus on the MECT reconstruction process, where the goal is to estimate material-specific parameter images from MECT measurements. These parameters may be the basis expansion coefficients or quantities related to them such as effective atomic number and density.

We developed a few different methods in this field of material parameter image reconstruction. Below we describe the methods and present experimental results. The methods vary in the choice of material parameters and/or algorithm but they all share the same goal of achieving reliable estimates of some material-specific parameter images from MECT measurements for the security application. In Section 6.1 we present an extension to the ρZ projection method of [Heismann et al., 2003], discussed in Section 3.3.4. This is a post-reconstruction dual-energy method which estimates the effective atomic number and density at each pixel based on the ratio between the reconstructed effective attenuation coefficients $\frac{\bar{\mu}_1(\vec{x})}{\bar{\mu}_2(\vec{x})}$. Our goal is to expand the range of materials the method applies to, which may be achieved by using more than two spectral weighting functions. In Section 6.2 we discuss a dynamic MECT reconstruction approach, which is potentially useful when the measurements acquired with different spectral functions, $I_1, I_2, ...$, are not geometrically aligned. In Section 6.3 we

present a generalization of the EDEC method proposed in [Stenner et al., 2007] and discussed in Section 3.2.3. We propose to represent the mapping from dual-energy measurements to basis material sinograms using kernel smoothing, which allows us to include simulated data in the calibration process. This is useful when the real measurements of the calibration materials are not sufficient. Lastly, in Section 6.5 we present a new structure-preserving model based reconstruction approach which mitigates metal artifacts and improves object localization in photoelectric and Compton coefficient images.

6.1 Extension of ρZ Projection for a larger set of materials

The ρZ projection method [Heismann et al., 2003], described in Section 3.3.4, estimates the effective atomic number $Z_{eff}(\vec{x})$ and density $\rho(\vec{x})$ based on the ratio between the reconstructed effective attenuation coefficients $\frac{\bar{\mu}_1(\vec{x})}{\bar{\mu}_2(\vec{x})}$.

The ρZ projection method was developed for medical applications and therefore only considers low-atomic number materials. A curve, denoted by $F(Z)$, is generated based on predictions of attenuation values of all the elements with atomic number lower than 30. An example of $F(Z)$ is shown in Figure 3·4. The method is based on inverting the curve, which is possible due to its monotonicity. In the security domain, a larger range of materials may appear, including high-atomic-number materials. When considering atomic numbers which are greater than 30 $F(Z)$ is no longer monotonic, and therefore not invertible. This will be shown below.

We would like to extend the method to include a greater range of materials, to potentially make it more useful for the security domain. We propose to (i) increase the number of spectra used to obtain multiple $F(Z)$ functions and (ii) estimate the material parameters based on the combination and reliability of the multiple $F(Z)$ functions. By using four different spectra, for example, we get four images of the

reconstructed effective attenuation: $\bar{\mu}_1(\vec{x})$, $\bar{\mu}_2(\vec{x})$, $\bar{\mu}_3(\vec{x})$ and $\bar{\mu}_4(\vec{x})$. With four values we can obtain six $F(Z)$ curves, as shown in Figure 6·1. Each curve can be used to produce an estimate of the effective atomic number, $Z_{eff,i}(\vec{x})$. The final estimate of the effective atomic number, $Z_{eff}(\vec{x})$, is then calculated as a weighted average of the individual estimates:

$$Z_{eff}(\vec{x}) = \sum_{i=1}^{6} c_i Z_{eff,i}(\vec{x}) \tag{6.1}$$

where c_i are some weighting coefficients which add up to 1.

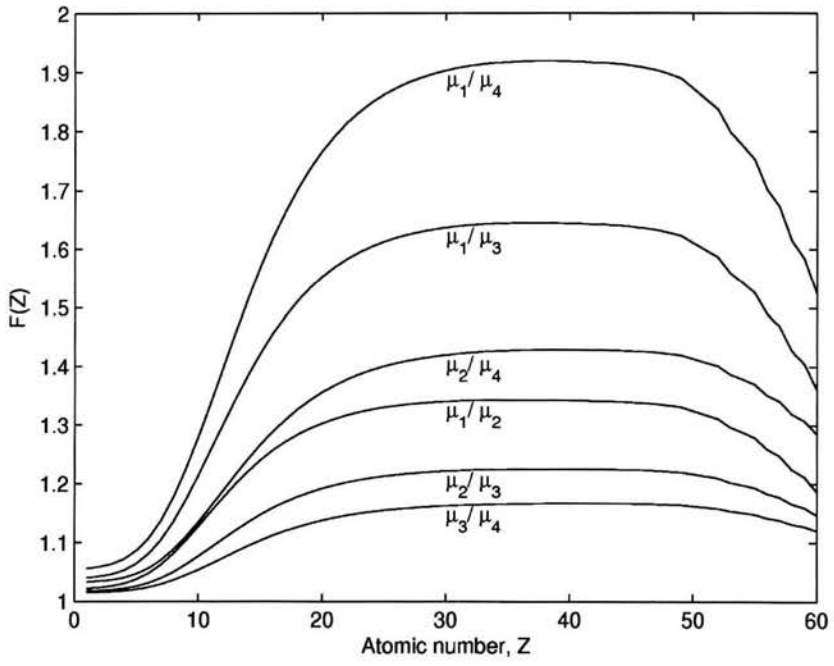


Figure 6·1: The six F(Z) curves. μ_1, μ_2, μ_3, μ_4 are the reconstructed attenuation values calculated by equation (3.30), using the 80, 100, 120, 140 kVp spectral weighting functions, respectively, of the Siemens SOMATOM scanner.

6.1.1 Experimental results

In this experiment we scanned a suitcase with some explosives simulants, purchased from A.I. explosives [Icar, 2009], and other materials. The Siemens SOMATOM Definition dual-source scanner at MGH was used. The scan was performed by Homer Pien, Synho Do, and Mannudeep K. Kalra. The measurements were obtained with four different source spectra: 80, 100, 120, and 140 kVp. An example of a cross section obtained with the 80 kVp spectrum is shown in Figure 6·2.

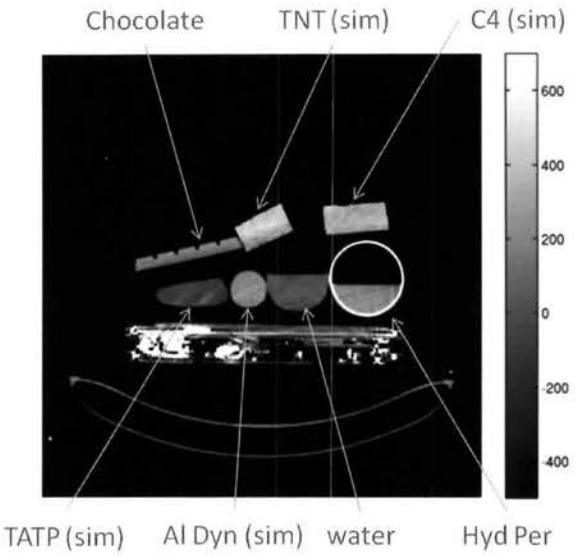


Figure 6·2: Cross section obtained with 80 kVp spectrum of the simulants phantom

We obtained an estimate of $Z_{eff}(\vec{x})$ in the following way. We chose 4 images, obtained with different spectra, which correspond to the same cross section. We used each of the six $F(Z)$ curves shown in Figure 6·1 to obtain an estimates $Z_{eff,i}(\vec{x})$. Then we calculated $Z_{eff}(\vec{x})$ according to Equation (6.1), with $c_i = 1/6$ for all i.

We calculated the mean and standard deviation of the Z_{eff} estimates for the different materials. The results are given in Table 6.1. It can be seen that for some materials, such as hydrogen peroxide and the TNT simulant, the estimates are better

than with the ρZ projection method, and for some materials such as water and TATP simulant the estimates are worse. This may be because the $F(Z)$ curve corresponding to μ_1 and μ_4 is the most informative (has the steepest slope). Perhaps the method would work better if the spectral weighting functions were further apart. In this scanner we were only able to work with the four spectra, 80, 100, 120, and 140 kVp, which have a large amount of overlap.

Material	Theoretical Z	Est. Z 4E		Est. Z 2E	
		mean	std	mean	std
HP Glass	7.6	8.0548	1.7044	6.4653	2.5927
HP Plastic	7.6	7.7172	1.0324	7.2269	1.2671
Alum. dynamite sim	8.62	9.7404	1.2263	8.8726	1.1290
TATP sim	6.7	9.2074	1.5978	6.8236	2.4192
C4 sim	7.12	7.5202	1.1744	6.8093	1.8860
TNT sim	7.1	7.2259	0.8904	6.8946	1.1562
Choc.	-	7.1702	1.1049	6.2390	1.6426
Shampoo	-	8.4201	0.8815	8.3213	1.0139
Honey	-	7.3586	0.7987	7.2299	0.9010
Soap	-	8.0869	1.2439	7.5453	1.5392
Water Water Bottle	7.4453	8.8070	1.3977	7.3012	2.1002
Water Plastic	7.4453	7.8296	0.7872	7.7977	0.7900

Table 6.1: $\hat{Z}_{eff}$ results for the materials in the simulants phantom. 2E refers to the ρZ projection method, and 4E refers to the extension of the method to four spectral functions.

6.2 MECT reconstruction for mismatched ray paths

This section addresses the problem of reconstructing basis coefficient images from MECT measurements when there is a ray mismatch in the measurements. In many systems measurements that are acquired with different spectral functions do not match geometrically. One example is the Siemens SOMATOM Definition dual-source CT scanner. This scanner has two X-ray sources which are separated by 90° and rotate simultaneously around the object. The scanner geometry is shown in Figure 3·6. The mismatch between the ray paths leads to difficulties in using typical MECT reconstruction methods.

We propose to reconstruct the basis expansion coefficients $a_k(\vec{x})$ from the misaligned measurements I_i using a model-based approach. Due to the large size of the problem in practice, we propose to use a statistical dynamic estimation method. The underlying field is reconstructed sequentially from the measurements. The ray paths at each time instance are taken into account in the reconstruction.

This method does not fall in either the pre post-reconstruction categories. The goal is to reconstruct the material-specific coefficients directly from the raw projection measurements.

We focus on the dual-source configuration of the SOMATOM scanner, with the two sources separated by 90° and each source set to a different spectrum. We also consider the LAC basis expansion model (3.11) with $N_b = 2$. The method may be extended to other scanner configurations and other LAC models.

In the MECT measurement model (2.17) the ray path L_j, which corresponds to some projection angle θ and distance r, is assumed to be the same for all the spectral weighting functions i. In the case of the dual-source scanner, at each time instance t the ray paths of source 1 have angle $\theta(t)$ and the ray paths of source 2 have angle $\theta(t) + 90°$, so the ray paths for the two sources are different. At time t the angle θ of

each source is fixed and we obtain N_r measurements from each source corresponding to the ray path distances r.

The measurement model is altered in the following way to reflect the dependency on the time and position of the sources:

$$I_{il}(t) = \int W_i(E) e^{-\int_{L_{il}(t)} \mu(\vec{x},E) dl} dE \tag{6.2}$$

where $i \in 1, 2$ is the source index, $l \in 1, ..., N_r$ is the index of the ray path distance, $I_{il}(t)$ is the measurement and $L_{il}(t)$ is the ray path.

By substituting the LAC decomposition (3.11) into the above equation, we obtain:

$$I_{il}(t) = \int W_i(E) e^{-\int_{L_{il}(t)} (a_1(\vec{x}) f_1(E) + a_2(\vec{x}) f_2(E)) dl} dE \tag{6.3}$$

$$= \int W_i(E) e^{-\left(\int_{L_{il}(t)} a_1(\vec{x}) dl\right) f_1(E) - \left(\int_{L_{il}(t)} a_2(\vec{x})) dl\right) f_2(E)} dE \tag{6.4}$$

Let $\boldsymbol{a}_1$ be a vector containing samples of $a_1(\vec{x})$ and $\boldsymbol{a}_2$ be a vector containing samples of $a_2(\vec{x})$. The line integrals of $a_1(\vec{x})$ and $a_2(\vec{x})$ can be written in vector-matrix form as follows:

$$\int_{L_{il}(t)} a_1(\vec{x}) dl = \boldsymbol{r}_{il}(t)^T \boldsymbol{a}_1 \tag{6.5}$$

$$\int_{L_{li}(t)} a_2(\vec{x}) dl = \boldsymbol{r}_{il}(t)^T \boldsymbol{a}_2 \tag{6.6}$$

where $\boldsymbol{r}_{il}(t)$ is the row of the forward projection matrix R corresponding to ray path $L_{il}(t)$.

Using (6.5) and (6.6), the measurement equation can be rewritten as follows:

$$I_{il}(t) = \int W_i(E) e^{-\boldsymbol{r}_{il}(t)^T \boldsymbol{a}_1 f_1(E) - \boldsymbol{r}_{il}(t)^T \boldsymbol{a}_2 f_2(E)} dE \tag{6.7}$$

$$= \int W_i(E) e^{-\left(\left[f_1(E)\boldsymbol{r}_{li}(t)^T \;\; f_2(E)\boldsymbol{r}_{il}(t)^T \right] \left[\begin{array}{c} \boldsymbol{a}_1 \\ \boldsymbol{a}_2 \end{array} \right] \right)} dE \tag{6.8}$$

$$= \int W_i(E) e^{-\boldsymbol{f}_{il}(t,E)^T \boldsymbol{a}} dE \tag{6.9}$$

where $\boldsymbol{f}_{il}(t,E) = \left[f_1(E)\boldsymbol{r}_{il}(t)^T \; f_2(E)\boldsymbol{r}_{il}(t)^T \right]^T$ and $\boldsymbol{a} = [\boldsymbol{a}_1^T \;\; \boldsymbol{a}_2^T]^T$. Note that the exponential is element-by-element.

Our goal is to estimate $\boldsymbol{a}$ from $I_{1l}(t)$ and $I_{2l}(t)$, $l = 1, ..., N_r$, $t = 1, ..., N_t$. This is a difficult problem since the measurement equation is nonlinear and involves an integral over energy. It has been suggested to perform tomographic reconstruction with the Kalman filter [Butala et al., 2007]. Following their ideas we apply a Kalman filer to solve the above problem. Since the problem is nonlinear, the extended Kalman filter (EKF) and iterated EKF (IEKF) can be used. IEKF has been previously used for tomographic reconstruction [George et al., 2009], but not for the multi-energy problem.

The general EKF system model is the following:

$$\begin{aligned} x(t+1) &= f(x(t),t) + G(x(t),t)w(t) \\ y(t) &= h(x(t),t) + v(t) \end{aligned} \tag{6.10}$$

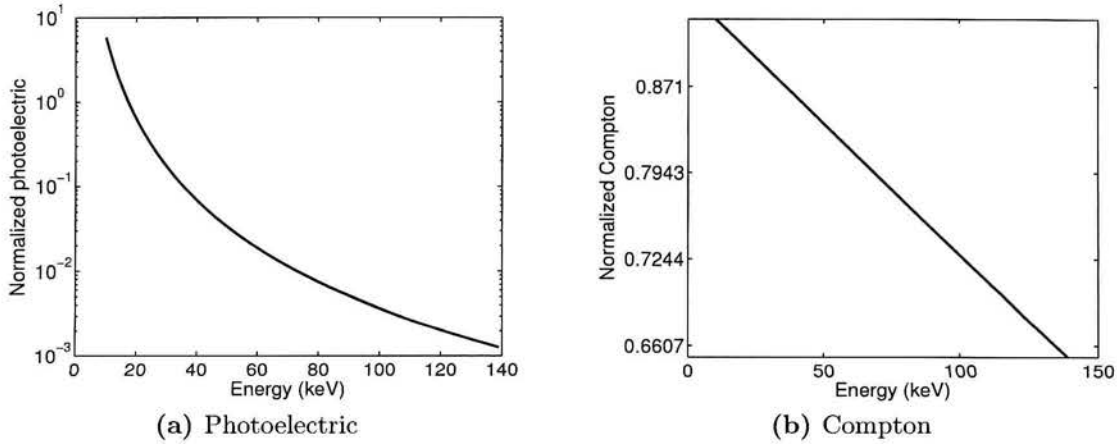
where $x(t)$ is the state, $y(t)$ is the observed measurement, $w(t)$ has covariance $Q(t)$ and $v(t)$ has covariance $R(x(t),t)$.

By comparing the EKF system model (6.10) to the measurement equation (6.9), we can say that $x(t)$ in (6.10) corresponds to $\boldsymbol{a}$, $y(t)$ corresponds to $[I_{11}(t) \; I_{12}(t) \; \cdots \; I_{21}(t) \; I_{22}(t) \cdots]^T$, $f(x(t),t)$ corresponds to $\boldsymbol{a}$, $G(x(t),t)$ corresponds

to zero and $h(x(t), t)$ corresponds to
$\left[\int W_{11}(E)e^{-\boldsymbol{f}_{11}(t,E)^T\boldsymbol{a}}dE \ \cdots \int W_{21}(E)e^{-\boldsymbol{f}_{21}(t,E)^T\boldsymbol{a}}dE \ \cdots\right]^T$.

6.2.1 Experimental results

In these experiments with simulated data we set the basis functions $f_1(E)$ and $f_2(E)$ as the photoelectric and Compton basis functions and we wish to reconstruct the photoelectric and Compton coefficients from the measurements modeled in (6.9). We created a 16×16 phantom with C4 and Honey. These materials have similar LACs. We calculated their normalized photoelectric and Compton coefficients by a least-squares fit to the normalized photoelectric and Compton basis functions shown in Figure 6·3. We generate a set of noise-free measurements according to (6.9) and (3.7) with the Siemens spectral weighting functions of 80 kVp and 140 kVp shown in Figure 2·10 and using Matlab's Radon function to create the rows of R. The sources rotated in steps of 1° around the object over a range of 180°. We added Gaussian noise to each measurement resulting in a 100 dB SNR.



(a) Photoelectric **(b)** Compton

Figure 6·3: Normalized photoelectric (left) and Compton (right) basis functions

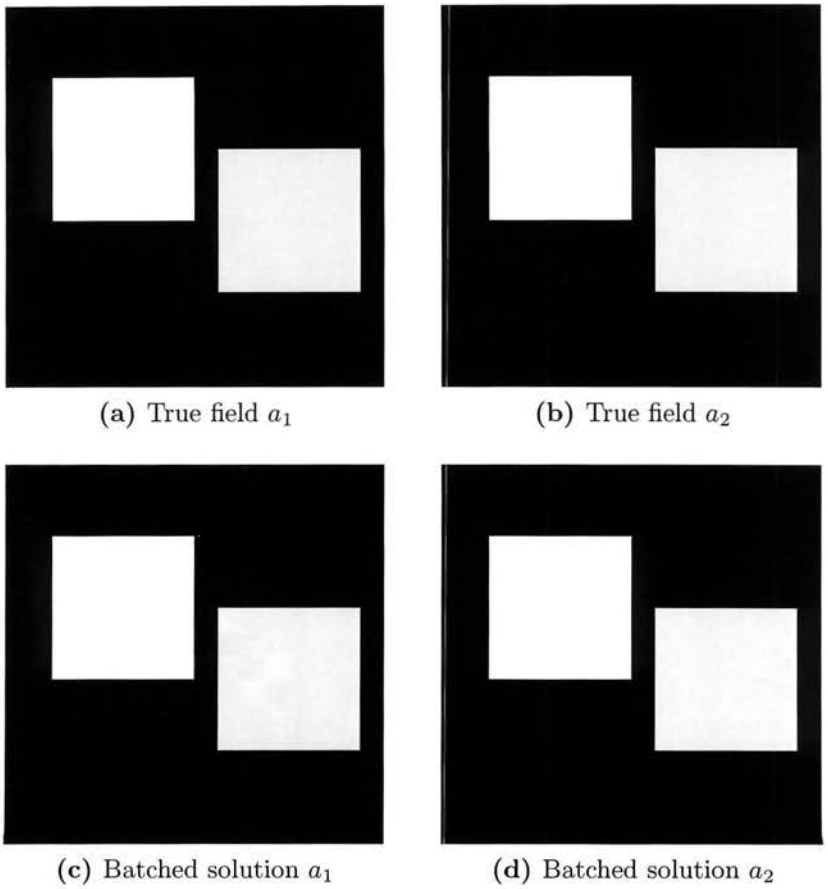
First we formulated the batched least-squares problem and solved it using the

Matlab optimization toolbox:

$$\hat{\boldsymbol{a}} = \arg\min_{\boldsymbol{a}} \left\{ (I_1^{measured} - I_1^{modeled}(\boldsymbol{a}))^2 + (I_2^{measured} - I_2^{modeled}(\boldsymbol{a}))^2 \right\} \tag{6.11}$$

where $I_i^{measured}$ is the set of measurements at all the time instances t and $I_i^{modeled}(\boldsymbol{a})$ is based on (6.9).

The true coefficient images of the phantom and the estimates given by the batched solution are shown in Figure 6·4.



(a) True field a_1 **(b)** True field a_2

(c) Batched solution a_1 **(d)** Batched solution a_2

Figure 6·4: Real images (top) and batched solution (bottom). Photoelectric coefficient images are on the left with gray-scale range [0 0.94], Compton images are on the right with gray-scale range [0 0.34].

Then we applied the IEKF to the simulated data. The filter parameters were

matched to the ones used in generating the measurements. Two different initializations were used, as described below.

In the IEKF, if we do not have a good initial guess for the state and we want the filter to ignore the initial guess, we must set the initial covariance to be extremely big. However, because of the nonlinerity in the measurement equation, the filter diverges when it is initialized by a large covariance and the initial guess is far from the true field. One way to solve this problem is by applying the filter to the same measurements several times (which corresponds to doing several full rotations of the CT scanner). In our experiments we performed 10 full rotations.

As an efficient way to initialize the algorithm with a reasonable starting point, we suggest the following method denoted "PR initialization":

1. We start with two sets of measurements obtained from the two sources. For each set of measurements, we compute the conventional reconstruction. This gives us $\bar{\mu}_1(\vec{x})$ and $\bar{\mu}_2(\vec{x})$.

2. We compute the effective energy for the two source spectra as follows:

$$\bar{E}_i = \frac{\sum_{j=1}^{N_E} E_j \cdot W_i(E_j)}{\sum_{k=1}^{N_E} W_i(E_k)} \tag{6.12}$$

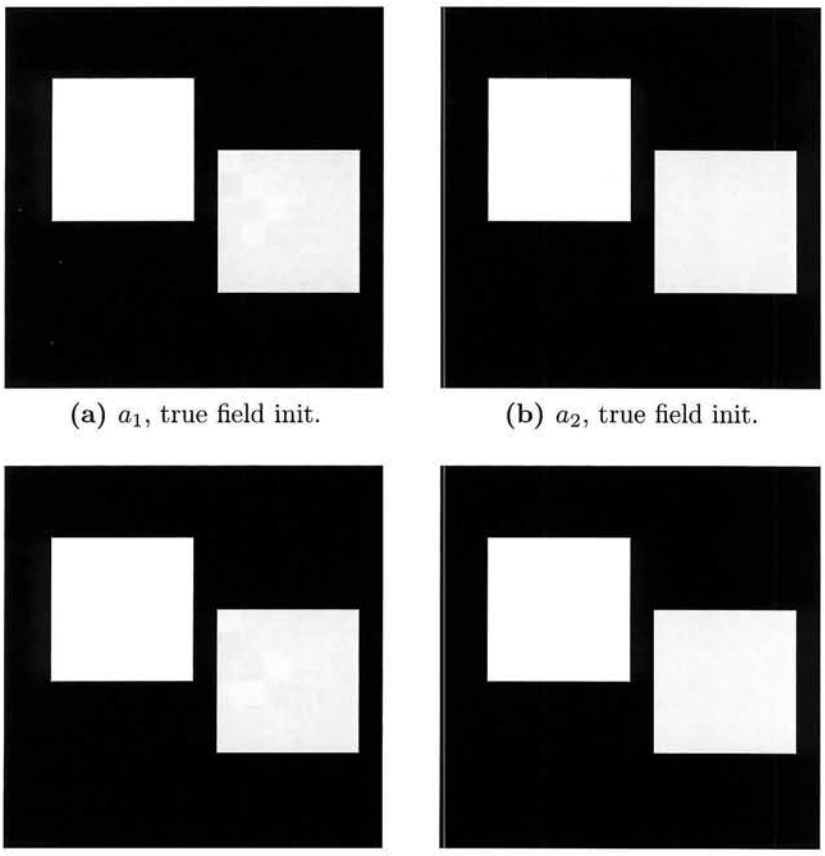
3. We assume that the measurements were taken by two monoenergetic sources with energies $\bar{E}_1$ and $\bar{E}_2$. In this case we can say that at each spatial location $\vec{x}$:

$$\begin{bmatrix} \bar{\mu}_1(\vec{x}) \\ \bar{\mu}_2(\vec{x}) \end{bmatrix} = \begin{bmatrix} f_1(\bar{E}_1) & f_2(\bar{E}_1) \\ f_1(\bar{E}_2) & f_2(\bar{E}_2) \end{bmatrix} \begin{bmatrix} a_1(\vec{x}) \\ a_2(\vec{x}) \end{bmatrix} \tag{6.13}$$

We can solve this set of equations for $a_1(\vec{x})$ and $a_2(\vec{x})$. The solution will be our initial mean. The initial covariance is set to $P = p_0 I$, where p_0 is a constant.

Figure 6·5 shows the estimates of the coefficient images obtained with the IEKF. Results are shown for initialization with the true fields and PR initialization. The

estimates with different initializations look very similar, and also look like the batched solution.



(a) a_1, true field init. **(b)** a_2, true field init.

(c) a_1, PR init. **(d)** a_2, PR init.

Figure 6·5: IEKF solutions. Top: initialization with true field. Bottom: PR initialization. Photoelectric coefficient images are on the left with gray-scale range [0 0.94], Compton images are on the right with gray-scale range [0 0.34].

We compared the PR initialization with initialization with the true field. We calculated the error at each rotation. The error was calculated as follows [Butala et al., 2009]:

$$e(t) \triangleq \frac{||\hat{\boldsymbol{x}}(t) - \boldsymbol{x}(t)||_2}{||\boldsymbol{x}(t)||_2} \tag{6.14}$$

The error curves can be seen in Figure 6·6. It can be seen that with the PR initialization, the IEKF quickly converges to the batched solution.

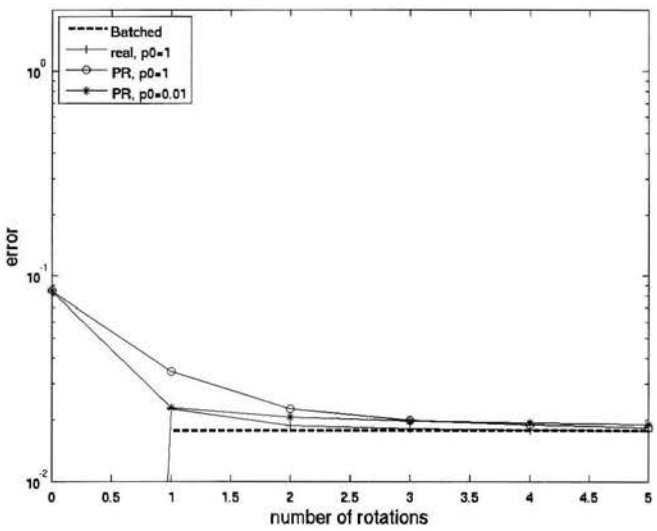


Figure 6·6: IEKF with different initializations: error vs. rotation number

6.3 Empirical dual-energy calibration with kernel smoothing

In [Stenner et al., 2007], the empirical dual-energy calibration (EDEC) method was presented, which allows decomposition into two basis material images using a calibration scan of a phantom composed of the same materials. The method was developed for medical dual-energy CT applications. The details of the method are given in Section 3.2.3. In EDEC, the nonlinear mapping of the dual-energy sinograms $\tilde{I}_1$ and $\tilde{I}_2$ to material sinograms A_1 and A_2 is done using the polynomial model (3.22). The polynomial coefficients are estimated from the calibration scan. One of the challenges of using EDEC for security, where the range of materials is much larger than in medical applications, is having enough samples of the calibration material sinograms to cover the range of values we would expect to see. Partial coverage of the measurement space would lead to inaccurate mapping under this model.

We propose a different way of mapping the dual-energy measurements to the material-specific sinograms using sample pairs of measurements and material sinograms. The method is based on kernel smoothing and we will call it K-EDEC. In K-EDEC the basis material sinograms for the calibration scan, denoted here by A_1^{cal} and A_2^{cal}, are estimated by forward projecting the material template images $t_1^{cal}(\vec{x})$ and $t_2^{cal}(\vec{x})$. The template images are derived in the same way as in EDEC, see Equation (3.24). The dual-energy sinograms of the calibration scan, $\tilde{I}_1^{cal}$ and $\tilde{I}_2^{cal}$, along with the estimated material sinograms, A_1^{cal} and A_2^{cal}, can be thought of as training data. We propose to estimate the non-linear mapping of the dual-energy measurements to the material sinograms by applying kernel smoothing based on the training data. Kernel smoothing is a more general form of mapping than the polynomial functions of EDEC, and it allows for adding additional training points from other calibration scans and also simulated data. This method can potentially improve the accuracy of the mapping.

Let the dual-energy measurements of a test scan be denoted as $\tilde{I}_1$ and $\tilde{I}_2$. The material-specific sinograms for the test scan, A_1 and A_2, may be estimated by:

$$A_{ij} = \frac{\sum_{l=1}^{N_s} K\left(\tilde{I}_{1j}, \tilde{I}_{2j}\tilde{I}_{1l}^{cal}, \tilde{I}_{2l}^{cal}\right) A_{il}^{cal}}{\sum_{l=1}^{N_s} K\left(\tilde{I}_{1j}, \tilde{I}_{2j}\tilde{I}_{1l}^{cal}, \tilde{I}_{2l}^{cal}\right)} \tag{6.15}$$

where j is the sinogram point index, N_s is the total number of sinogram points and $K\left(\tilde{I}_{1j}, \tilde{I}_{2j}\tilde{I}_{1l}^{cal}, \tilde{I}_{2l}^{cal}\right)$ is a kernel function.

A common choice for the kernel function, and the one we will use, is the radial basis function (RBF) kernel with parameter σ:

$$K\left(x_1, x_2, y_1, y_2\right) = e^{\frac{-\left((x_1-y_1)^2+(x_2-y_2)^2\right)}{2\sigma}} \tag{6.16}$$

Once the material sinograms of the test scan, A_1 and A_2, are estimated, the material coefficient images $a_1(\vec{x})$ and $a_2(\vec{x})$ are reconstructed from them by applying standard FBP.

As mentioned before, the training data, $\tilde{I}_1^{cal}$, $\tilde{I}_2^{cal}$, A_1^{cal} and A_2^{cal}, used in the kernel smoothing (6.15) does not have to be limited to the data obtained from the calibration scan. Synthetic simulated data may be added or even replace the calibration scan data. We define the following three ways of collecting training data:

1. K-EDEC(C): data from the calibration scan only

2. K-EDEC(C+S): data from the calibration scan and other synthetic data

3. K-EDEC(S): synthetic data only

The variations using simulated data, K-EDEC(C+S) and K-EDEC(S), require knowledge of the system spectra and the LACs of the basis-materials. The EDEC and K-EDEC(C) methods do not require that knowledge. If the system spectra

and the LACs are known then another way we consider of mapping the dual-energy data to material-sinograms is via the sinogram least squares (SLS) formulation in Equation (3.15), where the solution is obtained using a nonlinear solver.

6.4 Experimental results

6.4.1 Experiments with simulated data

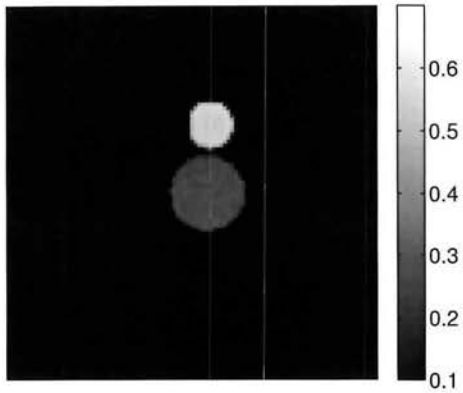
To compare the performance of EDEC and K-EDEC using ground truth information, we performed the following experiment with simulated data. We consider specifically K-EDEC(C) since we want to compare the performance when the same calibration data is available to both methods.

We created a calibration phantom composed of graphite and aluminum, and a test phantom composed of graphite, aluminum and plastic. The phantoms were 101×101 pixels. We simulated dual-energy measurements of the phantoms according to the Poisson measurement model (values of I_i in Equation (3.6) were set as the mean of a Poisson random variable). The forward projection operator R was generated using Matlab's 'radon' function with rays at angles $\theta = 0, 1, ..., 179°$, and 145 rays per projection. The matrix F contains the LACs of the two basis materials. For the spectral weighting functions we used the Imatron scanner 95 and 130 kVp spectra shown in Figure B·1b. We normalized the spectra to sum to 1 and multiplied them by 10^{20}, which corresponds to almost no noise.

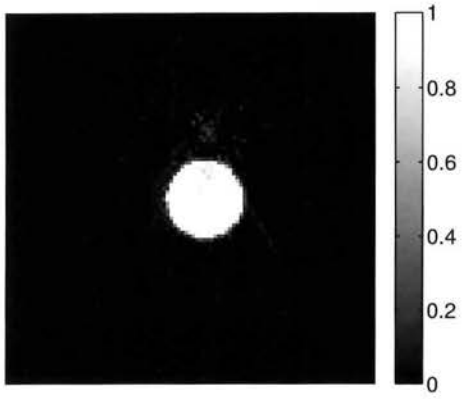
We applied EDEC and K-EDEC(C) to the simulated measurements. In EDEC we used $S = T = 4$ as in [Stenner et al., 2007], which provides 25 sinogram basis functions $b_n(\tilde{I}_1, \tilde{I}_2)$. In K-EDEC(C) we selected the kernel width, σ, using a cross-validation loop on the calibration data. The selected value was $\sigma = 0.0489$.

The decomposition of the calibration phantom is shown in Figure 6·7 and the decomposition of the test phantom is shown in Figure 6·8. On the top we show the

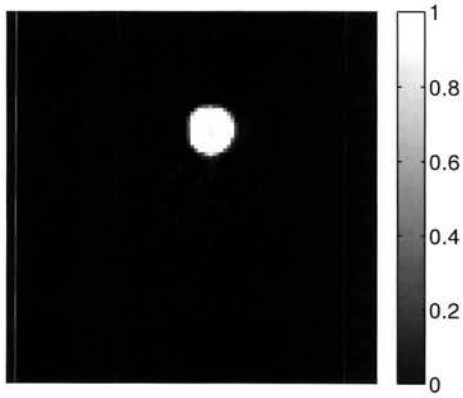
standard FBP reconstructed image $\bar{\mu}_2(\vec{x})$ obtained with the high energy spectrum of 130 kVp. The objects in these images look homogeneous and no significant artifacts are visible. This is due to the relatively low noise level in the measurements. The middle row in the figures show the results with EDEC and the bottom row shows the results with K-EDEC(C). It can be seen that EDEC and K-EDEC(C) produce very similar results. Both methods perform well on the calibration phantom. The graphite image of the test phantom is more noisy for K-EDEC(C) than EDEC. Overall the methods show comparable performance, so K-EDEC(C) can potentially be used as an alternative to EDEC.



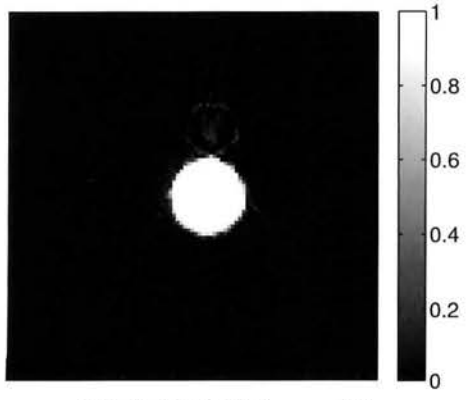
(a) 130 kVp reconstructed image



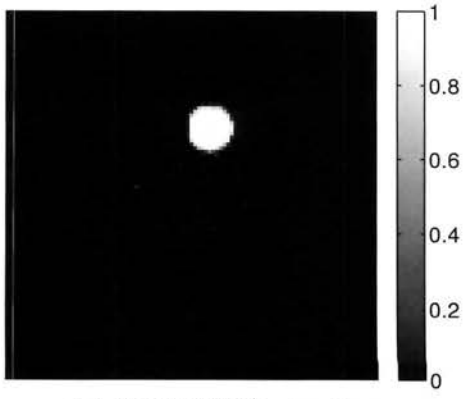
(b) EDEC: graphite



(c) EDEC: aluminum

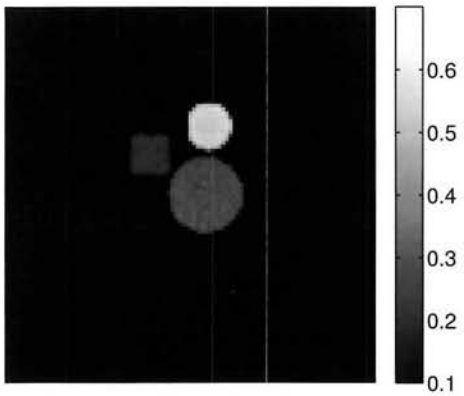


(d) K-EDEC(C): graphite

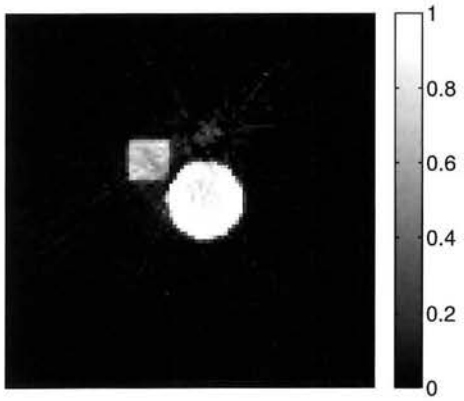


(e) K-EDEC(C): aluminum

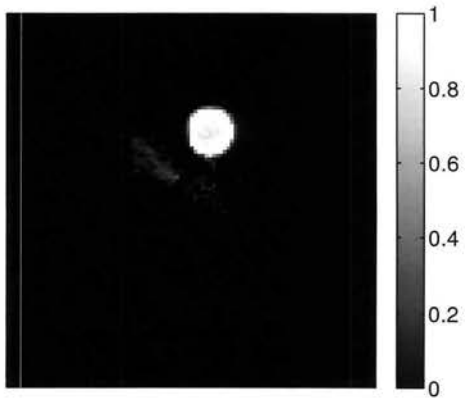
Figure 6·7: EDEC and K-EDEC(C) simulation results for the calibration scan containing graphite (bottom rod) and aluminum (top rod). Top: FBP reconstructed image from 130 kVp measurements. Middle: basis material images obtained with EDEC. Bottom: basis material images obtained with K-EDEC(C).



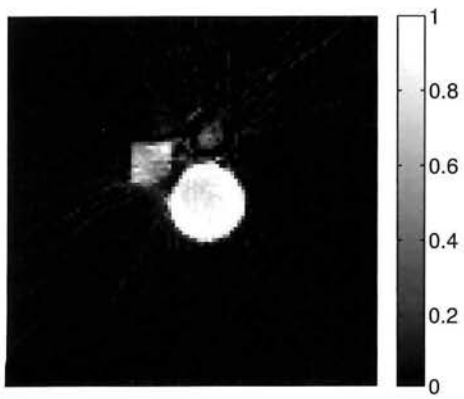
(a) 130 kVp reconstructed image



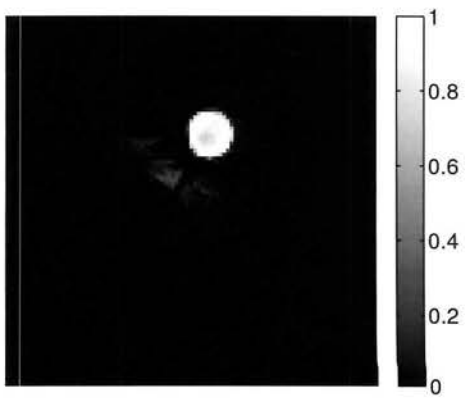
(b) EDEC: graphite



(c) EDEC: aluminum



(d) K-EDEC(C): graphite



(e) K-EDEC(C): aluminum

Figure 6·8: EDEC and K-EDEC(C) simulation results for the test scan containing graphite (bottom rod), aluminum (top rod) and plastic (square). Top: FBP reconstructed image from 130 kVp measurements. Middle: basis material images obtained with EDEC. Bottom: basis material images obtained with K-EDEC(C).

6.4.2 Experiments with real data

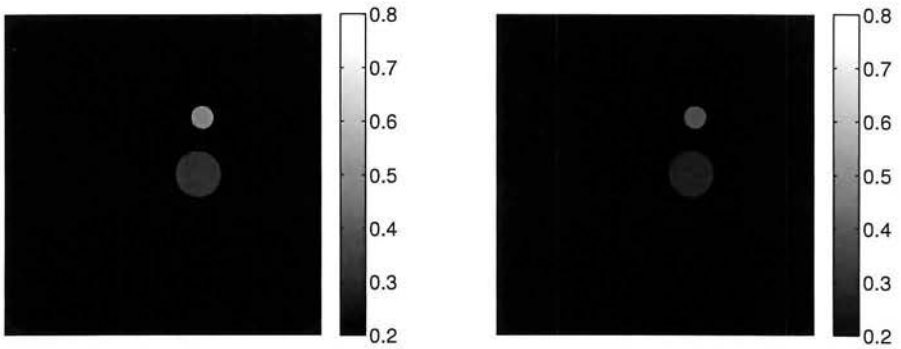
We tested the EDEC and K-EDEC methods on the Imatron scans database described in Appendix B. The database includes dual-energy scans of different objects obtained with a 95 kVp and 130 kVp source spectra.

Based on the analysis in Secion 3.5.3 and the materials we were able to obtain in practice, we chose two pairs of calibration materials - graphite and magnesium and graphite and aluminum. One calibration phantom was created with graphite and magnesium rods and another calibration phantom was created with graphite and aluminum rods. The rods in the first phantom were smaller than the rods in the second phantom. The effective attenuation images $\bar{\mu}_1(\vec{x})$ and $\bar{\mu}_2(\vec{x})$ of the calibration phantoms are shown in Figure 6·9.

We implemented K-EDEC(C), K-EDEC(C+S) and K-EDEC(S). We generated the synthetic data by simulating noise-free measurements according to Equation (3.6). The spectral weighting functions were the Imatron functions shown in Figure B·1b. We used the Imatron forward projection operator as R. The matrix F contained the LACs of the two basis materials. The kernel parameter σ in K-EDEC was found using cross validation of the calibration data. For the graphite and magnesium calibration it was 0.0043 and for the graphite and aluminum calibration it was 0.0089.

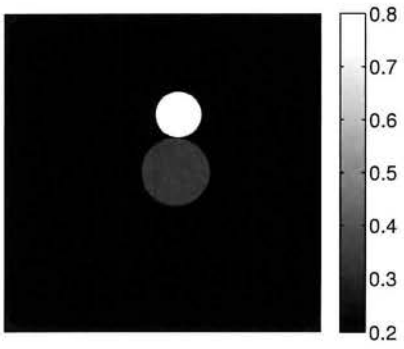
We also applied the SLS method to compare with EDEC and K-EDEC. SLS is based on solving the least-squares problem (3.15). We used Matlab's 'lsqnonlin' function to solve for the basis-material sinograms and then applied FBP to obtain the basis-material images.

Figures 6·10-6·14 show the results with EDEC, K-EDEC(C), K-EDEC(C+S), K-EDEC(S) and SLS for a slice of a water bottle. The graphite and magnesium calibration phantom was used. Each figure shows the reconstructed basis-material images as well as an estimate of the LAC at 60 keV obtained by linearly combining the

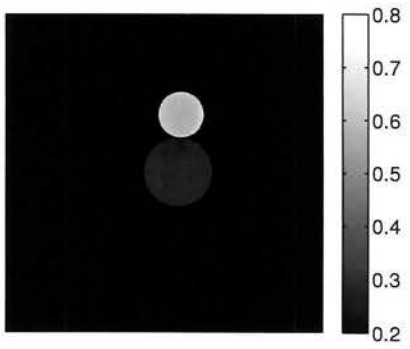


(a) 95 kVp: graph. and mag.

(b) 130 kVp: graph. and mag.



(c) 95 kVp: graph. and alu.



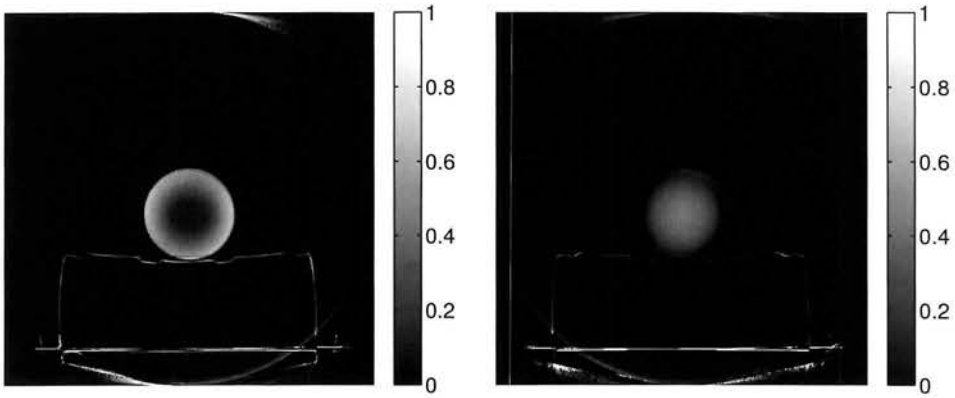
(d) 130 kVp: graph. and alu.

Figure 6·9: FBP reconstructions of a slice of the calibration phantom from 95 and 130 kVp measurements. Top: graphite and magnesium phantom. Bottom: graphite and aluminum phantom. The units are cm^{-1}.

basis-material images using the LACs of graphite and magnesium. It can be seen that K-EDEC(C) generates artifacts inside the water region. In EDEC the graphite and magnesium images are not homogeneous throughout the water region but the resulting LAC at 60 kEV is relatively homogeneous. The same can be seen in the K-EDEC(C+S) results. K-EDEC(S) and SLS provide similar results. In both methods the material images are relatively homogeneous, as well as the LAC at 60 keV.

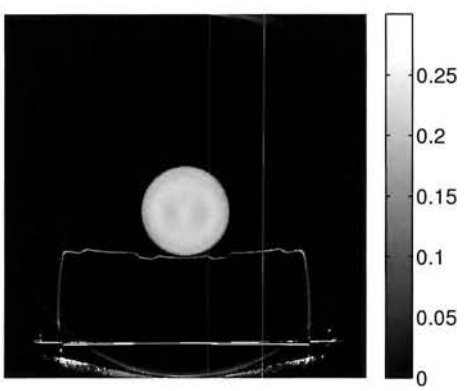
Figure 6·15 shows the results with EDEC on the same water bottle slice, but using the graphite and aluminum calibration phantom. Compared to Figure 6·10, the basis-material images are more homogeneous. This may be due to the fact that

the rods in the graphite and aluminum calibration scan were larger than the rods in the graphite and magnesium scan (see Figure 6·9). Larger calibration objects provide a larger span of measurements and may lead to more accurate mapping from the measurements to basis-material sinogram.



(a) graphite image

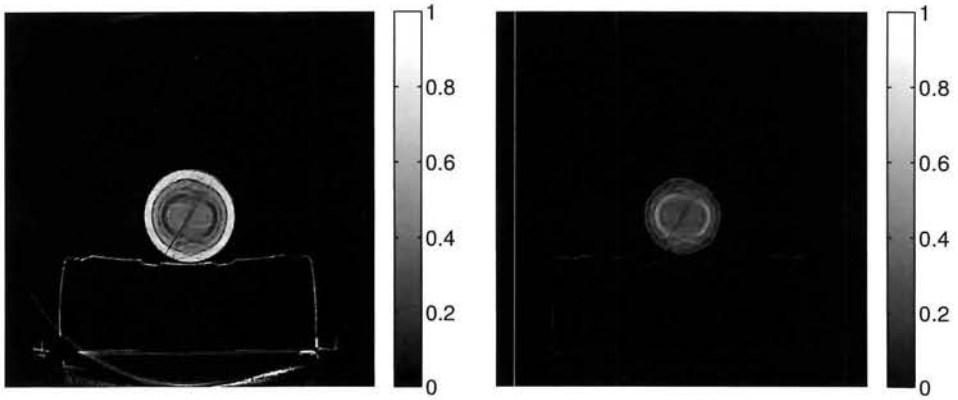
(b) magnesium image



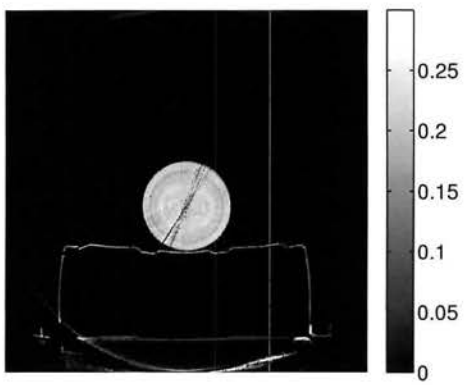
(c) LAC at 60 keV

Figure 6·10: EDEC results for a water scan using graphite and magnesium calibration. Top left: graphite image. Top right: magnesium image. Bottom: estimated LAC at 60 keV in units of cm^{-1}.

When the system spectra and basis material LACs are not known, both EDEC and K-EDEC(C) may be used. The results suggest that the performance of both methods is highly affected by the calibration phantom design and choice of calibration materials. In the security domain, the scans have very high clutter and may include



(a) graphite image (b) magnesium image



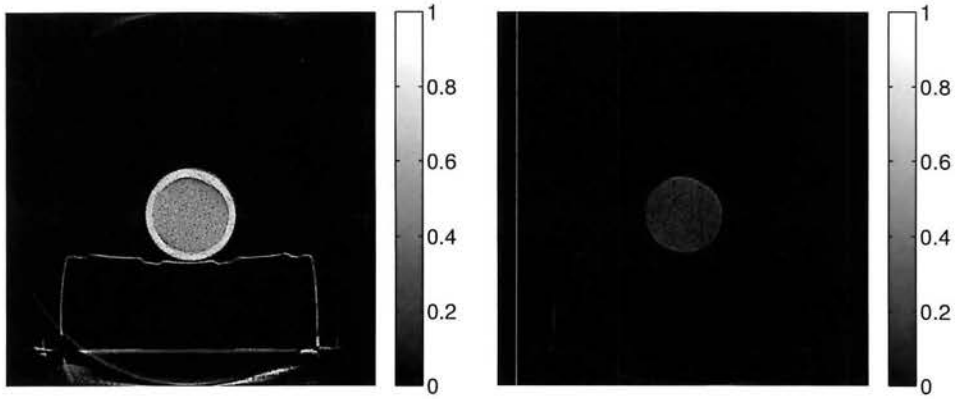
(c) LAC at 60 keV

Figure 6·11: K-EDEC(C) results for a water scan using graphite and magnesium calibration. Top left: graphite image. Top right: magnesium image. Bottom: estimated LAC at 60 keV in units of cm^{-1}.

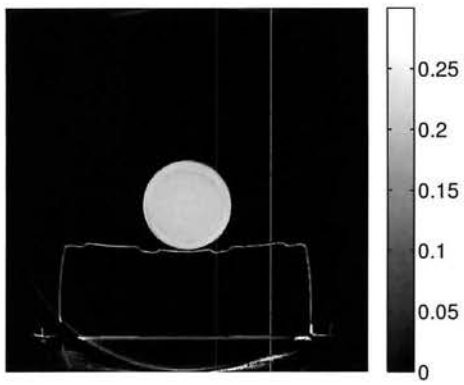
dense materials. Creating a good calibration phantom for security is very challenging because the calibration phantom measurements should be able to span the space of all possible measurements. Therefore, the use of these methods in security may not be appropriate.

We saw that K-EDEC(C) does not improve the material coefficient estimates compared to EDEC. Perhaps the performance of K-EDEC(C) may be enhanced by using different choices of kernel functions.

When the system spectra and basis material LACs are known, the results show



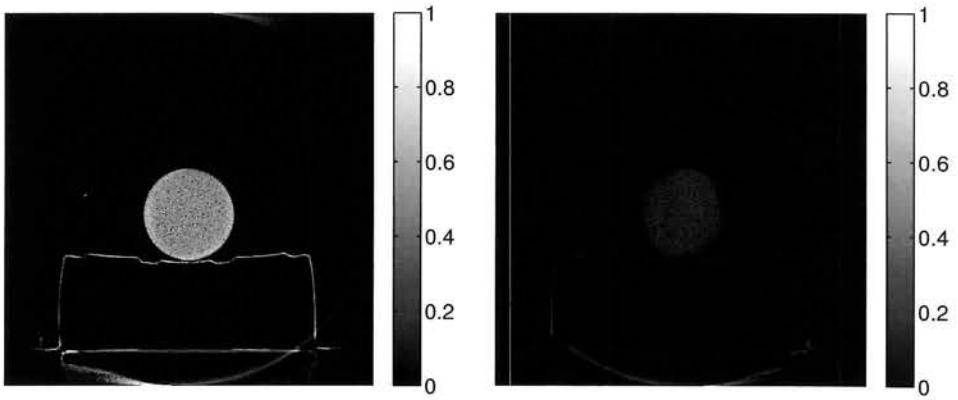
(a) graphite image (b) magnesium image



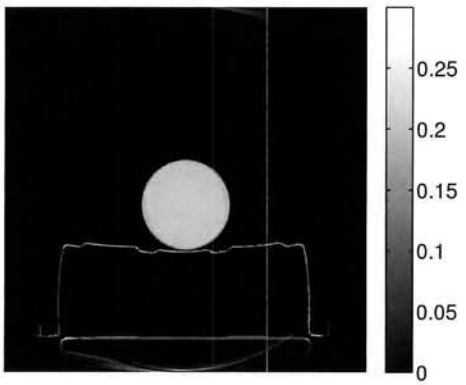
(c) LAC at 60 keV

Figure 6·12: K-EDEC(C+S) results for a water scan using graphite and magnesium calibration. Top left: graphite image. Top right: magnesium image. Bottom: estimated LAC at 60 keV in units of cm^{-1}.

that better estimates may be obtained using K-EDEC(C+S), K-EDEC(S) and SLS, with SLS showing the best performance. The synthetic calibration data helps to compensate for the limited data from the calibration scan.

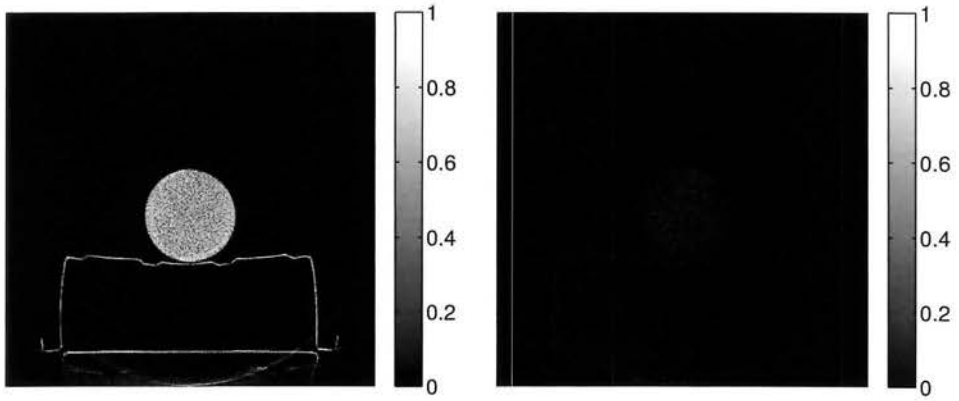


(a) graphite image **(b)** magnesium image

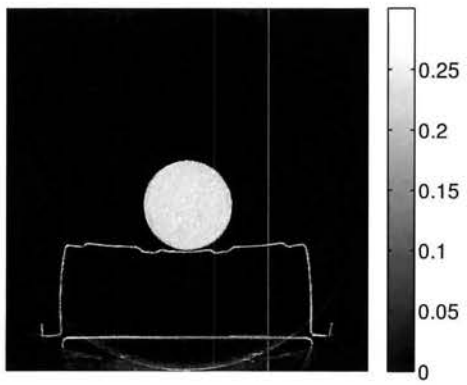


(c) LAC at 60 keV

Figure 6·13: K-EDEC(S) results for a water scan using graphite and magnesium calibration. Top left: graphite image. Top right: magnesium image. Bottom: estimated LAC at 60 keV in units of cm^{-1}.

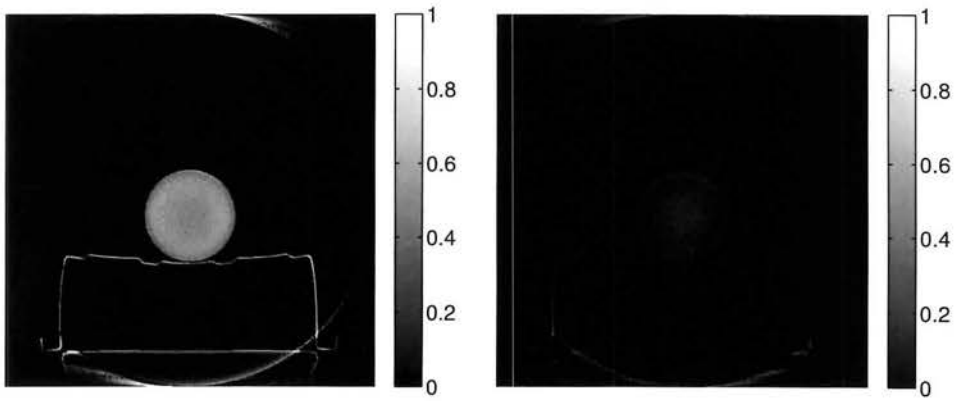


(a) graphite image (b) magnesium image



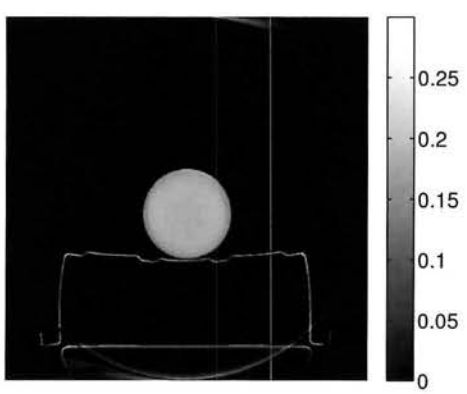
(c) LAC at 60 keV

Figure 6·14: SLS results for a water scan using graphite and magnesium calibration. Top left: graphite image. Top right: magnesium image. Bottom: estimated LAC at 60 keV in units of cm^{-1}.



(a) graphite image

(b) aluminum image



(c) LAC at 60 keV

Figure 6·15: EDEC results for a water scan using graphite and aluminum calibration. Top left: graphite image. Top right: magnesium image. Bottom: estimated LAC at 60 keV in units of cm^{-1}.

6.5 Structure-preserving MECT inversion

In this section we present a new model-based MECT inversion method for security, which provides estimates of material-dependent basis coefficient images. In the security application many different materials may be scanned in various degrees of clutter and metal objects are common. Image noise and metal artifacts are more severe and can lead to less reliable estimates of the material parameters from MECT measurements compared to the medical field. Therefore, a rigorous inversion technique is required.

Our aim is improving the image inversion step in pre-reconstruction MECT methods, described in Section 3.2. In current methods the inversion is usually performed by applying FBP to each coefficient sinogram individually. Since the different coefficient images are of the same scene, the boundaries in the images should be the same. We propose a framework which uses the mutual boundary field information and jointly inverts the coefficient images. This approach helps to preserve the uniformity of homogeneous object regions and the connectivity of object boundaries.

When X-rays travel through dense materials and metal, which are common in baggage, they are substantially attenuated and the resulting measured intensity may be lower than the detector noise level. In the tomographic inversion process these unreliable measurements can lead to streaks and artifacts in the reconstructed image. In single-energy CT data weighting has been used as a way to de-emphasize the contribution of the unreliable measurements to the overall solution [Kisner et al., 2013]. We incorporate a version of this approach in our MECT inversion.

We focus on dual-energy measurements and the Photo-Compton LAC decomposition model (3.11) although this work may be extended to more than two energies and to other decomposition models. Given the basis coefficient sinograms the goal is to generate basis coefficient images with reduced noise and artifacts for high-cluttered

luggage scans. We form the images as the solution of a unified optimization problem which explicitly models the physical tomographic projection process. The basis coefficient sinograms are inverted jointly. Metal induced streaking is reduced by appropriately down-weighting unreliable data. A boundary-preserving prior based on [Mumford and Shah, 1989] is incorporated to improve object localization. In particular, we estimate a mutual boundary-field along with the photoelectric and Compton coefficient images. The boundary field provides accurate object localization and allows smoothing inside the objects.

We consider the discretized MECT problem (3.6), where the samples of the basis coefficient images are contained in $\boldsymbol{a}_1$ and $\boldsymbol{a}_2$, each of size $N_p \times 1$. We assume that the sinograms A_1 and A_2 of dimensions $N_d \times 1$ have been estimated from the dual-energy measurements I_1 and I_2 using least squares (3.15) or other methods, and are given as the input to our method. We assume that I_1 was measured with the lower energy spectrum. We also consider specifically the photoelectric and Compton basis functions for the model of the LAC.

We formulate the problem of estimating $\boldsymbol{a}_1$, $\boldsymbol{a}_2$, and the mutual boundary field $\boldsymbol{s}$ shared by $\boldsymbol{a}_1$ and $\boldsymbol{a}_2$ as an optimization problem where the following energy is minimized:

$$\begin{aligned} \underset{(\boldsymbol{a}_1,\boldsymbol{a}_2,\boldsymbol{s})}{\text{minimize}} \quad & \Big\{ ||A_1 - R\boldsymbol{a}_1||^2_{W_m} + ||A_2 - R\boldsymbol{a}_2||^2_{W_m} + \lambda_1^2||D\boldsymbol{a}_1||^2_{W_s} + \lambda_2^2||D\boldsymbol{a}_2||^2_{W_s} \\ & + \lambda_3^2||\boldsymbol{a}_1||_2^2 + \lambda_4^2||\boldsymbol{a}_2||_2^2 + \lambda_5^2||D\boldsymbol{s}||_2^2 + \lambda_6^2||\boldsymbol{s}||_2^2 \Big\} \qquad (6.17) \\ \text{subject to} \quad & \boldsymbol{a}_1, \boldsymbol{a}_2 \geq 0 \end{aligned}$$

where λ_i, $i = 1, ..., 6$, are non-negative regularization parameters, W_m is a data weighting matrix, $W_s = \text{diag}((1 - \boldsymbol{s})^2)$ (the square is element-wise), R is the tomographic system forward projection operator, and D is a derivative operator. The

weighted norm is defined as $||v||_M^2 = v^T M v$.

The individual components in (6.17) contribute to the overall solution as follows:

1. $||A_k - R\boldsymbol{a}_k||_{W_m}$ is a data term that captures the fidelity to the observed basis coefficient sinograms.

2. $||\boldsymbol{a}_k||_2$ and $||D\boldsymbol{a}_k||_{W_s}$ serve to regularize the inversion. Our experience is that the inclusion of both these terms leads to better reconstruction than including just one of them.

3. $||\boldsymbol{s}||_2$ and $||D\boldsymbol{s}||_2$ serve to stabilize the boundary field.

In the formulation (6.17) the tomographic forward projection operator R is explicitly used. In addition, as we explain next, the sinogram data are weighted through W_m. Also, explicit use is made of an object boundary field $\boldsymbol{s}$. We call the overall method structure-preserving dual-energy (SPDE).

6.5.1 Data weighting W_m

In the presence of metal and high clutter some rays are significantly attenuated and the measured values for these rays are very small. Since not many photons go through, these data points are less reliable. We apply explicit data weighting to account for this phenomenon.

To generate W_m we use the high-energy sinogram $\tilde{I}_2$, which are the measurements I_2 transformed to the normalized negative-log space (2.23). The weighting matrix W_m is given by

$$\text{diag}(W_m) = \frac{c}{\tilde{I}_2^2 + c} \tag{6.18}$$

where c is a constant. This weighting reduces the contribution of the unreliable rays which go through dense metal objects. The weighting is based on the high-energy

sinogram because it is more reliable. An example of the function with $c = 5$ is shown in Figure 6·16.

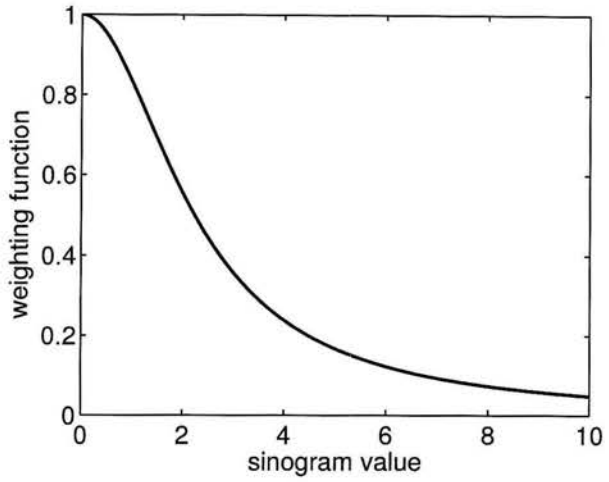


Figure 6·16: Data weighting function (6.18) with $c = 5$

6.5.2 Solution approach

The cost function in (6.17) depends on three coupled variables - $\boldsymbol{a}_1$, $\boldsymbol{a}_2$, and $\boldsymbol{s}$ - and the resulting optimization problem is non-quadratic. In the absence of the non-negativity constraint, the following equations must hold at the optimum, where the derivative of the cost function is zero:

$$(R^T W_z R + \lambda_1^2 D^T W_s D + \lambda_3^2)\boldsymbol{a}_1 = R^T W_z A_1 \tag{6.19}$$

$$(R^T W_z R + \lambda_2^2 D^T W_s D + \lambda_4^2)\boldsymbol{a}_2 = R^T W_z A_2 \tag{6.20}$$

$$(B + \lambda_5^2 D^T D)\boldsymbol{s} = Bu \tag{6.21}$$

where B is diagonal, $B_{jj} = \lambda_1^2[D\boldsymbol{a}_1]_j^2 + \lambda_2^2[D\boldsymbol{a}_2]_j^2 + \lambda_6^2$, and u is defined by

$$u_j = \frac{\lambda_1^2[D\boldsymbol{a}_1]_j^2 + \lambda_2^2[D\boldsymbol{a}_2]_j^2}{\lambda_1^2[D\boldsymbol{a}_1]_j^2 + \lambda_2^2[D\boldsymbol{a}_2]_j^2 + \lambda_6^2}$$

We iteratively solve (6.19) and (6.20) for $\boldsymbol{a}_1$ and $\boldsymbol{a}_2$ while keeping $\boldsymbol{s}$ fixed, and solve (6.21) for $\boldsymbol{s}$ while keeping $\boldsymbol{a}_1$ and $\boldsymbol{a}_2$ fixed.

We enforce the non-negativity constraint in (6.17) by projecting the solution of (6.19) and (6.20) onto the constraint set at every iteration. This is not the optimal non-negative solution however we used this solution due to large problem size.

6.5.3 Practical implementation

Since problem (6.17) is non-quadratic, an effective initialization scheme is needed. To avoid local minima and guide the solution to a globally acceptable answer, we first solve (6.17) with one set of regularization parameters giving more emphasis to the Compton terms. This approach exploits the fact that the Compton sinogram is more informative on object structure than the photoelectric sinogram. In this manner we obtain a more reliable boundary field $\boldsymbol{s}$ early on. Then we switch to another set of parameters which give equal weights to the photoelectric and Compton terms. This allows the boundary field we obtained to control smoothing in both the photoelectric and Compton images. The exact details of the implementation will be given in Section 6.5.4.

6.5.4 Experimental results

Experimental setup

We tested our method on the Imatron scans database, described in Appendix B. These are dual-energy scans of different objects in bags obtained with a 95 kVp and 130 kVp source spectra. The photoelectric and Compton sinograms were estimated from the dual-energy measurements using Matlab's 'lsqnonlin' least-square function and Equation (3.5). As a baseline method we applied the Imatron FBP inversion algorithm to the photoelectric and Compton sinograms individually. We used code provided by Dr. Patrick La Riviere from Univeristy of Chicago, which is based on

the Imatron inversion software. In results to follow we label this method FBP.

The data weighting parameter c in (6.18) was set to 5. This choice is based on the sinogram values of rays going through metal (around 6-8). This gives the weighting function shown in Figure 6·16.

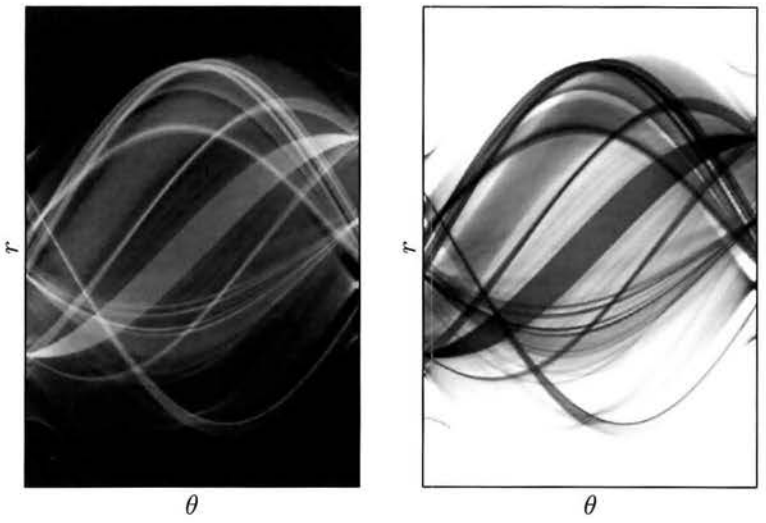
Finding the regularization parameters λ_i in (6.17) was a difficult task, mainly due to the large problem size. As explained in Section 6.5.3, we begin the iterations with one set of regularization parameters and then switch to another set. The first set of regularization parameters we used was: $\lambda_1 = 0, \lambda_2 = 3, \lambda_3 = 0, \lambda_4 = 0, \lambda_5 = 0.1, \lambda_6 = 0.1$. With this set the boundary field is derived only from the Compton image and a relatively large weight ($\lambda_2 = 3$) is given to the Compton smoothing term. This allows to obtain a reliable estimate of the boundary field, however with this set the inversion of the photoelectric image is not regularized at all and the Compton image is over smoothed. The second set of regularization parameters was: $\lambda_1 = 2, \lambda_2 = 2, \lambda_3 = 2, \lambda_4 = 0, \lambda_5 = 0.1, \lambda_6 = 0.1$. The iterations with this set start with the boundary field estimate obtained with the first set. The second set provides more moderate smoothing of the Compton image and also applies smoothing to the photoelectric image based on the estimated boundary field. The number of iterations was chosen empirically. A total of ten iterations were performed, five with the first set of parameters and 5 with the second set.

Reconstruction results

We consider three example slices from the Imatron scans. The slices contain metal and have different degrees of clutter. Slice 1 has a bottle of water in between magnesium and silicon rods. In slice 2 there is a bottle of water and a thin rubber sheet. In slice 3 there is a Teflon cube, a bottle of water and a stack of rubber sheets.

In Figure 6·17 we show the data weights applied in the reconstruction of example slice 2. The high energy sinogram is shown on the left and the corresponding data

weights are shown on the right. The weights were calculated according to Equation 6.18. The high values in the sinogram, which correspond to rays going through metal and dense objects, are mapped to low weights.

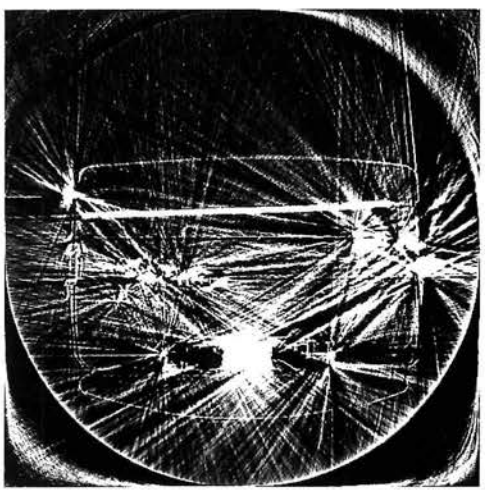


(a) Sinogram (b) Data weights

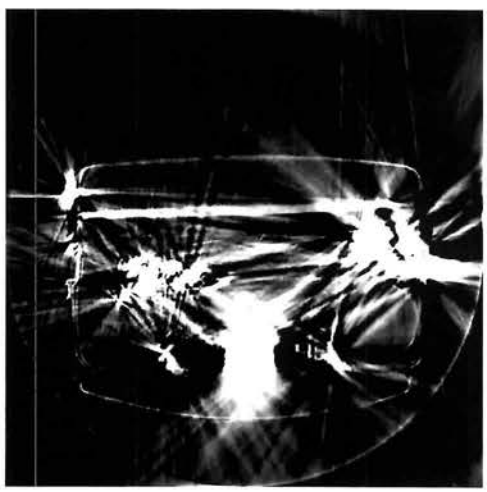
Figure 6·17: Data weights for example slice 2. The high energy sinogram is shown on the left and the corresponding data weights are shown on the right. Low weights are given to less reliable high sinogram values.

Figure 6·18 shows the first photoelectric and Compton image estimates, obtained after the iterations with the first set of regularization parameters, and the final photoelectric and Compton image estimates obtained after the iterations with the second set of regularization parameters for example slice 2. The first estimate of the photoelectric image is much more noisy and has many streaks compared to the final photoelectric estimate. The first estimate of the Compton image is much smoother than the final Compton estimate and the details of the objects in the bags are less clear. Figure 6·19 shows the corresponding boundary field estimates. The first boundary field is controlled only by the Compton coefficient, which is more stable, and therefore it is clearer and less noisy than the second.

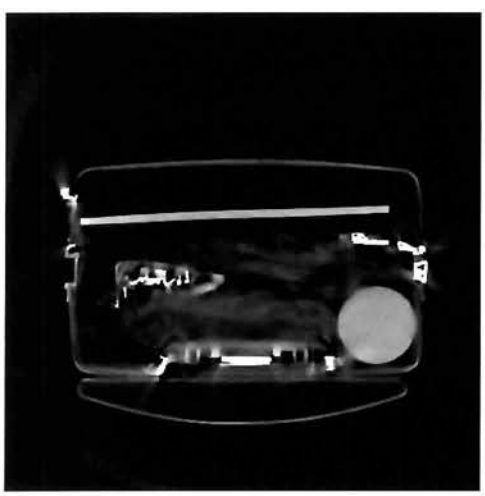
Figure 6·20 shows the final estimates of the photoelectric and Compton coefficient



(a) Photoelectric: first estimate



(b) Photoelectric: final estimate

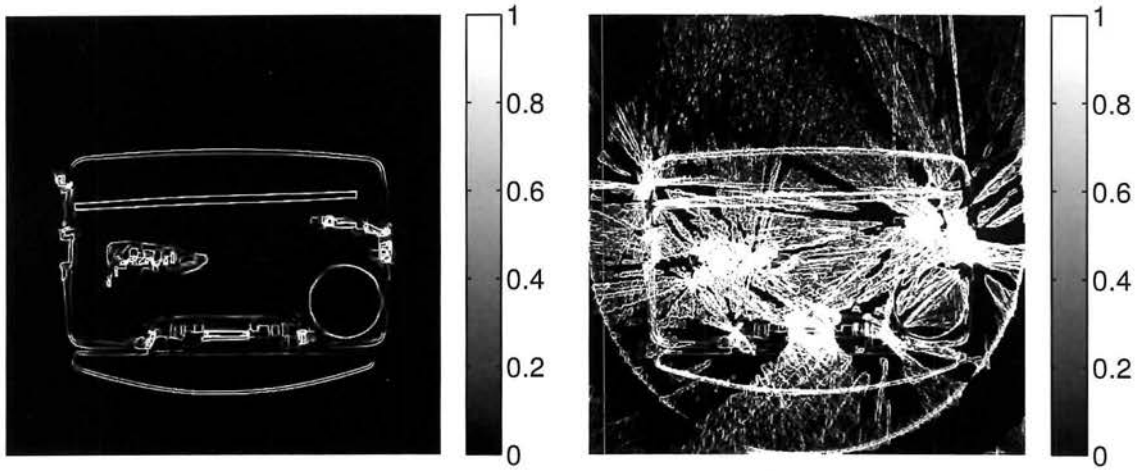


(c) Compton: first estimate



(d) Compton: final estimate

Figure 6·18: Estimated photoelectric (top) and Compton (bottom) coefficient images given by SPDE for example slice 2. Left: images obtained after the iterations with the first set of regularization parameters. Right: images obtained after the iterations with the second set of regularization parameters.The photoelectric image is in units of keV^3 and gray scale range [1000, 10000]. The Compton image is in units of cm^{-1} and gray scale range [0, 0.3].



(a) First boundary field (b) Final boundary field

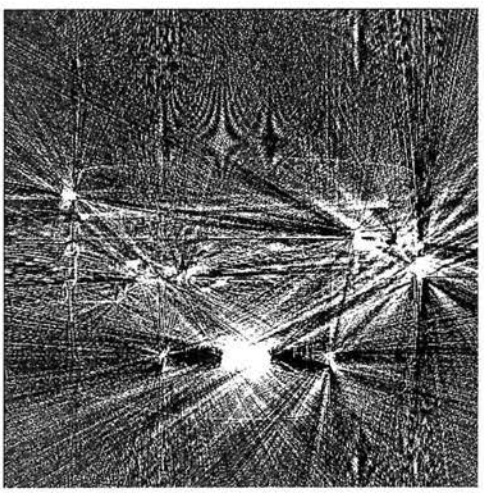
Figure 6·19: Estimated boundary field given by SPDE for example slice 2. Left: boundary field obtained after the iterations with the first set of regularization parameters. Right: final boundary field obtained after the iterations with the second set of regularization parameters.

images obtained with SPDE and the results obtained with FBP for example slice 2. It can be seen that the streaks in the water bottle on the bottom right and in the sheet on the top in the Compton image are reduced in the SPDE result compared to FBP. Overall the SPDE results have less noise compared to FBP.

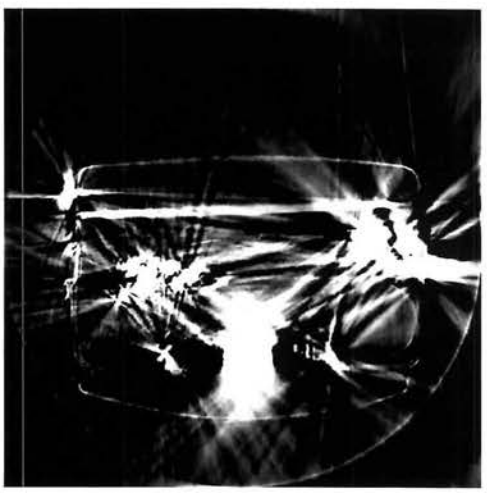
Figure 6·21 shows the estimates of the photoelectric and Compton coefficient images obtained with FBP and SPDE for example slice 1. The SPDE photoelectric image is less noisy than the FBP image but some artifacts in the water bottle are noticeable. The SPDE and FBP Compton images are comparable.

Figure 6·22 shows the estimates of the photoelectric and Compton coefficient images obtained with FBP and SPDE for example slice 3. In the SPDE Compton estimate the thick black streak appearing in the bottom of the Teflon cube is much less visible than in the FBP result.

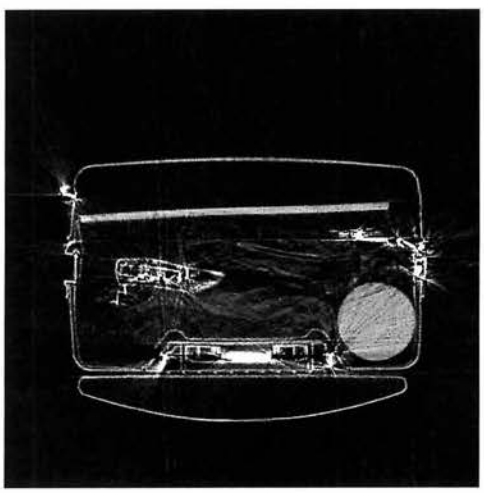
Overall, the figures demonstrate that SPDE significantly reduces noise and improves object localization. Reduction in metal artifacts is especially noticeable in the



(a) FBP: photoelectric



(b) SPDE: photoelectric

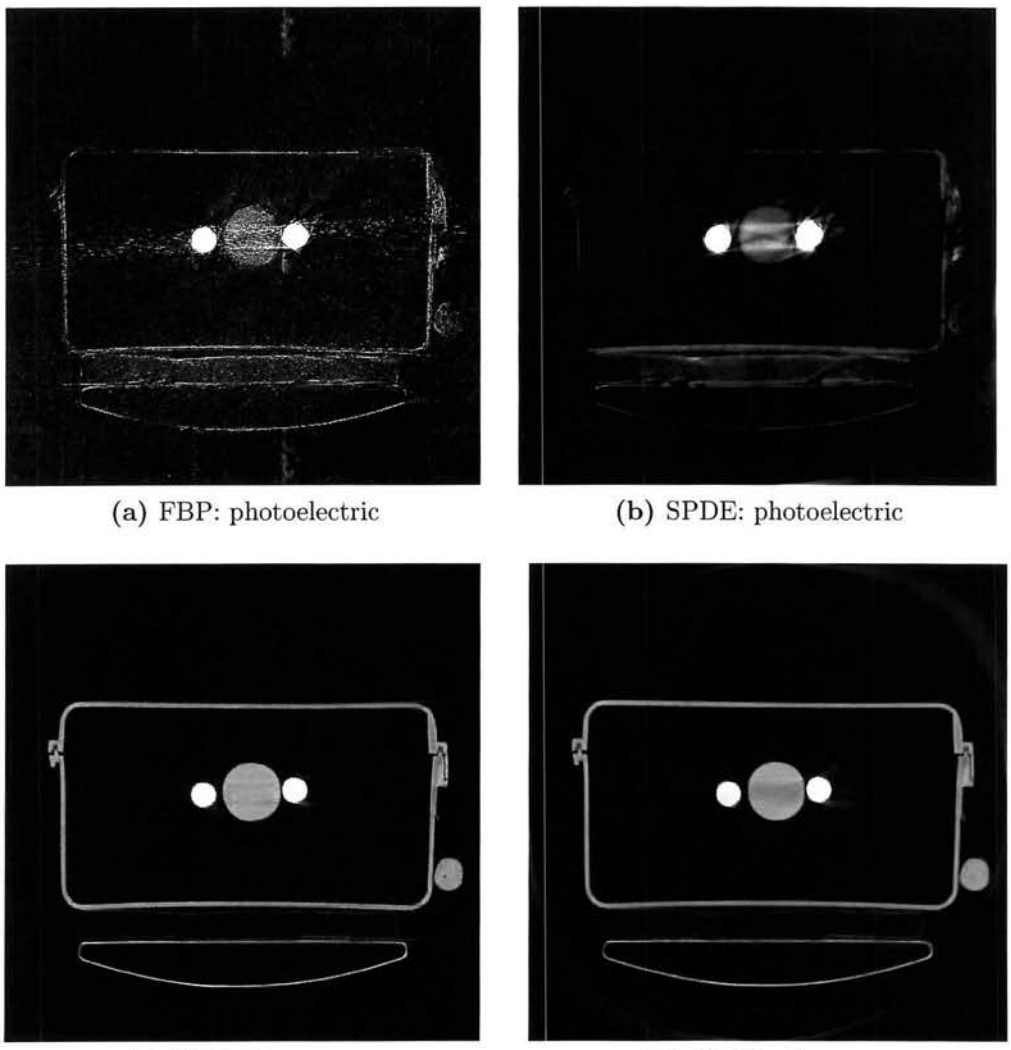


(c) FBP: Compton



(d) SPDE: Compton

Figure 6·20: Photoelectric and Compton coefficient images given by FBP (left) and SPDE (right) for example slice 2. The objects in this slice include a bottle of water and a thin rubber sheet. Image units and display ranges are the same as in Figure 6·18.



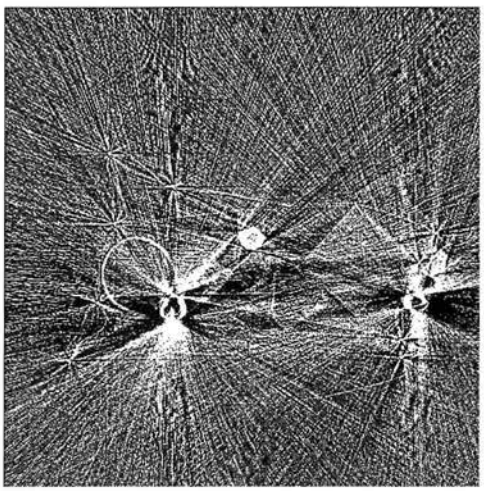
(a) FBP: photoelectric

(b) SPDE: photoelectric

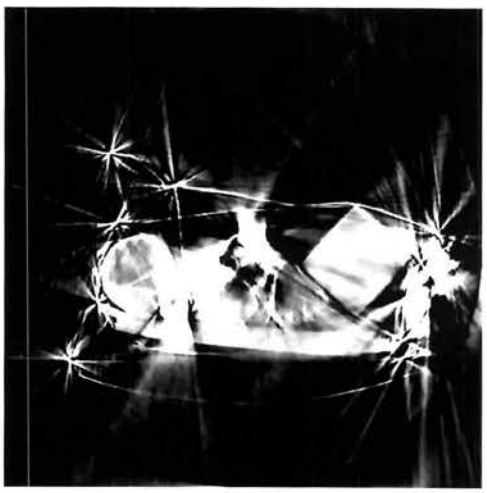
(c) FBP: Compton

(d) SPDE: Compton

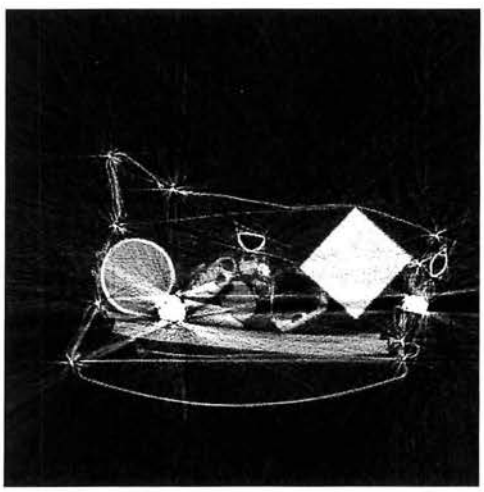
Figure 6·21: Photoelectric and Compton coefficient images given by FBP (left) and SPDE (right) for example slice 1. In this slice there is a bottle of water in between magnesium and silicon rods. Image units and display ranges are the same as in Figure 6·18.



(a) FBP: photoelectric



(b) SPDE: photoelectric



(c) FBP: Compton



(d) SPDE: Compton

Figure 6·22: Photoelectric and Compton coefficient images given by FBP (left) and SPDE (right) for example slice 2. The objects in this slice include a teflon cube, a bottle of water and a stack of rubber sheets. Image units and display ranges are the same as in Figure 6·18.

reconstructed Compton images.

Quantitative evaluation

For the dataset we used, ground truth labeling masks for a few selected objects were provided by Stratovan Corp. The labeled objects included 11 water bottles, 4 doped water bottles and 13 rubber sheets. Using these ground truth object masks we computed the signal to noise ratio (SNR) for the reconstructed photoelectric and Compton images. SNR is defined as the mean divided by the standard deviation inside the object region. High values of SNR indicate homogeneity.

Figure 6·23 shows the mean percent improvement in SNR of SPDE relative to FBP for each of the materials. It can be seen that in both Compton and photoelectric images the SNR has improved significantly for all the materials.

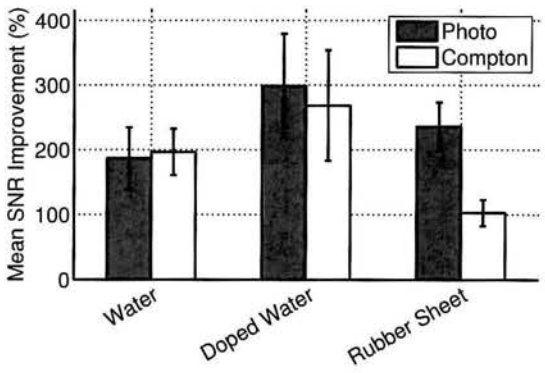


Figure 6·23: Mean percent improvement in SNR of SPDE relative to FBP. The mean was calculated across the selected objects. The errorbars represent standard error.

6.6 Summary

In this chapter we presented new methods for reconstructing material-specific parameters from MECT measurements in the context of security. The challenges in security are the large range of materials which should be considered, including metals and other dense objects, and the high clutter in the bags. Streaks and metal artifacts in the reconstructed images are prevalent. The proposed methods attempt to address these issues and provide more reliable reconstructions, compared to current methods.

In Section 6.1 we presented a post-reconstruction method, which is based on the ρZ projection method proposed in [Heismann et al., 2003]. The idea was to use more than two spectral measurements in an attempt to expand the range of materials covered. We showed that in some cases the effective atomic number estimates improved compared to the ρZ projection method but overall the improvement was not significant. We believe that the method performance is affected by how much overlap the system spectral functions have and in the system we used the overlap was very high. Also, a very simple model was used to predict the effective attenuation values. Using a more precise model may improve the performance of the method. The method may also perform better on a system with spectral weighting functions which have minimal overlap.

In Section 6.2 we proposed a new dynamic MECT reconstruction approach, which may be useful when the measurements acquired with different spectral functions are not geometrically aligned. The method reconstructs basis coefficient images directly from the MECT measurements. An iterative solution approach based on the Kalman Filter was proposed. We showed that the results converge to the batched least-squares solution. The method currently works for small simulated phantoms. More work is needed to apply the method to real systems.

In Section 6.3 we presented the K-EDEC method, which is a generalization of the

EDEC method proposed in [Stenner et al., 2007]. The main idea was to replace the polynomial model used in EDEC to map the dual-energy measurements to basis material sinograms with a more flexible data based mapping which uses kernel smoothing. Since the data from the calibration scan may be limited, additional calibration data may be simulated and incorporated in the kernel smoothing. We saw that K-EDEC provided comparable results to EDEC in some cases and showed slight improvement in others. The limitation of K-EDEC is that in order to simulate additional calibration data the system spectral weighting functions must be known, as well as the LACs of the calibration materials. If these are known then a solution which is as good as the K-EDEC solution can also be obtained with the sinogram least squares method. A different possible direction for improving the EDEC approach is to extend the decomposition to more than two basis materials. This will allow to span more of the measurement space and potentially improve the accuracy of the results.

Lastly, in Section 6.5 we presented the SPDE model-based approach for jointly inverting the basis coefficient images from the basis coefficient sinograms. We showed that using data weighting and a mutual boundary-field in the regularization helps to reduce noise and metal artifacts in the basis coefficient images. The work on SPDE was submitted to the 2014 ICASSP conference [Martin et al., 2014a].

Chapter 7

Material identification using MECT

In MECT systems for security, potential threats are found by identifying and segmenting the scanned objects. Typically, one set of images (e.g., the conventional effective attenuation image) is used for object segmentation and another set of images (e.g., the photoelectric and Compton coefficient images) is used for object labeling and discrimination of the resulting segmented areas. These two processes of segmentation and labeling are currently decoupled. The segmentation process, which is usually based on single-energy data, is challenging due to image streaks and metal artifacts. Multi-energy material information is not exploited, even though it can benefit the segmentation. In addition, as we saw in Chapter 6, the reconstruction of reliable material parameter images for labeling the materials is not straight forward and may result in loss of information needed for discrimination. In this chapter we propose a method to perform object identification and segmentation jointly using MECT measurements. This joint approach allows for material information to be used for segmentation and may potentially improve the detection performance. The typical decoupled approach and the new proposed joint approach are illustrated in Figure 7·1.

We consider the following formulation of the problem. We would like to use MECT measurements to estimate a material label image such as the one shown in Figure 7·2. Each pixel in the image may only contain one of a few material labels. The color of the pixel represents the material label.

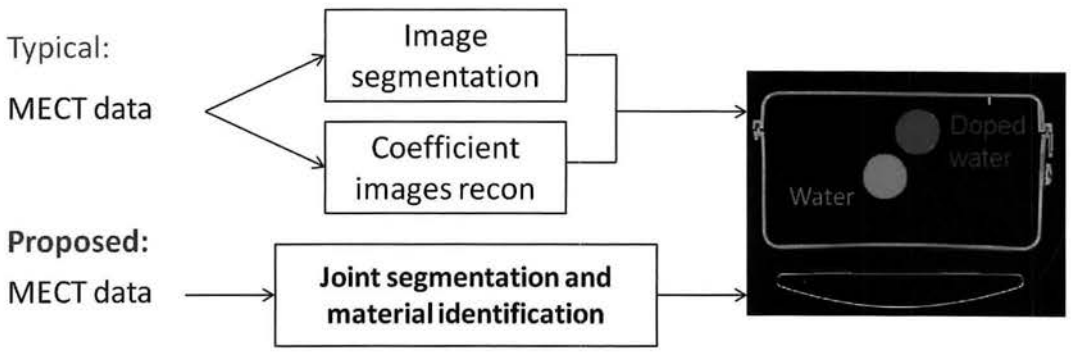


Figure 7·1: Object segmentation and labeling: decoupled (typical) versus joint (proposed) paths

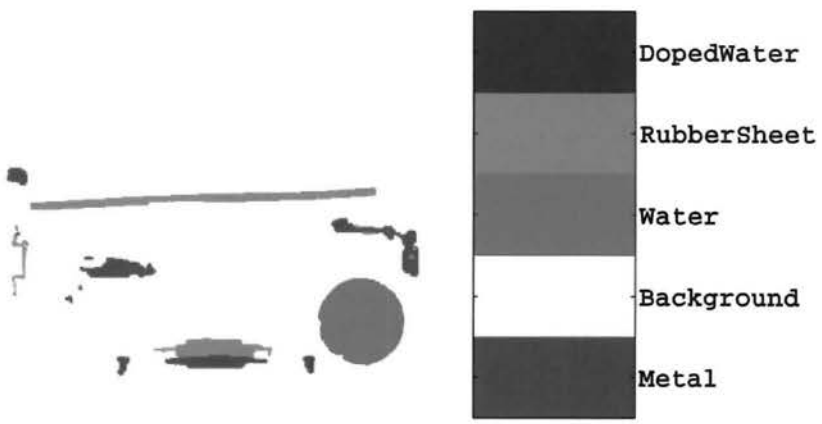


Figure 7·2: Example of a material label image. The color in each pixel represents the materials label.

The general framework we will use is given by:

$$\begin{aligned} &\underset{\boldsymbol{l}}{\text{minimize}} \quad h_{Data}(I, \boldsymbol{l}) + \lambda h_{Prior}(\boldsymbol{l}) \\ &\text{subject to} \quad l_i \in \{1, 2, ..., N_m, N_m + 1\} \quad \text{for } i = 1, ..., N_p \end{aligned} \tag{7.1}$$

where N_m is the number of possible material labels (usually small) with the $N_m + 1$ label representing background, $I = \{I_1, I_2, ..., I_{N_s}\}$ is the collection of multi-energy measurements, N_p is the total number of pixels, $\boldsymbol{l}$ is the $N_p \times 1$ material map with l_i being the material label at pixel i, and λ is a non-negative regularization parameter.

The function $h_{Data}(I, \boldsymbol{l})$ is a data fidelity term that captures the material appearance models and the function $h_{Prior}(\boldsymbol{l})$ captures prior information on the behavior of the label field $\boldsymbol{l}$. Since we are optimizing over the set of possible discrete material labels at each pixel, this is a discrete optimization problem, which in general is difficult to solve. Note that this labeling is not merely a multi-level segmentation task. We jointly segment objects and identify the materials they are made of.

In this chapter we propose two specific formulations based on (7.1). In the first formulation, described in Section 7.1, the data term is based directly on the sensing physics, relating the observed sinograms to a dictionary of material LACs. While this approach exploits the complete physical sensing model as well as knowledge of material X-ray behavior, it requires detailed knowledge of system parameters such as sensing geometry, spectral shapes, material LACs, etc., and can be computationally demanding. As a result we also consider a second formulation, described in Section 7.2, where in the data term is derived from training data using learning-based approach. In this approach, we start from conventionally formed effective attenuation images for each multi-energy experiment and learn the conditional appearance model for each material of interest from training data. As a result explicit physical models of the tomographic system and material LACs are not needed. We frame this problem as a graph-based optimization problem which we efficiently solve using graph cut methods [Boykov et al., 2001].

7.1 Dictionary based material labeling

We present a unified approach for the estimation of the material label image from MECT measurements, which takes into account the system model information and the way the materials are observed. A dictionary-based model of the measured sinograms is developed. The LACs of the materials of interest are used as the dictionary

elements. The data fidelity term is based on matching this model to the measurements. The material labels are given by the estimated dictionary coefficients. We use a Markov random field (MRF) type model for the prior term, which captures our belief that the label field should display spatial coherence. This spatial coherence reflects the behavior of objects in the scene and serves to further our goal of preventing splitting of objects.

Specifically, we create the following dictionary of LACs of a few materials of interest:

$$D = \left[\boldsymbol{\mu}_1 \ \boldsymbol{\mu}_2 \cdots \boldsymbol{\mu}_{N_m}\right] \tag{7.2}$$

where $\boldsymbol{\mu}_i$ is an $N_e \times 1$ vector representing the LAC of material i as a function of energy and N_e is the number of discretized energy levels. The number of possible materials is N_m. D is of size $N_e \times N_m$.

The assumption is that at every spatial location or pixel j there is only one material and its label is l_j, and that its LAC is given by one of the columns of D. Consequently, the LAC of the material at pixel j is given by the product $D\boldsymbol{c}_j$, where the coefficient vector $\boldsymbol{c}_j$ is

$$\boldsymbol{c}_j = \begin{cases} (1,0,0,...,0)^T & \text{if } l_j = 1 \\ (0,1,0,...,0)^T & \text{if } l_j = 2 \\ \quad\vdots & \\ (0,0,0,...,1)^T & \text{if } l_j = N_m \\ (0,0,0,...,0)^T & \text{if } l_j = N_m + 1 \text{ (background)} \end{cases} \tag{7.3}$$

Let C denote the $N_m \times N_p$ coefficient matrix, such that column $\boldsymbol{c}_j$ is the coefficient vector for pixel j. The matrix $M_{N_p \times N_e}$, which contains the LAC at every pixel and energy level, can be written as

$$M = C^T D^T \tag{7.4}$$

Substituting (7.4) into the MECT measurement model (2.22) gives the following representation of the vector I_i of MECT measurements with spectral weighting

function i:

$$I_i = e^{-RC^T D^T} \boldsymbol{w}_i \tag{7.5}$$

where $R_{N_d \times N_p}$ is the forward projection matrix and $\boldsymbol{w}_i$ holds samples of the ith spectral weighting functions.

Using (7.5) and (2.23), the model for the measured sinogram (measurements in the normalized negative log space) as a function of the coefficient matrix C is the following:

$$\tilde{I}_i(\boldsymbol{c}_1, ..., \boldsymbol{c}_{N_p}) = \tilde{I}_i(C) = -\ln \left(\frac{e^{-RC^T D^T} \boldsymbol{w}_i}{\sum_{k=1}^{N_e} w_{ik}} \right) \tag{7.6}$$

Note that the exponent and logarithm are element-wise operators, not matrix operators.

Based on the formulation (7.1) and model (7.6), the following minimization problem is constructed:

$$\begin{aligned} \underset{(\boldsymbol{c}_1, ..., \boldsymbol{c}_{N_p})}{\text{minimize}} \quad & \sum_{i=1}^{N_s} \left(\tilde{I}_i - \tilde{I}_i(\boldsymbol{c}_1, ..., \boldsymbol{c}_{N_p}) \right)^2 + \lambda \sum_{\{j,k\} \in \mathcal{N}} \mathbb{1}\{\boldsymbol{c}_j \neq \boldsymbol{c}_k\} \\ \text{subject to} \quad & \boldsymbol{c}_j \in \{(1,0,0,...)^T, (0,1,0,...)^T, ..., (0,0,...,0)^T\}, \\ & \text{for } j = 1, ..., N_p \end{aligned} \tag{7.7}$$

where index i corresponds to the spectral weighting function, N_s is the total number of spectral weighting functions, $\tilde{I}_i$ is the measured sinogram with the ith spectral weighting function, $\tilde{I}_i(\boldsymbol{c}_1, ..., \boldsymbol{c}_{N_p})$ is the ith modeled sinogram by (7.6), λ is a non-negative regularization parameter, indices j and k are pixel indices, and $\mathcal{N}$ is a pixel-neighborhood. $\mathbb{1}\{\boldsymbol{c}_j \neq \boldsymbol{c}_k\}$ is an indicator function - it is equal to zero if all the elements of column $\boldsymbol{c}_j$ and column $\boldsymbol{c}_k$ are the same, and one otherwise.

The first summation in (7.7) is the data fidelity term. It is defined as the squared

error between the measured sinogram and the dictionary-based model of it. More generally this term could correspond to the log-likelihood arising in the sensing model. The second summation in (7.7) is the MRF prior term. This term penalizes any differences in dictionary coefficient vectors for pixels in a small neighborhood $\mathcal{N}$. Different coefficient vectors correspond to different labels and the desire is increase the coherency of the label field.

Solving problem (7.7) directly is computationally prohibitive. We obtain a solution iteratively by solving for one column of C at a time while keeping the other columns fixed. Since there is a relatively small number of possibilities for the values of the column (it may only be one of N_m possibilities listed in Equation (7.3)), all the possibilities may be tested and the one which provides the lowest value of the cost function is selected. We call this the "dictionary labeling method".

7.1.1 Experimental results

We implemented the method and tested it on real dual-energy data from the Imatron scans database described in Appendix B. These are dual-energy scans of different objects in bags obtained with a 95 kVp and 130 kVp source spectra. To increase the speed, we sampled the LACs and spectral weighting functions at only 10 energy levels from 10 to 150 keV. We performed ten iterations of the method (going through all the pixels ten times). For the prior term we used an 8-connected neighborhood.

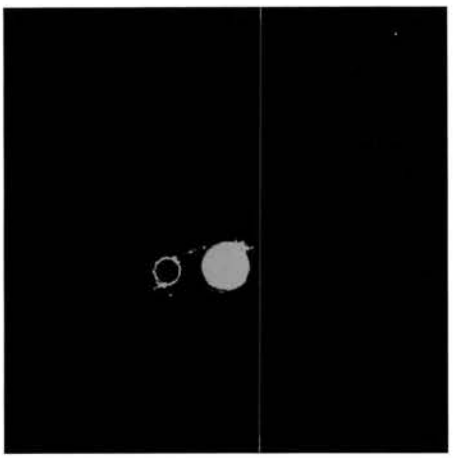
We initialized the labeling as follows: (i) we applied one iteration of a post-reconstruction method described in [Heismann and Balda, 2010], which gave us rough estimates of the LAC at every pixel, (ii) at each pixel the estimated LAC was compared to the dictionary LACs and to a vector of all zeros (for background label) and the label for that pixel was set to the material for which the LAC was the closest (in the sense of Euclidean distance).

In the first experiment we constructed the dictionary with the LACs of graphite

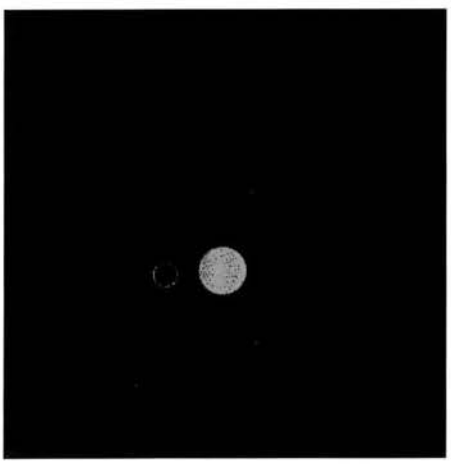
and magnesium, providing three possible material labels: graphite, magnesium and background (air). We applied the method to a slice containing graphite and magnesium rods. The labeling results are shown in Figure 7·3. We also calculated the MSE between the measurements and the model of the measurements based on the labeling result. The MSE as a function of iteration is shown in Figure 7·4. It can be seen that relative to the initialization, the labeling is improved by the method. In addition, adding an MRF prior helps to make the objects more homogeneous.

In the second experiment, we constructed the dictionary with the LACs of graphite, magnesium, and silicon providing four possible material labels: graphite, magnesium, silicon and background (air). We applied the method to a slice which had graphite, magnesium and silicon rods which were placed in foam inside a plastic case. The results are shown in Figures 7·5 and 7·6. The labeling results seem to be accurate and again we see that the MRF prior helps object homogeneity. It is interesting to note that many pixels around the objects are labeled as graphite as opposed background. This may be happening because the objects were supported by foam, which has higher attenuation than air and may be mistaken as graphite.

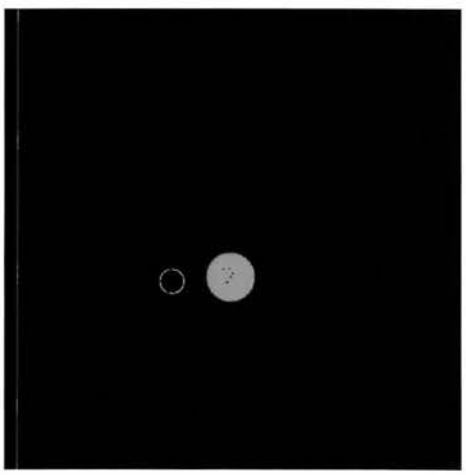
The dictionary labeling method allows to directly label the scanned materials from MECT measurements. The results show that the method can achieve accurate labeling and that using the MRF prior helps to get more homogeneous results. The limitation of the method is that it is highly time consuming (a matter of days with current Matlab-based implementation). Other solution approaches, such as projection-based graph cuts [Tuysuzoglu et al., 2013], should be considered as well.



(a) Initialization

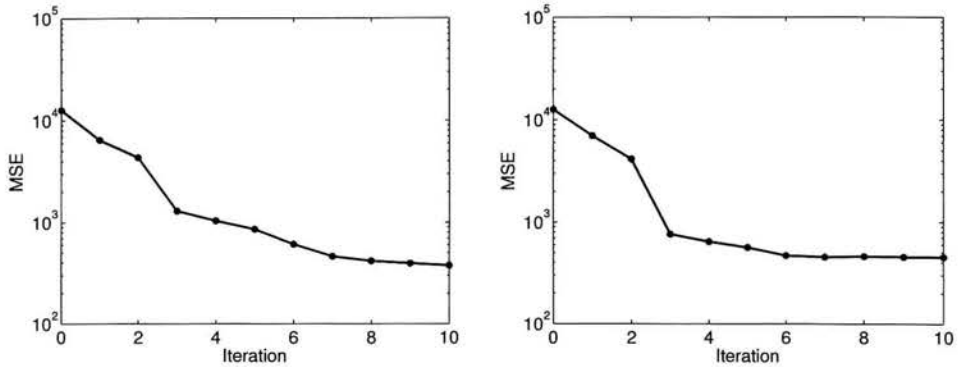


(b) Final, $\lambda = 0$



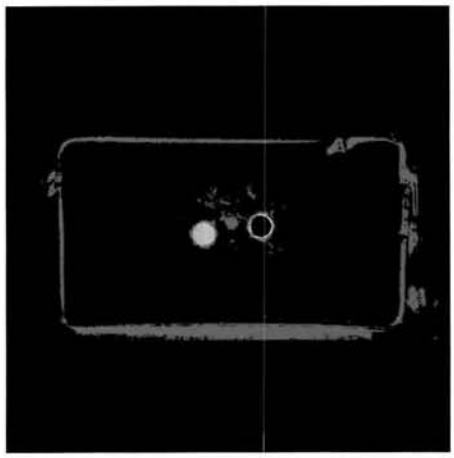
(c) Final, $\lambda = 0.007$

Figure 7·3: Material label images for a slice with graphite and magnesium rods using the dictionary labeling method. The graphite rod is on the right. Dictionary was composed of graphite and magnesium LACs. Graphite is labeled in green, magnesium is labeled in red and background is labeled in dark blue. Top: initialization. Bottom left: result with no MRF prior. Bottom right: result with an MRF prior.



(a) MSE, $\lambda = 0$ (b) MSE, $\lambda = 0.007$

Figure 7·4: MSE between measurements and modeled measurements using the labeling result shown in Figure 7·3. Dictionary was composed of graphite and magnesium LACs. Left: without MRF prior. Right: with MRF prior.



(a) Initialization

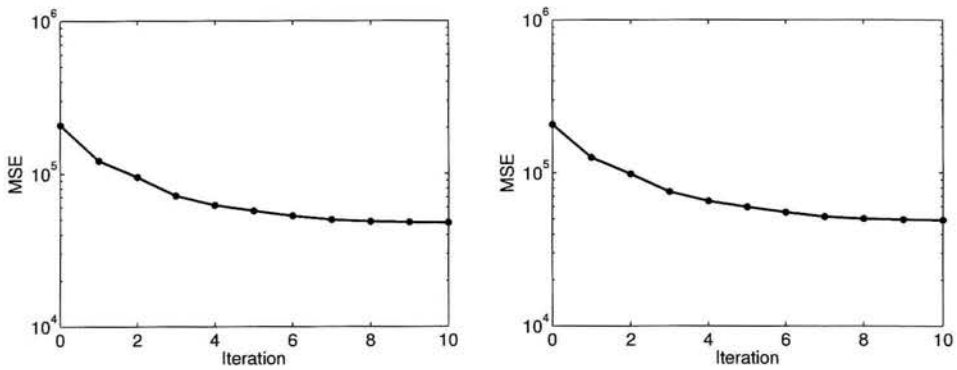


(b) Final, $\lambda = 0$



(c) Final, $\lambda = 0.007$

Figure 7·5: Material label images using the dictionary labeling method for a slice with graphite, magnesium and silicon rods placed with foam in a plastic container. The graphite rod is in the middle and silicon is on the right. Dictionary was composed of graphite, magnesium and silicon LACs. Graphite is labeled in light blue, magnesium is labeled in yellow, silicon is labeled in red and background is labeled in dark blue. Top: initialization. Bottom left: result with no MRF prior. Bottom right: result with an MRF prior.



(a) MSE, $\lambda = 0$ **(b)** MSE, $\lambda = 0.007$

Figure 7·6: MSE between measurements and modeled measurements using the labeling result shown in Figure 7·5. Dictionary was composed of graphite, magnesium and silicon LACs. Left: without MRF prior. Right: with MRF prior.

7.2 Learning-based graph-cut material labeling

The dictionary labeling method described in the previous section incorporates the complete sensing model and physics of the problem. However, the system model may not be explicitly known or may not be accurate, and also the method's high computational cost makes it difficult to use in practice. Here we present an image-based formulation which does not require knowledge of the system model and can be solved more efficiently. The method starts with effective attenuation images obtained by applying standard FBP individually to each of the MECT sinograms. These images are usually easily available since they are the typical output of the scanner software. Based on a machine learning perspective, the aim is to directly learn the mapping from these images to material label distributions.

The effective attenuation images may contain streaks and metal artifacts, and the desire is to avoid carrying them over to the material label image. Therefore, we also down-weight unreliable data (points in the vicinity of metal objects) and incorporate an object boundary-field to control the smoothing. The overall problem is solved using an efficient graph-cut algorithm. We call this method "learning-based graph-cut labeling".

We focus here on dual-energy measurements ($N_s = 2$), although the method may be extended to more than two spectral measurements. We represent the effective attenuation image, obtained by applying standard FBP reconstruction to sinogram $\tilde{I}_i$, by vector $\bar{\boldsymbol{\mu}}_i$ of dimensions $N_p \times 1$. Given $\bar{\boldsymbol{\mu}}_1$ and $\bar{\boldsymbol{\mu}}_2$, the goal is to find an optimal labeled image $\boldsymbol{l}$. Following the formulation (7.1), the data fidelity term is the first summation and the smoothing prior term is the second summation in the expression

below:

$$\underset{\boldsymbol{l}}{\text{minimize}} \quad \sum_{j=1}^{N_p} v_j \left(-\ln p\left(\left[\begin{array}{c} \bar{\mu}_{1j} \\ \bar{\mu}_{2j} \end{array} \right] \middle| l_j \right) \right) + \lambda \sum_{\{j,k\} \in \mathcal{N}} \mathbb{1}\{l_j \neq l_k\} \left(\frac{1}{|s_j - s_k|} \right) \quad (7.8)$$

$$\text{subject to} \quad l_i \in \{1, ..., N_m + 1\} \quad \text{for } i = 1, ..., N_p$$

where $\bar{\mu}_{ij}$ is jth element of $\bar{\boldsymbol{\mu}}_i$, v_j is the data weighting for pixel j, s_j is the boundary field at pixel j (assumed to known, to be discussed later), $p([\bar{\mu}_{1j}\ \bar{\mu}_{2j}]^T|l_j)$ is the value of the learned appearance model for data $[\bar{\mu}_{1j}\ \bar{\mu}_{2j}]^T$ given the label l_j, λ is a non-negative regularization parameter, and $\mathcal{N}$ is a pixel-neighborhood. $\mathbb{1}\{l_j \neq l_k\}$ is an indicator function - it is equal to zero if l_j and l_k are the same, and one otherwise.

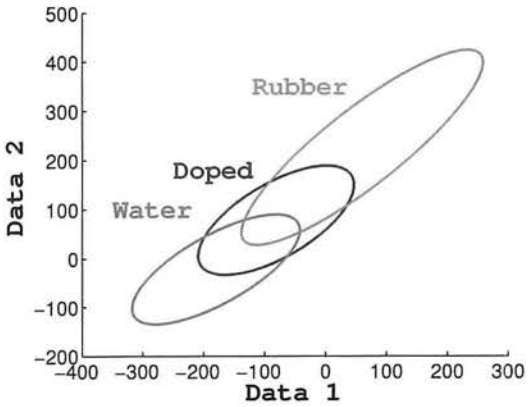
The formulation (7.8) includes three main components:

1. The likelihood based data fidelity term $p([\bar{\mu}_{1j}\ \bar{\mu}_{2j}]^T|l_j)$ is calculated based on learned appearance models. Estimation of the appearance models is based on labeled training images. This can potentially be a significant advantage over the dictionary based labeling method which requires explicit knowledge of the system model for calculating the data fidelity term. It also has the potential to capture more complicated appearance behavior.

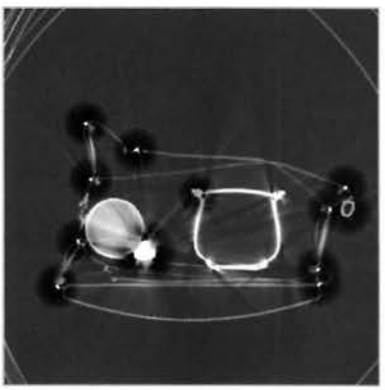
2. Data points near metal tend to be unreliable because of the artifacts they induce. To account for this, these points are down-weighted using weights v_j. This down weighting mitigates the impact of image distortion due to the presence of metal.

3. *Prior* knowledge of the boundary field $\boldsymbol{s}$ is assumed and is used to prevent undesired splitting of objects due to artifacts. The formulation penalizes pixels which are in the same neighborhood, have different labels, and have similar boundary field values. The idea is that in a small neighborhood pixels should have the same label unless there is an edge. This helps to maintain connectivity of the object regions in the face of the metal artifacts.

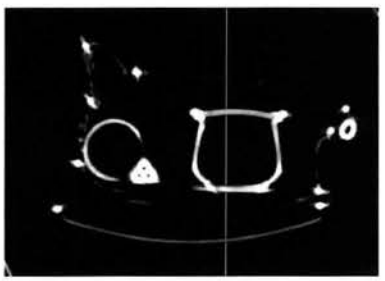
Figure 7·7 shows the main components of the method for an example slice from the Imatron scans database. Implementation details are given in the following section.



(a) Learn appearance models



(b) Down-weight data close to metal



(c) Estimate boundary to control smoothing

Figure 7·7: Illustration of the main components of the learning-based graph-cut labeling method. Top left figure shows the learned material appearance models. Top right figure shows an example of the data weighting scheme. Data points close to metal are given lower weights. The bottom figure shows the boundary-field used in the smoothing term.

7.2.1 Method implementation

Using training data with known material labels, we estimate the conditional probability density functions $p([\bar{\mu}_{1j}\ \bar{\mu}_{2j}]^T|l_j)$ by fitting a Gaussian to the data values for each label. Example scatter plots of the data we used are shown in the experiments Section 7.2.2. The Gaussian model seemed sufficient for this data, but in general

other density estimation methods, such as KDE [Hastie et al., 2005], may also be considered.

We derive the boundary-field $\boldsymbol{s}$ used in the prior term as the solution to the following minimization problem:

$$\underset{\boldsymbol{s}}{\text{minimize}} \quad ||D\bar{\boldsymbol{\mu}}_2||^2_{W_s} + \lambda_1^2||D\boldsymbol{s}||^2_2 + \lambda_2^2||\boldsymbol{s}||^2_2 \tag{7.9}$$

where $W_s = \text{diag}((1-\boldsymbol{s})^2)$, and D is the derivative operator. Setting the derivative of (7.9) to zero yields the following equation which must hold at the optimum:

$$(B + \lambda_1^2 D^T D)s = Bz \tag{7.10}$$

where B is a diagonal matrix with $B_{ii} = [D\boldsymbol{\mu}]_i^2 + \lambda_2^2$, and z is a vector defined by

$$z_i = \frac{[D\boldsymbol{\mu}]_i^2}{[D\boldsymbol{\mu}]_i^2 + \lambda_2^2}$$

Equation (7.10) is a linear inverse problem and can be solved with the least Squares with QR-factorization algorithm (LSQR) [Paige and Saunders, 1982].

In addition to using explicit object boundaries, a data weighting scheme is applied to mitigate the metal artifacts. It is based on the distance of the data points from metal objects. Given a binary metal map $\boldsymbol{l}^{metal}$ of size $N_p \times 1$ (with one for metal and zero for background), the data weighting map at pixel j, v_j, is obtained using the following expression:

$$v_j = \begin{cases} 1 & \text{if } l_j^{metal} = 1 \text{ or } d_j > d_{max} \\ \frac{d_j}{d_{max}} & \text{otherwise} \end{cases} \tag{7.11}$$

where d_j is the distance from pixel j to the closest metal pixel and d_{max} is a pre-defined threshold.

The binary metal map $\boldsymbol{l}^{metal}$ used in (7.11) is found by setting $v_j = 1$ for $j =$

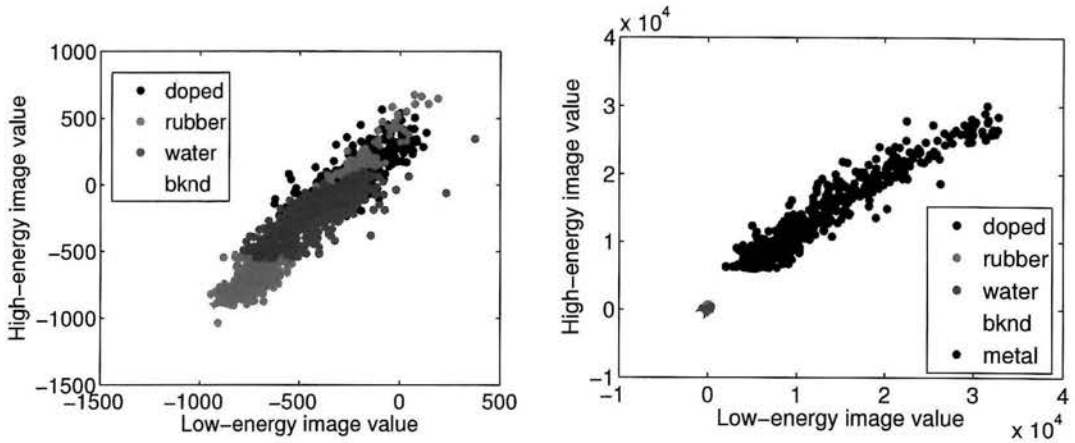
$1, ..., N_p$, and solving (7.8) with just two labels - metal and background. This is an easier problem to solve than the overall multi-label problem since the two classes are well separated.

Problem (7.8) is a discrete optimization problem. The efficient graph-cut algorithm [Boykov et al., 2001] is well matched to the discrete nature of the problem and performs very well. In particular, the alpha-expansion algorithm is used. It has been the leading choice for multi-label discrete problems in many imaging and computer vision problems. It is guaranteed to converge in a finite number of steps and the local minimum it finds is within a known factor of the global optimum [Boykov et al., 2001].

7.2.2 Experimental results

We applied the learning-based graph cut labeling method to the Imatron scans database described in Appendix B. We estimated the appearance models for water, doped water, rubber sheet, metal and background (everything else). We used 130 and 95 kVp reconstructed attenuation images from a cluttered set and an uncluttered set of scans as our training data. We extracted pixel values from the images for each of the materials and fit a two-dimensional Gaussian to them. This gave us the models $p([\bar{\mu}_{1j}\ \bar{\mu}_{2j}]^T|l_j)$. A scatter plot of the 130 kVp values versus the 95 kVp values for the different labels is shown in Figure 7·8.

For the derivation of the edge-field, we solved (7.9) using Matlab's 'lsqr' function with regularization parameters $\lambda_1 = 40$ and $\lambda_2 = 100$. The parameter d_{max} used in the calculation of the data weighting map was set to 40 pixels which corresponds to a distance of 37mm. The regularization parameter λ was set to 100 for the initial estimation of the metal labeling l^{metal} and was set to 0.12 for the final estimation of all the material labels. These parameters were found empirically using a subset of the slices.



(a) without metal **(b)** without metal

Figure 7·8: Scatter plots of the high energy image values $\bar{\mu}_2$ versus the low energy image values $\bar{\mu}_1$ of the training data for the different material labels. Left: without the metal label. Right: with the metal label.

In the formulation (7.8), the term $1/|s_j - s_k|$ is calculated. This may theoretically result in infinity, or extremely high values. In practice we use a maximum value of 100000 for the expression to prevent integer overflow.

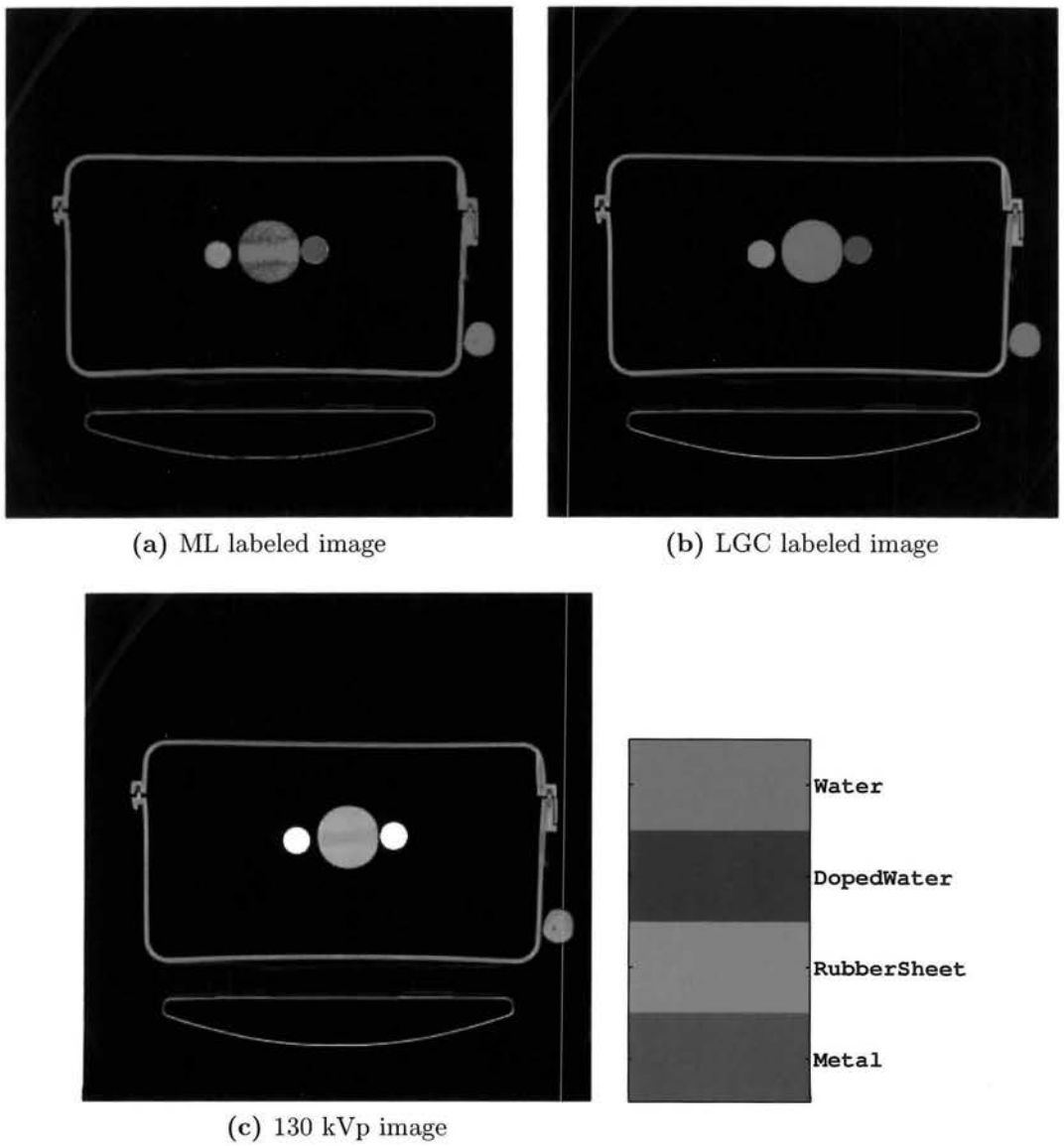
As a comparison point we implemented the maximum-likelihood solution, where the labeling is based solely on the learned appearance models:

$$\underset{\boldsymbol{l}}{\text{minimize}} \sum_{j=1}^{N_p} \left(-\ln p \left(\begin{bmatrix} \bar{\mu}_{1j} \\ \bar{\mu}_{2j} \end{bmatrix} | l_j \right) \right) \qquad \text{subject to } l_i \in \{1, ..., N_m + 1\} \qquad (7.12)$$

In the results to follow we will call the learning-based graph cut method (7.8) LGC and the maximum-likelihood method (7.12) ML.

Figures 7·9-7·14 show the results for six selected slices in medium and high clutter levels. The labeled material image (all labels besides 'background') is overlaid on the 130 kVp reconstructed attenuation image. The results are shown for both the ML and LGC methods. It can be seen that the LGC labeled images are much more smooth than the ML results. With LGC successful direct labeling in the presence

of metal, shading and streaking is achieved in most cases. In some highly cluttered cases, objects may be mislabeled but object localization is not corrupted by the metal induced streaks. (e.g., Figure 7·12).



(a) ML labeled image

(b) LGC labeled image

(c) 130 kVp image

Figure 7·9: Results for example slice 1. The slice has a water bottle in between magnesium and silicon rods. Top left: ML labeled image overlaid on the 130 kVp attenuation image. Top right: LCG labeled image overlaid on the 130 kVp attenuation image. Bottom: 130 kVp effective attenuation image. The attenuation images are in HU units displayed in the range [-1000, 1500]



(a) ML labeled image



(b) LGC labeled image



(c) 130 kVp image

Figure 7·10: Results for example slice 2. The slice has a water bottle on the right and a rubber sheet on top. Top left: ML labeled image overlaid on the 130 kVp attenuation image. Top right: LCG labeled image overlaid on the 130 kVp attenuation image. Bottom: 130 kVp effective attenuation image. The attenuation images are in HU units displayed in the range [-1000, 1500]

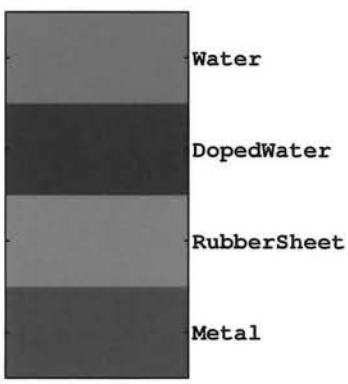


(a) ML labeled image



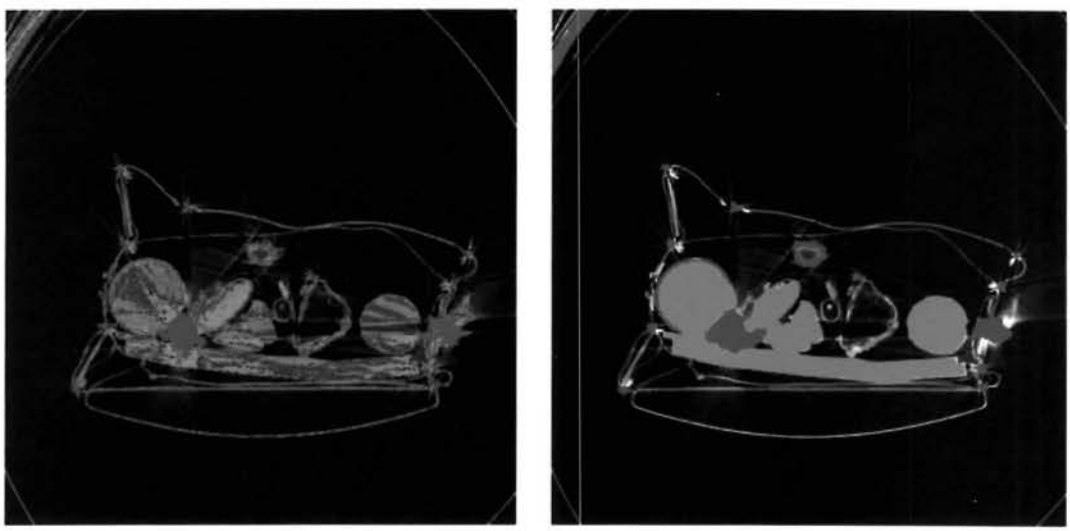
(b) LGC labeled image





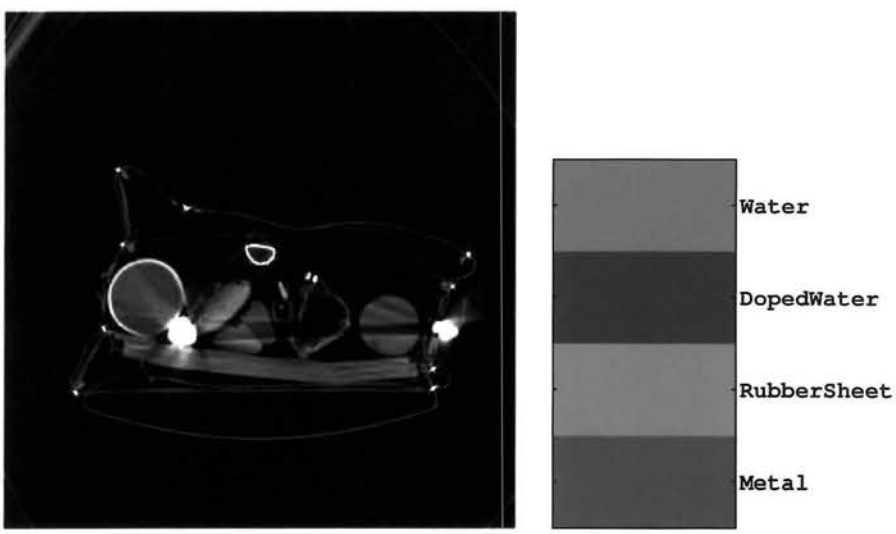
(c) 130 kVp image

Figure 7·11: Results for example slice 3. The slice has a water bottle on the right and a rubber sheet on top. Top left: ML labeled image overlaid on the 130 kVp attenuation image. Top right: LCG labeled image overlaid on the 130 kVp attenuation image. Bottom: 130 kVp effective attenuation image. The attenuation images are in HU units displayed in the range [-1000, 1500]



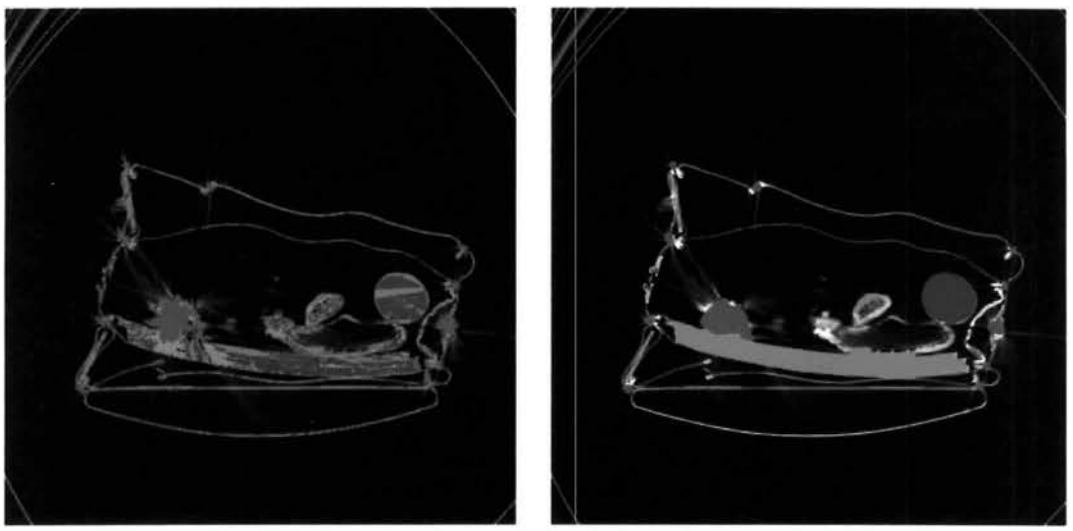
(a) ML labeled image

(b) LGC labeled image



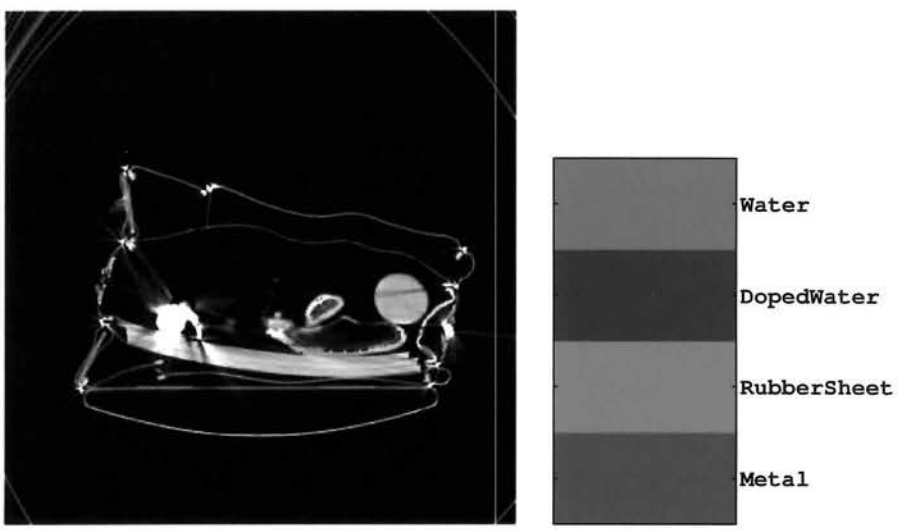
(c) 130 kVp image

Figure 7·12: Results for example slice 4. The slice has a stack of rubber sheets on the bottom and a bottle of doped water on the right. Top left: ML labeled image overlaid on the 130 kVp attenuation image. Top right: LCG labeled image overlaid on the 130 kVp attenuation image. Bottom: 130 kVp effective attenuation image. The attenuation images are in HU units displayed in the range [-1000, 1500]



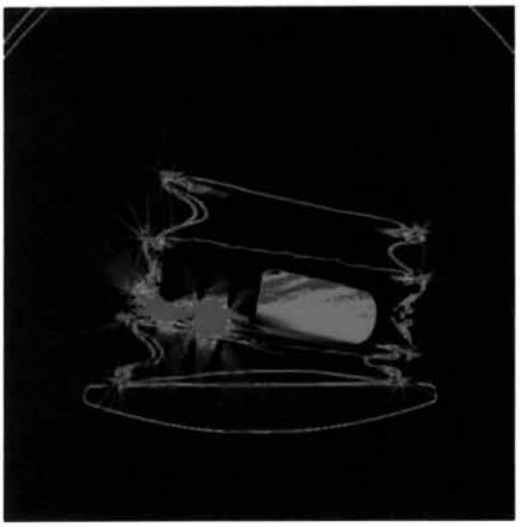
(a) ML labeled image

(b) LGC labeled image

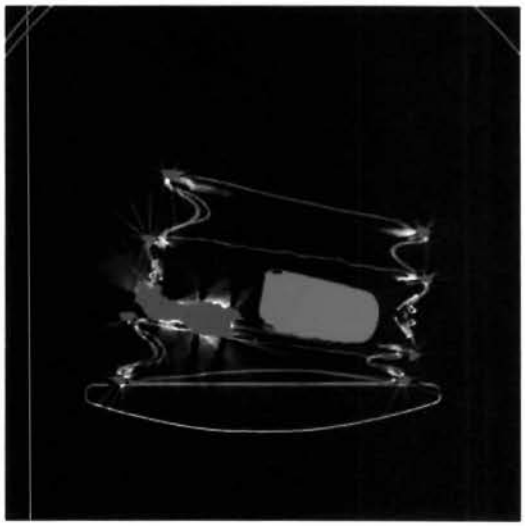


(c) 130 kVp image

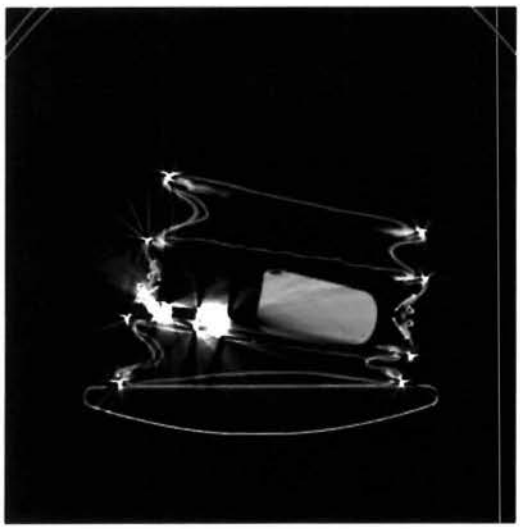
Figure 7·13: Results for example slice 5. The slice has a stack of rubber sheets on the bottom and a bottle of doped water on the right. Top left: ML labeled image overlaid on the 130 kVp attenuation image. Top right: LCG labeled image overlaid on the 130 kVp attenuation image. Bottom: 130 kVp effective attenuation image. The attenuation images are in HU units displayed in the range [-1000, 1500]

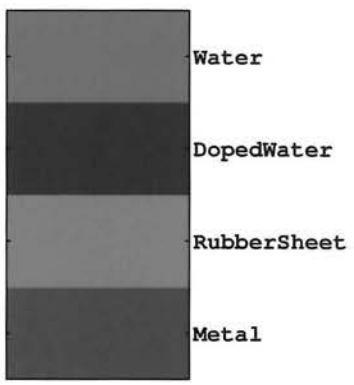


(a) ML labeled image



(b) LGC labeled image





(c) 130 kVp image

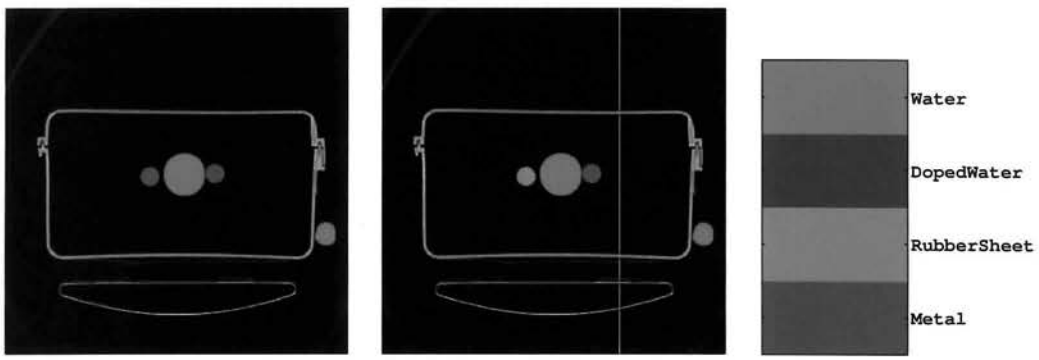
Figure 7·14: Results for example slice 6. The slice has a bottle of water on the right. Top left: ML labeled image overlaid on the 130 kVp attenuation image. Top right: LCG labeled image overlaid on the 130 kVp attenuation image. Bottom: 130 kVp effective attenuation image. The attenuation images are in HU units displayed in the range [-1000, 1500]

Single versus dual energy

Here we study the effect the number of spectral measurements on the performance of the learning-based labeling method using measurements. We compared the single-energy case, where we only consider the effective attenuation image $\bar{\boldsymbol{\mu}}_2$, and the dual-energy case, where we use both $\bar{\boldsymbol{\mu}}_1$ and $\bar{\boldsymbol{\mu}}_2$. For the single energy case the regularization parameter λ for the final labeling estimation was set to 0.1.

The single and dual-energy results for a few slices are shown in Figure 7·15. For Slice 1, the magnesium and silicon rods are both labeled as metal in the single-energy case, as opposed to the dual-energy case. However, since magnesium and silicon were not explicitly modeled, both results may be considered correct. For Slice 2, the single and dual energy results are very similar. For slice 3, part of the rubber sheets are labeled as doped water in the single-energy result, but are labeled correctly in the dual-energy result.

Overall, it seems that using dual-energy measurements may improve the results relative to single-energy, but satisfactory results may be obtained even with just single-energy measurements.



(a) Slice 1: Single energy (b) Slice 1: Dual energy

(d) Slice 2: Single energy (e) Slice 2: Dual energy

(f) Slice 5: Single energy (g) Slice 5: Dual energy

Figure 7·15: Learning-based labeled images obtained with single energy data (left) and dual-energy data (right) overlaid on the 130KVP image.

7.3 Summary

In this chapter we presented a framework for directly segmenting and labeling the scanned objects from multi-energy measurements. Two novel formulations were proposed. In the first formulation a dictionary-based approach is used and the material label image is estimated directly from MECT sinogram data. This formulation requires knowledge of the physical sensing model and the material LACs. Smoothing of the material label image is incorporated via an MRF prior. An iterative algorithm was proposed for obtaining an approximate solution, since solving the batched problem is computationally prohibitive. We showed that the method can achieve accurate material labeling and that using the MRF prior helps to get more homogeneous results. The main limitation of the method is that it is highly time consuming. Future work would include deriving a more efficient solution approach.

In the second formulation the material map is estimated from reconstructed effective attenuation images. Since it is an image-based approach it can be solved much more efficiently than the first formulation. In this formulation the appearance models are learned from training data and knowledge of the system model or the material LACs is not needed. The prior term is based on a boundary field estimate, which provides smoothing of the labeled image inside the objects and clear object boundaries. We proposed an efficient graph-cut solution. We showed that successful material labeling in the presence of metal, shading and streaking can be achieved. These results will be presented at the 2014 SPIE Electronic Imaging conference [Martin et al., 2014b]. The limitation of the method is that it requires a sufficient amount of training data, which may be difficult to obtain for some materials of interest. Perhaps simulations may be used to obtain additional training data in those cases. Another issue is that the effective attenuation images, obtained with FBP, may contain severe streaks and artifacts, which may carry over to the material label image or lead to

labeling errors. The performance of the method may be improved using attenuation images reconstructed by iterative methods which incorporate metal artifact reduction, such as the method in [Kisner et al., 2013], instead of FBP. Another direction which may improve performance is using reconstructed basis coefficient images with reduced artifacts, such as the photoelectric and Compton images obtained with SPDE (see Section 6.5).

Chapter 8

Conclusion

In this dissertation learning and adaptive model-based methods were developed to address the challenges of multi-energy material discrimination for security. Below we summarize the work presented and the main contributions.

In the first part of the dissertation we studied the fundamental information available in the LAC curves of materials which can be used for explosives discrimination. In Chapter 4 we estimated the intrinsic dimensionality of the LACs of different explosive and benign materials using a database which we created. The results suggested that there is information useful for discrimination in higher than two dimensional representations, contrary to the prevailing wisdom in the medical domain. In Chapter 5, we presented a learning-based approach for choosing LAC-based features specifically for the task of explosives versus non-explosives classification. We showed that using adaptive classification-aware methods for feature selection may improve detection of explosives relative to conventional basis-decompositions such as photo-Compton.

In Chapter 6 we presented new methods for reconstructing material-specific parameters from MECT measurements in the context of security. In Section 6.1 we presented a post-reconstruction method, which is based on the ρZ projection method proposed in [Heismann et al., 2003]. The new method showed improvement in the effective atomic number and density estimated images in some cases. We believe that the method performance was affected by the large overlap in the system spectral functions we used, but it has potential to provide improved results on other systems.

In Section 6.2 we proposed a new dynamic MECT reconstruction approach, which may be useful when the measurements acquired with different spectral functions are not geometrically aligned. We showed that the results converge to the batched least-squares solution for a small simulated phantom. In Section 6.3 we presented the K-EDEC method, which replaces the polynomial model used in EDEC with a more flexible data based mapping based on kernel smoothing. We showed that K-EDEC may be used as an alternative to EDEC and has potential to perform better than EDEC using additional simulated calibration data. However, when simulated data is considered, another existing solution approach may be used, which provides comparable results. In Section 6.5 we presented the SPDE model-based approach for jointly inverting the basis coefficient images from the basis coefficient sinograms. We showed that using data weighting and a mutual boundary-field in the regularization helps to significantly reduce noise and metal artifacts in the basis coefficient images.

In Chapter 7, we presented a framework for directly segmenting and labeling the scanned objects from multi-energy measurements. Two novel formulations were proposed. In the first formulation a dictionary-based approach is used and the material label image is estimated directly from MECT sinogram data. We showed that the method can achieve accurate material labeling and that using the MRF prior helps to get more homogeneous results. The main limitation of the method is that it is highly time consuming. In the second formulation the material map is estimated from reconstructed effective attenuation images. The appearance models are learned from training data. The prior term is based on a boundary field estimate, which provides smoothing of the labeled image inside the objects and clear object boundaries. We proposed an efficient graph-cut solution. We showed that successful material labeling in the presence of metal, shading and streaking can be achieved.

8.1 Future work

Ideas for future work under the three main topics covered in the dissertation are presented below.

1. Fundamental information contained in X-ray attenuation curves of materials

   - Incorporate X-ray sensing model into LAC dimensionality estimation and LAC-based feature optimization.
   - Incorporate optimized LAC features into MECT reconstruction.
   - Add more material LACs and LAC variations to the database.

2. Estimation of material specific parameters from MECT data

   - Improve the ρZ projection method by using a more precise model to predict the effective attenuation values and a system with well separated spectral functions.
   - Extend the EDEC approach to more than two basis materials. This will allow to span more of the measurement space and potentially improve the accuracy of the results.
   - Develop methods for direct reconstruction of basis coefficient images from MECT measurements without estimating the basis coefficient sinograms.
   - Extend SPDE to other choices of basis coefficients and more than two energies.

3. Direct material identification from MECT data

   - Develop an efficient solution approach to the dictionary-based labeling problem, perhaps using projection-based graph-cuts.

- Extend the learning-based graph cut method to include simulated training data for materials for which the real training data is insufficient.
- Improve the performance of the learning-based graph cut method by using attenuation images reconstructed by iterative methods which incorporate metal artifact reduction, instead of FBP. Alternatively, reconstructed basis coefficient images with reduced artifacts, such as the photoelectric and Compton images obtained with SPDE, may used.
- Combine structure-preserving MECT inversion and material identification in unified framework

Appendix A

Compounds LAC database

We collected information on the chemical composition of different explosive and non-explosive materials, for a total of 320 materials. The list contains 124 explosives and 196 non-explosives. Of the non-explosives, 12 materials are biological (can be found in the body). For each material, using its chemical formula, we constructed its LAC by linearly combining the attenuation coefficients of its constituent elements according to their relative weights [Berger et al., 2005]. The values of the LAC of each material are for energy levels ranging from 10 keV to 150 keV in steps of 1keV for a total of 141 energy levels. The materials are listed in the table below, along with their chemical composition, material class and reference.

Table A.1: Properties of the materials in the Compounds Dataset

	Name and Formula	Density (g/cm^3)	Class	Reference
1.	*1,1,1-trichloroethane* H1.5C1Cl1.5	1.32	Benign	[Katz et al., 2002]
2.	*1,2-Dinitrobenzene* H2C3N1O2	1.59	Explosive	[URI, 2008]
3.	*1,3,3-Trinitroazetidine (TNAZ)* H1.333C1N1.333O2	1.84	Explosive	[URI, 2008]
4.	*1,3,5-Trinitrobenzene* H1C1N1O2	1.76	Explosive	[URI, 2008]
5.	*2,3-Dinitrotoluene* H3C3N1O2	1.2625	Explosive	[URI, 2008]
6.	*2,6-bis(picrylamino)]-3,5 dinitropyridine (PYX)* H1C2.429N1.571O2.286	1.75	Explosive	[URI, 2008]
7.	*2-Nitrotoluene* H7C7N1O2	1.163	Explosive	[URI, 2008]
8.	*2-propanol* H8C3O1	0.786	Benign	[Katz et al., 2002]
9.	*3-Nitro-1,2,4-triazol-5-one (NTO)* H1C1N2O1.5	1.93	Explosive	[URI, 2008]
10.	*A-150 TISSUE-EQUIVALENT PLASTIC* H219.248C140.813N5.458O7.131F2Ca1	1.127	Benign	[ESRF, 2001]

Continued on Next Page...

Table A.1 – Continued

	Name and Formula	Density	Class	Reference
11.	*ABS*	1.027	Benign	[Walter et al., 2006]
	H18.843C16.643N1			
12.	*ADIPOSE TISSUE (ICRU-44)*	0.95	Benign, Bio	[ESRF, 2001]
	H4009.77C1765.152N17.718O616.014Na1.542S			
	...1.106Cl1			
13.	*AIR, DRY (NEAR SEA LEVEL)*	0.001205	Benign	[ESRF, 2001]
	C1N5222.887O1403.204Ar31.101			
14.	*ALANINE*	1.424	Benign	[ESRF, 2001]
	H7C3N1O2			
15.	*AMATOL*	1.71	Explosive	[Dobratz and Crawford, 1985]
	H7.161C1N3.645O5.694			
16.	*AN*	1.725	Explosive	[Dobratz and Crawford, 1985]
	H2N1O1.5			
17.	*ANFO*	0.84	Explosive	Web
	H12.912C1N5.479O8.219			
18.	*AP*	1.95	Explosive	[Dobratz and Crawford, 1985]
	H4N1O4Cl1			
19.	*Acetic acid*	1.049	Benign	[Katz et al., 2002]
	H2C1O1			
20.	*Acetone*	0.791	Benign	[Katz et al., 2002]
	H6C3O1			
21.	*Acetylsalicylic acid*	1.4	Benign	[Katz et al., 2002]
	H2C2.25O1			
22.	*Acrylic*	1.175	Benign	[Walter et al., 2006]
	H3.981C2.458O1			
23.	*Air*	0.0012047	Benign	[ESRF, 2001]
	N167.203O44.857Ar1			
24.	*Aluminium*	2.7	Benign	[ESRF, 2001]
	Al1			
25.	*Aluminium ammonium sulfate*	1.64	Benign	[Katz et al., 2002]
	H4N1O8Al1S2			
26.	*Aluminium sulfate*	2.672	Benign	[Katz et al., 2002]
	O6Al1S1.5			
27.	*Ammonia*	0.771	Benign	Web
	H3N1			
28.	*Ammonium carbonate*	1.5	Benign	[Katz et al., 2002]
	H8C1N2O3			
29.	*Ammonium chloride*	1.5274	Benign	[Katz et al., 2002]
	H4N1Cl1			
30.	*Ammonium dinitramide ADN*	1.885	Explosive	[Akhavan, 2004]
	H1N1O1			
31.	*Amylum*	1.5	Benign	[Katz et al., 2002]
	H2C1.2O1			
32.	*Ascorbic acid*	1.65	Benign	[Katz et al., 2002]
	H1.333C1O1			
33.	*B-100 BONE-EQUIVALENT PLASTIC*	1.45	Benign, Bio	[ESRF, 2001]
	H42.318C29.124N1O1.306F5.741Ca2.87			
34.	*B4C*	2.52	Benign	[ESRF, 2001]
	B4C1			
35.	*BAKELITE*	1.25	Benign	[ESRF, 2001]
	H5.429C6.143O1			
36.	*BLOOD, WHOLE (ICRU-44)*	1.06	Benign, Bio	[ESRF, 2001]
	H5651.319C511.456N131.571O2600.38Na2.429			
	...P1.803S3.483Cl4.726K2.857Fe1			
37.	*BN*	2.25	Benign	[ESRF, 2001]
	B1N1			

Continued on Next Page...

Table A.1 – Continued

	Name and Formula	Density	Class	Reference
38.	*BONE, CORTICAL (ICRU-44)*	1.92	Benign, Bio	[ESRF, 2001]
	H775.495C296.687N68.936O625.058Na1Mg1.89			
	...:2P76.45S2.151Ca129.066			
39.	*BRAIN, GREY/WHITE MATTER (ICRU-44)*	1.04	Benign, Bio	[ESRF, 2001]
	H1702.017C193.559N25.183O713.495Na1.395P			
	...2.071S1Cl1.357K1.23			
40.	*BREAST TISSUE (ICRU-44)*	1.02	Benign, Bio	[ESRF, 2001]
	H3728.383C979.984N75.934O1167.767Na1.542			
	...P1.145S2.211Cl1			
41.	*BTF*	1.901	Explosive	[Dobratz and Crawford, 1985]
	C1N1O1			
42.	*Bakelite*	1.7	Benign	Web
	H3C2Cl1			
43.	*Baratol*	2.63	Explosive	[Dobratz and Crawford, 1985]
	H1.828C2.552N3.103O8.207Ba1			
44.	*Barium Nitrate*	3.24	Explosive	[URI, 2008]
	N2O6Ba1			
45.	*Baronal*	2.32	Explosive	[Akhavan, 2004]
	H4.027C5.638N4.416O10.833Al2.906Ba1			
46.	*BeO*	3.01	Benign	[ESRF, 2001]
	Be1O1			
47.	*Beryllium*	1.845	Benign	[ESRF, 2001]
	Be1			
48.	*Black powder*	1.95	Explosive	[Dobratz and Crawford, 1985]
	H1C20N22O72S20K58			
49.	*Boracitol*	1.54	Explosive	[Dobratz and Crawford, 1985]
	H7.151B1.83C2.321N1O7.491			
50.	*Boric acid*	1.435	Benign	[Katz et al., 2002]
	H3B1O3			
51.	*C-552 AIR-EQUIVALENT PLASTIC*	1.76	Benign	[ESRF, 2001]
	H173.098C295.231O2F173.099Si1			
52.	*CADMIUM TELLURIDE*	6.2	Benign	[ESRF, 2001]
	Cd1Te1			
53.	*CALCIUM SULFATE*	2.96	Benign	[ESRF, 2001]
	O4S1Ca1			
54.	*CARBON DIOXIDE*	0.0018421	Benign	[NIST, 2011]
	C1O2			
55.	*CEF*	1.425	Explosive	[Dobratz and Crawford, 1985]
	H12C6O4P1Cl3			
56.	*CELLULOSE NITRATE*	1.49	Benign	[NIST, 2011]
	H3.348C2.609N1O4.174			
57.	*COMP A-3*	1.672	Explosive	[Dobratz and Crawford, 1985]
	H2C1N1.316O1.316			
58.	*COMP A-5*	1.757	Explosive	[Dobratz and Crawford, 1985]
	H2C1N1.854O1.854			
59.	*COMP B*	1.742	Explosive	[Dobratz and Crawford, 1985]
	H1.3C1N1.074O1.315			
60.	*COMP B-3*	1.75	Explosive	[Dobratz and Crawford, 1985]
	H1.224C1N1.049O1.302			
61.	*COMP C-3*	1.62	Explosive	[Dobratz and Crawford, 1985]
	H1.489C1N1.232O1.368			
62.	*COMP C-4*	1.67	Explosive	[Dobratz and Crawford, 1985]
	H1.945C1N1.352O1.379			
63.	*CONCRETE, BARITE (TYPE BA)*	3.35	Benign	[ESRF, 2001]
	H72.341O396.143Mg1Al3.153Si7.573S68.412C			
	...a25.473Fe17.301Ba68.632			

Continued on Next Page...

Table A.1 – Continued

	Name and Formula	Density	Class	Reference
64.	*CONCRETE, ORDINARY*	2.3	Benign	[ESRF, 2001]
	H420.939C3.971O689.879Na12.7Mg1Al14.197S			
	...i208.232K4.932Ca20.574Fe2.212			
65.	*Cab-O-Sil*	2.3	Explosive	[Dobratz and Crawford, 1985]
	O2Si1			
66.	*Caffeine*	1.23	Benign	[Katz et al., 2002]
	H5C4N2O1			
67.	*Calcium Hypochlorite*	2.35	Explosive	[URI, 2008]
	O2Cl2Ca1			
68.	*Calcium carbonate*	2.71	Benign	Web
	C1O3Ca1			
69.	*Calcium chloride*	2.15	Benign	[Katz et al., 2002]
	Cl2Ca1			
70.	*Calcium hydroxide*	2.211	Benign	[Katz et al., 2002]
	H2O2Ca1			
71.	*Calcium oxide*	3.35	Benign	[Katz et al., 2002]
	O1Ca1			
72.	*Calcium phosphate*	3.14	Benign	[Katz et al., 2002]
	H4O8P2Ca1			
73.	*Calcium sulfate*	2.96	Benign	[Katz et al., 2002]
	O4S1Ca1			
74.	*Carbon*	1	Benign	[ESRF, 2001]
	C1			
75.	*Carbon dioxide, solid*	1.4	Benign	[Katz et al., 2002]
	C1O2			
76.	*Carbonic acid*	1	Benign	[Katz et al., 2002]
	H2C1O3			
77.	*Chromatin*	1.527	Benign	[ESRF, 2001]
	H1665C821.354N288.667O519P35.667S1			
78.	*Citric acid*	1.665	Benign	[Katz et al., 2002]
	H1.333C1O1.167			
79.	*Copper*	8.96	Benign	[ESRF, 2001]
	Cu1			
80.	*Cr2O3*	5.21	Benign	[ESRF, 2001]
	O1.5Cr1			
81.	*CsI*	4.51	Benign	[ESRF, 2001]
	I1Cs1			
82.	*Cyclotol 60/40*	1.68	Explosive	[Dobratz and Crawford, 1985]
	H1.225C1N1.054O1.314			
83.	*Cyclotol 75/25*	1.77	Explosive	[Dobratz and Crawford, 1985]
	H1.449C1N1.326O1.511			
84.	*DATB*	1.837	Explosive	[Dobratz and Crawford, 1985]
	H1C1.2N1O1.2			
85.	*DECN*	1.39	Explosive	[Dobratz and Crawford, 1985]
	H4C2N1O3.5			
86.	*DIPAM*	1.79	Explosive	[Dobratz and Crawford, 1985]
	H1C2N1.333O2			
87.	*DNPA*	1.77	Explosive	[Dobratz and Crawford, 1985]
	H4C3N1O3			
88.	*DOP*	0.986	Explosive	[Dobratz and Crawford, 1985]
	H9.5C6O1			
89.	*Diazodinitrophenol (DDNP)*	1.63	Explosive	[URI, 2008]
	H1C3N2O2.5			
90.	*Dicyanodiamide*	1.4	Explosive	[URI, 2008]
	H2C1N2			
91.	*Dna*	1.7	Benign	[ESRF, 2001]
	H11.452C9.936N3.774O6.097P1			

Continued on Next Page...

Table A.1 – Continued

	Name and Formula	Density	Class	Reference
92.	*E-3 M CERIC AMMONIUM SULFATE SOLUTION* H7338.62N4.001O3757.053S30.585Ce1	1.03	Benign	[ESRF, 2001]
93.	*EDNP* H6C3.5N1O3	1.28	Explosive	[Dobratz and Crawford, 1985]
94.	*EL-506A* H3.972C2.231N1O3.028	1.48	Explosive	[Dobratz and Crawford, 1985]
95.	*EL-506C* H6.31C3.736N1O3.08	1.48	Explosive	[Dobratz and Crawford, 1985]
96.	*EYE LENS (ICRU-44)* H3376.649C575.593N144.274O1431.457Na1.54 ...2P1.145S3.317Cl1	1.07	Benign, Bio	[ESRF, 2001]
97.	*Estane* H39.474C27.053N1O9.263	1.18	Explosive	[Dobratz and Crawford, 1985]
98.	*Ethanol* H6C2O1	0.802	Benign	Web
99.	*Ethanol* H6C2O1	0.789	Benign	[Katz et al., 2002]
100.	*Ethylene Glycol Dinitrate (EGDN)* H2C1N1O3	1.48	Explosive	[URI, 2008]
101.	*Ethylene diamine dinitrate (EDDN)* H5C1N2O3	1.577	Explosive	[URI, 2008]
102.	*Ethylene glycol* H3C1O1	1.1132	Benign	[Katz et al., 2002]
103.	*Explosive D* H1.5C1.5N1O1.75	1.717	Explosive	[Dobratz and Crawford, 1985]
104.	*FEFO* H3C2.5N2O5F1	1.607	Explosive	[Dobratz and Crawford, 1985]
105.	*FERROUS SULFATE (STANDARD FRICKE)* H112359.651O57408.588Na1S409.086Cl1.032F ...e1.029	1.024	Benign	[ESRF, 2001]
106.	*FPC 461* H1.8C2F1.2Cl1	1.7	Explosive	[Dobratz and Crawford, 1985]
107.	*Fiberglass* Be1S2I1La1	0.032	Benign	Web
108.	*Fluorite* F2Ca1	3.18	Benign	[ESRF, 2001]
109.	*GADOLINIUM OXYSULFIDE* O2S1Gd2	7.44	Benign	[ESRF, 2001]
110.	*GAFCHROMIC SENSOR* H11.11C6.297N1O1.5	1.3	Benign	[ESRF, 2001]
111.	*GLASS, BOROSILICATE (PYREX)* B43.634O397.082Na14.438Al5.081Si158.145K ...1	2.23	Benign	[ESRF, 2001]
112.	*GLASS, LEAD* O276.361Si81.373Ti4.778As1Pb102.563	6.22	Benign	[ESRF, 2001]
113.	*GaAs* Ga1As1	5.32	Benign	[ESRF, 2001]
114.	*Glucose* H2C1O1	1.54	Benign	[Katz et al., 2002]
115.	*Glycerol* H2.667C1O1	1.261	Benign	[Katz et al., 2002]
116.	*Gold* Au1	19.3	Benign	[ESRF, 2001]
117.	*Graphite* C1	1.682	Benign	[ESRF, 2001]
118.	*H-6* H518C378N322O402Al148Cl1.8Ca1	1.791	Explosive	[Dobratz and Crawford, 1985]

Continued on Next Page...

Table A.1 – Continued

	Name and Formula	Density	Class	Reference
119.	*H2O2 30p* H1.688O1	1.09	Benign	[Heismann et al., 2003]
120.	*H2SO4 29p* H19.961O10.98S1	1.24	Benign	[Heismann et al., 2003]
121.	*HBX-1* H524C412N314O414Al126Cl1.8Ca1	1.76	Explosive	[Dobratz and Crawford, 1985]
122.	*HBX-3* H436C332N242O320Al258Cl1.8Ca1	1.882	Explosive	[Dobratz and Crawford, 1985]
123.	*HMX* H2C1N2O2	1.9	Explosive	[Dobratz and Crawford, 1985]
124.	*HNAB-I* H1C3N2O3	1.799	Explosive	[Dobratz and Crawford, 1985]
125.	*HNAB-II* H1C3N2O3	1.75	Explosive	[Dobratz and Crawford, 1985]
126.	*HNO-3 16p* H37.726N1O21.363	1.078	Benign	[Heismann et al., 2003]
127.	*HNO-3 31p* H16.571N1O10.785	1.156	Benign	[Heismann et al., 2003]
128.	*HNS* H1C2.333N1O2	1.74	Explosive	[Dobratz and Crawford, 1985]
129.	*Helium* He1	0.0001663	Benign	[ESRF, 2001]
130.	*Heptanitrocubane HpNC* H1C8N7O14	2.028	Explosive	[Akhavan, 2004]
131.	*Hexamethylenetriperoxidediamine (HMTD)* H6C3N1O3	1.57	Explosive	[URI, 2008]
132.	*Hexanitrohexaazaisowurtzitane (CL-20)* H1C1N2O2	2.04	Explosive	[URI, 2008]
133.	*Honey* H2.833C1O1.417	1.36	Benign	[Walter et al., 2006]
134.	*Hydrochloric acid* H1Cl1	1.18	Benign	[Katz et al., 2002]
135.	*Hydroquinone* H3C3O1	1.3	Benign	[Katz et al., 2002]
136.	*Iodine* I1	4.933	Benign	[Katz et al., 2002]
137.	*Iron* Fe1	7.86	Benign	[Katz et al., 2002]
138.	*Iron (III) oxide* O1.5Fe1	5.242	Benign	[Katz et al., 2002]
139.	*Iron(III) chloride* Cl3Fe1	2.898	Benign	[Katz et al., 2002]
140.	*KOH 15-7p* H24.842O12.921Na1	1.132	Benign	[Heismann et al., 2003]
141.	*Kel-F 800* H1C4F5.5Cl1.5	2.02	Explosive	[Dobratz and Crawford, 1985]
142.	*Kerosene* H2.167C1	0.78	Benign	[Katz et al., 2002]
143.	*LITHIUM TETRABORATE* Li1B2O3.5	2.44	Benign	[ESRF, 2001]
144.	*LUNG TISSUE (ICRU-44)* H1997.701C170.903N43.267O915.179Na1.701P ...1.262S1.829Cl1.654K1	1.05	Benign, Bio	[ESRF, 2001]
145.	*LX-01-0* H2.454C1N1.112O2.23	1.23	Explosive	[Dobratz and Crawford, 1985]
146.	*LX-02-1* H162C92.333N31O99.667Si1	1.44	Explosive	[Dobratz and Crawford, 1985]

Continued on Next Page...

Table A.1 – Continued

	Name and Formula	Density	Class	Reference
147.	*LX-04-1* H4.962C2.981N4.423O4.423F1	1.889	Explosive	[Dobratz and Crawford, 1985]
148.	*LX-07-2* H7.486C4.229N6.943O6.943F1	1.892	Explosive	[Dobratz and Crawford, 1985]
149.	*LX-08-0* H8.78C3.86N1.62O5.9Si1	1.439	Explosive	[Dobratz and Crawford, 1985]
150.	*LX-09* H137C71.5N129.5O136F1	1.867	Explosive	[Dobratz and Crawford, 1985]
151.	*LX-10* H15.647C8.353N15.176O15.176F1	1.896	Explosive	[Dobratz and Crawford, 1985]
152.	*LX-14-0* H1.921C1N1.704O1.75	1.849	Explosive	[Dobratz and Crawford, 1985]
153.	*LX-15* H32.25C76.25N31.75O63.25F3.25Cl1	1.752	Explosive	[Dobratz and Crawford, 1985]
154.	*LX-16* H50.4C32.2N24.4O72.8F1	1.767	Explosive	[Dobratz and Crawford, 1985]
155.	*LX-17-0* H40.37C42.407N39.815O39.815F3.704Cl1	1.944	Explosive	[Dobratz and Crawford, 1985]
156.	*Latex* H1.6C1	0.92	Benign	[Katz et al., 2002]
157.	*Lead* Pb1	11.34	Benign	[Katz et al., 2002]
158.	*Lead azide* N6Pb1	4.8	Explosive	[Dobratz and Crawford, 1985]
159.	*Lead styphnate* H3C6N3O9Pb1	3.06	Explosive	[Dobratz and Crawford, 1985]
160.	*LiOH 6-7p* H62.834O31.917Na1	1.061	Benign	[Heismann et al., 2003]
161.	*Lipid* H9.921C5O1	1	Benign	[ESRF, 2001]
162.	*Lithium fluoride* Li1F1	2.635	Benign	Web
163.	*Lucite* H4C2.5O1	1.19	Benign	Web
164.	*MAGNESIUM TETRABORATE* B4O7Mg1	2.53	Benign	[ESRF, 2001]
165.	*MEN-II* H5.308C1.549N1O2.331	1.017	Explosive	[Dobratz and Crawford, 1985]
166.	*MERCURIC IODIDE* I2Hg1	6.36	Benign	[ESRF, 2001]
167.	*MS20 TISSUE SUBSTITUTE* H3173.112C1913.534N50.054O458.886Mg211.1 ...6Cl1	1	Benign	[NIST, 2011]
168.	*MUSCLE, SKELETAL (ICRP)* H139395.035C12534.17N2759.01O65862.311Na ...45.546Mg10.914P81.134S104.929Cl31.11K107 ....838Ca1.045Fe1Zn1.068	1.04	Benign	[NIST, 2011]
169.	*MUSCLE, SKELETAL (ICRU-44)* H3587.689C422.102N86.058O1573.273Na1.542 ...P2.289S3.317Cl1K3.627	1.05	Benign, Bio	[ESRF, 2001]
170.	*MUSCLE-EQUIVALENT LIQUID, WITH SUCROSE* H38.507C5.139N1O17.536	1.11	Benign	[NIST, 2011]
171.	*MUSCLE-EQUIVALENT LIQUID, WITHOUT SUCROSE* H39.971C3.949N1O18.336	1.07	Benign	[NIST, 2011]
172.	*Magnesium* Mg1	1.738	Benign	Web

Continued on Next Page...

Table A.1 – Continued

	Name and Formula	Density	Class	Reference
173.	*Magnesium hydroxide*	2.3446	Benign	[Katz et al., 2002]
	H2O2Mg1			
174.	*Magnesium sulfate*	2.664	Benign	[Katz et al., 2002]
	O4Mg1S1			
175.	*Manganese dioxide*	5.026	Benign	[Katz et al., 2002]
	O2Mn1			
176.	*Mercury*	13.546	Benign	[Katz et al., 2002]
	Hg1			
177.	*Mercury Fulminate*	4.42	Explosive	[Akhavan, 2004]
	C2N2O2Hg1			
178.	*Methanol*	0.7918	Benign	[Katz et al., 2002]
	H4C1O1			
179.	*Methyl alcohol*	0.809	Benign	Web
	H4C1O1			
180.	*Methyl salicylate*	1.174	Benign	[Katz et al., 2002]
	H4C4N1O1.5Na1			
181.	*Methylene blue*	1.757	Benign	[Katz et al., 2002]
	H18C16N3S1Cl1			
182.	*Metrioltrinitrate (TMETN)*	1.46	Explosive	[URI, 2008]
	H3C1.667N1O3			
183.	*MgO*	3.58	Benign	[ESRF, 2001]
	O1Mg1			
184.	*Minol-2*	1.7	Explosive	[Dobratz and Crawford, 1985]
	H3.892C1.662N2.068O3.459Al1			
185.	*MoSi2*	6.31	Benign	[ESRF, 2001]
	Si2Mo1			
186.	*Mylar*	1.4	Benign	[ESRF, 2001]
	H2C2.5O1			
187.	*NC 12p N*	1.653	Explosive	[Dobratz and Crawford, 1985]
	H3.111C2.667N1O4.222			
188.	*NC 13-35p N*	1.656	Explosive	[Dobratz and Crawford, 1985]
	H2.8C2.4N1O4			
189.	*NC 14-14p N*	1.659	Explosive	[Dobratz and Crawford, 1985]
	H2.333C2N1O3.667			
190.	*NH-3 10p*	0.96	Benign	[Heismann et al., 2003]
	H20.016N1O8.508			
191.	*NH-3 25p*	0.916	Benign	[Heismann et al., 2003]
	H8.672N1O2.836			
192.	*NH-3 5p*	0.98	Benign	[Heismann et al., 2003]
	H38.923N1O17.961			
193.	*NM*	1.13	Explosive	[Dobratz and Crawford, 1985]
	H3C1N1O2			
194.	*NQ*	1.775	Explosive	[Dobratz and Crawford, 1985]
	H4C1N4O2			
195.	*NaOH 10p*	1.093	Benign	[Heismann et al., 2003]
	H40.963O20.982Na1			
196.	*NaOH 20p*	1.189	Benign	[Heismann et al., 2003]
	H18.761O9.881Na1			
197.	*Naphthalene*	1.14	Benign	[Katz et al., 2002]
	H1C1.25			
198.	*NiO*	6.67	Benign	[ESRF, 2001]
	O1Ni1			
199.	*Nickel*	8.876	Benign	[ESRF, 2001]
	Ni1			
200.	*Nickel*	8.9	Benign	[Katz et al., 2002]
	Ni1			

Continued on Next Page...

Table A.1 – Continued

	Name and Formula	Density	Class	Reference
201.	*Nitrobenzene* H5C6N1O2	1.205	Explosive	[URI, 2008]
202.	*Nitrocellulose* H2.333C2N1O3.667	1.67	Explosive	[URI, 2008]
203.	*Nitrogen (liquid)* N1	0.808	Benign	[Katz et al., 2002]
204.	*Nitroglycerin* H1.667C1N1O3	1.596	Explosive	[Dobratz and Crawford, 1985]
205.	*Nitroguanidine* H4C1N4O2	1.71	Explosive	[Akhavan, 2004]
206.	*Nucleosome* H140.333C106.336N34.333O46.333P5.333S1	1.5	Benign	[ESRF, 2001]
207.	*Nylon* H11.255C6.033N1O1.129	1.129	Benign	[Walter et al., 2006]
208.	*OVARY (ICRU-44)* H2036.491C151.371N33.497O938.394Na1.701P ...1.262S1.219Cl1.103K1	1.05	Benign, Bio	[ESRF, 2001]
209.	*Octanitrocubane ONC* C1N1O2	1.98	Explosive	[Akhavan, 2004]
210.	*Octol 75/25* H1.449C1N1.326O1.511	1.843	Explosive	[Dobratz and Crawford, 1985]
211.	*Oxalic acid* H1C1O2	1.9	Benign	[Katz et al., 2002]
212.	*PARAFFIN WAX* H2.08C1	0.93	Benign	[NIST, 2011]
213.	*PBX-9007* H1.635C1N1.234O1.239	1.697	Explosive	[Dobratz and Crawford, 1985]
214.	*PBX-9010* H27C15.444N27O27F2.889Cl1	1.822	Explosive	[Dobratz and Crawford, 1985]
215.	*PBX-9011* H1.838C1N1.416O1.509	1.795	Explosive	[Dobratz and Crawford, 1985]
216.	*PBX-9205* H1.716C1N1.361O1.372	1.72	Explosive	[Dobratz and Crawford, 1985]
217.	*PBX-9404-3* H275C140N257O269P1Cl3	1.865	Explosive	[Dobratz and Crawford, 1985]
218.	*PBX-9407* H38C20.143N36.286O36.286F1.286Cl1	1.81	Explosive	[Dobratz and Crawford, 1985]
219.	*PBX-9501* H1.946C1N1.769O1.83	1.855	Explosive	[Dobratz and Crawford, 1985]
220.	*PBX-9502* H58.684C60.526N58.158O58.158F3.421Cl1	1.942	Explosive	[Dobratz and Crawford, 1985]
221.	*PBX-9503* H60C56.842N59.474O59.474Cl1	1.936	Explosive	[Dobratz and Crawford, 1985]
222.	*PETN* H2C1.25N1O3	1.78	Explosive	[Dobratz and Crawford, 1985]
223.	*PHOTOGRAPHIC EMULSION (KODAK TYPE AA)* H10.855C6.293N1.847O3.659Br1Ag1	2.2	Benign	[ESRF, 2001]
224.	*PHOTOGRAPHIC EMULSION (STANDARD NUCLEAR)* H568.993C244.714N56.104O168.045S2.397Br1 ...77.709Ag178.774I1	3.815	Benign	[ESRF, 2001]
225.	*PLASTIC SCINTILLATOR (VINYLTOLUENE)* H1.107C1	1.032	Benign	[ESRF, 2001]
226.	*POLYETHYLENE* H2C1	0.94	Benign	[NIST, 2011]
227.	*POLYVINYL CHLORIDE* H3C2Cl1	1.406	Benign	[ESRF, 2001]

Continued on Next Page...

Table A.1 – Continued

	Name and Formula	Density	Class	Reference
228.	*PTX-1*	1.68	Explosive	[Akhavan, 2004]
	H1.091C1.152N1O1.404			
229.	*PTX-2*	1.7	Explosive	[Akhavan, 2004]
	H1.323C1N1.007O1.574			
230.	*PVA-4*	1.6	Explosive	[Akhavan, 2004]
	H1.849C1N1.428O1.554			
231.	*PVC*	1.364	Benign	[Walter et al., 2006]
	H3.641C2.199Cl1			
232.	*Paradichlorobenzene*	1.3	Benign	[Katz et al., 2002]
	H2C3Cl1			
233.	*Parylene-C*	1.29	Benign	[ESRF, 2001]
	H7C8Cl1			
234.	*Pentolite 50/50*	1.71	Explosive	[Dobratz and Crawford, 1985]
	H1.837C1.806N1O2.496			
235.	*Picratol*	1.63	Explosive	[Akhavan, 2004]
	H1.321C2.161N1O2.173			
236.	*Picric acid*	1.76	Explosive	[Dobratz and Crawford, 1985]
	H1C2N1O2.333			
237.	*Polycarbonate*	1.179	Benign	[Walter et al., 2006]
	H4.838C5.385O1			
238.	*Polycarbonate Kimfol*	1.2	Benign	[ESRF, 2001]
	H4.667C5.333O1			
239.	*Polyimide*	1.43	Benign	[ESRF, 2001]
	H5C11N1O2.5			
240.	*Polypropylene*	0.949	Benign	[Walter et al., 2006]
	H2.002C1			
241.	*Polystyrene*	1.019	Benign	[Walter et al., 2006]
	H1.05C1			
242.	*Polystyrene exp.*	1.12	Explosive	[Dobratz and Crawford, 1985]
	H1C1			
243.	*Polyurethane 40A*	1.184	Benign	[Walter et al., 2006]
	H73.758C53.824N1O21.415			
244.	*Polyurethane 80A*	1.235	Benign	[Walter et al., 2006]
	H31.035C22.43N1O10.126			
245.	*Potassium Chlorate*	2.32	Explosive	[URI, 2008]
	O3Cl1K1			
246.	*Potassium Dichromate*	2.676	Explosive	[URI, 2008]
	O3.5K1Cr1			
247.	*Potassium bitartrate*	1.05	Benign	[Katz et al., 2002]
	H5C4O6K1			
248.	*Potassium bromide*	2.75	Benign	[Katz et al., 2002]
	K1Br1			
249.	*Potassium chloride*	1.984	Benign	[Katz et al., 2002]
	Cl1K1			
250.	*Potassium ferricyanide*	1.89	Benign	[Katz et al., 2002]
	C6N6K3Fe1			
251.	*Potassium hydroxide*	2.044	Benign	[Katz et al., 2002]
	H1O1K1			
252.	*Potassium nitrate*	2.1	Explosive	[URI, 2008]
	N1O3K1			
253.	*Potassium perchlorate*	2.52	Explosive	[URI, 2008]
	O4Cl1K1			
254.	*Potassium permanganate*	2.703	Benign	[Katz et al., 2002]
	O4K1Mn1			
255.	*Protein*	1.35	Benign	[ESRF, 2001]
	H81C54.835N14.833O14.833S1			

Continued on Next Page...

Table A.1 – Continued

	Name and Formula	Density	Class	Reference
256.	*RADIOCHROMIC DYE FILM (NYLON BASE)*	1.08	Benign	[ESRF, 2001]
	H14.329C7.715N1O1.281			
257.	*RDX*	1.806	Explosive	[Dobratz and Crawford, 1985]
	H2C1N2O2			
258.	*Rutile*	4.26	Benign	[ESRF, 2001]
	O1.999Ti1			
259.	*SODIUM IODIDE*	3.667	Benign	[NIST, 2011]
	Na1I1			
260.	*STILBENE*	0.9707	Benign	[NIST, 2011]
	H1C1.167			
261.	*Salt*	2.17	Benign	Web
	Na1Cl1			
262.	*Sapphire*	3.97	Benign	[ESRF, 2001]
	O1.5Al1			
263.	*SiC*	3.217	Benign	[ESRF, 2001]
	C1Si1			
264.	*Silicon*	2.33	Benign	Web
	Si1			
265.	*Silicon dioxide*	2.648	Benign	[Katz et al., 2002]
	O2Si1			
266.	*Silicon nitride*	3.44	Benign	[ESRF, 2001]
	N1.333Si1			
267.	*Silver*	10.5	Benign	[Katz et al., 2002]
	Ag1			
268.	*Silver Nitrate*	4.35	Explosive	[URI, 2008]
	N1O3Ag1			
269.	*Silver azide*	5.1	Explosive	[Akhavan, 2004]
	N3Ag1			
270.	*Sodium Bicarbonate*	2.159	Benign	Web
	H1C1O3Na1			
271.	*Sodium Chlorate*	2.5	Explosive	[URI, 2008]
	O3Na1Cl1			
272.	*Sodium acetate*	1.528	Benign	[Katz et al., 2002]
	H3C2O2Na1			
273.	*Sodium bicarbonate*	2.2	Benign	[Katz et al., 2002]
	H1C1O3Na1			
274.	*Sodium bisulfate*	1.8	Benign	[Katz et al., 2002]
	H1O4Na1S1			
275.	*Sodium borate*	1.73	Benign	[Katz et al., 2002]
	B2O3.5Na1			
276.	*Sodium carbonate*	2.54	Benign	[Katz et al., 2002]
	C1O3Na2			
277.	*Sodium chloride*	2.165	Benign	[Katz et al., 2002]
	Na1Cl1			
278.	*Sodium hydroxide*	2.13	Benign	[Katz et al., 2002]
	H1O1Na1			
279.	*Sodium hypochlorite*	1.11	Benign	Web
	O1Na1Cl1			
280.	*Sodium nitrate*	2.267	Explosive	[URI, 2008]
	N1O3Na1			
281.	*Sodium nitrate*	2.257	Benign	[Katz et al., 2002]
	N1O3Na1			
282.	*Sodium silicate*	2.4	Benign	[Katz et al., 2002]
	O3Na2Si1			
283.	*Sodium sulfate*	2.664	Benign	[Katz et al., 2002]
	O4Na2S1			

Continued on Next Page...

Table A.1 – Continued

	Name and Formula	Density	Class	Reference
284.	*Sodium sulfite* O3Na2S1	2.633	Benign	[Katz et al., 2002]
285.	*Sodium thiosulfate* O1.5Na1S1	1.667	Benign	[Katz et al., 2002]
286.	*Sucrose* H2C1.091O1	1.587	Benign	[Katz et al., 2002]
287.	*Sulfur* S1	2.07	Benign	[Katz et al., 2002]
288.	*Sulfuric acid* H2O4S1	1.84	Benign	[Katz et al., 2002]
289.	*Sylgard 182* H6C2O1Si1	1.05	Explosive	[Dobratz and Crawford, 1985]
290.	*TACOT* H1C3N2O2	1.85	Explosive	[Dobratz and Crawford, 1985]
291.	*TATB* H1C1N1O1	1.938	Explosive	[Dobratz and Crawford, 1985]
292.	*TESTIS (ICRU-44)* H3257.355C255.306N44.227O1482.924Na2.695 ...P1S1.932Cl1.747K1.584	1.04	Benign, Bio	[ESRF, 2001]
293.	*TETRYL* H1C1.4N1O1.6	1.73	Explosive	[Dobratz and Crawford, 1985]
294.	*TISSUE, SOFT (ICRU FOUR-COMPONENT)* H54.075C4.979N1O25.652	1	Benign	[ESRF, 2001]
295.	*TISSUE, SOFT (ICRU-44)* H1793.844C211.051N43.029O784.42Na1.542P1 ....717S1.658Cl1K1.36	1.06	Benign, Bio	[ESRF, 2001]
296.	*TISSUE-EQUIVALENT GAS (METHANE BASED)* H40.25C15.125N1O10.125	0.001064	Benign	[ESRF, 2001]
297.	*TISSUE-EQUIVALENT GAS (PROPANE BASED)* H40.741C18.945N1O7.333	0.001826	Benign	[ESRF, 2001]
298.	*TNM* C1N4O8	1.65	Explosive	[Dobratz and Crawford, 1985]
299.	*TNT* H1.667C2.333N1O2	1.654	Explosive	[Dobratz and Crawford, 1985]
300.	*TOLUENE* H1.143C1	0.8669	Benign	[NIST, 2011]
301.	*Talc* H1O6Mg1.5Si2	2.8	Benign	Web
302.	*Teflon* C1F2.024	2.127	Benign	[Walter et al., 2006]
303.	*Teflon* C1F2	2.2	Benign	[ESRF, 2001]
304.	*Tetrazene* H8C2N10O1	1.7	Explosive	[Akhavan, 2004]
305.	*Tetrytol 70/30* H1.164C1.629N1O1.698	1.61	Explosive	[Akhavan, 2004]
306.	*Theobromine* H4C3.5N2O1	1.6	Benign	Web
307.	*TiN* N1Ti1	5.22	Benign	[ESRF, 2001]
308.	*Torpex* H3.021C2.698N2.493O3.285Al1	1.81	Explosive	[Akhavan, 2004]
309.	*Triacetonetriperoxide (TATP)* H3C1.5O1	1.18	Explosive	[URI, 2008]
310.	*Triethyleneglycol dinitrate (TEGDN)* H6C3N1O4	1.335	Explosive	[URI, 2008]

Continued on Next Page...

Table A.1 – Continued

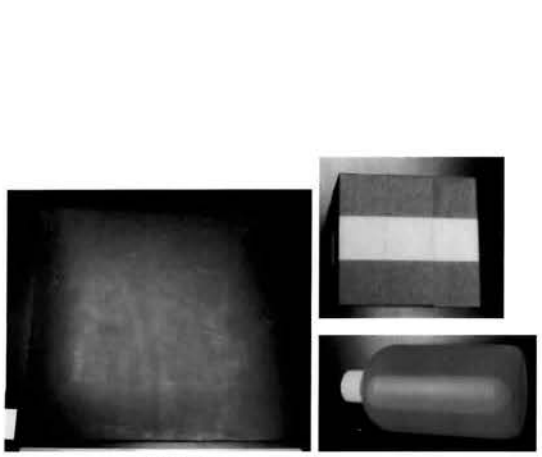
	Name and Formula	Density	Class	Reference
311.	*Tungsten (wolfram)*	19.3	Benign	[Katz et al., 2002]
	W1			
312.	*ULE*	2.205	Benign	[ESRF, 2001]
	O26.659Si12.33Ti1			
313.	*Urea*	1.32	Benign	[Katz et al., 2002]
	H4C1N2O1			
314.	*Vinegar*	1.01	Benign	Web
	H2C1O1			
315.	*Viton A*	1.8	Explosive	[Dobratz and Crawford, 1985]
	H1C1.429F1.857			
316.	*Water*	0.9982	Benign	[Walter et al., 2006]
	H2O1			
317.	*XTX-8003*	1.556	Explosive	[Dobratz and Crawford, 1985]
	H13.481C6.667N3.741O12.259Si1			
318.	*XTX-8004*	1.579	Explosive	[Dobratz and Crawford, 1985]
	H14C6N8O9Si1			
319.	*Zerodur*	2.53	Benign	[ESRF, 2001]
	Li2O123Al25Si28P8Ti1Zn1.5Zr1			
320.	*Zinc*	7.14	Benign	[Katz et al., 2002]
	Zn1			

Appendix B

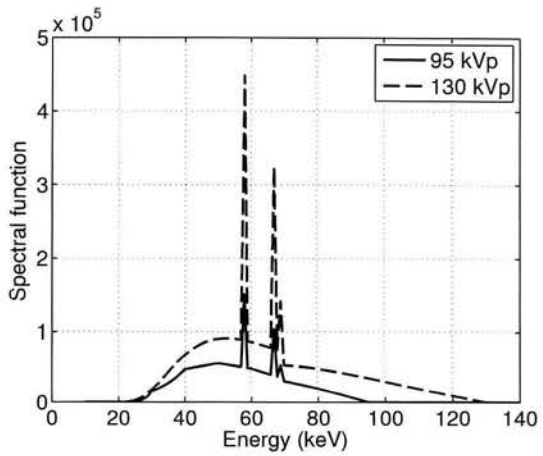
Imatron scans database

In 2012-2013, the ALERT center of excellence led a project entitled Reconstruction Advances in CT Based Object Detection Systems, which is also known as Task Order Three (TO3) [Crawford et al., 2013]. For this project, a database of projection and image data corresponding to scans of objects of interest in the presence of various amounts of clutter was created. Some of the work in this thesis was developed for this project and this database was used to test the performance of the proposed methods.

The data was acquired by the Imatron C300 electron-beam medical scanner. Examples of the objects scanned is shown in Figure B·1a.



(a) Scanned objects



(b) Estimated spectra

Figure B·1: Left: examples of objects appearing in the scans: a thin rubber sheet, a water bottle, and a Teflon cube. Right: estimates of the Imatron system spectra used when acquiring dual-energy measurements.

Dual-energy data was measured by repeating the same scan with 95kVp and 130kVp source spectra. The 95 kVp scan was performed with a tube current of 630 mA and exposure time of 0.5s. The 130 kVp scan was performed with a tube current of 630 mA and exposure time of 0.1s.

An estimate of the spectra is shown in Figure B·1b. It was modeled by Dr. Taly Gilat Schmidt from Marquette University using the SPEC78 software [Cranley et al., 1997].

In our work, we processed two-dimensional scan slices. For the methods requiring sinogram data we used rebinned parallel sinograms with 720 angles and 1024 bins. The reconstructed images were 512× 512 with pixel spacing of 0.928 mm.

We also used code for Imatron FBP inversion provided by Dr. Patrick La Riviere from Univeristy of Chicago, as well as an estimate of the Imatron forward projection matrix provided by Penchong Jin from Purdue University. The filter in FBP was a sharp filter.

References

Achterhold, K., Bech, M., Schleede, S., Potdevin, G., Ruth, R., Loewen, R., and Pfeiffer, F. (2013). Monochromatic computed tomography with a compact laser-driven x-ray source. *Scientific Reports*, 3:1313.

Akhavan, J. (2004). *The Chemistry of Explosives*. Royal Society of Chemistry.

Alvarez, R. E. (2011). The dimensionality of attenuation coefficients. `http://www.aprendtech.com/blog/Post5/MuDim2.html`.

Alvarez, R. E. and Macovski, A. (1976). Energy-selective reconstruction in X-ray computerized tomography. *Physics in Medicine and Biology*, 21(5):733–744.

Barnes, E. (2008). GE focuses on high-res CT with launch of LightSpeed CT750 scanner. `http://www.auntminnie.com`.

Berger, M., Hubbell, J., Seltzer, S., Chang, J., Coursey, J., Sukumar, R., and Zucker, D. (2005). XCOM: Photon cross section database. `http://physics.nist.gov/xcom`.

Boykov, Y., Veksler, O., and Zabih, R. (2001). Fast approximate energy minimization via graph cuts. *IEEE Transactions on Pattern Analysis and Machine Intelligence*, 23(11):1222–1239.

Butala, M., Frazin, R., Chen, Y., and Kamalabadi, F. (2007). A Monte Carlo technique for large-scale dynamic tomography. In *IEEE International Conference on Acoustics, Speech and Signal Processing, ICASSP 07*, volume 3, pages 1217–1220.

Butala, M. D., Frazin, R. A., Chen, Y., and Kamalabadi, F. (2009). Tomographic imaging of dynamic objects with the ensemble Kalman filter. *IEEE Transactions on Image Processing*, 18(7):1573–1587.

Cattell, R. B. (1966). The Scree test for the number of factors. *Multivariate Behavioral Research*, 1(2):245–276.

Chen, H.-T., Chang, H.-W., and Liu, T.-L. (2005). Local discriminant embedding and its variants. In *IEEE Computer Society Conference on Computer Vision and Pattern Recognition, CVPR 05*, volume 2, pages 846 – 853.

Cranley, K., Gilmore, B., Fogarty, G. W. A., Desponds, L., and Sutton, D. G. (1997). Catalogue of diagnostic X-ray spectra and other data. *Institute of Physics and Engineering in Medicine (IPEM) Report 78.*

Crawford, C., Martz, H., and Karl, W. C. (2013). Research and development of reconstruction advances in CT-based object detection systems - final report. Technical report, ALERT DHS Center of Excellence.

Dobratz, B. and Crawford, P. (1985). *LLNL Explosives Handbook: Properties of Chemical Explosives and Explosive Simulants.* Lawrence Livermore National Laboratory.

Duan, X., Wang, J., Yu, L., Leng, S., and McCollough, C. H. (2011). CT scanner X-ray spectrum estimation from transmission measurements. *Medical Physics*, 38:993–997.

Eger, L., Do, S., Ishwar, P., Karl, W. C., and Pien, H. (2011a). A learning-based approach to explosives detection using multi-energy X-ray computed tomography. In *IEEE International Conference on Acoustics, Speech and Signal Processing, ICASSP 11*, pages 2004–2007.

Eger, L., Ishwar, P., Karl, W. C., and Pien, H. (2011b). Classification-aware dimensionality reduction methods for explosives detection using multi-energy X-ray computed tomography. In *Proceedings of SPIE*, volume 7873, page 78730Q.

Eilbert, R. F. and Krug, K. D. (1993). Aspects of image recognition in Vivid technologies' dual-energy X-ray system for explosives detection. In *Proceedings of SPIE*, volume 1824, pages 127–143.

Engler, P. and Friedman, W. D. (1990). Review of dual-energy computed tomography techniques. *Materials Evaluation*, 48:623–629.

ESRF (2001). ESRF Scientific Computing: Compounds database. `http://www.esrf.eu/UsersAndScience/Experiments/TBS/SciSoft`.

Fessler, J. A., Elbakri, I. A., Sukovic, P., and Clinthorne, N. H. (2002). Maximum-likelihood dual-energy tomographic image reconstruction. In *Proceedings of SPIE*, volume 4684, pages 38–49.

Foley, D. and Sammon, J.W., J. (1975). An optimal set of discriminant vectors. *IEEE Transactions on Computers*, C-24(3):281 – 289.

Fukunaga, K. and Mantock, J. M. (1983). Nonparametric discriminant analysis. *IEEE Transactions on Pattern Analysis and Machine Intelligence*, PAMI-5(6):671 –678.

George, A. K., Arai, A. E., and McVeigh, E. R. (2009). Time-resolved cardiac CT reconstruction using a nonlinear Kalman-filter based algorithm. In *IEEE International Symposium on Biomedical Imaging: From Nano to Macro, ISBI 09*, pages 859 –862.

Golub, G. and Reinsch, C. (1970). Singular value decomposition and least squares solutions. *Numerische Mathematik*, 14:403–420.

Gordon, B. M., Weedon, H., Izrailit, I., Fox, T. R., and Moore, J. F. (1997). Dual energy power supply. US Patent 5661774.

Hastie, T., Tibshirani, R., Friedman, J., and Franklin, J. (2005). The elements of statistical learning: data mining, inference and prediction. *The Mathematical Intelligencer*, 27(2):83–85.

Heismann, B. J. and Balda, M. (2010). Evaluation of an image-based algorithm for quantitative spectral CT applications. In *Proceedings of SPIE*, volume 7622, page 76223M.

Heismann, B. J., Leppert, J., and Stierstorfer, K. (2003). Density and atomic number measurements with spectral X-ray attenuation method. *Journal of Applied Physics*, 94(3):2073–2079.

Hsu, C.-W., Chang, C.-C., and Lin, C.-J. (2003). A practical guide to support vector classification. Technical report, Department of Computer Science, National Taiwan University.

Hussein, E. M. A. and Waller, E. J. (1998). Review of one-side approaches to radiographic imaging for detection of explosives and narcotics. *Radiation Measurements*, 29(6):581 – 591.

Icar, A. (2009). A.I. explosives. `http://www.aiexplosives.com`.

Ihler, A. (2003). Kernel density estimation toolbox for MATLAB (R13). `http://www.ics.uci.edu/~ihler/code/`.

Johnson, T. R. C., Krau, B., Sedlmair, M., Grasruck, M., Bruder, H., Morhard, D., Fink, C., Weckbach, S., Lenhard, M., Schmidt, B., Flohr, T., Reiser, M. F., and Becker, C. R. (2007). Material differentiation by dual energy CT: initial experience. *European Radiology*, 17(6):1510–1517.

Kaiser, H. F. (1960). The Application of Electronic Computers to Factor Analysis. *Educational and Psychological Measurement*, 20(1):141–151.

Kak, A. C. and Slaney, M. (2001). *Principles of Computerized Tomographic Imaging*. Society of Industrial and Applied Mathematics.

Kalender, W., Klotz, E., and Kostaridou, L. (1988). An algorithm for noise suppression in dual energy CT material density images. *IEEE Transactions on Medical Imaging*, 7:218–224.

Kanamori, T., Hido, S., and Sugiyama, M. (2009). Efficient direct density ratio estimation for non-stationarity adaptation and outlier detection. In Koller, D., Schuurmans, D., Bengio, Y., and Bottou, L., editors, *Advances in Neural Information Processing Systems 21*, pages 809–816.

Katz, D. A., O'Brien, T., Bonham, D., Rubeck, M. L., and Khalsa, G. R. (2002). Common chemicals and supplies in and around your home. `http://www.chymist.com/Common%20chemicals.pdf`.

Kisner, S. J., Jin, P., Bouman, C. A., Sauer, K., Garms, W., Gable, T., Oh, S., Merzbacher, M., and Skatter, S. (2013). Innovative data weighting for iterative reconstruction in a helical CT security baggage scanner. In *IEEE International Carnahan Conference on Security Technology, ICCST 13*.

Kullback, S. (1997). *Information Theory and Statistics*. Courier Dover Publications.

Lehmann, L. A. and Alvarez, R. E. (1986). Energy selective radiography: a review. In J. Kareiakes, S. T. and Orton, C., editors, *Digital Radiography: Selected Topics*, pages 145–188. New York: Plenum.

Lehmann, L. A., Alvarez, R. E., Macovski, A., Brody, W. R., Pelc, N., Reiderer, S. J., and Hall, A. L. (1981). Generalized image combinations in dual KVP digital radiography. *Medical Physics*, 8(5):659–667.

Liu, X., Yu, L., Primak, A., and McCollough, C. (2009). Quantitative imaging of element composition and mass fraction using dual-energy CT: Three-material decomposition. *Medical Physics*, 36:1602.

Lord, S. M. (2011). Aviation security: TSA has enhanced its explosives detection requirements for checked baggage, but additional screening actions are needed. Technical Report GAO-11-740, US Government Accountability Office (GAO).

Maass, C., Baer, M., and Kachelriess, M. (2009). Image-based dual energy CT using optimized precorrection functions: A practical new approach of material decomposition in image domain. *Medical Physics*, 36:3818–3829.

Macovski, A. (1983). *Medical Imaging Systems*. Prentice-Hall.

Madsen, R. E., Hansen, L. K., and Winther, O. (2004). Singular value decomposition and principal component analysis. Technical report.

Martin, L., Karl, W. C., and Ishwar, P. (2014a). Structure-preserving dual-energy reconstruction for luggage screening. Submitted to the IEEE International Conference on Acoustics, Speech and Signal Processing, ICASSP 14.

Martin, L., Tuysuzoglu, A., Ishwar, P., and Karl, W. C. (2014b). Joint metal artifact reduction and material discrimination in X-ray CT using a learning-based graph-cut method. In *SPIE Electronic Imaging Conference*.

Mathworks (2013). Equation solving algorithms. `http://www.mathworks.com/help/optim/ug/equation-solving-algorithms.html`.

Mumford, D. and Shah, J. (1989). Optimal approximations by piecewise smooth functions and associated variational problems. *Communications on Pure and Applied Mathematics*, 42(5):577–685.

NIST (2011). NIST Chemistry WebBook. `http://webbook.nist.gov/chemistry`.

Noh, J., Fessler, J., and Kinahan, P. (2009). Statistical sinogram restoration in dual-energy CT for PET attenuation correction. *IEEE Transactions on Medical Imaging*, 28(11):1688–1702.

O'Sullivan, J. A. and Benac, J. (2007). Alternating minimization algorithms for transmission tomography. *IEEE Transactions on Medical Imaging*, 26(3):283–297.

Paige, C. C. and Saunders, M. A. (1982). LSQR: An algorithm for sparse linear equations and sparse least squares. *ACM Transactions on Mathematical Software (TOMS)*, 8(1):43–71.

Petersilka, M., Bruder, H., Krauss, B., Stierstorfer, K., and Flohr, T. G. (2008). Technical principles of dual source CT. *European Journal of Radiology*, 68(3):362 – 368.

Platten, D. (2007). CT technology, dose and performance - an imPACT course - artefacts. `http://www.impactscan.org/`.

Raich, R., Costa, J. A., Damelin, S. B., and Hero, III, A. O. (2008). Classification Constrained Dimensionality Reduction. *arXiv:0802.2906v2*.

Remeysen, K. and Swennen, R. (2006). Beam hardening artifact reduction in microfocus computed tomography for improved quantitative coal characterization. *International Journal of Coal Geology*, 67(12):101 – 111.

Sammon, J.W., J. (1969). A nonlinear mapping for data structure analysis. *IEEE Transactions on Computers*, C-18(5):401 – 409.

Schubert, H. and Kuznetsov, A. (2004). *Detection of Bulk Explosives: Advanced Techniques against Terrorism*. Kluwer Academic Publishers.

Shikhaliev, P. M. (2009). Projection X-ray imaging with photon energy weighting: experimental evaluation with a prototype detector. *Physics in Medicine and Biology*, 54(16):4971.

Sidky, E. Y., Yu, L., Pan, X., Zou, Y., and Vannier, M. (2005). A robust method of X-ray source spectrum estimation from transmission measurements: Demonstrated on computer simulated, scatter-free transmission data. *Journal of Applied Physics*, 97(12):124701.

Singh, S. and Singh, M. (2003). Explosives detection systems (EDS) for aviation security. *Signal Processing*, 83(1):31–55.

Smith, R. C. and Connelly, J. M. (2011). CT Technologies. In Marshall, M. and Oxley, J. C., editors, *Aspects of Explosives Detection*, pages 131–145. Elsevier Science.

Steidley, J. W. (2008). Exploring the spectrum: Advances and potential for spectral CT. `http://www.healthcare.philips.com/main/products/ct/products/spectral_ct/index.wpd`.

Stenner, P., Berkus, T., and Kachelriess, M. (2007). Empirical dual energy calibration (EDEC) for cone-beam computed tomography. *Medical Physics*, 34:3630.

Sugiyama, M. (2011). Unconstrained least-squares importance fitting (uLSIF) MATLAB code. `http://sugiyama-www.cs.titech.ac.jp/~sugi/software/uLSIF/`.

Sukovic, P. and Clinthorne, N. (2000). Penalized weighted least-squares image reconstruction for dual energy X-ray transmission tomography. *IEEE Transactions on Medical Imaging*, 19(11):1075 –1081.

Tenenbaum, J. B., Silva, V. d., and Langford, J. C. (2000). A global geometric framework for nonlinear dimensionality reduction. *Science*, 290(5500):2319–2323.

Thompson, A. C. et al. (2009). *X-ray Data Booklet*. Lawrence Berkeley National Laboratory, University of California Berkeley, CA.

Tuysuzoglu, A., Karl, W. C., Castanon, D., and Unlu, M. S. (2013). Joint reconstruction and segmentation of electron tomography data. In *Proceedings of SPIE*, volume 8657, page 86570T.

URI (2008). University of Rhode Island Explosives Database. `http://expdb.chm.uri.edu/`.

Velez-Reyes, M. and Jimenez, L. O. (1998). Subset selection analysis for the reduction of hyperspectral imagery. In *IEEE International Geoscience and Remote Sensing Symposium Proceedings, IGARSS 98*, volume 3, pages 1577 –1581.

Walter, D. J., Tkaczyk, E. J., and Wu, X. (2006). Accuracy and precision of dual energy CT imaging for the quantification of tissue fat content. In *Proceedings of SPIE*, volume 6142, page 61421G.

Wang, X., Meier, D., Taguchi, K., Wagenaar, D. J., Patt, B. E., and Frey, E. C. (2011). Material separation in X-ray CT with energy resolved photon-counting detectors. In *Proceedings of SPIE*, volume 7961, page 79611V.

Wickens, T. D. (2001). *Elementary Signal Detection Theory.* Oxford University Press.

Wikipedia (2012). Factor analysis — wikipedia, the free encyclopedia. [Online; accessed 9-February-2012].

Ying, Z., Naidu, R., and Crawford, C. R. (2006). Dual energy computed tomography for explosive detection. *Journal of X-ray Science and Technology*, 14(4):235–256.

Ying, Z., Naidu, R., Guilbert, K., Schafer, D., and Crawford, C. (2007). Dual energy volumetric X-ray tomographic sensor for luggage screening. In *IEEE Sensors Applications Symposium, SAS 07*, pages 1–6.

Yu, L., Primak, A. N., Liu, X., and McCollough, C. H. (2009). Image quality optimization and evaluation of linearly mixed images in dual-source, dual-energy CT. *Medical Physics*, 36:1019–1024.

Zhang, G., Cheng, J., Zhang, L., Chen, Z., and Xing, Y. (2008). A practical reconstruction method for dual energy computed tomography. *Journal of X-Ray Science and Technology*, 16(2):67–88.

Zhang, J., Yang, G., Lee, Y., Chang, S., Lu, J., and Zhou, O. (2007). MO-E-L100J-07: Multiplexing radiography for ultra-fast computed tomography: A feasibility study. *Medical Physics*, 34(6):2527.

Vita

[redacted]

[redacted]

[redacted]

[redacted]

[redacted]

[redacted]